Control of the Unsteady Flow in a Stator Blade Row Interacting with Upstream Moving Wakes

by

Theodore V. Valkov

Baccalauréat es Sciences Pures et Appliquées, Lycée Pierre Mendés-France, Tunis (1985)
B.S. Mechanical Engineering, Ecole Polytechnique de Montréal, Québec (1990)

SUBMITTED TO THE DEPARTMENT OF
AERONAUTICS AND ASTRONAUTICS
IN PARTIAL FULFILLMENT OF THE
REQUIREMENTS FOR THE DEGREE OF

Master of Science
in
Aeronautics and Astronautics
at the
Massachusetts Institute of Technology

May, 1992

Signature of Author Signature redacted
Department of Aeronautics and Astronautics
May, 1992

Certified by Signature redacted
Dr. Choon S. Tan
Thesis Supervisor
Principal Research Engineer

Accepted by Signature redacted
Professor Harold Y. Wachman
Chairman, Departmental Graduate Committee

Control of the Unsteady Flow in a Stator Blade Row Interacting with Upstream Moving Wakes

by

Theodore V. Valkov

Submitted to the Department of Aeronautics and Astronautics
in May 1992 in partial fulfillment of the requirements for the Degree of
Master of Science in Aeronautics and Astronautics

Abstract

A computational study of the unsteady flow in a 2-D stator blade row interacting with upstream rotor wakes has been carried out. A direct spectral-element Navier-Stokes solver has been used for the laminar flow regime (Re<10,000). Turbulent calculations (Re>10^6) are based on the Baldwin-Lomax turbulence model. The rotor wakes are represented by velocity distortions moving along the inlet boundary of the computational domain.

After interception, the rotor wake migrates towards the pressure surface of the stator blades where it forms a pair of counter-rotating vortices. A moving series of such vortex pairs is the dominant form of unsteady flow over the pressure surface. The unsteady flow over the suction surface is characterized by a street of co-rotating vortices, produced in the leading edge region. These vortices consist of boundary layer fluid distorted and detached by the passing wakes. Downstream of the leading edge, each of these vortices induces an associated, opposite-sign vortex. The blade loading fluctuations arising from wake interaction, are of two kinds. First, a strong pressure pulse occurs on the leading edge upon wake interception. This pulse is a potential flow effect associated with the excess tangential velocity in the wake. Second, a moving pattern of pressure fluctuations, associated with the vortices, is present over the blade surface. The pressure fluctuations are negative on the suction surface, and positive on the pressure surface. The unsteady flow features over the suction surface can be adequately represented by linearized perturbation calculations, where the disturbance flow associated with the wakes is linearized about a steady viscous flow.

Three parameters influence the unsteady flow over the suction surface—stator blade loading, excess wake momentum in the stator frame, and wake reduced frequency. The strength of the disturbance flow vortices is directly proportional to the wake momentum and decreases at higher reduced frequencies. An adverse pressure gradient results in stronger vortices and pressure fluctuations. On the pressure surface, the amount of unsteady flow depends on the excess wake momentum only.

Strategies for controlling the unsteady flow are simulated using appropriate blade surface boundary conditions. Fluid removal from the suction surface prevents formation of vortices and reduces the associated loading disturbances. Fluid injection from the pressure surface reduces the pressure fluctuations there.

Thesis advisor: Dr. Choon S. Tan
Title: Principal Research Engineer

Acknowledgements

This thesis is dedicated to my parents, who taught me the importance of hard work and courage for achieving one's goals in life. These lessons were most valuable on the road to and into M.I.T.

I would like to express my special gratitude to Dr. Choon S. Tan, for his friendship as well as for his patient direction, which he constantly provided in his quality of academic advisor.

I wish to extend my special thanks to Professor Edward M. Greitzer for his friendly suggestions and criticisms. The guidance he provided in the early phase of the research has been extremely valuable, and this is gratefully acknowledged.

The insightful comments and suggestions of Professor N.A. Cumpsty were extremely helpful in my work. His interest in the project and his openness are much appreciated. I wish also to thank Professor M. Giles and Professor I.A. Waitz for their useful comments.

I am particularly grateful to Dr. John Adamczyk, Senior Aerospace Scientist at the NASA-Lewis Research Center, for his special interest in the project. Dr. Adamczyk also provided access to the NASA computer facilities, which was essential in the course of my work and is duly acknowledged herein.

My thanks go also to Dr. E. McFarland for making available the PCPANEL computer program, used to obtain irrotational flow solutions. Credit for the development of PCPANEL is given to the Internal Fluid Mechanics Division of the NASA Lewis Research Center.

Support for this project was provided by the Applied Research Laboratory at Pennsylvania State University, under contract N00039-88-C-0051 and the supervision of Dr. William C. Zierke. This support is gratefully acknowledged.

Contents

List of Symbols

a_b	Half-width of a B-vortex.
A	Velocity defect of the wake in the rotor frame.
$A^+(s)$	Pressure gradient function in the Baldwin-Lomax model.
$A_{lmjk}(1)$	Pressure step matrix.
$A_{lmjk}(D)$	Viscous step matrix.
B	Wake thickness parameter.
B^+_{lmjk}	Surface integral operator.
$\tilde{B}_{lmj(k)}$	Local interpolant integral.
c	Stator blade chord.
c_x	Axial component of the stator blade chord.
c_r	Rotor blade chord.
C	Wake intensity parameter.
C_D	Drag coefficient of the rotor blade.
C_K, C_W	Constants in the Baldwin-Lomax model (C_W=0.25; C_K=0.3).
C_p	Static pressure coefficient.
$(C_{p,max})^+_{LE}$	Peak positive pressure coefficient at the leading edge upon interception.
d_w	Distance between the pressure surface and the wake vortices.
D	Effective viscosity; $D = \nu_t + 1/Re$.
D_{jk}	Discretized local derivative operator.
e	Neper constant, $e = \ln^{-1}(1)$.

$\mathbf{e}_d$	Unit vector in the direction of d.
$E(x)$	Integer part of x.
$F(n)$	Function appearing in the Baldwin-Lomax model.
F_K	Klebanoff intermittency factor.
F_W	Wake factor.
h_j	Local Lagrangian interpolant.
i	$\sqrt{-1}$, except when appearing as index.
$I(q)$	Functional of the variable q.
$I_I(f, \mathbf{u})$	Surface integral of type I.
$I_{II}(f, \mathbf{u})$	Surface integral of type II.
J	Jacobian of the local coordinate transformation.
J_o	Wall-normal flux of vorticity.
k	Von Karman constant (k=0.41).
K_1, K_2	Constants in the Baldwin-Lomax model (K_1=0.0168; K_2=1.6).
l	Mixing length.
n	Coordinate normal to the blade surface.
n^+	Law-of-the-wall coordinate.
n_c	Crossover distance between the inner and outer regions.
N	Degree of the expansion in series (Herein N=7).
N_B	Number of B-vortices at given time.
N_r	Number of blades in the rotor.
N_s	Number of blades in the stator.
p	Non-dimensional pressure.
P	Stator-to-rotor blade ratio.
$\bar{P}$	Base (steady) flow pressure field.
Q_E	Set of all spectral elements in the computational domain.
Q_I	Set of the spectral elements on the inlet boundary.
Q_L	Set of the spectral elements on the leading edge.

Q_O	Set of the spectral elements on the outflow boundary.
Q_P	Set of the spectral elements on the pressure surface.
Q_S	Set of the spectral elements on the suction surface.
$r(\omega)$	Largest root of the non-linear equation $2ABCr\exp(-Br^2) = \omega$.
R_a	Artificial viscosity parameter.
Re	Reynolds number based on c_x and U_∞
s	Coordinate along the blade surface.
S	Spacing-to-blade-chord ratio of the stator.
S_r	Spacing-to-blade-chord ratio of the rotor.
t	Non-dimensional time.
t_0	Instant of wake interception by the stator leading edge.
T	Non-dimensional wake passing period.
T_m	Tchebychev polynomial of degree m.
$\mathbf{u}$	Non-dimensional velocity vector in the stationary frame.
u	Non-dimensional axial velocity component in the stationary frame.
u_w	Non-dimensional streamwise velocity component in the wake.
u^+	Law-of-the-wall streamwise velocity component.
U_∞	Axial velocity component far upstream of the stator.
$\bar{\mathbf{U}}$	Base (steady) flow velocity field.
U_D	Velocity difference along lines of constant s.
v	Non-dimensional tangential velocity component in the stationary frame.
v_n	Prescribed normal velocity on the blade surface.
v_w	Non-dimensional crosswise velocity component in the wake.
V	Rotor blade tangential velocity.
w	Flow velocity within the wake, in the rotating frame.
W	Flow velocity outside the wake, in the rotating frame.
x	Non-dimensional axial coordinate in the stationary frame.
x_r	Streamwise coordinate from the rotor blade in the rotating frame.

x_w	Coordinate along the wake centerline in the stationary frame.
y	Non-dimensional tangential coordinate in the stationary frame.
y_r	Normal coordinate from the rotor blade/wake center in the rotating frame.
y_w	Normal coordinate from the wake centerline in the stationary frame.
y_{te}	Tangential location of the trailing edge.

Calligraphic symbols

$\mathcal{A}(x)$	Leading edge pressure pulse shape.
$\mathcal{B}$	Moving pressure disturbance amplitude.
$\mathcal{C}_k$	Amplitude of the kth harmonic of the wake passing frequency.
$\mathcal{S}$	Characteristic space scale.
$\mathcal{T}$	Characteristic time scale.

Greek symbols

β	Wake skew angle.
Γ_B	Circulation of a given B-vortex.
Γ_W	Circulation of a given wake vortex.
δ	Wake thickness in the rotor frame.
δ_{ij}	Kronecker delta function.
Δt	Non-dimensional time increment in the numerical method.
$(\Delta C_p)^+_{PS}$	Peak amplitude of the high-pressure disturbances on the pressure surface.
$(\Delta C_p)^-_{SS}$	Peak-to-peak amplitude of the low-pressure disturbances on the suction surface.
ς	Local coordinate associated with the index j.
η	Local coordinate associated with the index k.
θ	Flow turning angle at the inlet of the stator passage.
κ	Reduced wake passing frequency.
λ_p	Source term in the pressure step.

λ_v	Source term in the viscous step.
Λ	Optimization constraint.
ν_t	Non-dimensional eddy viscosity coefficient.
$\nu_{t,i}$	Inner region eddy viscosity coefficient.
$\nu_{t,o}$	Outer region eddy viscosity coefficient.
ρ; ρ_∞	Density of the working fluid.
σ	Suction/Blowing coefficient.
ϕ	Flow coefficient.
Φ	Velocity potential.
ψ	Head coefficient.
ω	Vorticity.
Ω	Rotor rotation frequency.
Ω_s	Stator blade pitching frequency.

Subscripts and superscripts

$()_b$	Referring to a node on the periodic boundary of the computational domain.
$()_i$	Referring to a node on the inlet boundary of the computational domain.
$()^i_{jk}$; $()_{jk,i}$	Discretized value at the collocation point (ζ_j, η_k) on element i.
$()_o$	Referring to a node on the outflow boundary of the computational domain.
$()_s$	Referring to a node on the solid boundary of the computational domain.
$()_{max}$; $()_m$	Referring to the maximum value of a variable.
$()_{min}$	Referring to the minimum value of a variable.
$()_{PS}$	Relative to the pressure surface.
$()_{SS}$	Relative to the suction surface.
$()_\infty$	Referring to the flow conditions far upstream of the stator.
$()^n$	Referring to the flowfield at time step n.
$()'$	Randomly fluctuating quantity (in turbulent flow).

Special notation

$\tilde{()}$	Referring to the disturbance flow = unsteady flow – steady flow.
$\bar{()}$	Referring to the steady flow = flow without wakes.
$\hat{()}$	Referring to the flow update from the viscous step.
$\hat{\hat{()}}$	Referring to the flow update from the pressure step.
$\bar{()}_R$	Time mean at every point of the spatial domain R.
$\breve{()}_R$	Time RMS at every point of the spatial domain R.
$\breve{()}_R$	Unsteadiness index over the spatial domain R.
$<>$	Ensemble average.
∇	Gradient operator.
$\tilde{\nabla}^i_{jk}$	Discretized gradient operator, not containing transformation Jacobians.
$\sum^{i \in Q}$	Sum taken over all the spectral elements in the set Q.
$\sum_{i,j,k,l\ldots}$	$\sum_i \sum_j \sum_k \sum_l \ldots$
$\sum_{i=\pm 1} q_i$	$q_1 + q_{-1}$

List of Figures

All supporting figures are attached in the following numerical order at the end of the thesis.

List of Tables

Chapter 1

Introduction and Review of Previous Work

1.1. Background

Turbomachinery flowfields are characterized by the presence of circumferential non-uniformities due to the individual blades in each blade row. These non-uniformities interact periodically with the blades on adjacent blade rows in relative motion, resulting in the production of unsteady flow. The unsteady flow leads to significant fluctuations of the blade loading; it also influences heat transfer, separation and boundary layer characteristics. For this reason, the interaction between blade rows in relative motion is often associated with undesirable effects such as noise and vibration; and may affect the reliability and the performance of the machine. In comparison to other sources of unsteady flow in turbomachinery, such as flutter, vortex shedding, turbulence and rotating stall; blade row interaction is often the dominant disturbing influence.

There are four different types of unsteady flow associated with blade row interaction, depending on the nature of the circumferential non-uniformities encountered by the blades :

- Interaction with moving static pressure field non-uniformities.
- Interaction with moving vortices from the upstream blade rows (e.g. tip vortices).
- Interaction with moving wakes shed from the upstream blade rows.
- Interaction with moving shock waves from the upstream blade rows.

The influence of the static pressure field around one blade row upon the flow around the other blade rows in relative motion, is generally known as *potential interaction.* As the static pressure field is strongest at the blade leading edge, the effects of potential interaction are consequently stronger on those blade rows upstream of the blade row under consideration. The potential effects decay exponentially with increased distance. Therefore, they are localized to the trailing edge region of the blades; and are of consequence only for closely spaced blade rows. In contrast, the vortices and wakes shed by a given blade row persist for considerable distance; they can be often detected several stages downstream.

This thesis presents an investigation of the periodic wake/blade row interaction. The investigation centers on (1) determining how wake interaction results in unsteady flow; and (2) establishing a cause-and-effect relationship between the unsteady flow features and the observed loading fluctuations. These questions are still largely unresolved. In this respect, the present work constitutes an original contribution to the study of unsteady flow in turbomachinery.

This work is motivated by the need for control strategies to reduce the undesirable unsteady effects in turbomachinery. Potential benefits arising from application of these strategies, range from noise reduction to reliability and performance improvements. Therefore, the work focuses on understanding the unsteady flow resulting from wake interaction, rather than on providing quantitative description of the flow for a particular turbomachine design.

For this reason, a single-stage blade row configuration, representative of a pump/compressor midspan section, is being used. In this configuration, wake interaction takes place between the stator blade row and the moving wakes from the upstream rotor. The results can be extended to the case of a pump/compressor rotor interacting with wakes from an upstream IGV or stator blade row, by a transformation of the velocity fields into the rotor rotating frame. In a turbine environment however, the wakes are directed against the suction surface of the blades. This must be taken into account if the results are extended to the case of turbine rotor/stator or stator/rotor interaction.

A two-dimensional model of the wake interaction, shown in Figure 1.1, is used in the investigation. In practice, wake interaction takes place in a three-dimensional environment, owing to the presence of secondary radial flow and passage vortices. The 2-D model was however selected, because it can address the above unresolved issues without additional complications and at lesser cost. Furthermore, the 2-D configuration provides guidelines for a future three-dimensional wake interaction study, which will also include the unsteady

effects of the upstream vortices. Finally, the 2-D results demonstrate the potential of the spectral-element method.

Most turbomachines (e.g. core jet engines, power generators, pumps and ship propellers) operate in the subsonic/incompressible range. For this reason, an incompressible flow assumption is used throughout the whole study. Incompressible analysis can adequately represent the unsteady flow phenomena in situations not involving shocks and supersonic regions.

1.2. Literature Review

In the last twenty years, considerable effort has been devoted to the study of wake interaction in turbomachinery, using both experimental and theoretical/computational approaches. One of the first theoretical models of wake interaction, is the wake chopping and rectification hypothesis by Kerrebrock and Mikolajczak [27]. This hypothesis postulates that the upstream wakes do not mix with the rest of the flow but instead migrate towards the pressure surface of the downstream blades under the effect of their higher momentum (This is for a compressor environment; in a turbine, the wakes would migrate towards the suction surface for the same reason). The inert-gas wake tracing experiments of Kumar and Kerrebrock [30] support this hypothesis.

The experimental work by Adachi et al. [1], was one of the first to provide detailed data on the unsteady pressure distributions and blade forces due to wake interaction. The authors instrumented the stator blade row in an axial flow blower. Their results show significant fluctuations of the stator blade force as the rotor wake is intercepted. As the center of the wake moves over the blade surface, a significant pressure peak occurs. The sign of this peak is negative on the suction surface and positive on the pressure surface. In addition, the authors were able to assess the relative importance of potential vs. wake-driven unsteady effects for various design configurations. It was found that the importance of wake interaction increases with the blade loading, flow capacity and number of blades.

Further experimental work to characterize the pressure and force fluctuations, has been carried out by several authors, including Arndt et al. [2], Dring et al. [14], Capece and Fleeter [7,8], Gallus [17], and Mankbadi [31]. The results from these experiments confirm the importance of the unsteady effects due to the interaction between rotating and stationary blade rows in modern turbomachinery.

The flowfield circumferential non-uniformities, due to the wakes and their interaction and transport through the downstream blade rows, have also received considerable attention by several authors. Among these, Binder et al. [5], Stauter, Dring and Carta [43], and Zierke and Okiishi [50] have obtained data on the circumferential fluctuations of the flow velocity, dynamic pressure and turbulence levels at the exit and between adjacent blade rows. This data shows evidence of strong interaction between fixed and stationary blade rows, and may be used to gain some insight on the wake transport through the blade row.

Experiments have also been carried out to study the influence of blade row interaction on the blade boundary layer in a turbomachine environment. The results from these studies demonstrate the presence of forced boundary layer transition from laminar to turbulent flow, under the effect of the passing wakes (see for instance Pfeil et al. [36]). Based of experimental data, Hodson [23] has developed a model of the wake-driven boundary layer transition.

Recently, several experimental investigations of three-dimensional unsteady flow associated with rotor/stator interaction, have been carried out. Schulz, Gallus and Lakshminarayana [41] have acquired experimental data on the unsteady pressures, blade boundary layers and wake transport through a stator passage in the presence of an upstream rotor. Their results indicate that the incidence change caused by the non-uniform velocity across the wake has a major impact on the unsteady pressure distribution on the blade. Upon interception of the wake by the blade, a peak in negative pressure on the suction side and a peak in positive pressure on the pressure side, are observed in the blade leading edge region. Poensgen and Gallus [37] have found that the unsteady flow due to rotor/stator interaction has a significant effect on hub corner separation in the stator. Their results also show that the rotor vortices interact with the stator passage vortices, giving them a periodic motion. Boletis and Sieverding [6] have shown experimentally that the unsteady flow in the stator stage is significantly affected by the tip clearance flow of the preceding rotor. Extensive velocity measurements by Hebert and Tiederman [22] indicate that the stator passage vortices are significantly distorted and weakened, and that large crossflows occur as the rotor wake passes through the stator blade row. Finally, the results of Joslyn, Dring and Sharma [26] indicate that the unsteady flow between blade rows in relative motion can be highly three-dimensional, even in the midspan region.

The first computational investigations of the unsteady flow due to rotor/stator interaction, were based on the inviscid compressible method developed by Erdos, Alzner and McNally [16] in 1977. Calculations of turbine stator-rotor interactions by Hodson [24], using

Erdos' technique, are in agreement with Kerrebrock's model. The computed results show that the wake fluid collects on the suction surface after being cut by the rotor blade, and forms two counter-rotating vortices. Hodson calculations were two-dimensional. Several modern inviscid solvers for unsteady flow have three-dimensional capability. A notable example of the use of such solvers, are the 3-D Euler calculations by Ni and Sharma [33] of hot streak transport through a multistage turbine.

During the last decade, advances in computer technology have made possible the simulation of unsteady flow using Navier-Stokes solvers. In general, this work has been focused on numerical algorithm issues and proof-of-concept demonstrations. However, several researchers have recently applied these advances to the study of unsteady two-dimensional wake interaction in turbomachinery. In particular, calculations by Rai and Madavan [38], Gundy-Burlet, Rai, Stauter and Dring [21] and Chen and Chakravarthy [9] agree with the measured time-averaged pressure distribution. The computed amplitudes of the pressure disturbances in the leading edge region also agree with the experimental data. Finally, the calculations are able to reproduce the velocity distribution across the upstream wakes. These calculations are based on a two-dimensional finite-difference discretization of the Navier-Stokes equations with a thin layer approximation.

The current state-of-the-art computational work is now concentrated on unsteady three-dimensional Navier-Stokes solvers. Notable work in this category is the UNSFLO code developed by Giles [19], which can address inviscid and viscous unsteady flows with quasi-three-dimensional effects. Taylor and Whitfield [47], Rai [39], and Chen [10] have also extended their finite-difference thin-layer methods to unsteady three-dimensional viscous flows.

Spectral-element methods have also been used for solving the unsteady Navier-Stokes equations (Patera [35], Korczak and Patera [28]). Three-dimensional implementation of the time-splitting spectral-element method has been recently used by Tan [45] in his investigation of a laminar horseshoe vortex flow. The solvers used in the present study of 2D wake-stator interaction, are largely based on Tan's code, and Patera and Korczak's methods. Recent advances in parallel computing make the spectral-element methods particularly promising for future three-dimensional studies of the vortex-stator interaction.

1.3. Technical Objectives

The objectives of this thesis are :

(1) To investigate the unsteady flow phenomena due to the interaction of two-dimensional moving rotor wakes with a two-dimensional stator blade row.

(2) To identify the physical mechanisms responsible for the production of unsteady flow.

(3) To identify the parameters that influence the unsteady flow.

(4) To develop flow control strategies for reducing the undesirable unsteady flow effects.

This study of the unsteady flow and its control shall be carried out for laminar as well as for turbulent ($\mathrm{Re} \geq 10^6$) flows.

1.4. Technical Approach

The following three-step approach is adopted in this thesis :

(1) Computation of the unsteady flow induced in the stator passage by the rotor wakes.

(2) Analysis of the computed results to (a) identify the unsteady flow features; and (b) understand how they are produced.

(3) Use of the results from step (2) to develop flow control strategies.

Since no experimental work accompanies the computational investigation, it is essential to use reliable computational procedures. Two such procedures are used herein. The first procedure is based on using a time-accurate incompressible Navier-Stokes solver. This procedure is equivalent to performing a *computational experiment* in a virtual 2-D stator blade row. Depending on the Reynolds number of the flow, one of the following solvers is used :

(1) Direct Navier-Stokes solver, with which the full Navier-Stokes equations are solved. This solver, developed by Tan [45] is limited to Reynolds numbers of the order of 10,000. Hardware limitations prevent using a computational grid capable of resolving the small-scale phenomena at higher Reynolds numbers. For this reason, all calculations based on this solver shall be referred to as *laminar calculations*.

(2) Turbulent Navier-Stokes solver, in which a modified Baldwin-Lomax turbulence model is used to represent the effects of the unresolved small-scale phenomena. This solver is used in calculations where the Reynolds number is of the order of a few millions; these shall be referred to as *turbulent calculations.*

The second procedure is based on using an inviscid, linearized perturbation solver. In this procedure, the unsteady flow due to the rotor wake/stator interaction is represented as a small inviscid disturbance, superimposed upon the steady viscous flow that would exist in the stator passage in the absence of rotor wakes. The linearized perturbation solver can be used to provide insight into the fluid mechanics of the unsteady flow, since the unsteady effects are decoupled from those associated with the Reynolds number, which are retained in the steady flow.

A time-splitting spectral-element numerical algorithm is used in the above flow solvers (Orszag and Kells [34], Patera [35], Korczak and Patera [28], Tan [45]). This algorithm offers high spatial resolution with minimal numerical dissipation.

According to Richardson [40], two different methods are available to represent the incoming rotor wakes. The first method, referred to as *patched zonal approach*, involves the computation of the flowfield around both rotor and stator blade rows. Interface interpolation is then used to connect moving and stationary computational domains.

In the second method, the rotor wakes are represented as prescribed periodic velocity distortions moving along the inlet boundary of the computational domain (Figure 1.2). This approach is considerably simpler and more efficient, as there is no need to compute the flow about the rotor. Since the potential flow influence of the stator blade row on the rotor is not of interest to this study, the second method has been selected for the investigation.

1.5. Thesis Organization

The present introductory chapter reviews previous investigations of the unsteady flow in axial turbomachinery; and outlines the technical objectives and approach. The remaining part of the thesis is divided in seven chapters, organized as follows.

Chapter Two is dedicated to the computational procedures used for simulating the unsteady flow due to wake-stator interaction. This chapter is divided into four parts. The first part presents the time-splitting spectral-element Navier-Stokes solver. The second part dis-

cusses the selection and implementation of the Baldwin-Lomax model used in the turbulent calculations. Some modifications to the model, motivated by the particular flow configuration, are considered. The third part presents the equations and numerical algorithm upon which the linearized perturbation flow solver is based. The final part of Chapter Two describes the rotor wake model.

The results from the computational investigation of wake interaction are presented and discussed in Chapters Three to Five for the case of a baseline rotor/stator configuration. In Chapter Three, the characteristic vortical and velocity disturbances in the stator passage are identified and related to the pressure fluctuations for the case of laminar flow. The case of turbulent flow is examined in Chapter Four, where the unsteady flow features are examined and compared to those from the laminar calculations. In Chapter Five, the results from the linearized perturbation calculations are likewise compared to those from the Navier-Stokes simulations. This comparison is used to identify the key physical mechanisms responsible for the production of unsteadiness.

In order to generalize the results to other rotor/stator configurations, a parametric study of the unsteady flow is carried out in Chapter Six. This study is used to identify the key parameters influencing the production of unsteadiness, and their effects.

Chapter Seven deals with the development of flow control strategies. A fluid removal strategy that effectively reduces the unsteadiness over the suction surface of the stator blade, is proposed and validated computationally. A fluid blowing strategy is shown to reduce the amplitude of the pressure fluctuations on the pressure surface of the stator blade. Finally, conclusions and recommendations for future work are presented in Chapter Eight.

Chapter 2

Computational Methods

This chapter presents the methods used in the computational investigation of the wake/stator interaction, namely (1) the Navier-Stokes solver; (2) the turbulence model used; (3) the linearized perturbation solver and (4) the wake model used.

2.1. Navier-Stokes Computational Procedure

2.1.1. Governing equations

Assuming incompressible flow, the unsteady flow in the stator passage is governed by the Navier-Stokes equations :

$$\nabla \cdot \mathbf{u} = 0 \tag{2.1}$$

$$\frac{\partial \mathbf{u}}{\partial t} + \mathbf{u} \cdot \nabla \mathbf{u} = -\nabla p + \nabla \left\{ (\frac{1}{Re} + \nu_t) \nabla \mathbf{u} \right\} \tag{2.2}$$

These equations have been made dimensionless as follows :

- Distance is normalized by the projected stator blade chord c_x
- Velocity is normalized by the axial velocity U_∞, far upstream of the stator
- Pressure is normalized by the dynamic head $(\rho U^2)_\infty$ far upstream of the stator
- Time is measured in units of c_x/U_∞.
- Eddy viscosity is normalized by $c_x(\rho U)_\infty$

Non-dimensional variables are used throughout the whole study. The following boundary conditions are used for the solution of the Navier-Stokes equations :

- Prescribed velocity profile along the inlet boundary of the computational domain. As shown in Figure 1.2, this represents the moving rotor wake.
- Periodic boundary conditions

$$u(x_b, y_b, t) = u(x_b, y_b + S, t) \tag{2.3}$$

- Prescribed velocity on the blade surface. As shown in Figure 1.2, this velocity may be different from zero if flow control strategies involving suction, blowing or small-amplitude blade motion are being used.
- Simple extrapolation outflow boundary condition, which assume that the flow does not evolve further in the streamwise direction aft of the outflow boundary.

$$\frac{\partial u}{\partial x}(x_o, y, t) = 0 \tag{2.4}$$

The coefficient ν_t appearing in the Navier-Stokes equations is a non-dimensional eddy viscosity coefficient. It represents the dissipative effects of the small eddies in turbulent flow. According to Kolmogoroff's hypothesis, the characteristic size of these eddies scales as $Re^{-3/4}$ (Sherman [42]). At Reynolds numbers of up to about 10,000 the spectral-element computational grid can provide adequate resolution of the small-scale flow features. Therefore, no eddy viscosity will be used in calculations where $Re \leq$10,000; these will be referred to as *direct* or *laminar calculations* in the following. A turbulence model will be used to estimate ν_t in calculations at the practical Reynolds numbers of the order of 10^6; these will be referred to as *turbulent* calculations.

2.1.2. Time discretization

A fractional time-splitting scheme (Orszag and Kells [34]) is used to advance the incompressible Navier-Stokes equations forward in time. Starting from an initial flowfield, the scheme updates the flow variables at each time increment in three fractional steps :

(1) Convective step, which extrapolates the change in velocity from time t to time $t + \Delta t$ due to convective effects only :

$$\hat{\mathbf{u}}^{n+1} = \mathbf{u}^n - \int_t^{t+\Delta t} \mathbf{u} \cdot \nabla \mathbf{u} dt \tag{2.5}$$

(2) Pressure step, which corrects the velocity update from the convective step

$$\hat{\hat{\mathbf{u}}}^{n+1} = \hat{\mathbf{u}}^{n+1} - \int_t^{t+\Delta t} \nabla p^{n+1} dt \tag{2.6}$$

using a pressure field p^{n+1} such that the updated velocity satisfies continuity.

(3) Viscous step, which corrects the velocity update from the pressure step to take into account dissipation effects, and which imposes the Dirichlet boundary conditions.

$$\mathbf{u}^{n+1} = \hat{\hat{\mathbf{u}}}^{n+1} - \int_t^{t+\Delta t} \nabla \left\{ (\frac{1}{Re} + \nu_t) \nabla \mathbf{u} \right\} dt \tag{2.7}$$

The above fractional time-stepping scheme has an $O(\Delta t)$ error. It may become unstable if the time step is too large for a given grid resolution and Reynolds number. The time step size used in our calculations ranges between 0.001 and 0.0002.

2.1.3. Spatial discretization of the equations

The spatial discretization of Eqs.(2.5-2.7) is performed as follows. The computational domain is divided into a number of *spectral elements* as shown in Figure 2.1. Inside each spectral element, the flow variables are expanded in series of local Lagrangian interpolants :

$$\left\{ \begin{array}{c} \mathbf{u} \\ p \end{array} \right\} = \sum_{j=0}^{j=N} \sum_{k=0}^{k=N} \left\{ \begin{array}{c} \mathbf{u}_{jk} \\ p_{jk} \end{array} \right\} h_j(\zeta) h_k(\eta) \tag{2.8}$$

where (ζ, η) is a set of natural coordinates local to each element, related to the physical coordinate system (x, y) by an isoparametric tensor-product mapping :

$$(x, y) = \sum_{j=0}^{j=N} \sum_{k=0}^{k=N} (x, y)_{jk} h_j(\zeta) h_k(\eta) \tag{2.9}$$

The local interpolants are based on Chebychev polynomials :

$$h_n(s) = \frac{2}{N} \sum_{m=0}^{m=N} \frac{1}{\bar{C}_m \bar{C}_n} T_m(s_n) T_m(s) \tag{2.10}$$

The indexed flow variables u_{jk} and p_{jk} are velocity and pressure values at the collocation point $()_{ij}$ in each element. The coordinates of the collocation points in the local coordinate system are

$$(\zeta, \eta)_{jk} = (\cos \frac{\pi j}{N}, \cos \frac{\pi k}{N}) \tag{2.11}$$

The periodic boundary conditions are implicitly implemented during the discretization process. For this purpose, the computational grid is generated so that the nodes on the upper

and lower boundaries have the same abscissas. An unique index $()^i_{jk}$ is then used for pairs of matching nodes on the periodic boundaries.

2.1.4. Discretized convective step

A fourth-order, discretized Runge-Kutta scheme is used to implement the convective step equation (Eq.2.5):

$$\hat{\mathbf{u}}^{n+1/4}_{jk,i} = \mathbf{u}^n_{jk,i} - \frac{\Delta t}{2}(\mathbf{u}\cdot\nabla\mathbf{u})^n_{jk,i} \tag{2.12a}$$

$$\hat{\mathbf{u}}^{n+1/2}_{jk,i} = \mathbf{u}^n_{jk,i} - \frac{\Delta t}{2}(\hat{\mathbf{u}}\cdot\nabla\hat{\mathbf{u}})^{n+1/4}_{jk,i} \tag{2.12b}$$

$$\hat{\mathbf{u}}^{n+3/4}_{jk,i} = \mathbf{u}^n_{jk,i} - \Delta t(\hat{\mathbf{u}}\cdot\nabla\hat{\mathbf{u}})^{n+1/2}_{jk,i} \tag{2.12c}$$

$$\hat{\mathbf{u}}^{n+1}_{jk,i} = \mathbf{u}^n_{jk,i} - \frac{\Delta t}{6}\left((\mathbf{u}\cdot\nabla\mathbf{u})^n + 2(\hat{\mathbf{u}}\cdot\nabla\hat{\mathbf{u}})^{n+1/4} + 2(\hat{\mathbf{u}}\cdot\nabla\hat{\mathbf{u}})^{n+1/2} + (\hat{\mathbf{u}}\cdot\nabla\hat{\mathbf{u}})^{n+3/4}\right)_{jk,i} \tag{2.12d}$$

The discretized velocity derivatives are computed using the $\tilde{\nabla}$ operator matrix; derived in Appendix A :

$$(\mathbf{u}\cdot\nabla\mathbf{u})_{jk} = \frac{1}{J_{jk}}\mathbf{u}_{jk}\cdot\sum_l\sum_m \tilde{\nabla}_{jklm}\mathbf{u}_{lm} \tag{2.13}$$

2.1.5. Discretized pressure step

The velocity update in the pressure correction step is implemented using a backward Euler time-stepping scheme of Eq.(2.6) :

$$\frac{\hat{\hat{\mathbf{u}}}^{n+1} - \hat{\mathbf{u}}^{n+1}}{\Delta t} = -\nabla p^{n+1} \tag{2.14}$$

With this formulation, the pressure field required for $\hat{\hat{u}}^{n+1}$ to satisfy the continuity equation, is governed by the following Poisson equation :

$$\nabla^2 p^{n+1} = \frac{1}{\Delta t}\nabla\cdot\hat{\mathbf{u}}^{n+1} \tag{2.15}$$

with the following Von Neuman boundary conditions along all prescribed-velocity boundaries of the computational domain :

$$\frac{\partial p^{n+1}}{\partial n} = \frac{\hat{\mathbf{u}}^{n+1}\cdot\mathbf{e}_n}{\Delta t} \tag{2.16}$$

Rather than directly solving the pressure equation, the numerical implementation uses its discretized weighted residual form. For this purpose, the associated functional :

$$I = \int_x \int_y \left[-\frac{1}{2}(\nabla p^{n+1})^2 - p^{n+1} \nabla \cdot (\frac{\hat{\mathbf{u}}^{n+1}}{\Delta t}) \right] dxdy + \int_s \left[p^{n+1} (\frac{\hat{\mathbf{u}}^{n+1}}{\Delta t}) \cdot \mathbf{e}_n \right] ds \tag{2.17}$$

is minimized with respect to arbitrary variations of the pressure at every collocation point:

$$\frac{\delta I}{\delta p^{n+1}_{jk,i}} \equiv 0 \tag{2.18}$$

As shown in Appendix A, the discretized form of Eq.(2.18) is a large linear equation :

$$\sum\nolimits^{i} \sum_j \sum_k A_{lmjk}(1)\, p^i_{jk} = \frac{1}{\Delta t} \sum\nolimits^{i} \lambda^i_{plm} \tag{2.19}$$

the right-hand side source term of which contains the boundary conditions:

$$\begin{aligned}
\sum\nolimits^{i} \lambda^i_{p_{jk}} \;=\; & \sum\nolimits^{i \in Q_E} \sum_l \sum_m \sum_p \sum_q \tilde{\nabla}^i_{pqjk} \left(\textstyle\sum_r \tilde{B}_{rpl} \sum_s \tilde{B}_{sqm} \right) \cdot \hat{\mathbf{u}}^{n+1}_{lm,i} \\
& + \sum\nolimits^{i \in Q_I} \sum_s \sum_l \sum_r y_{r0,i} D_{rs} \delta_{q0} \tilde{B}_{slp} (\hat{\mathbf{u}}^{n+1} \cdot \hat{e}_x)_{l0,i} \\
& - \sum\nolimits^{i \in Q_O} \sum_s \sum_l \sum_r y_{rN,i} D_{rs} \delta_{qN} \tilde{B}_{slp} (\hat{\mathbf{u}}^{n+1} \cdot \hat{e}_x)_{lN,i} \\
& + \sum\nolimits^{i \in Q_L} \sum_s \sum_l \sum_r y_{rN,i} D_{rs} \delta_{qN} \tilde{B}_{slp} (\hat{\mathbf{u}}^{n+1} \cdot \mathbf{e}_n)_{lN,i} \\
& + \sum\nolimits^{i \in Q_S} \sum_r \sum_m \sum_s y_{Ns,i} D_{sr} \delta_{Np} \tilde{B}_{rmq} (\hat{\mathbf{u}}^{n+1} \cdot \mathbf{e}_n)_{Nm,i} \\
& + \sum\nolimits^{i \in Q_P} \sum_r \sum_m \sum_s y_{0s,i} D_{sr} \delta_{0p} \tilde{B}_{rmq} (\hat{\mathbf{u}}^{n+1} \cdot \mathbf{e}_n)_{0m,i}
\end{aligned} \tag{2.20}$$

As the coefficients of the pressure matrix A_{lmjk} depend only on the grid geometry, the matrix inverse is computed in a separate pre-processing stage via static condensation. This procedure allows for Eq.(2.19) to be solved directly at each time step. It accelerates considerably the solution, but has the drawback of requiring large amounts of memory.

2.1.6. Discretized viscous step

The viscous step is discretized in time using an implicit Crank-Nicholson scheme for Eq.(2.7)

$$\left[\nabla(D\nabla) - \frac{2}{\Delta t} \right] \mathbf{u}^{n+1} = -\nabla(D\nabla \mathbf{u}^n) - \frac{2}{\Delta t} \hat{\mathbf{u}}^{n+1} \tag{2.21}$$

where D is the effective kinematic viscosity, defined as :

$$D = 1/Re + \nu_t \tag{2.22}$$

Equation (2.24) is solved using the following weighted-residual formulation :

$$\frac{\delta}{\delta \mathbf{u}_{jk,i}^{n+1}} \int_x \int_y \left[-\frac{1}{2} D(\nabla \mathbf{u}^{n+1})^2 + \left\{ \nabla(D \nabla \mathbf{u}^n) + \frac{2}{\Delta t} \hat{\hat{\mathbf{u}}}^{n+1} \right\} \cdot \mathbf{u}^{n+1} \right] dxdy \equiv 0 \tag{2.23}$$

The discretized form of the above equation, derived in Appendix A, is :

$$\sum^{i} \sum_{l} \sum_{m} \left[A_{jklm}(D) + \frac{2}{\Delta t} B^{+}_{jklm} \right] \mathbf{u}_{lm,i}^{n+1} = \sum^{i} \lambda_{jk}^{i} \tag{2.24}$$

where the right-hand source term is given by :

$$\lambda_{lm}^{i} = \frac{2}{\Delta t} \sum_{j} \sum_{k} \left[B^{+}_{lmjk} \hat{\hat{\mathbf{u}}}_{jk,i}^{n+1} + A_{lmjk}(D) \mathbf{u}_{jk,i}^{n} \right] \tag{2.25}$$

In contrast to the pressure step, the prescribed-velocity boundary conditions in the viscous step are implemented by padding the appropriate rows in the foregoing linear equation with zeros and ones.

In the case of zero eddy viscosity, the viscous matrix is constant in time. As shown in Appendix A, it may be then computed as:

$$A_{lmjk}(D) = \frac{1}{Re} A_{lmjk}(1) \tag{2.26}$$

This allows one to determine the matrix inverse in the preprocessing stage, and to solve Eq.(2.24) directly at each time step. This is the technique used in the laminar flow calculations. If a turbulence model is used, the viscous matrix must be recomputed at each time step as shown in Appendix A. In this case, an iterative preconditioned conjugate-gradient method (Cline [11]) is used to solve Eq.(2.24). This method, while still more efficient than inverting A_{lmjk} at each step, requires an order-of-magnitude more CPU time than an identical-size laminar calculation. Therefore, whenever possible, laminar calculations will be used to simulate the unsteady flow in the stator stage.

2.2. Turbulence Model

In order to simulate wake interactions at high Reynolds numbers, an eddy viscosity turbulence model is implemented in the Navier-Stokes solver. The eddy viscosity represents the effects of shear stresses arising from velocity fluctuations, the scale of which is too small to be resolved by the computational grid. Turbulent shear stresses and eddy viscosity are related by the following tensor equation :

$$< \overline{u'_i u'_j} >= \nu_t \nabla \mathbf{u} + \underbrace{\frac{2}{3}\delta_{ij} < \overline{u'_i u'_i} >}_{p'} \tag{2.27}$$

which yields the closed-form momentum equation, shown as Eq.(2.2). The use of eddy viscosity in the unsteady Navier-Stokes equations is justified when the time scales associated with the small-scale fluctuations are much smaller than the time scales associated with the unsteady flow. This is the case for the unsteady flow produced by the rotor wakes, where the characteristic time scale is the wake passing period ($\sim$ 0.05 to 1.0 non-dimensional time units). In comparison, the characteristic time scales of the turbulent fluctuations are of the order of $Re^{-1/2}$ (Sherman [42], in this case $\sim 10^{-3}$ non-dimensional time units).

2.2.1. Selection of the turbulence model

A turbulence model is a computational procedure which predicts the local value of the eddy viscosity coefficient without actually computing the small-scale velocity fluctuations. Turbulence models are based on experimental data, and introduce uncertainty into the computed flow solution. There is no turbulence model specifically tailored to the unsteady flow due to wake interaction. For this reason, the following two most commonly used turbulence models were considered :

- The Baldwin-Lomax algebraic model (Baldwin and Lomax [3]).
- The K-ϵ model (reviewed by Benocci [4]).

The K-ϵ turbulence model is based on a rational representation of the dynamics of the turbulent quantities. However, its computational implementation presents significant numerical problems. More important, this model is very sensitive to several empirical constants appearing in the ϵ equation (Benocci [4], Giles [18], Dawes [13]).

On the other hand, the Baldwin-Lomax model is relatively independent from such empirical constants. It is also widely used for boundary-layer, as well as for separated and

shear layer turbulent flows (Baldwin and Lomax [3], Giles [18], Vandromme [48]). On the basis of these considerations, it was decided to use the Baldwin-Lomax model for turbulent Navier-Stokes calculations of moving wake interaction.

2.2.2. Baldwin-Lomax model

This section presents the Baldwin-Lomax model in its original formulation, intended for computing steady turbulent flow about an airfoil. As shown in Figure 2.2, the Baldwin-Lomax model divides the flowfield into three distinct regions—inner, outer and wake region. Different formulas are used to estimate the eddy viscosity in each of these regions. To insure a continuous distribution, the eddy viscosity in the inner and outer regions is computed according to :

$$\nu_t = \begin{cases} \nu_{t,i} & n \leq n_c \\ \nu_{t,o} & n > n_c \end{cases} \tag{2.28}$$

where the cross-over distance n_c is the smallest distance from the blade surface at which the values from the inner and from the outer formulas are equal. The Prandtl-Van Driest mixing-length formulation is used in the *inner region* :

$$\nu_{t,i} = l^2|\omega| \tag{2.29}$$

where the mixing-length is calculated according to :

$$l = kn\left[1 - e^{-n^+/A^+}\right] \tag{2.30}$$

In terms of non-dimensional quantities, the law-of-the-wall coordinate n^+ is given by

$$n^+ = n\sqrt{Re\frac{\partial u}{\partial n}_{n=0}} \tag{2.31}$$

The function $A^+(s)$ represents the effect of the pressure gradient on the boundary layer :

$$A^+(s) = 26\left[1 + 11.8\frac{dp}{ds}\sqrt{Re(\frac{\partial u}{\partial n})^3}\right]^{-1/2}_{n=0} \tag{2.32}$$

In the absence of strong pressure gradients, the following approximation may be used

$$A^+(s) \approx 26 \tag{2.33}$$

In the *outer region*, the following formula is used for computing the eddy viscosity :

$$\nu_{t,o} = K_1 K_2 F_W(s) F_K(n) \tag{2.34}$$

where the $F_K(n)$ is the Klebanoff intermittency factor, given by

$$F_K(n) = \left[1 + 5.5C_K^6 \left(\frac{n}{n_{max}}\right)^6\right]^{-1} \tag{2.35}$$

and where the wake factor is defined as :

$$F_W(s) = \min \left\{ \begin{array}{l} n_{max}F_{max} \\ C_W n_{max} U_D^2 / F_{max} \end{array} \right\} \tag{2.36}$$

The quantity n_{max} is defined as the locus of the maximum F_{max}, of the function :

$$F(n) = n|\omega| \left[1 - e^{-n^+/A^+}\right] \tag{2.37}$$

at a fixed value of s. The quantity U_D represents the difference between the maximum and minimum total velocity in the profile, also at a fixed value of s :

$$U_D^2 = (|u|_{max} - |u|_{min})^2 \tag{2.38}$$

For unseparated flows, the $|u|_{min}$ term is taken to be zero. For separated flows, one must take into consideration the change of flow direction in the above definition of $|u|_{min}$. It is to be noted that the product $n_{max}F_{max}$ is equivalent to $\delta^* U_e$ in the Clauser formulation [3]. Therefore, $n_{max}(s)$ is physically representative of the local boundary layer thickness.

In the *free shear flow* (or *wake*) region of Figure 2.2, the eddy viscosity is computed using only the outer formula (Eqs. 2.34-2.38). In this case the exponential term of Eq.(2.37) is set to zero, i.e. the quantity n_{max} is defined as the locus of the maximum F_{max} of the function :

$$F(n) = n|\omega| \tag{2.39}$$

The constants appearing in the foregoing relations are those used by Baldwin and Lomax [3] (and derived originally by Cebeci) :

Constant	*Value*
C_W	0.25
C_K	0.3
k	0.4
K_1	0.0168
K_2	1.6

Table 2.1.
Constants appearing in the Baldwin-Lomax model.

These constants have been empirically determined for the case of compressible flow. No specific values for the case of incompressible flow have been found in the literature. Reference [48] suggests that the values for compressible flow can be used in the incompressible case.

2.2.3. Modified Baldwin-Lomax model

The foregoing Baldwin-Lomax model cannot be directly used to study the unsteady flow produced by incoming wakes for two reasons:

(1) The presence of free vortical disturbances over the blade surface biases the calculation of n_{max} and F_{max} (Figure 2.3). This leads to unrealistic values of the eddy viscosity in the outer region.

(2) The direct use of Eqs.(2.34-2.39) is impractical for computing the eddy viscosity within the wake. This is due to the need for continuously monitoring the location of the wakes centerlines, from which the n coordinates are measured.

To overcome the first difficulty, n_{max} has been re-defined as the smallest distance at which :

$$\frac{dF(n)}{dn} = 0 \tag{2.40}$$

where $F(n)$ is given by Eq.(2.39). In the absence of wakes, this definition is fully equivalent to that from the classical model. In the presence of wakes, Eq.(2.40) gives a value of n_{max} which is representative of the physical meaning of this quantity - boundary layer thickness. Had the original formulation been used in presence of wakes, one would obtain a value of n_{max} close to the mid-passage line (cf. Figure 2.3).

To overcome the second difficulty, an approximate closed-form version of Eq.(2.34) is used to estimate the amount of eddy viscosity in the region of flow dominated by the wake vortical disturbances :

$$\nu_t = \frac{eK_1K_2\sqrt{V_r^2+1}}{8C\sqrt{B}}\left[1+5.5C_K^6B^3r^6\right]^{-1} \tag{2.41}$$

where r is the largest root of the non-linear equation :

$$re^{-Br^2} = \frac{|\omega|}{2ABC} \tag{2.42}$$

and where A, B and C are wake characteristics described in Appendix B. This formula is derived from Eqs.(2.34-2.38) for the case of a Gaussian velocity distribution across the incoming wakes. The details on this derivation can be found in Appendix B.

2.3. Linearized Perturbation Computational Procedure

2.3.1. Linearized perturbation equations.

The unsteady flowfield in the stator cascade can be split into two physically distinct parts

$$\mathbf{u}(x,y,t) = \bar{\mathbf{U}}(x,y) + \tilde{\mathbf{u}}(x,y,t) \tag{2.43}$$

$$p(x,y,t) = \bar{P}(x,y) + \tilde{p}(x,y,t) \tag{2.44}$$

The first part of the unsteady flow, $\bar{\mathbf{U}}(x,y)$, is a known steady-state flowfield that would exist in the stator passage in the absence of wakes; it will be referred to as *base flow* in the following. This flow can be determined prior to the moving-wake calculations by using reliable Navier-Stokes solvers. The second part of the unsteady flow, $\tilde{\mathbf{u}}(x,y,t)$, is the fluctuating velocity field due to the incoming rotor wakes and to their interaction with the stator blade. In the following, it will be referred to as *disturbance flow*. The full equations of motion governing the disturbance flow can be obtained by substituting Eqs.(2.43-2.44) into the Navier-Stokes equations. This yields a conservation equation

$$\nabla \cdot \tilde{\mathbf{u}} = 0 \tag{2.45}$$

and a disturbance momentum transport equation :

$$\frac{\partial \tilde{\mathbf{u}}}{\partial t} + \bar{\mathbf{U}} \cdot \nabla \tilde{\mathbf{u}} + \tilde{\mathbf{u}} \cdot \nabla \bar{\mathbf{U}} + \tilde{\mathbf{u}} \cdot \nabla \tilde{\mathbf{u}} = -\nabla \tilde{p} + \nabla \left\{ (\frac{1}{Re} + \nu_t) \nabla \tilde{\mathbf{u}} \right\} \tag{2.46}$$

In the *linearized perturbation* solver, the disturbance flow is linearized about the base flow. In addition, it is assumed that the disturbance flow is inviscid. With this simplification, the disturbance flow equation (2.46) becomes :

$$\frac{\partial \tilde{\mathbf{u}}}{\partial t} + \bar{\mathbf{U}} \cdot \nabla \tilde{\mathbf{u}} + \tilde{\mathbf{u}} \cdot \nabla \bar{\mathbf{U}} = -\nabla \tilde{p} \tag{2.47}$$

This equation will be referred to as *linearized perturbation equation*. Whereas the outflow and periodicity boundary conditions applying to this equation are the same as for the Navier-Stokes equations, the inflow and blade surface boundary conditions are modified as follows.

- Inflow B.C.: The velocity distribution prescribed along the inlet boundary of the computational domain contains only the disturbance from the wake :

$$\tilde{\mathbf{u}}(x_i,y,t) = \mathbf{u}(x_i,y,t) - \bar{\mathbf{U}}(x_i,y) \tag{2.48}$$

- Surface B.C.: Free-slip boundary conditions are applied to the disturbance flow :

$$\tilde{\mathbf{u}}(x_s, y_s, t) \cdot \mathbf{e}_n \equiv 0 \tag{2.49}$$

The linearized solver offers several advantages over a full Navier-Stokes simulation. First, the unsteady flow effects are separated from the viscous effects, which are still retained in the base flow vortical features (e.g. boundary layer). Second, the solution of the linearized equations is faster and requires less memory than a corresponding Navier-Stokes simulation. Moreover, for a given stator design, the base flow needs to be computed only once.

2.3.2. Numerical solution of the linearized equations

A two-step time-splitting scheme, similar to that used in §2.1.2, is employed to solve the linearized equation. The scheme is advanced in time as follows :

(1) Application of a convective step to advance the flowfield from time t to $t + \Delta t$

$$\hat{\tilde{\mathbf{u}}}^{n+1} = \tilde{\mathbf{u}}^n - \int_t^{t+\Delta t} (\bar{\mathbf{U}} \cdot \nabla \tilde{\mathbf{u}} + \tilde{\mathbf{u}} \cdot \nabla \bar{\mathbf{U}}) dt \tag{2.50}$$

(2) Application of a corrective pressure step to compute the disturbance pressure from

$$\nabla^2 \tilde{p}^{n+1} = \frac{1}{\Delta t} \nabla \cdot \hat{\tilde{\mathbf{u}}}^{n+1} \tag{2.51}$$

$$\text{B.C.:} \qquad \frac{\partial p^{n+1}}{\partial n} = \frac{1}{\Delta t} \hat{\tilde{\mathbf{u}}}^{n+1} \cdot \mathbf{e}_n \tag{2.52}$$

and to enforce the divergence-free condition on the updated flowfield at time $t + \Delta t$

$$\tilde{\mathbf{u}}^{n+1} = \hat{\tilde{\mathbf{u}}}^{n+1} - \Delta t \nabla \tilde{p}^{n+1} \tag{2.53}$$

A spectral-element discretization of the flowfield variables, identical to that used for the Navier-Stokes equations in §2.1.3, is employed to solve the time-split linearized equations. The discretized formulation of the convective step is based on Runge-Kutta integration (Eq.2.12). The discretized formulation of the pressure step is identical to that in §2.1.5.

2.3.3. Artificial viscosity stabilization scheme.

The foregoing time-splitting formulation of the linearized equations is unconditionally unstable. An artificial viscosity step can be added to stabilize the linearized solver. This step modifies the solution from the disturbance pressure step as follows :

$$\left[\frac{1}{R_a}\nabla^2 - \frac{2}{\Delta t}\right]\tilde{\mathbf{u}}^{n+1} = -\frac{1}{R_a}\nabla^2\tilde{\mathbf{u}}^{n} - \frac{2}{\Delta t}\hat{\tilde{\mathbf{u}}}^{n+1} \tag{2.54}$$

In order to preserve a free-slip interface between the blade surface and the disturbance flow, the velocity values from the pressure step are used as boundary conditions to this equation. A spectral-element discretization, identical to that from §2.1.6, is employed to solve Eq.(2.54).

The amount of artificial viscosity used has a net impact on the behavior of the computed disturbance flow. As shown in Figure 2.4, for values of the artificial viscosity parameter $1/R_a$ less than some critical value $1/R_{a,crit}$, the disturbances are amplified. For large values of $1/R_a$, the wake disturbances become too diffusive.

Ideally, the linearized calculations should be carried out using this critical value, which provides barely enough artificial diffusivity to compensate for the instability. The critical value is however difficult to estimate. In this work, linearized calculations based on artificial viscosity use a value of R_a equal to the averaged Reynolds number of the base flow:

$$\frac{1}{R_a} = \iint_{Q_E} D dx dy \tag{2.55}$$

This choice insures that the diffusion acting on the disturbances is approximately equal to that from the full Navier-Stokes calculations.

2.4. Wake model

2.4.1. Velocity profile in the rotating frame

As stated in §1.4., a moving inlet velocity distortion will be used to simulate the incoming wakes produced by the upstream rotor. The rotor wake will be first represented in the rotor rotating frame shown in Figure 2.5. In this frame, a Gaussian velocity profile may be assumed for the velocity distribution across the wake :

$$\frac{w(y_w)}{W} = 1 - Ae^{-By_w^2} \tag{2.56}$$

In this equation, the quantity A is the velocity defect in the wake at the streamwise location of the inlet boundary of the computational domain. The quantity B is representative of the wake thickness, defined as the distance between locations with velocity equal to 99% of the free-stream value.

$$\delta = \sqrt{\frac{4}{B} \ln 100A} \tag{2.57}$$

The velocity defect and wake thickness are related to the characteristics of the rotor blade by the following equations, based on a model adopted by Kerrebrock and Mikolajczak [27].

$$A = \frac{2.42\sqrt{C_D}}{2x_r/c_r + 0.6} \tag{2.58}$$

$$\delta = \frac{c_r}{2}\sqrt{\frac{2C_D(x_r + 0.15c_r)}{c_r}} \tag{2.59}$$

According to Gostellow [20], the velocity profile in the far wake of a turbomachinery blade is indeed of the Gaussian type. The velocity profile in the near wake ($x_r/c_r \leq 0.3$) is not Gaussian—it rather approximates the suction and pressure surface boundary layers velocity distribution. The present investigation uses a Gaussian distribution everywhere in the wake, assuming that the effects of variations in the velocity profile are of considerably smaller scale than the characteristic size of the unsteadiness.

2.4.2. Velocity profile in the stationary frame

Since all flow calculations take place in the stator frame, it is necessary to transform the above velocity distribution before using it in the inlet boundary conditions. The velocity of a fluid element in the fixed stator frame, $\mathbf{u}$, is related to the velocity of the same element in the rotating frame, $\mathbf{w}$, by the following transformation :

$$\mathbf{u} = \mathbf{w} + \mathbf{V} \tag{2.60}$$

where $\mathbf{V}$ is the relative velocity between the two frames, equal to the tangential velocity of the rotor blade V times $\mathbf{e}_y$. From Eq.(2.56), the velocity profile across the wake in the non-rotating frame is found to be :

$$\left\{ \begin{array}{c} u(y_w) \\ v(y_w) \end{array} \right\} = \left\{ \begin{array}{l} 1 - Ae^{-By_w^2} \\ (1 - Ae^{-By_w^2})\tan\theta + Ae^{-By_w^2}V \end{array} \right\} \tag{2.61}$$

where the y_w coordinate is still measured from the center of the moving disturbance. A typical instantaneous velocity distribution across the wake, as seen in the fixed stator frame, is shown in Figure 2.6. Note that, in the fixed frame, the wake has excess tangential velocity in the direction of rotation of the rotor. The mechanism for production of excess velocity is illustrated by the velocity triangles in Figure 2.7.

2.4.3. Dynamic periodicity simulation

To simulate the motion of a series of the above velocity disturbances along the inlet boundary, the velocity at any time and at any point of the inlet boundary is computed from

$$\left\{ \begin{array}{l} u(y,t) \\ v(y,t) \end{array} \right\} = \left\{ \begin{array}{l} 1 - Af(y,t) \\ (1 - Af(y,t)) \tan\theta + Af(y,t)V \end{array} \right\} \qquad \forall y \in [0, S] \tag{2.62}$$

where $f(y,t)$ is a moving pair of overlapped Gaussian disturbances

$$f(y,t) = \exp\left[-B\mathcal{E}^2(\frac{y - Vt}{S}, P)\right] + \exp\left[-B\left(1 - \mathcal{E}(\frac{y - Vt}{S}, P)\right)^2\right] \tag{2.63}$$

with spatial period determined by the stator-to-rotor blade ratio

$$P = \frac{N_s}{N_r} \tag{2.64}$$

In Eq.(2.63), the tangential velocity of the disturbances is assumed equal to the tangential velocity of the rotor blade. The function $\mathcal{E}(y,P)$, used to simulate spatial periodicity, is defined as follows :

$$\mathcal{E}(y,P) = \left\{ \begin{array}{ll} y/P - E(y/P) & y \geq 0 \\ E(y/P) - y/P & y < 0 \end{array} \right. \tag{2.65}$$

The computational methods presented in this chapter will be used next to simulate the unsteady flow in a stator blade row subjected to the moving wake disturbances.

Chapter 3

Unsteady Laminar Flow Calculations

3.1. Computational set-up

The two-dimensional rotor-stator configuration used in the present computational investigation is shown in Figure 3.1. It is representative of the midspan geometry of an axial pump designed following the procedures in Reference [44]. The detail of the design calculations can be found in Appendix C. Tables 1 and 2 below summarize the *non-dimensional* values of the principal design parameters of the stator and rotor blade rows

Design parameter	*Value*
Stator blade stagger angle	12 degrees
Stator spacing-blade chord ratio	0.4
Inlet flow turning angle	25 degrees
Blade section	Eppler 4% thick
Design Reynolds number	1,000,000
Rotor-Stator blade ratio	1:1
Rotor-Stator gap	0.2

Table 3.1.
Principal parameters of the 2-D stator blade row.

Design parameter	*Value*
Rotor blade stagger angle	60 degrees
Rotor spacing-blade chord ratio	0.4
Flow turning angle	6.6 degrees
Blade section	NACA 2304
Design Reynolds number	2,500,000
Rotor blade tangential velocity	2.0
Rotor wake thickness	0.10
Rotor wake velocity defect	0.75

Table 3.2.
Principal parameters of the 2-D rotor blade row.

The choice of a low spacing-blade chord ratio, which is about 2-3 times smaller than that of an ordinary axial pump (Stepanoff [44]), is motivated by computational and data storage considerations. This has no qualitative impact on the results, since the wake thickness is an order of magnitude smaller than the blade spacing. This assertion has been verified by previous calculations with spacing ratios of 0.75 and 1.00.

The choice of an 1:1 rotor-stator blade ratio allows one to limit the computational domain to a single blade passage, and has been also determined by computational and data storage considerations. Such an integer blade ratio is not representative of actual turbomachinery, where non-congruent blade ratios are used in order to prevent the interaction between blades in adjacent rows from taking place simultaneously. These non-congruent blade ratios result in an unsteady potential flow pattern rotating circumferentially (Cumpsty [12]).

This phenomenon cannot be observed with the present 1:1 ratio. This limitation is fully compatible with the objectives of the study, which concentrates on understanding wake interaction at the blade level. The characteristic size of the unsteady phenomena arising from blade/wake interaction is considerably smaller than the stator circumference; therefore the nature of these phenomena will not be affected by the rotating potential flow pattern.

All the results presented in this chapter are from direct Navier-Stokes calculations without turbulence model, and at an off-design Reynolds number of 10,000. The spectral-element discretization of the computational domain for these calculations is shown in Figure 3.2. The purpose of these laminar calculations is to illustrate the dynamics of the unsteady flow produced by the rotor wakes, without introducing the uncertainty associated with turbulence modeling.

3.2. Flowfield in absence of moving wakes

In order to avoid extensive laminar separation, an Eppler blade section [15] is used for the stator blade row. The undisturbed flowfield in the stator passage, shown in Figure 3.3, reveals the presence of separated flow in the trailing edge region of the blades. The velocity contours in Figure 3.4 indicate that the boundary layer over the suction surface is fairly thick. As a result, vorticity is present at relatively large distances away from the blade surface. The thickness of the vortical boundary layer may be appreciated in Figure 3.5.

Even in the absence of moving wakes, the flow about the stator blade is unsteady due to the shedding of vortices from the trailing edge. These vortices may be seen in Figures 3.3 and 3.5. The unsteady effects of vortex shedding are however small, compared to the average loading and to the wake-induced unsteady effects that will be subsequently discussed. This is shown in Figure 3.6, where the amplitude of the loading fluctuations due to shedding is only a few percents of the average loading.

3.3. Unsteady flow over the suction surface of the stator blade

To visualize the unsteady effects due to the interaction of rotor wakes with the stator, it is useful to subtract the steady flow that would exist in absence of rotor wakes, from the calculated unsteady flow. The resultant flow shall be referred to as ***unsteady disturbance flow***. Shown in Figure 3.7j is a disturbance flowfield at a time instant when a rotor wake is approaching the stator blade leading edge. The incoming wake appears as a high-momentum stream directed towards the pressure surface of the stator blade.

As shown in Figure 3.7a, a distinct vortical region is produced on each side of the leading edge upon interception of the wake. These vortical regions are lifted away from the blade surface as they move downstream (Figures 3.7c to 3.7e). We shall refer to these vortical regions as *B-regions* (over the suction surface) or *BP-regions* (over the pressure surface).

Further downstream along the suction surface, the B-region can be seen to evolve into one vortex, which shall be referred to as *B-vortex* (Figures 3.7g to 3.7j). As new incoming wakes interact periodically with the leading edge, the unsteady flow over the suction surface of the stator blade is characterized by a row of B-vortices produced near the leading edge and discharged above the stator blade trailing edge. This is illustrated on Figures 3.8a-j.

Figures 3.8a-j indicate that, at a given time, the number of B-vortices over the suction surface is larger than the number of wakes. This can be explained by considering that the production and the evolution of the B-region takes place in, or at the edge of the boundary layer, where the convection velocity is smaller than the free-stream velocity. The effect of velocity difference can be appreciated by sequentially examining the disturbance vorticity contours on Figures 3.7a to 3.7i. In Figure 3.7a, the B-region is at the same location as the wake centerline, whereas in Figure 3.7i, a substantial lag can be seen between these two vortical structures.

Examination of the disturbance vorticity contours in Figures 3.8a-i, shows that the boundary layer under the row of B-vortices is characterized by a series of flat vortical disturbances of alternating sign; further referred to as *P1-regions* (positive sign) and *N1-regions* (negative sign). The total number of P1 and N1 regions is twice that of the B-vortices. Each P1-region lies on the blade surface directly beneath a B-vortex; whereas each N1-region appears to be located between two successive B-vortices.

The presence of P1 and N1 regions in the unsteady flow solution can be explained by the low static pressure field induced by each B-vortex. For this purpose, it is convenient to define a *wall-normal flux of vorticity*:

$$\mathbf{e}_n \cdot \mathbf{J}_o = -\frac{1}{Re}\mathbf{e}_n \cdot (\nabla\omega) \tag{3.1}$$

Hornung [25] has derived the following equation governing the flux of vorticity

$$\mathbf{e}_n \cdot \mathbf{J}_o = -\mathbf{e}_n \times \left[\frac{d\mathbf{u}}{dt} + \nabla p\right] \tag{3.2}$$

In the present case, the thickness of a vortical disturbance is an order of magnitude smaller than its longitudinal size. Neglecting the effects of variations in the n-direction as well as the convective and inertia effects, Equation (3.2) may be transformed into an ordinary differential equation :

$$J_o \approx -\frac{dp}{ds} \qquad \text{at n=0.} \tag{3.3}$$

From the foregoing equations, it follows that the wall-normal flux of vorticity is positive in regions of decreasing static pressure, and negative in regions of increasing static pressure. As shown in Figure 3.9, this will result in wall-normal positive flux upstream of a B-vortex, and wall-normal negative flux downstream of it. Integration of Eq.(3.3) yields positive and negative vorticity disturbances on the blade surface, the amplitude of which is in agreement with the Navier-Stokes calculations. The location of the predicted positive/negative disturbances is also coincident with that from the numerical calculations.

As shown in Figures 3.10 and 3.11, each P1-region is characterized by disturbance velocity directed against the flow in the boundary layer. In contrast, each N1-region exhibits a disturbance velocity in the flow direction. Consequently, the disturbance flowfield near the blade surface is characterized by interleaved regions of alternating-sign velocity, which move downstream with the row of B-vortices. This results in a moving up-and-down pattern of the shear stress distribution on the surface, shown in Figure 3.12a.

A small positive *P-vortex*, moving in the downstream direction nearby the blade surface, can be also seen in Figure 3.10. This vortex contains vorticity from the P1-region, which is distorted and lifted off from the surface by the velocity field of the B-vortex. In the present case, the P-vortex is small and has no noticeable effect on the blade loading. In other circumstances, examined in Chapter Six, larger B-vortices may result in significant amount of P1-type vorticity being produced and detached from the surface. This leads to strong P-vortices, forming a paired vortex street with the B-vortices.

The row of B-vortices, and the associated boundary layer P/N-type vortical disturbances, appear to be the dominant form of unsteady flow produced by the rotor wake over the suction surface of the stator blade. The computed results indicate that the fluid in the incoming wake is not part of the unsteady flow features over the suction surface.

Formation of vortices at the leading edge of a stator cascade subjected to incoming wakes has been experimentally observed by Taylor [46], but no details are provided by the author. An indirect evidence supporting the formation of B-vortices has been found in Wilder's extensive LDV measurements of the flowfield around a 2-D airfoil interacting with a discrete 2-D vortex at a Reynolds number of 20,000 [49]. According to the data, the large local angle of attack induced by the incoming vortex results in the production of a separated vortical region at the L.E., which subsequently moves downstream along the airfoil surface. This region is very similar to the B-vortex observed herein, where the interception of the incoming wake creates a similar large angle of attack at the leading edge.

3.4. Intra-stator wake transport and unsteady flow over the pressure surface of the stator blade

The unsteady flow near the pressure surface of the stator blade appears to be different in nature from the unsteady flow over the suction surface. Examination of the disturbance flowfield indicates that the unsteady flow near the pressure surface is the result of :

(1) Migration of the rotor wake fluid from the middle of the stator passage towards the pressure surface.

(2) Evolution of the rotor wake into vortices of alternating sign. These vortices will be referred to as W^+ *vortices* (CCW sense of rotation) and W^- *vortices* (CW sense of rotation).

This process is shown in Figures 3.8a to 3.8j. As a result, the unsteady flow over the pressure surface is dominated by a series of counter-rotating W-vortices grouped together. Each vortex group corresponds to a rotor wake at a distinct stage of its evolution. The unsteady effects associated with the BP-vortical region produced at the leading edge upon wake interception, appears to be considerably smaller than those associated with its counterpart B-vortex on the suction surface. Likewise, they appear negligible when compared to those associated with the wake vortices.

The computed results indicate that the wake does not penetrate the pressure surface boundary layer. For this reason, the distance between the surface and the wake vortices appears to scale as the local boundary layer thickness. Thin P1 and N1-type boundary layer vortical disturbances can be observed on the pressure surface. These disturbances are similar to those observed on the suction surface, and can be explained by the pressure field of the wake vortices (cf.§3.3).

The migration of the rotor wake towards the pressure surface of the stator blade can be explained by the excess of tangential velocity in the wake (Kerrebock and Mikolajczak hypothesis [27]). Supporting evidence for the wake migration can be found in several experimental and computational studies, discussed in Section 1.2.

3.5. Pressure field disturbances

The unsteady flowfield features discussed above produce a characteristic pattern of static pressure disturbances on the stator blade surface. This pattern, illustrated in Figures 3.13a-b, consists of :

(1) An intense, short-duration high-pressure pulse on the pressure side of the stator blade leading edge; produced upon wake interception.

(2) An intense, short-duration low-pressure pulse on the suction side of the stator blade leading edge; produced upon wake interception.

(3) A sequence of low-pressure peaks (depressions) moving downstream along the suction surface of the blade. The chordwise location of each depression is identifiable with that of a B-vortex. This may be appreciated by correlating Figure 3.13a to Figure 3.8a; and Figure 3.13b to Figure 3.8e.

(4) A sequence of pressure disturbances moving downstream along the pressure surface of the blade. The chordwise location of each disturbance is identifiable with that of a group of wake vortices. This may be appreciated by correlating Figure 3.13a to Figure 3.8a; and Figure 3.13b to Figure 3.8e.

The leading edge high-pressure pulse, shown in Figure 3.14a, is associated with the higher total pressure fluid in the rotor wake. The peak value of this pulse can be predicted by the following formula :

$$C^{+}_{p,max} = \left(\frac{1-A}{\cos\theta}\right)^2 + 2A(1-A)V\tan\theta + A^2V^2 \tag{3.4}$$

which is derived from Bernoulli's equation in Appendix D. With the wake characteristics used, this formula gives a peak pressure coefficient $C^{+}_{p,max}$ of 2.5. This value is in good agreement with the Navier-Stokes calculations in Figure 3.14a. A more important result from Eq.(3.4) is that the magnitude of the L.E. pressure pulse increases as the square of the wake strength and the rotor speed.

The amplitude of the leading edge low-pressure pulse, shown in Figure 3.14b, could not be directly computed from Bernoulli's equation. This pulse appears to be associated with the increase of local angle of attack when the wake is intercepted, as shown by the correlation between Figures 3.15a and 3.15b. The duration and rise time of the leading edge pressure pulses correlate with the wake width and velocity profile.

Each low-pressure disturbance observed on the suction surface is a reflection of the low static pressure region in the core of a nearby B-vortex. This is shown by Figures 3.16a and 3.16b, where one can see a close correlation between disturbance velocity and static pressure contours. Over most of the blade surface, the peak-to-peak amplitude of the low pressure disturbances can be roughly approximated by the following formula, derived in Appendix D

$$(\Delta C_p)^{-} = \frac{99}{24\pi^2}\left(\frac{\Gamma_B}{a_b}\right)^2 \tag{3.5}$$

In this equation, Γ_B is the total circulation of the B-vortex responsible for the pressure disturbance and a_b is the half-width of the vortex, in non-dimensional units. Over the midchord section of the stator blade, the circulation and half-width of the B-vortices have a relatively

constant value of 0.05 and 0.04 respectively. In this case, Equation (3.5) predicts a depression of 0.65. This value is in surprisingly good agreement with the Navier-Stokes simulation ($(\Delta C_p)^-$=0.44), considering the number of simplifications used to derive the formula. A more important results from Eq.(3.5) is that the amplitude of the pressure fluctuations on the suction surface varies as the strength of the B-vortices squared. Therefore, small changes in the strength of the B-vortices may have significant effect on the amount of loading fluctuations.

Each pressure disturbance observed on the pressure surface consists of low-pressure regions associated with the cores of the two wake vortices, interleaved with a high pressure region where the disturbance flow is directed against the blade surface and results in a stagnation-point flow. This may be appreciated by correlating the pressure contours in Figure 3.17a to the disturbance velocity field in Figure 3.17b.

Over the forward part of the stator blade, the pressure in this stagnation region is directly related to the wake momentum. Further downstream, the stagnation-point flow is mainly induced by the system of counterrotating vortices into which the wake has evolved. In this case, the peak amplitude of the high-pressure disturbance may be represented by the following equation, derived in Appendix D :

$$(\Delta C_p)^+ \sim \left(\frac{b_w \Gamma_W}{\pi d_w}\right)^2 \tag{3.6}$$

where b_w is a geometry factor, d_w is the distance between the wake vortices and the pressure surface, and Γ_W is the circulation of each wake vortex. Assuming that most of the wake fluid is contained in the pair of W-vortices adjacent to the surface, Γ_W is directly proportional to the wake velocity defect, wake thickness and rotor velocity. Therefore, the amplitude of the high-pressure disturbances will be sensitive to small changes in the wake strength and/or the distance between surface and wake vortices. It is to be noted that this distance appears to scale as the local boundary layer thickness.

The presence of a positive pressure fluctuation on the pressure surface, and of a negative pressure fluctuation on the suction surface as the center of the wake moves past a given point on the stator blade, has been experimentally observed by Adachi [1]. The presence of an intense positive pressure peak on the pressure side, and of an intense negative pressure peak on the suction side of the leading edge has been reported in several experimental investigations, including Adachi [1], Arndt [2], Gallus [17], and Schulz et al. [41].

3.6. Flow fluctuations RMS

RMS or amplitude-average distributions of the fluctuating flow variables have been used by a number of authors (e.g. Arndt [2], Chen [9], Mankbadi [31]) to visualize the unsteady effects of wake interaction. In addition, the RMS distribution may be used to locate the regions of flow with strongest fluctuations, which is of interest for unsteadiness reduction.

The procedure for calculating the RMS distributions can be found in Appendix E, along with the definitions of other relevant unsteadiness metrics. In the present study, RMS distributions are evaluated for the flow variables and locations shown in Table 3.3.

Location	Variable	Purpose
Suction surface	Static Pressure	Assess unsteady loading
Pressure surface	Static Pressure	Assess unsteady loading
Trailing edge plane	Vorticity	Asses exit non-uniformities

Table 3.3.
Locations for evaluating the RMS distributions.

The RMS distribution of the static pressure on the blade surface is shown in Figure 3.18. The large RMS values in the leading edge region are the result of the intense local pressure peaks, occurring upon wake interception.

An interesting feature of the pressure fluctuations is the presence of "peaks" and "troughs" in the RMS distribution over most of the blade. This non-uniform RMS distribution can be explained by splitting the unsteady static pressure coefficient into two parts :

$$C_p(s,t) = \underbrace{\mathcal{A}(s)\sin(\frac{2\pi t}{T})}_{I} + \underbrace{\mathcal{B}\sin(\frac{2\pi t}{T} + \frac{N_B \pi s}{U_\infty})}_{II} \tag{3.7}$$

where the first term represents the instantaneous loading resulting from the wake impinging on the leading edge; and the second term represents a moving-wave-like disturbance due to the B-vortices (suction side) or wake vortices (pressure side). It can be readily shown that the RMS distribution for functions of the above form is similar to that shown in Figure 3.18; and that the number of peaks in the RMS distribution is equal to the number of B-vortices (suction side) or to the number of wakes (pressure side) within the stator passage.

The vorticity RMS distribution on the trailing edge plane, shown in Figure 3.19, reveals

(1) The discharge of B-vortices from a distinct location over the suction surface.

(2) The shedding of A-vortices from the trailing edge.

(3) The discharge of wake vortices over a broad interval under the pressure surface.

Global unsteadiness indexes, defined in Appendix E, can be used to compare the unsteadiness levels in different regions of the flowfield or to compare the levels of unsteadiness from two different cases. In laminar flow, the pressure fluctuations on the suction surface are more important than those on the pressure surface. This may be appreciated by examining the RMS distribution in Figure 3.18; the corresponding unsteadiness indexes are $\check{C}_{p_{SS}} = 0.127$ and $\check{C}_{p_{PS}} = 0.115$. The amplitude and the sharpness of all fluctuations increases with the Reynolds number.

3.7. Effects of the Reynolds number

In typical axial turbomachinery, the Reynolds number is of the order of a few millions and the flow is turbulent. It is thus necessary to find out whether the results for laminar flow at a Reynolds number of 10,000 would carry over to turbulent flow situations.

Prior to the implementation of a turbulence model in the Navier-Stokes code, several moving wake laminar calculations were carried out at off-design Reynolds numbers ranging from 5,000 to 75,000. Computer memory requirements were the limiting factor for the grid resolution used in these calculations.

As illustrated in Figure 3.20, the unsteady flow features in the computed results are similar to those observed in the calculation at a Reynolds number of 10,000. In particular :

- The disturbance flow over the suction surface is dominated by series of counterrotating B and P vortices. The B-vortices are produced at the leading edge upon wake interception. The P-vortices are generated by the B-vortices, as discussed in §3.3.
- The disturbance flow over the pressure surface is dominated by the migration of wake fluid there and its evolution of a system of counterrotating vortices.
- The unsteady blade loading is characterized by moving pressure disturbances associated with these vortical features.

As the Reynolds number in the laminar calculations is increased, the effects of the disturbances become sharper and stronger (Figure 3.21). This behavior indicates that, with the present computational resources, the very small scales cannot be adequately resolved at Reynolds numbers of practical interest. Therefore, a turbulence model is required to represent the transfer of energy from the large scale disturbances towards the very small scale eddies of turbulent flow. The computed results presented in the next chapter use a Baldwin-Lomax turbulence model to study the dynamics of the unsteadiness in a turbulent flow regime.

Chapter 4

Unsteady Turbulent Flow Calculations

The computational set-up and spectral-element grid used for the turbulent calculations in this chapter, are identical to those presented in §3.1. Using the modified Baldwin-Lomax turbulence model, steady-state and moving-wake Navier-Stokes calculations have been carried out at Reynolds numbers of 1,000,000 and 3,000,000. As the computed results at these two Reynolds numbers are similar, only the results at Re=1,000,000 shall be presented here.

4.1. Flowfield in absence of moving wakes

The undisturbed flow about the stator blade at a Reynolds number of 1,000,000 exhibits several features characteristic of turbulent flows. A comparison between Figure 4.1 and Figure 3.4, indicates that the boundary layer is thinner and remains attached over a larger portion of the blade surface in comparison to the laminar case at Re=10,000. As shown in Figure 4.2, most of the boundary layer vorticity is now concentrated near the blade surface. These features can be also observed in Figure 4.3, which compares the boundary layer velocity profiles from the laminar and turbulent calculations.

The computed velocity profiles at Re=1,000,000 have been compared to those predicted by the empirical relationship known as *law-of-the-wall*:

$$n^+ = u^+ + e^{-5k}\left[e^{ku^+} - 1 - ku^+ - \frac{(ku^+)^2}{2} - \frac{(ku^+)^3}{6}\right] \tag{4.1}$$

in which:

$$u^+ = u \sqrt{Re/\frac{\partial u}{\partial n} |_{n=0}} \tag{4.2}$$

$$n^+ = n \sqrt{Re\frac{\partial u}{\partial n} |_{n=0}} \tag{4.3}$$

Equation (4.1) is a good approximation to velocity measurements in the very thin viscous sublayer ($0 < n^+ < 50$), which contains the steepest velocity gradients. The law-of-the-wall is independent of the body geometry and of the pressure gradient (see e.g. Sherman [42]); this makes it suitable for direct comparison with the computed data.

The results of the comparison are shown in Figure 4.4 for the particular chordwise position $x = 0.25$. For values of the law-of-the-wall coordinate n^+ of less than eight, the computed profile agrees with the law-of-the-wall. For larger values of n^+ however, the computed velocity profile is steeper. This difference may be due to (a) using a turbulence model that is not specifically tailored for fitting the law-of-the-wall; and/or (b) insufficient resolution in the "knee" region of the law-of-the-wall curve. It is to be noted that the first three collocation points of the spectral grid are located at values of n^+ of 0, 1.8 and 6.7 respectively; thus providing enough resolution in the region where law-of-the-wall and calculations agree. On the other hand, owing to the use of Chebychev polynomials, the subsequent three collocation points are at n^+ of 13.3, 20.3 and 26.6, which is within the "knee" region. It is to be noted that the difference between the computed profile and the law-of-the-wall are unlikely to have an impact on the following results; because they are confined to the extremely thin viscous sublayer. The flow in the rest of the boundary layer is conditioned by the turbulent eddy viscosity, the value of which allows the spectral grid to resolve the local flow features.

The static pressure distribution at Re=1,000,000 (Figure 4.5a) is similar to that obtained from an inviscid calculation of the steady flow in the stator passage (Figure 5.9). In the absence of rotor wakes, the pressure fluctuations associated with vortex shedding from the trailing edge are negligible.

However, the time-averaged static pressure distribution in the presence of wakes is quite different from that of the above steady flow. This may be appreciated by comparing Figure 4.5a to Figure 4.5b, which shows a significant increase of the time-mean blade loading in the forward part of the blade. This increase can be explained by the averaged effect of the leading edge pulses. It is to be noted that the averaged inlet velocity in presence of wake is different from the steady flow velocity, owing to the excess tangential momentum of the wake. Steady-state calculations with this averaged velocity will be made in the near future,

to assess whether the resulting pressure distribution is the same as the time-average from the unsteady case.

4.2. Velocity and vorticity disturbances

To visualize the disturbances due to the rotor wakes, the above steady flow shall be subtracted from the calculated unsteady flow in the presence of wakes. Successive snapshots of the disturbance vorticity field at a Reynolds number of 1,000,000 are shown in Figures 4.6a to 4.6j. The disturbance flow features at high Reynolds number are similar to those observed in the laminar flow calculations. In particular, the unsteady flow over the suction surface is dominated by a series of B-vortices. Within the stator passage, the wake fluid moves away from the suction surface towards the pressure surface, where it evolves into series of counterrotating vortices.

The process for production of B-vortices in turbulent flow is identical to that in laminar flow. As shown in Figure 4.6a, the interception of the rotor wake by the stator blade leading edge results in the production of a vortical B-region of negative sign. This region is subsequently lifted away from the surface and carried downstream (Figures 4.6c-f). Each B-region evolves eventually into a clockwise B-vortex (Figures 4.6g-j).

The B-region and B-vortices appear to be weaker than those observed in the laminar flow calculations at Reynolds numbers of and above 10,000. This difference appears to be related to the thinner boundary layer in turbulent flow. This idea will be further developed in Chapter Five, which discusses the mechanism for B-vortex production.

On both pressure and suction surface, the B-vortices and the wake vortices induce P1 and N1-type vortical disturbances in the laminar sublayer. These disturbances, visible in Figure 4.6a-j, are qualitatively similar to those already observed in the laminar flow calculations, but are considerably thinner. As shown in Figures 4.6a-j, the wake vortices in turbulent flow are closer to the pressure surface. This may be explained by the thinner boundary layer on the pressure surface.

It is to be noted that the highest eddy viscosity values occur inside the envelope of motion of the B-vortices, shown in Figure 4.7. This suggests that turbulent diffusion may significantly affect the strength of the fully developed B-vortices; and consequently, reduce the amplitude of the pressure fluctuations on the suction surface.

4.3. Pressure disturbances

As shown in Figures 4.8a-b, the pressure disturbances on the blade surface exhibit a characteristic pattern similar to that from the laminar flow calculations. This similarity is the result of the causal connection between the unsteady vortical structures and the pressure disturbances; described again as follows.

(1) The series of moving *low-pressure peaks* on the suction surface are associated with the low-static pressure region in the core of each B-vortex. This is shown by the correlation between Figures 4.9a and 4.9b.

(2) The series of moving *pressure disturbances* on the pressure surface are likewise the result of the nearby wake vortices, which produce regions where the flow is directed against the blade surface. This is shown by the correlation between Figures 4.10a and 4.10b.

(3) The intense *pressure pulses* arising on the leading edge at the moment of wake interception are due to the conversion of the higher total pressure of the wake fluid into static pressure by the stopping action of the blade surface. This is shown by the correlation between Figures 4.11a and 4.11b.

The amplitude of the pressure disturbances moving along the pressure surface is approximately equal to that of the laminar case. This may be appreciated by comparing the pressure RMS distribution in Figure 4.12 to that in Figure 3.18. On the other hand, the series of low-pressure peaks on the suction surface at a Reynolds number of 1,000,000 are about twice as weak as the corresponding peaks in the laminar calculation at Re=10,000. This noticeable difference may be attributed to the weaker B-vortices in turbulent flow, and to the non-linear relationship between pressure fluctuations and vortex strength. As a result, the loading fluctuations on the suction surface in turbulent flow become less important than those on the pressure surface.

Similar observations can be made about the vorticity RMS distribution on the trailing edge plane, shown in Figure 4.13 for a Reynolds number of 1,000,000. The distribution is qualitatively similar to that from the laminar flow calculations (Figure 3.19); however, the RMS peak due to the discharge of B-vortices is considerably smaller.

The similarity between the turbulent results and those from the previous chapter suggests that the mechanisms for unsteady flow production during wake/stator interaction, are the same in laminar and turbulent flows. This observation has two important implications. First,

one may gain insight into the unsteady fluid mechanics of wake interaction from calculations at moderately low Reynolds numbers, using direct Navier-Stokes codes. This requires an order of magnitude less time and computer resources, and is taken advantage of in Chapter Six. Second, proof-of-concept studies of flow control strategies can be based on laminar flow studies. This is taken advantage of in Chapter Seven.

4.4. Effects of the turbulence model

The use of a turbulence model introduces an uncertainty in the high Reynolds number calculations. Before generalizing the above conclusions, it is necessary to determine to what extent the differences between the laminar and turbulent flow results are sensitive to the empirical constants in the turbulence model.

For this purpose, moving wake calculations have been carried out using the original form of the Baldwin-Lomax model (cf. §2.2.1). The resulting eddy viscosity values acting on the unsteady flow structures are considerably higher (Figure 4.14).

The computed results show the production of a B-vortex over the suction surface as the wake is intercepted by the leading edge (Figure 4.15). However, this vortex is weak and it dissipates before reaching the aft portion of the blade surface. As a result, the pressure disturbances over the suction surface are small and decay rapidly (Figure 4.16). Over the pressure surface, the nature of the unsteady flow is not significantly affected by the larger eddy viscosity values.

Therefore, the uncertainties associated with the particular turbulence model used, can have a significant bearing on the amount of suction surface unsteadiness, but not on its nature. It is to be noted that the foregoing high-eddy viscosity calculations are unlikely to be representative of the flow in actual situations. As observed by Taylor [46], the vortical wakes are present far downstream of the interacting blade rows. This would not happen if the diffusion due to the turbulence model used was as high as above.

The Baldwin-Lomax model used for the turbulent flow calculations is based on several simplifying assumptions, such as turbulence isotropy and equilibrium, no memory of the upstream events and no transition. A considerable number of more sophisticated turbulence models, featuring such refinements, is available. These have however a local effect. Therefore, using a turbulence model other than Baldwin-Lomax' may improve the quantitative

reliability of the results, but would not reveal fundamental features of the unsteadiness dynamics other than those observed in the present study. This statement is confirmed by the linearized perturbation calculations, which seek to clarify the physical mechanisms behind the production of unsteady flow.

Chapter 5

Linearized Perturbation Calculations

5.1. Interpretation of the linearized equations

In the linearized perturbation calculations, the unsteady flowfield in the stator is decomposed into two parts :

$$U(x,y,t) = \bar{\mathbf{U}}(x,y) + \tilde{\mathbf{u}}(x,y,t) \tag{5.1}$$

$$P(x,y,t) = \bar{P}(x,y) + \tilde{p}(x,y,t) \tag{5.2}$$

The first term in the above, $\bar{\mathbf{U}}(x,y)$, is a known steady-state viscous flowfield that would exist in the absence of rotor wakes. This *base flow* can be obtained using accurate Navier-Stokes solvers. The second term, $\tilde{\mathbf{u}}(x,y,t)$ is the disturbance flowfield due to the wake perturbation. This *disturbance flowfield* contains the unsteady effects of interest in the rotor wake/stator interaction. In the linearized calculations, the disturbance flowfield is linearized about the base flow and is assumed to be inviscid. The resulting disturbance flow equations, derived in Chapter 2, are :

$$\frac{\partial \tilde{\mathbf{u}}}{\partial t} + \underbrace{\bar{\mathbf{U}} \cdot \nabla \tilde{\mathbf{u}}}_{I} + \underbrace{\tilde{\mathbf{u}} \cdot \nabla \bar{\mathbf{U}}}_{II} = -\nabla \tilde{p} \tag{5.3}$$

$$\text{B.C.:} \qquad \tilde{\mathbf{u}}(x_s, y_s, t) \cdot \mathbf{e}_n = 0 \tag{5.4}$$

The results from the numerical solution of the linearized equations are compared to those from the full Navier-Stokes equations, written here in terms of disturbance flow velocity:

$$\frac{\partial \tilde{\mathbf{u}}}{\partial t} + \underbrace{\bar{\mathbf{U}} \cdot \nabla \tilde{\mathbf{u}}}_{I} + \underbrace{\tilde{\mathbf{u}} \cdot \nabla \bar{\mathbf{U}}}_{II} + \underbrace{\tilde{\mathbf{u}} \cdot \nabla \tilde{\mathbf{u}}}_{III} = -\nabla \tilde{p} + \underbrace{\nabla \tilde{\mathbf{u}} \left\{ (\frac{1}{Re} + \nu_t) \nabla \tilde{\mathbf{u}} \right\}}_{IV} \tag{5.5}$$

$$\text{B.C.:} \qquad \tilde{\mathbf{u}}(x_s, y_s, t) = 0 \tag{5.6}$$

This comparison can provide insight into the fluid mechanics of the unsteady flow, since each term in the foregoing equations represents a specific physical process that can be individually examined as follows :

(1) Term I represents the convection of the disturbance flow by the base flow $\bar{\mathbf{U}}$. The effects of this term should be present in both Navier-Stokes and linearized calculations.

(2) Term II represents the distortion of the base flow vorticity by the unsteady disturbance flow. This term is significant in regions where the base flow is rotational (e.g. boundary layer). Its effects should be present in both Navier-Stokes and linearized calculations.

(3) Term III represents the self-advection of the disturbance flow, and is present only in the non-linear (Navier-Stokes) calculations.

(4) Term IV represents the diffusion of the disturbance flow under the effects of the steady and unsteady shear stresses, present only in the Navier-Stokes calculations.

Moving-wake linearized-perturbations calculations have been carried out using a laminar base flow at a Reynolds number of 10,000 (from §3.2), and a turbulent base flow at at Reynolds number of 1,000,000 (from §4.1). The results are compared to those from the Navier-Stokes calculation in order to (1) clarify the physical mechanisms involved in the production of unsteadiness; and (2) to explain the differences and similarities between the laminar and turbulent flow calculations. An artificial viscosity parameter R_a of 10,000, has been used.

5.2. Linearized calculations with laminar base flow.

This section compares the key features of (a) the unsteady flow from the laminar Navier-Stokes calculation at a Reynolds number of 10,000; to (b) the results from an inviscid linearized calculation with a viscous base flow at a Reynolds number of 10,000.

The unsteady flow phenomena over the suction surface of the stator blade are adequately represented by the linearized perturbation calculations. The results show production of B-vortices at the leading edge of the stator blade (Figures 5.1a to 5.1e). These results agree with those from the Navier-Stokes simulation quantitatively as well as qualitatively.

On the other hand, the linearized calculations cannot adequately represent the migration of the wake across the stator passage, and the resulting unsteadiness on the pressure surface. As shown in Figures 5.2a and 5.2b, the high-vorticity wake fluid does not move away from the suction surface towards the pressure surface, and does not roll up into discrete vortices. This is not surprising, because these phenomena are associated with the self-advection of the wake fluid. The self-advection is represented by the non-linear term $\tilde{\mathbf{u}} \cdot \nabla \tilde{\mathbf{u}}$, which is absent from the linearized calculations.

As a consequence, the linearized calculations cannot describe the pressure disturbances on the pressure surface. The small pressure disturbances seen on the pressure surface in Figures 5.3a-b are due to the BP-vortex, which is produced at the leading edge at the moment of wake interception (cf. §3.3), and is thus present in the linearized calculations too. The pressure disturbances on the suction surface are in good agreement with those from the Navier-Stokes calculation. This is due to the qualitative and quantitative agreement of the computed unsteady vortical features over the suction surface.

5.3. Linearized calculations with turbulent base flow.

This section compares the principal features of (a) the unsteady flow from the turbulent Navier-Stokes calculation at a Reynolds number of 1,000,000; to (b) the results from an inviscid linearized calculation with a turbulent base flow at a Reynolds number of 1,000,000. The comparison yields the following observations :

(1) On the suction surface, the linearized calculations show the production of B-vortices of comparable magnitude, which induce similar pressure disturbances. This is shown in Figures 5.4a-e and Figures 5.6e-b.

(2) On the pressure surface, the linearized calculations cannot represent the wake migration and evolution into discrete vortices and the resulting pressure disturbances. This is shown in Figures 5.5a-b and Figures 5.6e-b.

The comparison of the results to those from the previous section, indicates that when a

turbulent base flow is used, the unsteadiness on the suction surface is smaller than that obtained with a laminar base flow. This may be appreciated by comparing Figure 5.6a-b to Figure 5.3a-b. Otherwise, the unsteady flow features are similar. Therefore, the results from linearized calculations of unsteady wake interaction with laminar and turbulent base flow are in agreement with the corresponding laminar and turbulent Navier-Stokes calculations, as far as the flow over the suction surface is concerned. This similarity gives a clue on the mechanisms involved in the production of the observed unsteady flow features.

5.4. Mechanisms for production of unsteady flow

The results from the linearized calculations indicate that the unsteady flow over the pressure surface of the stator blade is produced by the self-advection of the high-momentum fluid in the rotor wake. The linearized perturbation approach is unfortunately unable to represent this flow adequately.

The presence of B-vortices in the linearized calculations, where the disturbances are treated as inviscid, suggests that the origin of B-vorticity lies in the viscous base flow. The production of a vortical B-region on the leading edge can be described as a distortion of the boundary layer vorticity by the wake disturbance velocity. This is illustrated in Figure 5.7, where part of the boundary layer vorticity is lifted off from the surface by the wake. This elongated vortical region is subsequently detached from the blade surface by the convective action of the wake. Once in the free stream, the B-region evolves into a B-vortex.

The B-vortex production mechanism proposed above can be fully represented by the distortion term $\tilde{\mathbf{u}} \cdot \nabla \bar{\mathbf{U}}$, common to both Eqs.(5.3) and (5.5). This mechanism can explain the following observations:

(1) The similar disturbance flow features in the laminar and turbulent flow regimes. In both cases, these features are produced by similar boundary layer disturbances.

(2) The weaker suction surface unsteadiness in turbulent flow with respect to that in laminar flow. In turbulent flow, the boundary layer is thinner and remains strongly attached to the blade surface. It would be less susceptible to distortion by the wakes.

(3) The identical sign for all B-vortices, which contain vorticity from the suction side boundary layer only.

(4) The good quantitative agreement between linearized and full Navier-Stokes calculations over the suction surface. Both can account for the base flow boundary layer distortion.

To confirm that the B-vortices are produced from the boundary layer under the effect of the incoming wake velocity, a linearized calculation with inviscid base flow has been carried out.

5.5. Linearized calculations with inviscid base flow

An inviscid base flow about the stator geometry previously used, has been generated using the PCPANNEL code by McFarland [32]. The inviscid base flowfield, in Figures 5.8a-b, is characterized by the absence of boundary layer. As shown in Figure 5.9, the static pressure distribution in inviscid flow is similar to that from the turbulent calculations.

Results from a linearized calculation with this base flow show an absence of B-vortices. As shown in Figures 5.10a-b, the rotor wakes are simply cut by the stator blade without other kind of interaction. The relative slip of the wakes as they move downstream within the stator passage is due to the circulation about the blade. As shown in Figures 5.11 and 5.12, no pressure disturbances over the blade surface, except for the leading edge pulses, are present.

These results confirm that the B-vortices are produced as the boundary layer vortical fluid is distorted and detached by the incoming wake. Therefore, the presence of a boundary layer plays a major role in the nature of the unsteady flow over the suction surface of the stator blade. The results also confirm that the leading edge pressure pulses are mainly a potential flow effect, associated with the higher velocity of the wake fluid.

Several parameters can affect the boundary layer characteristics and its response to the wakes. The effect of these parameters on the unsteady flow is examined in the next chapter.

Chapter 6

Parametric Study of the Unsteady Flow

6.1. Range of investigation

The foregoing results have been obtained with the particular rotor/stator configuration discussed in §3.1, further referred to as *baseline* configuration. To generalize the results to other rotor/stator configurations, a parametric study is carried out to examine the effects of various design parameters on the unsteady flow arising from wake interaction.

Four design parameters are considered in the study—stator blade loading, wake thickness, wake velocity defect and wake reduced frequency. The stator blade loading is one of the principal parameters affecting the boundary layer. Changes in loading are simulated here by varying the flow angle θ at the stator inlet. The wake thickness, velocity defect and reduced frequency are the principal parameters that are expected to influence the boundary layer response to wake disturbances.

Only one of the above four parameters is allowed to change at once with respect to the baseline case. The unsteady flowfield is then computed using the laminar Navier-Stokes solver at a Reynolds number of 10,000. The results are compared to those from Chapter Three, in order to determine how each parameter influences the unsteady flow. Table 6.1 summarizes the values assumed by each parameter in these calculations.

It is to be noted that the computational grid used here (Figure 6.1) has half the resolution of the grid from the baseline calculations. As shown in Figures 6.2a-c, this has no significant effect on the computed baseline flow, and therefore should not have any bearing on the

comparison of the results from the parametric study to the higher-resolution baseline flow.

Parameter	*Trial Values*	*Baseline Value*
Stator loading	θ =30 deg.; θ =20 deg.;	θ =25 deg.
Wake strength	A=33%	A=75 %
Wake thickness	δ=20%; δ=20%	δ=10%
Wake reduced frequency	κ =2.5; κ =7.5	κ =5.0

Table 6.1. Parameter values used in the parametric study.

6.2. Effects of the stator blade loading

6.2.1. High loading case

The undisturbed flowfield in the stator passage for an inlet turning angle of 30 degrees is shown in Figure 6.3. The corresponding pressure distribution, in Figure 6.4, exhibits a strong adverse pressure gradient over the forward part of the suction surface. As shown in Figure 6.5, this results in a thicker boundary layer with respect to the baseline case. The increase in boundary layer thickness at the reference location of 0.25 chords downstream of the leading edge, is nearly 25%.

These changes have a dramatic impact on the unsteady flow induced by the upstream wakes. As shown in Figures 6.6a-b, there is a fundamental change in the disturbance vortical features over the suction surface. In addition to the B-vortices, produced at the leading edge, the disturbance flowfield is also characterized by another row of moving vortices, closely associated with the B-vortices but having an opposite sign. These vortices, referred to as P-vortices, are produced over the foremost 25% of the stator blade chord; and are comparable in strength to the B-vortices.

The mechanism for production of P-vortices appears to involve distortion and detachment of the boundary layer vorticity under the influence of the B-vortices. This process was already discussed in §3.3, where small P-vortices were seen to originate from the P1-type boundary layer vortical disturbance. Herein, each P-vortex is considerably larger, and contains another positive vortex, which is produced at the leading edge during the wake approach. This is examined in time as follows.

(1) Shown in Figure 6.7a is a close-up of the disturbance vorticity contours at time t_0, corresponding to the approach of a rotor wake. On this figure, one can identify a B-

vortex produced by a previous interaction; a positive-sign boundary-layer disturbance induced by the B-vortex that will be referred to as *P1 region*; and a small positive vortical region on the leading edge that will be referred to as *P2 region*. The P2-region appears to be produced on the leading edge upon wake approach, and was not observed in the baseline calculations. The B-vortex and the P1-region are stronger than those observed in the baseline calculations.

(2) Figure 6.7b refers to time $t_0 + 0.3T$. A new wake is interacting with the leading edge and is producing a vortical B-region. The P2-region from Figure 6.7a has not moved considerably, since it is convected with a local velocity smaller than the free-stream velocity. As a consequence, the new B-region is in close proximity of the P2-region.

(3) Figure 6.7c refers to time $t_0 + 0.5T$. The wake is moving away from the suction surface, leaving behind a vortical group consisting of the B-vortex, a P2-vortical region, and the P1-region induced by the B-vortex.

(4) Figure 6.7d refers to time $t_0 + 0.9T$. As the above group has moved downstream, the P2-vortical region has evolved into a P2-vortex. Because the P2 and the B-vortex are of opposite sign, the flowfield between a P2 and a B-vortex belonging to the same group is characterized by a velocity component directed against the blade surface. For the same reason, the flowfield between two successive groups is characterized by a velocity component directed *away* from the blade surface. This type of flow further distorts the vortical P1-region, as shown in Figure 6.7d.

(5) Figures 6.7e to 6.7g refer to the time interval $[t_0 + 1.1T;\ t_0 + 1.3T]$. On Figure 6.7e, one can see that the flow induced by the P2 and B-vortices has significantly distorted the vortical P1-region, part of which is being detached from the blade surface. On Figures 6.7f and 6.7g, one can see that this detached part of the P1-region fuses with the P2 vortex to form a single P-vortex.

The process of boundary layer distortion and vortex interaction described above, appears to be completed over the first 25% of the stator chord. The unsteady flow over the rest of the suction surface is characterized by a fully developed vortex street of counter-rotating B- and P-vortices, with the B-vortices being confined closer to the surface.

The counter-rotating vortex street results in a characteristic pattern of pressure fluctuations on the suction surface. This pattern, illustrated in Figures 6.8a-b, consists of a row of

moving low-pressure peaks interleaved with substantial high-pressure disturbances. The low-pressure peaks are consequence of the low-pressure regions in the vortex cores—they were also observed in the baseline calculation (cf.§3.5). The high pressure-peaks are associated to a stagnation-point region, where the disturbance flow induced between a B/P-vortex pair is directed against the blade surface.

These pressure fluctuations are considerably stronger with respect to the baseline case. This can be explained by (1) the stronger B-vortices produced at the leading edge; and (2) by the additional perturbing effect of the P-vortices. As shown in Figure 6.9, the RMS levels on the suction surface are about three times larger than in the baseline case; although the time-mean lift coefficient has increased only about 1.5 times.

The production of P-vortices and the stronger unsteady flow over the suction surface can be explained by the strong adverse pressure gradient, which is the principal difference between high-loading and baseline calculations. The adverse pressure gradient facilitates boundary layer distortion and detachment, thereby resulting in the production of stronger B-vortices. On their turn, these B-vortices induce a correspondingly stronger P1-region via the mechanism represented by Equations (3.1-3.3). Further downstream, this P1-region is detached from the blade surface, under the combined effect of the stronger B-vortex velocity field and the adverse pressure gradient. The resulting P-vortex is substantially larger than in the baseline calculation. Finally, the production of the P2-region near the leading edge appears to be the result of a flow readjustment following the detachment of the B-region.

6.2.2. Low loading case

The undisturbed flowfield in the stator passage for an inlet turning angle of 20 degrees is shown in Figure 6.10. At the reference location of $s = 0.25c$, the suction surface boundary layer is 13% thinner with respect to the baseline case (Figure 6.5). The static pressure distribution, in Figure 6.11, shows the presence of a favorable pressure gradient, which extends for almost 0.2 chords downstream of the leading edge.

As shown in Figures 6.12a-b, the unsteady flow features at low loading are qualitatively similar to those from the baseline calculation. However, the pressure disturbances over the suction surface are considerably smaller, owing to the weaker B-vortices. This may be appreciated by comparing Figures 6.13a-b to Figures 3.13a-b; and Figure 6.14 to Figure 3.18.

It is to be noted that the unsteady flow over the pressure surface is not significantly

affected by loading variations in the 20-30 degrees range used herein. This is explained by the origin of the unsteadiness over the pressure surface, which is associated with the wake migration rather than with boundary layer disturbances.

6.3. Effects of the wake strength

The wake strength is represented by the velocity defect as seen in the rotating frame. A 75% defect is used in the baseline calculations. As per Appendix C, this value corresponds to a relatively small rotor-stator spacing of 0.2 stator chords. To study the effect of larger spacings, a calculation with a velocity defect of 30% was carried out. This value corresponds to a rotor-stator spacing of about 0.5 chords.

The computed results, in Figures 6.15a-b, show an unsteady flow that is qualitatively similar to the baseline case. The unsteady flow features are however considerably weaker. Over the suction surface, weaker B-vortices produce pressure fluctuations with amplitude only half of that observed in the baseline case. The leading edge pulses and the pressure fluctuations on the pressure surface are substantially smaller. This is explained by the quadratic relation between pressure and vortex strength (Eqs. 3.4-3.6); and may be appreciated by comparing Figure 6.16 to Figure 3.13a, and Figure 6.17 to Figure 3.18.

6.4. Effects of the wake thickness

6.4.1. Wake thickness of 0.2 stator chords

The effects of wake thickness were investigated while keeping the velocity defect to a constant value of 75%. Increasing the wake thickness is thus equivalent to proportionally increasing the total momentum of the wake. As shown in Figures 6.18a-b, this results in an unsteady flow, that is not only considerably stronger, but also different in nature from the baseline case. In particular, the disturbance flow over the suction surface is characterized by a street of counter-rotating B-vortices and P-vortices. The B-vortices are about two times stronger than in the baseline case.

Successive snapshots of the disturbance vorticity field (Figures 6.19a-6.19c), indicate that each P-vortex originates from a P1-region that has been produced, distorted and detached

by a B-vortex. This is described as follows. Shown in Figure 6.19a is a large B-vortex, being produced at the leading edge of the stator blade. In Figures 6.19b-c, one can see this B-vortex inducing a P1-type boundary-layer disturbance on the blade surface. Further downstream, this disturbance is detached from the surface and evolves into a P-vortex. This mechanism is similar to that observed in the high-loading case; except that here the P-vortex is produced without intervention of a P2-region or a strong adverse pressure gradient.

The pressure fluctuations on the suction surface exhibit a pattern of moving peaks and depressions, shown in Figures 6.20a-b. This pattern is characteristic of the counter-rotating vortex street. The amplitude of these pressure fluctuations is considerably larger than that from the baseline case. This may be appreciated by comparing Figures 6.20a-b to Figures 3.13a-b; and Figure 6.21 to Figure 3.18.

For the particular case of 20% wake thickness, the wake fluid cannot fully evolve into wake vortices. This is shown in Figures 6.18a-b; and may be explained by the interference of successive wakes, the spacing of which is comparable to the thickness. As a result, the pressure fluctuations on the pressure surface are weaker than in the baseline case.

Finally, the leading edge pressure peaks occurring upon interception have the same amplitude as in the baseline case, but their duration and width are twice as large. This is so because the amplitude of the peaks is related to the total pressure in the wake fluid (unchanged), whereas the duration of the peaks is related to the wake width (twice as large).

6.4.2. Wake thickness of 0.05 stator chords

In this case the unsteady flow features are identical to that from the baseline calculations. This may be seen in Figures 6.22a-b, which shows B-vortices over the suction surface and wake vortices over the pressure surface. However, both types of vortices are about half as strong as those from the baseline case. This results in significantly weaker pressure fluctuations; which may be appreciated by comparing Figure 6.23 to Figures 3.13a, and Figure 6.24 to Figure 3.18.

6.5. Effect of the wake reduced frequency

The reduced frequency is defined herein as the ratio of the wake convection time through the stator blade row (c_s/U_∞) to the wake passing period (S_r/V). With the present non-

dimensional formulation, the convection time is equal to unity, and the reduced frequency becomes :

$$\kappa = \frac{V}{S_r} = \frac{V}{P \times S} \tag{6.1}$$

Changes in reduced frequency can be implemented by either changing the tangential velocity of the rotor blade, or by changing the spacing-blade chord ratio. Since the spacing ratio is limited by the available computational resources, the first approach was used. Increasing the rotor blade velocity has however the undesirable effect of increasing the total momentum of the wake and decreasing its thickness in the non-rotating frame. Therefore, the effects of the wake passing frequency are somewhat related to the effects of the wake strength in the following results.

6.5.1. Reduced frequency of 2.5

To obtain a reduced frequency of 2.5, the non-dimensional tangential velocity of the rotor blade is reduced to unity. No new unsteady flow features are observed in this case. As shown in Figures 6.25a to 6.25d, the wake fluid migrates towards the pressure surface; where it forms two counter-rotating wake vortices. The pressure fluctuations on the pressure surface are extremely weak in comparison to the baseline case; so are the leading edge peaks. This may be appreciated by comparing Figures 6.26a-b to Figure 3.13a-b, and Figure 6.27 to Figure 3.18. These weaker pressure fluctuations can be fully accounted for by the smaller excess tangential velocity of the wake fluid. They are not related to the reduced frequency.

Although the excess tangential momentum of the wake at a reduced frequency of 2.5 is smaller, the B-vortices over the suction surface are larger and stronger in comparison the to baseline case. This indicates that the boundary layer is more readily distorted and detached by lower-frequency wake disturbances. The stronger B-vortices create P1-type boundary layer disturbances as they moves downstream. These disturbances are eventually detached from the surface to become fully developed P-vortices, seen over the aft part of the stator blade in Figures 6.25a-d. The production of P-vortices leads to the growth of the pressure fluctuations over the aft part of the suction surface, shown in Figures 6.26a-b and 6.27.

6.5.2. Reduced frequency of 7.5

To obtain a reduced frequency of 7.5, the non-dimensional tangential velocity of the rotor blade is increased to three units. The computed disturbance vorticity contours in the

stator passage are shown on Figures 6.28a-b; one can see that the unsteady flow features are identical to the baseline case.

In particular, the unsteady flow over the suction surface is characterized by a row of B-vortices. The number of B-vortices is larger than in the baseline case, due to the higher number of wake interception per unit of convection time. For this reason, these vortices tend to "fuse" together as shown in Figures 6.28a-b. At higher reduced frequency, the B-vortices are weaker with respect to the baseline case, even if the excess tangential momentum of the wake is now larger. This confirms that the amount of boundary layer vorticity detached from the leading edge is directly related to the reduced frequency of the wakes.

The resulting pressure fluctuations on the suction surface are noticeably smaller than in the baseline case, owing to the weaker B-vortices. This may be appreciated by comparing Figures 6.29a-b to Figures 3.13a-b; and Figure 6.30 to Figure 3.18. The stronger pressure fluctuations on the pressure surface, seen on these figures, can be fully accounted for by the larger excess tangential velocity of the rotor wake. They do not appear to be directly related to the reduced frequency.

6.6. Conclusions from the parametric study

Three parameters were found to influence the unsteady flow over the suction surface of the stator blade, and the amplitude of the resulting pressure fluctuations.

- The pressure gradient.
- The total momentum of the wake.
- The reduced wake passing frequency.

A favorable pressure gradient reduces the amount of B-vorticity detached from the leading edge. An adverse pressure gradient has the opposite effect. With a particularly strong adverse pressure gradient, each B-vortex is subsequently able to detach part of the associated P1-region from the blade surface, and eject it into the free stream, where is evolves into a P-vortex. In the presence of such a gradient, the unsteady flow is characterized by a vortex street of counter-rotating B and P vortices; whereas only B-vortices are observed in normal/low loading cases. The strength of the B-vortices also increases proportionally to the excess tangential momentum of the wake, and decreases as the wake reduced frequency

is increased. Even in the absence of a strong adverse pressure gradient, sufficiently large B-vortices can produce, further downstream, an associated vortex street of opposite-sign P-vortices.

The amplitude of the pressure fluctuations on the suction surface grows as the square of the strength of the B and P-vortices. An adverse pressure gradient thus results in stronger fluctuations. Particularly strong pressure fluctuations are observed in the presence of a counter-rotating B/P vortex street. In such situation, the pressure disturbances consist of alternating high- and low-pressure regions; the high-pressure regions being due to the stagnation-point flow induced by opposite-sign vortices.

The unsteady flow over the pressure surface of the stator blade is dominated by the migration of the wake fluid; and is relatively insensitive to the stator blade loading. The amplitude of the pressure disturbances on the pressure surface increases as the square of the wake vortices strength. A larger excess of tangential momentum in the wake will consequently result in stronger pressure disturbances. The amplitude of the leading edge pressure peaks arising upon wake interception grows as the square of the excess tangential velocity in the wake; the duration of the peaks scales as the wake width.

The above conclusions are based on laminar simulations of the unsteady flow in the stator passage. Since the unsteadiness features are the same in laminar and turbulent flow, these conclusions may be expected to carry over to the turbulent regime.

Chapter 7

Control of the Unsteady Flow

7.1. Definition of flow control strategies

An unsteady flow *control strategy* is a specific action or design modification, the purpose of which is to reduce or eliminate the undesirable aspects of the unsteady flow induced by the rotor wakes. The following aspects of the unsteady flow may be deemed undesirable in view of improving the noise and vibration characteristics of a typical turbomachine:

- Static pressure fluctuations on the blade surface.
- Production and discharge of B-vortices.
- Production and discharge of wake vortices.
- Vortex shedding from the trailing edge.
- Turbulence generation during boundary layer-wake interaction.

Conceptually, the unsteady flow control strategies can be divided into two groups - active and passive. A passive strategy is an integral part of the pump design. It cannot be turned on and off by the user, and its action cannot be controlled. The following are examples of possible passive strategies :

- Designing the stator blade to obtain a less adverse or a favorable pressure gradient on the foremost part of the suction surface. This would result in a thinner boundary layer in the leading edge region, that would be more resistant to distortion and detachment by the rotor wake.

- Designing the rotor blade to result in thinner wakes, which, according to the calculations, produce less unsteadiness.

Active strategies act directly on the unsteady flow in a manner that can be controlled by the user, by a feedback circuit, or by computer logic. The active strategies considered have been classified into three types :

- Stator-based active but steady strategies, such as suction, blowing or fluid injection along the stator blade surface at a constant rate.
- Stator-based active but unsteady strategies, such as (1) suction, blowing or fluid injection along the stator blade surface at a variable rate and/or location; and (2) periodic pitching and/or translatory motion of the entire stator blade or part of it.
- Upstream-based active strategies. These involve the production of vortical disturbances upstream of the stator, which would act to cancel the wake-induced vortical disturbances in the unsteady flow at the stator. For instance, shed vortex cancellation occurring naturally in the stator discharge (Taylor [46]) can be used for this purpose.

The present work is concentrated on active strategies of the first type. The principal objective is to demonstrate the potential effectiveness of a particular strategy (proof-of-concept), but not to design the flow control system itself. A computational approach, based on the spectral-element Navier-Stokes solver, is used for validating the proposed strategies. As shown below, these strategies are simulated by using appropriate boundary conditions

For fluid suction : $$\mathbf{u}(x_s, y_s, t) = -\sigma(x_s, y_s, t)\mathbf{e}_n \tag{7.1}$$

For fluid injection : $$\mathbf{u}(x_s, y_s, t) = +\sigma(x_s, y_s, t)\mathbf{e}_n \tag{7.2}$$

For small pitch motion about C : $$\mathbf{u}(x_s, y_s, t) = \mathbf{\Omega}_s \times (\mathbf{OP} - \mathbf{OC})e^{\iota\Omega_s t} \tag{7.3}$$

It is to be noted that upstream-based flow control strategies can be represented through an appropriate temporally and spatially varying inlet distortion.

7.2. Control strategy for the suction surface

The idea of using fluid removal to reduce the unsteadiness over the suction surface is based on the hypothesis that B-vortices are produced from boundary layer fluid distorted and

detached by the rotor wakes. If the boundary layer in the leading edge region can be removed or made significantly thinner, the unsteadiness over the suction surface should decrease.

The best way to achieve this is to use suction that is not uniformly distributed along the blade surface. The suction coefficient, defined as

$$\sigma = \frac{v_n}{U_\infty} \tag{7.4}$$

should have a larger value near the leading edge where the B-vortex is produced in the boundary layer. Smaller suction amounts can be also applied to the aft part of the stator blade, in order to prevent local disturbances of the boundary layer by the B-vortices.

A computational experiment was carried out to demonstrate the effectiveness of such suction control strategy in the presence of rotor wakes. The Reynolds number for the experiment is 10,000. The suction coefficient distribution used is shown in Figure 7.1, and is steady in time.

The results from this experiment show a flowfield over the suction surface that is virtually unsteadiness-free. Steady distributed suction prevents the production of B-vortices and the associated vortex shedding from the trailing edge. This may be appreciated by comparing the disturbance vorticity contours in Figure 7.2 to those in Figures 3.8a-i. As a consequence, the blade loading distribution, in Figure 7.4, is free of moving low-pressure peaks. The loading RMS levels on the suction surface are significantly lower. This may be appreciated by comparing Figure 7.3a to Figure 7.3b, where the global $\check{C}_{p_S}S$ index is reduced by 40%. The fluctuations in the vorticity field across the stator trailing edge plane are also considerably reduced, as seen in Figure 7.5.

However, the low-pressure pulse on the suction side of the leading edge cannot be removed with the amounts of suction used to date. This could be accounted for by the inviscid flow origins of the pulse.

7.3. Control strategy for the pressure surface

The unsteady flow over the pressure surface is dominated by the migration of wake fluid and its evolution in counter-rotating vortices. This process appears somewhat difficult to influence from the stator blade surface. For this reason, the work on pressure surface control strategies is focused on reducing the blade loading disturbances there, rather than on eliminating the wake vortices.

According to Equation 3.5, a reduction of the pressure fluctuations can be achieved by increasing the distance between wake vortices and the pressure surface. Steady fluid blowing, distributed non-uniformly along the pressure surface, is employed for this purpose. The blowing coefficient distribution, used in the following proof-of-concept calculation, is shown in Figure 7.6.

As shown by comparing Figure 7.7a to Figure 7.7b, distributed blowing results in a noticeable reduction of the pressure fluctuations. The reduction may be attributed to the convective effect of the blowing velocity, which prevents the wake fluid from migrating close to the surface. Blowing also eliminates the pressure surface boundary layer, and produces the relatively thick shear layer seen in Figure 7.8. Finally, the amounts of blowing used in this experiment are large enough to also influence the flow over the suction surface, where the B-vortex pattern is altered. This may be attributed to the change of pressure coefficient distribution, which extends to the suction surface and appears as a favorable pressure gradient. It is to be noted that improvements of the pressure surface RMS levels can be obtained for smaller values of the blowing coefficient than those shown in Figure 7.6.

7.4. Strategy optimization

One of the drawbacks of suction or blowing, is that energy must be expended for removing or adding fluid. For this reason, it is interesting to determine the optimal distribution of the suction/blowing coefficient that reduces the unsteadiness to a specified level with the removal of a minimal amount of fluid.

For this purpose, the blade surface is divided into N_P panels. The suction/blowing distribution is represented as a set of coefficient $\sigma_{i;\ i=1...N}$ constant over each panel. A negative coefficient represents fluid removal; while a positive coefficient represents fluid injection. At the junction of two panels, the coefficients are averaged in order to avoid a static pressure discontinuity that would result otherwise. The discretized optimization problem is then stated as follows :

$$\text{Minimize :} \quad Q = \int_0^1 |\sigma(x)| ds \approx \sum_{i=1}^{i=N_P} |\sigma_i| ds_i \tag{7.5}$$

$$\text{Subject to :} \quad \begin{cases} \Lambda_k \leq \Lambda_{k,max} \\ \sigma_i \geq 0 \quad \text{for blowing.} \\ \sigma_i \leq 0 \quad \text{for suction.} \end{cases} \tag{7.6}$$

where $\Lambda_{k,max}$ is a set of maximum allowable values for the set of unsteadiness global indexes Λ_k, used as constraints. The global unsteadiness indexes used are defined in Appendix E.

This optimization problem is solved using an algorithm that takes advantage of the linear character of the objective function and of the uniform behavior of the constraints, to obtain a converged solution with less iterations than standard optimization methods. The algorithm proceeds as follows :

(1) Start with a distribution σ_i known to satisfy the constraints.

(2) Moving from the trailing edge towards the leading edge, reduce each σ_i by say 15%.

(3) Evaluate the sets of indexes Λ_k after reducing each σ_i. If the set satisfies the constraint in Eq.(7.6), keep the reduced set of coefficients.

(4) Moving from leading edge towards trailing edge, repeat steps (2) and (3).

(5) Repeat steps (2) to (4) until no reduction is possible in the set of σ_i.

An example of optimized suction distribution with constraints $\check{C}_{p,SS[0.1<s<0.9]} \leq 0.085$ and $\check{W}_{SS} \leq 3.0$, is shown in Figure 7.1. The values of these constraints correspond to a level of unsteadiness on the suction surface comparable to that in Figures 7.2-7.5. The blowing coefficient distribution on Figure 7.6 can be likewise optimized, although the actual calculations were not carried out.

In the case of distributed suction, it is possible to reduce the amount of optimization CPU time, by judiciously estimating the initial suction distribution. Simple semi-analytical methods, based on boundary layer theory, may be used for this purpose. For instance, Sherman [42, pp.367-370] presents a numerical method that estimates the suction distribution required to obtain specific growth rate of the boundary layer thickness. In the present case, this growth rate should be set to zero over the foremost part of the stator blade. This would reduce the thickness of the vortical boundary layer in the leading edge region, resulting in smaller B-vortices.

Chapter 8

Conclusion and Recommendations

8.1. Summary

This thesis presented an investigation of the 2-D unsteady flow in a stator blade row interacting with wakes from an upstream rotor. Computational Fluid Mechanics (CFD) are used as a tool to describe and understand the wake interaction at the engineering level.

Spectral-element Navier-Stokes solvers and a linearized perturbation solver are used to simulate the unsteady flow. To visualize the disturbance effects of the upstream wakes, the steady flow that would exist in the stator passage in absence of wakes is subtracted from the computed unsteady flow. The resultant disturbance flowfield exhibits highly characteristic vortical features, that would be difficult to observe had the total unsteady flow quantities been used.

8.2. Conclusions

The following conclusions have been reached from the foregoing computational study of wake interaction.

(1) During their transport through the stator passage, the rotor wakes migrate towards the pressure surface of the stator blades where they evolve into pairs of counter-rotating vortices. These vortices are the dominant form of unsteady flow over the pressure surface. Their strength is directly related to the excess of tangential momentum in the

wake.

(2) The unsteady flow over the suction surface of the stator blade is characterized by a moving row of vortical disturbances (B-vortices), produced at the leading edge of the stator blade upon wake interception. The B-vortices consists of boundary layer vorticity, which is distorted and detached from the surface by the convective action of the wakes.

(3) Three parameters influence the unsteady flow over the suction surface— the pressure distribution over the stator blade, the excess of tangential momentum in the wake, and the wake reduced frequency. The strength of the B-vortices is directly proportional to the wake momentum, and decreases at higher reduced frequencies. A favorable pressure gradient results in weaker vortices; whereas an adverse gradient has the opposite effect. In several situations, the B-vortices produced at the leading edge may be sufficiently strong to subsequently detach opposite-sign vorticity from the boundary-layer disturbances they induce. This results in the formation of a vortex street of counter-rotating B and P-vortices, extending over most of the suction surface.

(4) The Reynolds number appears to have no qualitative effect on the nature of the unsteady flow—the features described above are common to the laminar and the turbulent flow regimes. The disturbances over the suction surface of the stator blade are however weaker in turbulent flow. This may be attributed to the thinner and strongly attached boundary layer.

(5) The stator blade loading fluctuations arising from wake interaction are of two kinds. First, an intense pressure pulse occurs on the leading edge at the moment of wake interception. This pulse is negative on the suction side of the leading edge, and positive on the pressure side. It is due to potential flow effects associated with the excess of tangential velocity in the wake. The amplitude of the pulse varies as the square of the wake velocity defect and the rotor blade velocity. Second, a series of moving pressure disturbances, associated with the foregoing vortices, is present over the blade surface. The pressure fluctuations are negative on the suction surface, and alternating positive/negative on the pressure surface. Their amplitude varies as the square of the vortices strength.

(6) It is possible to reduce the unsteady flow effects associated with wake interaction, using appropriate active control strategies. A proof-of-concept calculation shows that suction

(fluid removal), applied to the suction surface, prevents the formation of B-vortices and reduces the associated RMS levels. Non-uniform distribution of the suction coefficient, with highest values in the leading edge region, yields optimal results. Unsteady flow control over the pressure surface appears more difficult owing to the external origin of the wake vortices. Fluid blowing from the pressure surface may be used to reduce the amplitude of the pressure fluctuations there.

This computational investigation demonstrates the potential of the spectral-element method for addressing current problems of fluid mechanics such as wake interaction. Computational methods used to study wake interaction should be able to account for (1) the boundary layer, the presence of which is essential for proper representation of the unsteady flow over the suction surface; and (2) the non-linear effects, which dominate the unsteady flow over the pressure surface. Both the Navier-Stokes and the linearized perturbation solvers used here have the first capability. However, the linearized solver cannot account for the non-linear effects—for this reason, it should be used with caution.

8.3. Recommendations

The present work should be pursued and completed by a study of the unsteady flow arising from interaction with the upstream rotor vortices. This interaction is highly three-dimensional in nature and may have considerable unsteady effects.

A computational approach is proposed for this study. Spectral-element Navier-Stokes and linearized solvers shall be used to (1) describe the wake/vortex intra-stator transport in three dimensions; (2) identify the unsteady flow features; (3) reveal the mechanisms responsible for the production of unsteady flow; and (4) develop strategies to reduce the unsteady effects. A more efficient use of the linearized solver can be made if the present artificial-viscosity scheme is replaced by a non-CPU intensive BTD-type stabilization scheme.

Such a computational investigation of 3-D unsteady vortex interaction in turbomachinery will be one of the first of its kind. The results can be used to develop flow control strategies to reduce the unsteady flow effects. Potential benefits from the application of such strategies range from noise reduction to reliability and performance improvements

Bibliography

[1] Adachi et al. 1974. Study on the Interference Between Moving and Stationary Blade Rows in Axial-Flow Blower. *Bulletin of the JSME*, **109**(109):904-911.

[2] Arndt N., Acosta A.J., Brennen C.E., Caughey T.K, 1990. Experimental Investigation of Rotor-Stator Interaction in a Centrifugal Pump With Several Vaned Diffusers. *ASME Journal of Turbomachinery*, **112**(1):98-108.

[3] Baldwin B., Lomax H., 1978. Thin-Layer Approximation and Algebraic Model for Separated Turbulent Flows. *AIAA paper 78-257.*

[4] Benocci C., 1991. *Modeling of Turbulent Heat Transport: A State of the Art.* Von Karman Institute Technical Memorandum TM-47.

[5] Binder A., Schroeder T., Hourmouziadis J., 1989. Turbulence Measurements in a Multistage Low-Pressure Turbine. *ASME Journal of Turbomachinery*, **111**(2):153-161.

[6] Boletis E., Sieverding, C.H., 1991. Experimental Study of the 3-D Flow Field in a Turbine Stator Preceded by a Full Stage. *ASME Jrnl. of Turbomachinery*, **112**(1):1-8.

[7] Capece V.R., Fleeter S., 1989. Experimental Investigation of Multistage Interaction Gust Aerodynamics. *ASME Journal of Turbomachinery*, **111**(4):409-417.

[8] Capece V.R., Fleeter S., 1987. Unsteady Aerodynamic Interactions in a Multistage Compressor. *ASME Journal of Turbomachinery*, **109**(3):420-428.

[9] Chen C.L., Chakravarthy S.R., 1990. Calculation of Unsteady Rotor-Stator Interaction. *AIAA paper No.90-1544.*

[10] Chen Y.S., 1988. 3-D Stator-Rotor Interaction of the SSME. *AIAA paper No.88-3095.*

[11] Cline A.K., 1976. Several Observations on the Use of Conjugate Gradient Methods. *ICASE Report No.76-22*, NASA-Langley Research Center.

[12] Cumpsty N.A., 1991. Journal note on Reference [43] below.

[13] Dawes W., February 1992. *Private communication.* Cambridge University.

[14] Dring R.P., Joslyn H.D., Hardin L.W., Wagner J.H., 1982. Turbine Rotor-Stator Interaction. *Journal of Engineering for Power*, **104**(4):729-742.

[15] Eppler E., 1990. *Airfoil Design Data.* Springer-Verlag.

[16] Erdos J.I., Alzner E., McNally W., 1977. Numerical Solution of Periodic Transonic Flow Through a Fan Stage. *AIAA Journal*, **15**(11):1559-1568.

[17] Gallus H.E., 1979. Unsteady Flow in Turbomachines: High Speed Blade-Wake Interactions. *VKI Lecture Series LS-1979-3*, Volume 2. Von Karman Institute.

[18] Giles M., Feb.1992. *Private communication.* Massachusetts Institute of Technology.

[19] Giles M., 1991. UNSFLO : A Numerical Method for the Calculation of Unsteady Flow in Turbomachinery. *Gas Turbine Laboratory Report #205.* Massachusetts Institute of Technology.

[20] Gostellow J.P., 1984. *Cascade Aerodynamics.* Pergamon Press

[21] Gundy-Burlet K.L., Rai M., Stauter R.C., Dring R.P., 1991. Temporally and Spatially Resolved Flow in a Two-Stage Axial Compressor: Part II - Computational Assessment. *ASME Journal of Turbomachinery*, **113**(2):227-232.

[22] Hebert G.J., Tiederman W.G., 1990. Comparison of Steady and Unsteady Secondary Flows in a Turbine Stator Cascade. *ASME Jrnl. of Turbomachinery*, **112**(4):625-632.

[23] Hodson H.P., 1990. Modeling Unsteady Transition and Its Effects on Profile Loss. *ASME Journal of Turbomachinery*, **112**(4):691-701.

[24] Hodson H.P., 1984. An Inviscid Blade-to-Blade Prediction of a Wake Generated Unsteady Flow. *ASME Paper 84-GT-43.*

[25] Hornung H., 1989. *Course AE-238 Lecture Notes.* California Institute of Technology.

[26] Joslyn H.D., Dring R.P., Sharma O.P., 1983. Unsteady Three-Dimensional Turbine Aerodynamics. *ASME Journal of Turbomachinery*, **105**(2):322-331.

[27] Kerrebrock J.L., Mikolajczak A.A, 1970. Intra-Stator Transport of Rotor Wakes and Its Effect on Compressor Performance. *ASME paper 70-GT-39.*

[28] Korczak K.Z, Patera A.T., 1986. An Isoparametric Spectral Element Method for Solution of the Navier-Stokes Equations in Complex Geometry. *Journal of Computational Physics.* **62**:361.

[29] Kovats A., 1964. *Design and Performance of Centrifugal and Axial Flow Pumps and Compressors.* MacMillan, New York.

[30] Kumar A., Kerrebrock J.L., 1971. Rotor Wake Transport in Turbomachine Stators. *Gas Turbine Laboratory Report #103.* Massachusetts Institute of Technology.

[31] Mankbadi R., 1989. A Study of unsteady Rotor-Stator Interactions. *ASME Journal of Turbomachinery*, **111**(4):394-400.

[32] McFarland E.R., 1984. A Rapid Blade-To-Blade Solution for Use in Turbomachinery Design. *ASME Journal of Engineering for Gas Turbines and Power*, **106**(2):376-382.

[33] Ni R., Sharma O., 1990. Using 3-D Euler Flow Simulations to Assess Effects of Periodic Unsteady Flow Through Turbines. *AIAA paper No. 90-2357.*

[34] Orszag S.A., Kells L., 1980. Journal of Fluid Mechanics, **96**.

[35] Patera A.T., 1984. A Spectral Element Method for Fluid Dynamics: Laminar Flow in a Channel Expansion. *Journal of Computational Physics*, **54**(3):98-108.

[36] Pfeil H., Herbst R., Schroder T., 1983. Investigation of the Laminar-turbulent Transition of Boundary Layers Disturbed by Wakes. *Journal of Engineering for Power,* **105**(1):130-137.

[37] Poensgen C., Gallus H.E., 1991. Three-Dimensional Wake Decay Inside of a Compressor Cascade and Its Influence on the Downstream Unsteady Flow Field: Part II-Unsteady Flow Field Downstream of the Stator. *ASME Journal of Turbomachinery,* **113**(2):190-197.

[38] Rai M.M., Madavan N.K., 1990. Multi-Airfoil Navier-Stokes Simulation of Turbine Rotor-Stator Interaction. *ASME Journal of Turbomachinery*, **112**(3):377-384.

[39] Rai M.M, 1987. Unsteady Three-Dimensional Navier-Stokes Simulations of Turbine Rotor-Stator Interaction. *AIAA paper No. 87-2058.*

[40] Richardson S., 1990. Analysis of Unsteady Rotor-Stator Interactions Using a Viscous Explicit Method. *AIAA paper No. 90-0342.*

[41] Schulz H.D., Gallus H.E, Lakshminarayana B.,1990. Three-Dimensional Separated Flowfield in the Endwall Region of an Annular Compressor Cascade in the Presence of Rotor-Stator Interaction, Parts I and II. *ASME Journal of Turbomachinery*, **112**(3):669-690.

[42] Sherman F.S, 1990. *Viscous Flow.* McGraw-Hill.

[43] Stauter R.C., Dring R.P., Carta F.O., 1991. Temporally and Spatially Resolved Flow in a Two-Stage Axial Compressor: Part I - Experiment. *ASME Journal of Turbomachinery*, **113**(2):219-226.

[44] Stepanoff A.J., 1967. *Centrifugal and Axial Flow Pumps.* J. Wiley & Sons.

[45] Tan C.S., 1989. A Multi-Domain Spectral Computation of Three-Dimensional Laminar Horseshoe Vortex Flow Using Incompressible Navier-Stokes equations. *Journal of Computational Physics*, **85**(1)

[46] Taylor E.S, 1971. Boundary Layers, Wake and Losses in Turbomachinery. *Gas Turbine Laboratory Report #105.* Massachusetts Institute of Technology.

[47] Taylor L.K., Whitfield D., 1991. Unsteady 3-D Incompressible Euler and Navier-Stokes Solver for Stationary and Dynamic Grids. *AIAA paper 91-1650.*

[48] Von Karman Institute, 1991. Turbulence Modeling for Compressible Flows and Implementation in Navier-Stokes Solvers, in *Introduction to Modeling of Turbulence. Von Karman Institute Lecture Series LS-1991-02.*

[49] Wilder M.C., Pesce M.N., Telionis D.P., Poling D.R., Dadone C., 1990. Blade-Vortex Interaction Experiments: Velocity and Vorticity Fields. *AIAA paper 90-0030.*

[50] Zierke W.C., Okiishi T.H., 1982. Measurement and Analysis of Total-Pressure Unsteadiness Data From an Axial-Flow Compressor Stage. ASME Journal of Turbomachinery, Vol.104 No.2. *ASME Journal of Turbomachinery*, **104**(2):479-488.

Appendix A

Spectral-Element Operators

A.1. Coordinate systems.

The following coordinate systems are used in the numerical solution of the flow equations.

(x, y) - Stator rectangular coordinate system, centered at the leading edge.

$(\varsigma, \eta)^i$ - Local coordinate system in element i (Figure 2.1).

A.2. Spatial discretization.

Expansion of flow variable $\mathbf{u}$ in spectral element i :

$$\mathbf{u}(\varsigma, \eta) = \sum_j \sum_k \mathbf{u}^i_{jk} h_j(\varsigma) h_k(\eta) \qquad (A.01)$$

Interpolation functions :

$$h_m(\varsigma) = \frac{2}{N} \sum_n \frac{1}{\bar{C}_m \bar{C}_n} T_n(\varsigma_m) T_n(\varsigma) \qquad (A.02)$$

$$h_m(\eta) = \frac{2}{N} \sum_n \frac{1}{\bar{C}_m \bar{C}_n} T_n(\eta_m) T_n(\eta) \qquad (A.03)$$

Collocation points in the natural coordinate system :

$$\varsigma_m = \eta_m = \cos(\frac{m\pi}{N}) \qquad (A.04)$$

Weighting coefficients :

$$\bar{C}_m = \begin{cases} 2 & m = 0, M \\ 1 & \text{otherwise} \end{cases} \qquad (A.05)$$

Orthogonality of interpolation functions :

$$h_m(\varsigma_n) = h_m(\eta_n) = \delta_{mn} \tag{A.06}$$

To simplify the writing, the element index i will be omitted from the spectral operators and flow variables in the following. A zero-order continuity between any two adjacent elements is insured by using an indexed array of global nodes for the entire spectral-element grid. The global nodes are the set of collocation points on the inter-element boundaries.

A.3. Partial derivatives in the local system

Partial derivatives expansion :

$$\mathbf{u}_\varsigma = \sum_l \sum_m \mathbf{u}_{lm} \frac{dh_l(\varsigma)}{d\varsigma} h_m(\eta) \tag{A.07}$$

$$\mathbf{u}_\eta = \sum_l \sum_m \mathbf{u}_{lm} h_l(\varsigma) \frac{dh_m(\eta)}{d\eta} \tag{A.08}$$

It is convenient to define a discretized local differential operator :

$$D_{pq} = \frac{dh_p}{d\varsigma}(\varsigma_q) \tag{A.09}$$

This yields :

$$(\mathbf{u}_\varsigma)_{pq} = \sum_l \sum_m D_{lp} \delta_{mq} \mathbf{u}_{lm} \tag{A.10}$$

$$(\mathbf{u}_\eta)_{pq} = \sum_l \sum_m D_{mq} \delta_{lp} \mathbf{u}_{lm} \tag{A.11}$$

A.4. Discretized Jacobians

The Jacobian of the local coordinate transformation is :

$$J = x_\varsigma y_\eta - x_\eta y_\varsigma \tag{A.12}$$

Using Eqs.(A.10-11), the following intermediate values are computed:

$$(x_\varsigma)pq = \sum_l \sum_m D_{lp} \delta_{mq} x_{lm} \tag{A.13a}$$

$$(x_\eta)_{pq} = \sum_l \sum_m D_{mq} \delta_{lp} x_{lm} \tag{A.13b}$$

$$(y_\varsigma)_{pq} = \sum_l \sum_m D_{lp}\delta_{mq} y_{lm} \tag{A.13c}$$

$$(y_\eta)_{pq} = \sum_l \sum_m D_{mq}\delta_{lp} y_{lm} \tag{A.13d}$$

The discretized Jacobian is :

$$J_{pq} = (x_\varsigma)_{pq}(y_\eta)_{pq} - (x_\eta)_{pq}(y_\varsigma)_{pq} \tag{A.14}$$

A.5. Discretized partial derivatives

Derivatives transformation from local to fixed cartesian system :

$$\begin{vmatrix} \mathbf{u}_x \\ \mathbf{u}_y \end{vmatrix} = \frac{1}{J} \begin{vmatrix} y_\eta & -y_\varsigma \\ -x_\eta & x_\varsigma \end{vmatrix} \begin{vmatrix} \mathbf{u}_\varsigma \\ \mathbf{u}_\eta \end{vmatrix} \tag{A.15}$$

Discretized partial derivatives :

$$(\mathbf{u}_x)_{pq} = \frac{1}{J_{pq}} \sum_l \sum_m \tilde{\nabla}_{X,pqlm} \mathbf{u}_{lm} \tag{A.16}$$

$$(\mathbf{u}_y)_{pq} = \frac{1}{J_{pq}} \sum_l \sum_m \tilde{\nabla}_{Y,pqlm} \mathbf{u}_{lm} \tag{A.17}$$

The discretized *partial derivative operators* are defined as :

$$\tilde{\nabla}_{X,pqlm} = D_{lp}(y_\eta)_{lq}\delta_{mq} - D_{mq}(y_\varsigma)_{pm}\delta_{lp} \tag{A.18}$$

$$\tilde{\nabla}_{Y,pqlm} = D_{mq}(x_\varsigma)_{pm}\delta_{lp} - D_{lp}(z_\eta)_{lq}\delta_{mq} \tag{A.19}$$

A.6. Discretized Nabla operator

All manipulations involving Nabla are discretized using the above partial derivative operators. For instance :

$$(\nabla \cdot \mathbf{u})_{pq} = \frac{1}{J_{pq}} \sum_l \sum_m \tilde{\nabla}_{pqlm} \cdot \mathbf{u}_{lm} \tag{A.20}$$

where

$$\tilde{\nabla}_{pqlm} = \tilde{\nabla}_{X,pqlm}\mathbf{e}_x + \tilde{\nabla}_{Y,pqlm}\mathbf{e}_y \tag{A.21}$$

A.7. Discretized line integrals

Flux integrals evaluated along one side of a spectral element :

$$L_I(f) = \int_\varsigma f\mathbf{u}\cdot\mathbf{n}ds = \int_\varsigma f(\mathbf{u}\cdot\mathbf{e}_x)y_\varsigma d\varsigma + \int_\varsigma f(\mathbf{u}\cdot\mathbf{e}_y)x_\varsigma d\varsigma \tag{A.22}$$

$$L_{II}(f) = \int_\eta f\mathbf{u}\cdot\mathbf{n}ds = \int_\eta f(\mathbf{u}\cdot\mathbf{e}_x)y_\eta d\eta + \int_\eta f(\mathbf{u}\cdot\mathbf{e}_y)x_\eta d\eta \tag{A.23}$$

are used to represent the pressure equation boundary conditions. The spectral element grid is generated so that the boundaries coincide with lines of constant local coordinates (Inflow: $\varsigma = 0$; Outlow: $\varsigma = 1$; Both leading edge C-type elements: $\varsigma = 1$; Suction surface elements: $\eta = 1$; Pressure surface elements: $\eta = 0$). This allows to re-write the flux integrals as :

$$\int_\varsigma f(\mathbf{u}\cdot\mathbf{e}_x)y_\varsigma d\varsigma = \sum_j\sum_k\sum_l\sum_m\sum_r\sum_s y_{rs}D_{rj}\delta_{sk}\tilde{B}_{jlp}(\mathbf{u}\cdot\mathbf{e}_x)_{lm}f_{lm}h_k(\eta_0)h_m(\eta_0)h_q(\eta_0) \tag{A.24}$$

$$\int_\varsigma f(\mathbf{u}\cdot\mathbf{e}_y)x_\varsigma d\varsigma = \sum_j\sum_k\sum_l\sum_m\sum_r\sum_s x_{rs}D_{rj}\delta_{sk}\tilde{B}_{jlp}(\mathbf{u}\cdot\mathbf{e}_y)_{lm}f_{lm}h_k(\eta_0)h_m(\eta_0)h_q(\eta_0) \tag{A.25}$$

$$\int_\eta f(\mathbf{u}\cdot\mathbf{e}_x)y_\eta d\eta = \sum_j\sum_k\sum_l\sum_m\sum_r\sum_s y_{rs}D_{sk}\delta_{rj}\tilde{B}_{kmq}(\mathbf{u}\cdot\mathbf{e}_x)_{lm}f_{lm}h_j(\varsigma_0)h_l(\varsigma_0)h_p(\varsigma_0) \tag{A.26}$$

$$\int_\eta f(\mathbf{u}\cdot\mathbf{e}_y)x_\eta d\eta = \sum_j\sum_k\sum_l\sum_m\sum_r\sum_s x_{rs}D_{sk}\delta_{rj}\tilde{B}_{kmq}(\mathbf{u}\cdot\mathbf{e}_y)_{lm}f_{lm}h_j(\varsigma_0)h_l(\varsigma_0)h_p(\varsigma_0) \tag{A.27}$$

Using Eq.(A.06) :

$$\int_\varsigma f(\mathbf{u}\cdot\mathbf{e}_y)x_\varsigma d\varsigma = \sum_j\sum_l\sum_r x_{r0}D_{rj}\delta_{q0}\tilde{B}_{jlp}(\mathbf{u}\cdot\mathbf{e}_y)_{l0}f_{l0} \tag{A.28}$$

$$\int_\varsigma f(\mathbf{u}\cdot\mathbf{e}_x)y_\varsigma d\varsigma = \sum_j\sum_l\sum_r y_{r0}D_{rj}\delta_{q0}\tilde{B}_{jlp}(\mathbf{u}\cdot\mathbf{e}_x)_{l0}f_{l0} \tag{A.29}$$

$$\int_\eta f(\mathbf{u}\cdot\mathbf{e}_y)x_\eta d\eta = \sum_k\sum_m\sum_s x_{0s}D_{sk}\delta_{p0}\tilde{B}_{kmq}(\mathbf{u}\cdot\mathbf{e}_y)_{0m}f_{0m} \tag{A.30}$$

$$\int_\eta f(\mathbf{u}\cdot\mathbf{e}_x)y_\eta d\eta = \sum_k\sum_m\sum_s y_{0s}D_{sk}\delta_{p0}\tilde{B}_{kmq}(\mathbf{u}\cdot\mathbf{e}_x)_{0m}f_{0m} \tag{A.31}$$

The *local interpolant integral of order 3*, appearing in the above, is defined as :

$$\tilde{B}_{abc} = \int_{-1}^{+1} h_a(\varsigma)h_b(\varsigma)h_c(\varsigma)d\varsigma \tag{A.32}$$

A.8. Surface integral of type I

A surface integral of type I is defined as :

$$I_I(f,\mathbf{u}) = \iint_i \mathbf{u} f \, dxdy \tag{A.33}$$

taken over an entire spectral element i. In local coordinates :

$$I_I(f,\mathbf{u}) = \int_{-1}^{+1}\int_{-1}^{+1} |J|\mathbf{u}(\varsigma,\eta) f(\varsigma,\eta) d\varsigma d\eta \tag{A.34}$$

Expansion in local interpolants :

$$I_I(f,\mathbf{u}) = \int_{-1}^{+1}\int_{-1}^{+1} \sum_l \sum_m \mathbf{u}_{lm} h_l(\varsigma) h_m(\eta) \sum_p \sum_q |J_{pq}| h_p(\varsigma) h_q(\eta) \sum_j \sum_k f_{jk} h_j(\varsigma) h_k(\eta) \tag{A.35}$$

A rearrangement of the terms yields :

$$I_I(f,\mathbf{u}) = \sum_l \sum_m \sum_p \sum_q \sum_j \sum_k \mathbf{u}_{lm} |J_{pq}| f_{jk} \tilde{B}_{jlp} \tilde{B}_{kmq} \tag{A.36}$$

The above can be written as :

$$I_I(f,\mathbf{u}) = \sum_l \sum_m \sum_j \sum_k \mathbf{u}_{lm} B^+_{lmjk} f_{jk} \tag{A.37}$$

where the *elementwise surface integral operator* B^+_{lmjk} is conveniently defined as :

$$B^+_{lmjk} = \sum_p \sum_q |J_{pq}| \tilde{B}_{jlp} \tilde{B}_{kmq} \tag{A.38}$$

A.9. Surface integral of type II

A surface integral of type II is defined as :

$$I_{II}(f,\mathbf{u}) = \iint_i f(\nabla \mathbf{u})^2 dxdy \tag{A.39}$$

taken over an entire spectral element i. In local coordinates :

$$I_{II}(f,\mathbf{u}) = \int_{-1}^{+1}\int_{-1}^{+1} f(\varsigma,\eta) J\nabla\mathbf{u}(\varsigma,\eta) \frac{1}{|J(\varsigma,\eta)|} \cdot J\nabla\mathbf{u}(\varsigma,\eta) d\varsigma d\eta \tag{A.40}$$

From Eq.(A.16) :

$$J\nabla\mathbf{u}(\varsigma,\eta) = \sum_j \sum_k \sum_r \sum_s \tilde{\nabla}_{rsjk} \cdot \mathbf{u}_{jk} h_r(\varsigma) h_s(\eta) \tag{A.41}$$

Expansion in local interpolants :

$$I_{II}(f,\mathbf{u}) = \int_{-1}^{+1}\int_{-1}^{+1} \sum_{c}\sum_{d} f_{cd} h_c(\varsigma) h_d(\eta) \sum_{a}\sum_{b} \frac{1}{|J_{ab}|} h_a(\varsigma) h_b(\eta) \times$$

$$\times \sum_{j}\sum_{k}\sum_{r}\sum_{s} \tilde{\nabla}_{rsjk} \cdot \mathbf{u}_{jk} h_r(\varsigma) h_s(\eta) \sum_{l}\sum_{m}\sum_{p}\sum_{q} \tilde{\nabla}_{pqlm} \cdot \mathbf{u}_{lm} h_p(\varsigma) h_q(\eta) d\varsigma d\eta \qquad (A.42)$$

A re-arrangement of the terms yields :

$$I_{II}(f,\mathbf{u}) = \sum_{c,d}\sum_{l,m,p,q}\sum_{a,b}\sum_{j,k,r,s} \tilde{\nabla}_{pqlm} \mathbf{u}_{lm} \frac{1}{|J_{ab}|} f_{cd} \tilde{B}_{cpar} \tilde{B}_{dqbs} \tilde{\nabla}_{rsjk} \mathbf{u}_{jk} \qquad (A.43)$$

where the *local interpolant integral of order 4* is defined as :

$$\tilde{B}_{abcd} = \int_{-1}^{+1} h_a(\varsigma) h_b(\varsigma) h_c(\varsigma) h_d(\varsigma) d\varsigma \qquad (A.44)$$

Further re-arrangement reduces Eq.(A.43) to the following general form :

$$I_{II}(f,\mathbf{u}) = \sum_{l}\sum_{m}\sum_{j}\sum_{k} \mathbf{u}_{lm} \cdot A_{lmjk}(f) \mathbf{u}_{jk} \qquad (A.45)$$

In the case of a spatially constant scalar field, $f = f_o$, the operator matrix $A^{\mathbf{i}}_{lmjk}$ is given by

$$A_{lmjk}(f) = f \sum_{l}\sum_{m}\sum_{j}\sum_{k} \tilde{\nabla}_{pqlm} \cdot \bar{B}_{pqrs} \tilde{\nabla}_{rsjk} \qquad (A.46)$$

where

$$\bar{B}_{pqrs} = \sum_{a}\sum_{b} \frac{1}{|J_{ab}|} \sum_{c}\sum_{d} \tilde{B}_{cpar} \tilde{B}_{dqbs} \qquad (A.47)$$

In the case when the scalar field f is not spatially constant, the operator matrix $A^{\mathbf{i}}_{lmjk}$ contains convolution sums of f:

$$A_{lmjk}(f) = \sum_{l}\sum_{m}\sum_{j}\sum_{k} \tilde{\nabla}_{pqlm} \cdot \bar{B}^{*}_{pqrs}(f) \tilde{\nabla}_{rsjk} \qquad (A.48)$$

$$\bar{B}^{*}_{pqrs}(f) = \sum_{a}\sum_{b} \frac{1}{|J_{ab}|} \sum_{c}\sum_{d} f_{cd} \tilde{B}_{cpar} \tilde{B}_{dqbs} \qquad (A.49)$$

A.10. Alternative computation of the viscous matrix

In the case where the scalar field f varies both spatially and in time, the operator A_{lmjk} needs to be re-evaluated at each time step. Eqs.(A.48-49) cannot be directly used for this purpose, because they typically represent a few tens of megaFLOPs (million floating point operations).

An order-of-magnitude gain in the required number of operations can be achieved if the scalar field is not directly included in the convolution sums. This approach is valid, provided the scalar field is sufficiently smooth. Starting from the definition of I_{II} :

$$I_{II}(f,\mathbf{u}) = \int_{-1}^{+1}\int_{-1}^{+1}[f(\varsigma,\eta)J\nabla\mathbf{u}(\varsigma,\eta)]\frac{1}{|J(\varsigma,\eta)|}J\nabla\mathbf{u}(\varsigma,\eta)d\varsigma d\eta \qquad (A.50)$$

and expanding the integrands as follows :

$$fJ\nabla\mathbf{u} = \sum_l\sum_m\sum_p\sum_q f_{pq}\tilde{\nabla}_{pqlm}\mathbf{u}_{lm}h_p(\varsigma)h_q(\eta) \qquad (A.51)$$

$$J\nabla\mathbf{u} = \sum_j\sum_k\sum_r\sum_s \tilde{\nabla}_{rsjk}\mathbf{u}_{jk}h_r(\varsigma)h_s(\eta) \qquad (A.52)$$

$$\frac{1}{J} = \sum_a\sum_b \frac{1}{J_{ab}}h_a(\varsigma)h_b(\eta) \qquad (A.53)$$

Yields :

$$A_{lmjk}(f) = \sum_p\sum_q\sum_r\sum_s f_{pq}\tilde{\nabla}_{pqlm}\bar{B}^{\diamond}_{pqrs}\tilde{\nabla}_{rsjk} \qquad (A.54)$$

with

$$\bar{B}^{\diamond}_{pqrs} = \sum_a\sum_b \frac{1}{J_{ab}}\tilde{B}_{apr}\tilde{B}_{bqs} \qquad (A.55)$$

A.11. Discretized pressure step

The quadratic form of the pressure equation (2.17), can be decomposed in term of the foregoing line and surface integrals as follows :

$$\begin{aligned}\Delta t I(p^{n+1}) = &-\Delta t\sum^{i\in Q_E} I_{II}(1,p^{n+1}) - \sum^{i\in Q_E} I_I(\nabla\cdot\breve{\mathbf{u}}^{n+1},p^{n+1})\\ &+\sum^{i\in Q_I} L_I(\breve{\mathbf{u}}^{n+1},p^{n+1}) - \sum^{i\in Q_O} L_I(\breve{\mathbf{u}}^{n+1},p^{n+1}) + \sum^{i\in Q_L} L_I(\breve{\mathbf{u}}^{n+1},p^{n+1})\\ &+\sum^{i\in Q_S} L_{II}(\breve{\mathbf{u}}^{n+1},p^{n+1}) + \sum^{i\in Q_P} L_{II}(\breve{\mathbf{u}}^{n+1},p^{n+1}) \qquad (A.56)\end{aligned}$$

After minimization with respect to each degree of freedom p^i_{lm}, a linear equation for the dicretized pressure is obtained :

$$\Delta t\sum^{i\in Q_E}\sum_l\sum_m A_{jklm}(1)p^i_{lm} = \sum^{i\in Q_E}\sum_l\sum_m\sum_p\sum_q\tilde{\nabla}_{pqjk}\left(\sum_r\tilde{B}_{rpl}\sum_s\tilde{B}_{sqm}\right)\cdot\hat{\mathbf{u}}_{lm}$$

$$+\sum^{i\in Q_I}\sum_s\sum_l\sum_r y_{r0}D_{rs}\delta_{q0}\tilde{B}_{slp}(\hat{\mathbf{u}}\cdot\mathbf{e}_x)_{l0} - \sum^{i\in Q_O}\sum_s\sum_l\sum_r y_{rN}D_{rs}\delta_{qN}\tilde{B}_{slp}(\hat{\mathbf{u}}\cdot\mathbf{e}_x)_{lN}$$

$$+\sum^{i\in Q_L}\sum_s\sum_l\sum_r y_{rN}D_{rs}\delta_{qN}\tilde{B}_{slp}(\hat{\mathbf{u}}\cdot\mathbf{e}_n)_{lN}+\sum^{i\in Q_S}\sum_r\sum_m\sum_s y_{Ns}D_{sr}\delta_{Np}\tilde{B}_{rmq}(\hat{\mathbf{u}}\cdot\mathbf{e}_n)_{Nm}$$

$$+\sum^{i\in Q_P}\sum_r\sum_m\sum_s y_{0s}D_{sr}\delta_{0p}\tilde{B}_{rmq}(\hat{\mathbf{u}}\cdot\mathbf{e}_n)_{0m} \qquad (A.57)$$

The pressure matrix $A_{lmjk}(1)$ is computed and inverted in a separate preprocessing stage. The RHS term, which contains the boundary conditions, is computed at each time step.

A.12. Discretized viscous step

The quadratic form of the viscous equation (2.23), can be decomposed in terms of the foregoing surface integrals as follows :

$$I(\mathbf{u}^{n+1})=-\sum^{i\in Q_E}\left[I_{II}(D,\mathbf{u}^{n+1})+\frac{2}{\Delta t}I_I(\mathbf{u}^{n+1},\mathbf{u}^{n+1})+\right.$$

$$\left.+\frac{2}{\Delta t}I_I(\hat{\hat{\mathbf{u}}}^{n+1},\mathbf{u}^{n+1})+I_I(\nabla D\nabla\mathbf{u}^n,\mathbf{u}^{n+1})\right] \qquad (A.58)$$

After minimization with respect to each degree of freedom $\mathbf{u}^i_{lm}$, a linear equation for the dicretized velocity is obtained :

$$\sum^{i\in Q_E}\sum_l\sum_m\left[A_{jklm}+\frac{2}{\Delta t}B^+_{jklm}\right]\mathbf{u}^{n+1}_{lm,i}=\sum^{i\in Q_E}\sum_j\sum_k\left[\frac{2}{\Delta t}B^+_{lmjk}\hat{\hat{\mathbf{u}}}^{n+1}_{jk,i}+A_{lmjk}\mathbf{u}^n_{jk,i}\right] \qquad (A.59)$$

The Dirichlet boundary conditions of the viscous step are directly implemented in the above velocity equation. For this purpose, the coefficients in all rows with indexes $()_{lm,i}$ corresponding to fixed-velocity collocation points are replaced by

$$A_{lmjk}=\begin{cases}0 & (j,k)\neq(l,m)\\ 1 & (j,k)\equiv(l,m)\end{cases} \qquad (A.60)$$

The corresponding righ-hand side element $()_{lm,i}$ is then replaced by the desired value of the surface velocity $u_{lm,i}$.

A.13. Local interpolant integrals

The local interpolant integrals $\tilde{B}_{kmp}$ and $\tilde{B}_{kmpq}$ can be computed semi-analytically, thereby minimizing the effects of truncation errors :

$$\tilde{B}_{kmpq}=\frac{1}{N^4}\sum_{a,b,c,d}\frac{1}{\bar{C}_a\bar{C}_b\bar{C}_c\bar{C}_d\bar{C}_k\bar{C}_m\bar{C}_p\bar{C}_q}\cos(\frac{ak\pi}{N})\cos(\frac{mb\pi}{N})\cos(\frac{nc\pi}{N})\cos(\frac{qd\pi}{N})\tilde{b}_{abcd} \qquad (A.61)$$

$$\tilde{B}_{kmp} = \frac{1}{N^3} \sum_a \sum_b \sum_c \frac{1}{\bar{C}_a \bar{C}_b \bar{C}_c \bar{C}_k \bar{C}_m \bar{C}_p} \cos(\frac{ak\pi}{N}) \cos(\frac{mb\pi}{N}) \cos(\frac{nc\pi}{N}) \tilde{b}_{abc0} \qquad (A.62)$$

where the coefficient b is computed from :

$$\tilde{b}_{abcd} = \sum_{i=\pm 1} \sum_{j=\pm 1} \sum_{k=\pm 1} \sum_{l=\pm 1} \mathcal{F}(1 + ia + jb + kc + ld) \qquad (A.63)$$

The function $\mathcal{F}$ is defined as :

$$\mathcal{F}(x) = \frac{1 - \cos \pi x}{x}; \qquad \mathcal{F}(0) = 1 \qquad (A.64)$$

Appendix B

Turbulent Wake Model

This appendix presents an analytical solution for the outer form of the original Baldwin-Lomax model, applied to a moving rotor wake. This solution allows one to estimate the value of the eddy viscosity in the outer domain, knowing only the local vorticity magnitude.

B.1. Vorticity profile

The wake velocity profile in the stationary frame (x, y), is given by Eq.(2.62)

$$\begin{aligned} u &= 1 - Ae^{-z} \\ v &= 1 - Ae^{-z}\tan\theta + Ae^{-z}V \end{aligned} \tag{B.1}$$

where z is an auxiliary variable, related to the distance y_w from the wake centerline by :

$$z = By_w^2 \tag{B.2}$$

The vorticity in the wake is approximately equal to the crosswise derivative of the streamwise velocity component :

$$\omega = \frac{\partial u_w}{\partial y_w} - \frac{\partial v_w}{\partial x_w} \approx \frac{\partial u_w}{\partial y_w} \tag{B.3}$$

$$\Rightarrow \qquad \omega = \frac{\partial y}{\partial y_w}\frac{\partial z}{\partial y}\frac{\partial u_w}{\partial z} = \frac{1}{\sin\beta}\frac{\partial z}{\partial y}\frac{\partial u_w}{\partial z} \tag{B.4}$$

where the wake skew angle β is given by the kinematic relation :

$$\tan\beta = \frac{1}{V} \tag{B.5}$$

The streamwise-crosswise coordinate system (x_w, y_w), moving with uniform velocity V, is shown in Figure 2.6. The streamwise velocity component in the wake is obtained by applying the following linear transformation :

$$\begin{bmatrix} u_w \\ v_w \end{bmatrix} = \begin{bmatrix} \sin\beta & -\cos\beta \\ \cos\beta & \sin\beta \end{bmatrix} \begin{bmatrix} u \\ v \end{bmatrix} \tag{B.6}$$

to the velocities from Eq.(B.1). This yields :

$$\begin{aligned} u_w &= (1 - Ae^{-z})\sin\beta - (1 - Ae^{-z}\tan\theta + Ae^{-z}V)\cos\beta \\ v_w &= (1 - Ae^{-z})\cos\beta + (1 - Ae^{-z}\tan\theta + Ae^{-z}V)\sin\beta \end{aligned} \tag{B.7}$$

The wake vorticity profile is then determined :

$$\omega(y_w) = 2AB\left[1 - \frac{\tan\theta}{\cos\beta} + \frac{V}{\tan\beta}\right] y_w e^{-By_w^2} = 2ABC\, y_w e^{-By_w^2} \tag{B.8}$$

where the intensity constant C may be reduced to :

$$C = 1 + V^2 - \frac{V\tan\theta}{\sqrt{V^2+1}} \tag{B.9}$$

According to the above, the maximum value of vorticity in the wake ω_{max}, and the location $y_{\omega,max}$ at which it occurs, are :

$$y_{\omega,max} = \frac{1}{\sqrt{2B}} \tag{B.10}$$

$$\omega_{max} = \sqrt{\frac{2A^2BC^2}{e}} \tag{B.11}$$

With the wake parameters used in the study, this gives $y_{\omega,max} = 0.018$ and $\omega_{max} = 115.0$. These values agree relatively well with those from the Navier-Stokes calculations (respectively 0.021 and 105.0).

B.2. Wake factor

The quantities $y_{w;max}$ and F_{max} from §2.2.2 are determined by maximizing the function

$$F(y_w) = y_w|\omega| = 2AC\, ze^{-z} \tag{B.12}$$

This yields :

$$y_{w;max} = \frac{1}{\sqrt{B}} \tag{B.13}$$

$$F_{max} = \frac{2AC}{e} \tag{B.14}$$

The maximum velocity difference is determined from Eq.(B.1), giving:

$$\Delta U^2 \approx A\sqrt{V^2+1} \tag{B.15}$$

The value of the wake factor follows from Eq.(2.36) :

$$F_W = \frac{e}{8}\frac{\Delta U^2}{AC\sqrt{B}} \tag{B.16}$$

B.3. Klebanoff factor

The Klebanoff intermittency factor is computed using the value of $y_{w;max}$ from Eq.(B.13)

$$F_K = \frac{1}{1+5.5C_K^6 B^3 y_w^6} \tag{B.17}$$

The explicit dependence of the Klebanoff factor on the distance from the wake centerline is solved by replacing y_w in the above by the largest root $r(\omega)$ of the equation

$$re^{-Br^2} = \frac{|\omega|}{2ABC} \tag{B.18}$$

where ω is the local value of the vorticity at the point where one seeks to compute the eddy viscosity. The reason for using the vorticity equation (B.08) for implicitly computing the Klebanoff factor, is that local vorticity values are readily available in the stationary coordinate system used in the calculations.

B.4. Freestream eddy viscosity

The above results directly relate the eddy viscosity to the local value of the vorticity:

$$\nu_t(x,y,t) = \frac{1}{8}K_1K_2e\frac{\sqrt{V^2+1}}{AC\sqrt{B}\left[1+5.5C_K^6B^3r^6(x,y,t)\right]} \tag{B.19}$$

The factors $A, B...V$ are constant for a given computational set-up of the stator cascade. It is to be noted that this formula is valid only in the outer region of the computational domain.

Appendix C

Rotor/Stator Stage Design

The 2-D wake/stator configuration, used in the study, is that from a cylindrical section at the mean hydraulic diameter D_m of a single-stage axial pump. The pump design is completed in four steps. In the first step, a preliminary design, based on performance specification, is carried out. In the second step, this design is modified in order to make the stator passage geometry more suitable to numerical calculations. The third step re-sizes the modified design so that it can meet the above performance specifications. Finally, the wake parameters corresponding to the modified rotor geometry, are determined. All design procedures are based on Stepanoff's "Centrifugal and Axial Flow Pumps" [44]. The notation used in the following is identical to that from the book, and is thereby not included in the list of symbols.

C.1. Preliminary design

C.1.1. Performance specifications for a typical application. The value of specific speed chosen is typical for an axial flow pump.

Characteristic	Specification
Head	20 ft.
Capacity	2000 gpm.
Specific Speed	10,000.

C.1.2. Impeller rotation speed and discharge angle. An average discharge angle β_2 of 22.5 degrees is assumed. This is a typical value for most axial pumps. The impeller rotation speed is given by :

$$N = \frac{N_S H^{3/4}}{\sqrt{Q}} = \frac{10,000 \times 20 ft^{3/4}}{\sqrt{2000 gpm}} = 2100 rpm \qquad (C.1)$$

C.1.3. Impeller head coefficient and mean hydraulic diameter. Using Fig.5.2. from Reference [44], the specific constants corresponding to the above design are found. The value of the speed constant K_u is 1.55. The value of the capacity constant K_m is 0.46. From the speed constant, the head coefficient and the mean hydraulic diameter are obtained as follows :

$$\psi = \frac{1}{2K_u^2} = 0.21 \tag{C.2}$$

$$D_m = \sqrt{\frac{gH}{\pi^2 N^2 \psi}} = \sqrt{\frac{32.2 \times 144 \times 20ft}{\pi^2 \times 35rps^2 \times 0.21}} = 6.0in \tag{C.3}$$

C.1.4. Velocities at D_m. From the definition of the specific constants, one obtains :

$$u = K_u\sqrt{2gH} = 55.6ft/s \tag{C.4}$$

$$c_m = K_m\sqrt{2gH} = 16.7ft/s \tag{C.5}$$

$$\phi = \frac{c_m}{u} = 0.3 \tag{C.6}$$

C.1.5. Impeller dimensions. From Eq.5.35 in Reference [44], the specific speed and hub ratio are related by the following :

$$N_S = 6830\sqrt{\frac{1-\nu^2}{1+\nu^2}}\frac{\phi^{0.5}}{\psi^{0.75}} \quad \Rightarrow \quad \nu = 0.42 \tag{C.7}$$

The impeller hub and outer diameter are calculated as :

$$D_o = \sqrt{\frac{2D_m^2}{1+\nu^2}} = 7.8in \tag{C.8}$$

$$D_h = \nu D_o = 3.3in \tag{C.9}$$

Verification of the flow rate :

$$Q = 0.25\pi c_m D_o^2(1-\nu^2) = 2045\text{gpm.} \tag{C.10}$$

C.1.6. Impeller entrance and exit velocity triangles. These are summarized in the following table for three spanwise locations; respectively at the hub, the mean hydraulic diameter, and near the tip of the impeller.

Variable	Value at D_h	at D_m	at D_o
β_1	28.6°	16.6°	13.0°
β_2	37.3°	22.5°	17.8°
u	$30.0ft/s$	$55.0ft/s$	$71.5ft/s$
c_{u2}	$8.5ft/s$	$15.6ft/s$	$20.1ft/s$

C.1.7. Impeller blading. Based on Fig. 8.7 from reference [44], a four-bladed impeller is chosen with spacing-to-blade-chord ratio l/t of 0.96. The corresponding blade spacing and chord are :

$$t = \pi D_m / N_R = 4.7in \tag{C.11}$$

$$l = t \times (l/t)_m = 4.5in \tag{C.12}$$

Munk's method, as described in Reference [44], was used to design the impeller blade section. This produced a NACA 2308 section with a stagger angle of 71 degrees at the mean diameter.

C.1.8. Impeller/Stator gap and stator velocity triangle. The recommended impeller/stator gap is 5% of the impeller diameter, i.e. 0.4 inches. The turning angle of the flow leaving the stator is zero degrees. The turning angle of the flow entering the stator is $\theta = \tan^{-1}(c_{u2}/C_m)$ = 43 degrees. This angle will be referred to as ***inlet angle***.

C.1.9. Preliminary stator blading at the mean hydraulic diameter. According to Reference [44], the optimal number of stator blades for a four-vaned impeller is between five and eight. A five-vaned stator was chosen. To determine the stator spacing-to-blade-chord, a formula based on airfoil theory is used (Kovats [29], p.375, p.416) :

$$\frac{l}{s} = \frac{2c_{u2}}{c_m} \frac{\sin \alpha_\infty}{k_l C_L} \tag{C.13}$$

According to Reference [29] the value of the interaction coefficient may be taken equal to one in the preliminary stage. With a recommended design lift coefficient of 0.5, the above gives a stator passage spacing-to-blade-chord ratio of 0.7 at the mean hydraulic diameter. The corresponding blade spacing and chord are :

$$t = \pi D_m / N_S = 3.8in \tag{C.14}$$

$$l = t \times (l/t)_m = 6.0in \tag{C.15}$$

Munk's method, as described in Reference [44], is then used to design the stator blade section. This gives a NACA 8308 section with a stagger angle of 25 degrees at the mean diameter.

C.2. Modified stator design

The 2-D configuration from Section C.1, was used in an initial study of the stator unsteady flow. The results from this study prompted the following modifications to be made in the stator passage design :

- The stator passage inlet angle was decreased from 43 to 25 degrees. This change was necessary to avoid massive separation of the flow over the suction surface of the stator blade in the laminar calculations. For the same reason, an Eppler blade section with 4% thickness was used instead of the NACA 8308 section. This resulted in a decrease of the lift coefficient to 0.35.

- The stator spacing-blade chord ratio at the mean diameter was decreased from 0.7 to 0.4 in order to reduce the number of spectral elements necessary at a given Reynolds number. This was done by using the maximum allowable number of blades (eight) for a pump of such size, rather than by increasing the blade chord.

- The impeller blade number and spacing-blade chord ratios were set equal to those of the stator, in order to limit the calculations to a single stator passage.

- The rotor blade linear velocity at the mean diameter was set to the double of the flow meridional velocity, in order to preserve the wake period of the original design.

The spacing-blade chord ratio does not have a significant influence on the unsteady flow in the stator passage. On the other hand, the stator blade loading and the wake frequency are of considerable importance, as shown in Chapter Six. The above changes lead to the wake/stator configuration shown in Figure 3.1 and used in the present study.

C.3. Validation and re-sizing of the modified design

It is necessary to verify whether a pump having the above impeller and stator characteristics may operate and meet the performance specifications. For this purpose, a procedure which is the inverse of the preliminary design process will be employed. In the modified design, the velocity triangles and spacing-blade chord ratio are imposed by computational requirements. Starting from these fixed characteristics, the pump will be re-sized to meet the specifications of §C.1.1.

C.3.1. Modified impeller velocity triangles. The modified impeller discharge angle is equal to 33 degrees, which is slightly below the 35 degrees limit for most axial pumps. The modified

impeller inlet angle is 26.6 degrees.

C.3.2. Modified design flow and head coefficients. The flow coefficient is given by

$$\phi = \left.\frac{c_m}{u}\right|_{D_m} = 0.5 \qquad (C.16)$$

Using Figure 9.12 from reference [44], the efficiency of the pump was estimated to be 80%. According to Figure 9.16 from reference [44], the specific speed ratio $\phi^{0.5}/\psi^{0.75}$ corresponding to this efficiency, to a specific speed of 15,000 and to a discharge angle of 33 degrees, is equal to 1.75. The head coefficient of the modified design is thus estimated to be :

$$\psi = (\frac{\phi^{0.5}}{1.75})^{1.33} = 0.18 \qquad (C.17)$$

It is to be noted that the specific speed of the new design has been increased to 15,000 from 10,000 in order to obtain a head coefficient within the usual range. The modified design has thus a specific speed in the highest range.

C.3.3. Modified impeller velocity and mean diameter. In order to meet the (2000 gpm capacity / 20 ft head) specification, the operating speed of the new impeller should be :

$$N = \frac{N_S \times H^{0.75}}{\sqrt{Q}} \approx 3000 rpm \qquad (C.18)$$

This corresponds to a mean hydraulic diameter of :

$$D_m = \sqrt{\frac{gH}{\pi^2 N^2 \psi}} = \sqrt{\frac{32.2 \times 144 \times 20 ft}{\pi^2 \times 50 rps^2 \times 0.18}} = 4.7 in \qquad (C.19)$$

It is to be noted that the modified design is more compact and operates at higher speed, which is in conformity with the higher specific speed. The flow meridional velocity at the mean hydraulic diameter is 31.5 ft/s. The linear velocity of the impeller blade there is 63 ft/s.

C.3.4. Modified impeller dimensions. The new hub ratio is estimated using Eq.5.35 in Reference [44] :

$$N_S = 6830\sqrt{\frac{1-\nu^2}{1+\nu^2}}\frac{\phi^{0.5}}{\psi^{0.75}} \quad \Rightarrow \quad \nu = 0.36 \qquad (C.20)$$

The resulting impeller hub and outer diameters are equal to 2.3 and 6.3 inches respectively.

C.3.5. Modified impeller blading. With eight blades and spacing-blade chord ratio of 0.4, the dimensions of the impeller passage are :

Vane spacing : 1.8 in
Vane chordlength : 4.6 in

Munk's method, as described in Reference [44] was used to design the modified impeller blade section. This produced a NACA 2304 section with a stagger angle of 60 degrees.

C.3.6. Modified stator blading. With eight blades and spacing-blade chord ratio of 0.4, the dimensions of the stator passage are :

Vane spacing : 1.8 in
Vane chordlength : 4.6 in

As per §C.2, an 4% thick Eppler blade section [15] at 12 degrees stagger angle is selected for the stator; based on laminar 2-D Navier-Stokes calculations at the mean hydraulic diameter.

It is to be noted that, in all calculations, the physical dimensions will be normalized by the axial component of the stator blade chord, i.e. by $4.6 \times \cos 12° = 4.5$ inches. All velocities will be normalized by the meridional flow velocity at the mean diameter, i.e. by 31.5 ft/s. For water (ν=1.1E-5 ft^2/s at 20 C°), the corresponding stator blade Reynolds number is equal to 1,070,000 at the mean diameter.

C.4. Wake characteristics

A 1.00 inch impeller-stator gap has been selected in the modified design. As the inlet boundary of the computational domain has been placed at 0.12 non-dimensional distance units in front of the leading edge (.55 in), it is necessary to estimate the rotor wake thickness and velocity defect at 0.45 inches past the rotor blade trailing edge.

The Reynolds number of the impeller blade section at the mean diameter is 2,500,000. The NACA 2304 section at 3.6 degrees incidence with respect to the relative inflow, has an estimated drag coefficient of 0.07. Using Eq.(2.58), the velocity defect is estimated to be

$$A = \frac{2.42\sqrt{C_D}}{2x_i/c_r + 0.6} = \frac{2.42\sqrt{0.07}}{2 \times 0.45in/4.6in + 0.6} = 0.763 \qquad (C.21)$$

In the study, a rounded value of 0.75 is used for the velocity defect. The characteristic wake half-width is then given by Eq.(2.59) :

$$\frac{\delta}{2} = \frac{c_r}{2}\frac{2C_D x_i}{c_r} = 0.27in \qquad (C.22)$$

The corresponding non-dimensional wake width is 0.12 (12% of the stator blade chord). In the interaction study, a rounded value of 0.1 is used, which corresponds to a wake thickness parameter B equal to 1,500 (Eq.2.57).

Appendix D

Pressure Disturbances

D.1. Leading edge high-pressure pulse

The largest total velocity in the wake (before interception) is given by Eq.(2.62) for $y = 0$

$$\left\{ \begin{array}{l} u_{max} \\ v_{max} \end{array} \right\} = \left\{ \begin{array}{l} (1-A)U_\infty \\ (1-A)U_\infty \tan\theta + AV \end{array} \right\} \qquad (D.1)$$

The static pressure in the wake before interception is approximately equal to the static pressure far upstream (the wake is a force-free vortex sheet). At the moment of interception, the above velocity is converted into static pressure along a streamline centered in the wake. Using Bernoulli's equation, the peak in static pressure thereby produced is :

$$p^+_{max} = p_\infty + \frac{1}{2\rho}\mathbf{u}^2_{max} \qquad (D.2)$$

The corresponding pressure coefficient is, by definition :

$$C^+_{p,max} = \frac{2(p_{max} - p_\infty)}{\rho U^2_\infty} \qquad (D.3)$$

Substitution of Eq.(F.1) into Eq.(F.3), yields

$$C^+_{p,max} = \left(\frac{1-A}{\cos\theta}\right)^2 + 2A(1-A)\tan\theta V + A^2V^2 \qquad (D.4)$$

This formula neglects the viscous decay of the wake before interception and the unsteady flow effects represented by the term $\partial\Phi/\partial t$. The resulting discrepancy between Eq.(D.4) and the Navier-Stokes calculations is negligible in the present case, where the inlet boundary is close to the leading edge.

D.2. Suction surface low-pressure disturbance

Examination of the vorticity contours in Figure 3.11 indicates that the disturbance vorticity inside a B-vortex is distributed linearly. Let (r, θ) be a cylindrical coordinate system with origin in the vortex center; and let $\theta = 0$ be the line pointing in the chordwise direction. Within the B-vortex, the disturbance vorticity profile may be approximated by

$$\omega = \omega_m \left(1 - \frac{r}{a}\right) \tag{D.5}$$

where ω_m is the peak value of the disturbance vorticity, occurring at the center of the vortex, and a is the distance at which the disturbance vorticity becomes unobservable (i.e. of the same order as the base flow vorticity). As shown in Figure 3.10, the disturbance velocity $\tilde{v}$ due to the vortex is almost entirely in the θ direction. Therefore, it can be approximately computed from

$$\tilde{v}_\theta = \int_0^r \omega dr = \omega_m \left(r - \frac{r^2}{2a}\right) \tag{D.6}$$

Figure 3.17a indicates that the pressure gradient is strongest along the line $\theta = 0$ (in the streamwise direction), and almost non-existent along the line $\theta = \pi/2$ (in the normal direction to the surface). This is due to the flat shape of the B-vortex. Neglecting the unsteady effects associated with the motion of the vortex, the equilibrium condition for a fluid element lying on the line $\theta = 0$ can be written as :

$$\frac{dp}{dr} = \frac{\rho \tilde{v}_\theta^2}{r} \tag{D.7}$$

Integrating this equation along the line $\theta = 0$, yields the pressure difference between the center of the B-vortex and the undisturbed flow immediately outside :

$$p(a_b) - p(0) = \frac{11}{48} \rho \omega_m^2 a_b^2 \tag{D.8}$$

where a_b is the half-width of the B-vortex (along the $\theta = 0$ line). Examination of the pressure contours in Figure 3.16a reveals that this difference is approximately equal to the peak-to-peak amplitude of the low-pressure disturbances on the suction surface. It is convenient to express the pressure difference in terms of pressure coefficient:

$$(\Delta C_p)_{SS}^- = \frac{p(a_b) - p(0)}{1/2 \rho U_\infty^2} = \frac{11}{24} \omega_m^2 a_b^2 \tag{D.9}$$

For the typical B-vortex shown in Figure 3.11, $\omega_m \approx 30$ non-dimensional units; and $a_b \approx 0.04$ chords. These values correspond to a disturbance peak-to-peak amplitude of :

$$(\Delta C_p)_{SS}^- = 0.65 \tag{D.10}$$

The circulation of the B-vortex may be defined as :

$$\Gamma_B = \int_0^{2\pi} \int_0^{a_b} \omega dA = \frac{\pi}{3} \omega_m a_b^2 \qquad (D.11)$$

where the effects of the flat vortex geometry have been neglected. Insertion of this equation into Eq.(D.9) yields :

$$(\Delta C_p)^- = \frac{99}{24\pi^2} \left(\frac{\Gamma_B}{a_b} \right)^2 \qquad (D.12)$$

For the above B-vortex, $\Gamma_B \approx 0.05$. The last equation involves the vortex circulation instead of the maximum vorticity; and is thus more appropriate from a physical point of view.

D.3. Pressure surface high-pressure disturbance

The high pressure region on the pressure surface is due to a stagnation of the disturbance flow produced by the wake vortices. The difference between the pressure in the stagnation region p_s and the pressure outside the stagnation region p_o, can be computed using Bernoulli's equation. This equation is applied along along the streamline containing the disturbance flow stagnation point, giving :

$$p_s + \frac{1}{2}\rho \bar{\mathbf{U}}^2 = p_o + \frac{1}{2}\rho(\bar{\mathbf{U}} + \tilde{\mathbf{u}})^2 \qquad (D.13)$$

where the unsteady and viscous effects have been neglected. As shown in Figure 3.17a, this pressure difference is approximately equal to the peak amplitude of the positive pressure disturbance, written here as:

$$(\Delta C_p)^+_{PS} \approx \frac{1}{2}\tilde{\mathbf{u}}^2 + \tilde{\mathbf{u}} \cdot \bar{\mathbf{U}} \qquad (D.14)$$

For the case of disturbance flow produced by a vortex pair, $\tilde{\mathbf{u}}$ and $\bar{\mathbf{U}}$ are nearly at right angles and the second term may be dropped. From the computed data, it appears that the distance between the wake vortex and the pressure surface is larger than the vortex core. For this reason, the disturbance velocity will be estimated using the inviscid Biot-Savart law

$$\tilde{u} = 2 \times b_w \frac{\Gamma_W}{2\pi d_w} \qquad (D.15)$$

where b_w is a geometrical factor and d_w is the distance between the wake vortices and the pressure surface. With this, the amplitude of the positive pressure disturbance is given by :

$$(\Delta C_p)^+_{PS} \approx \left(\frac{b_w \Gamma_W}{\pi d_w} \right)^2 \qquad (D.16)$$

Appendix E

Glossary and Unsteady Flow Metrics

E.1. Glossary

Unsteadiness : The quantitative amount of fluctuations in the flowfield variables, in the blade loading and in the discharged fluid produced by the incoming rotor wakes.

Steady Flow : Implicitly, the computed flow in the stator in absence of rotor wakes.

Unsteady Flow : Implicitly, the computed flow in the stator in presence of rotor wakes.

Disturbance Flowfield : The flowfield obtained by subtracting the steady flow that would exist in absence of rotor wakes, from the unsteady calculated flowfield. Plots of the disturbance flowfield are particularly useful, because they clearly show the evolution of the rotor wakes and the unsteady flow features.

Time period : The time period implicitly used in the following is the time between the passing of two rotor wakes, given by :

$$T = \frac{S_r}{V} = \frac{2\pi P}{N_s \Omega} \qquad (E.1)$$

In all unsteady calculations to date, the dominant frequency is the wake passing frequency, although multiples thereof are observed in the leading edge region. This is due to the short-duration, intense L.E. pressure pulse upon wake interception.

E.2. Time-mean distributions

For a deterministic unsteadiness, the time-mean distribution of the stator blade (pressure) loading along the chord is computed as :

$$\bar{C}_p(s) = \frac{1}{T}\int_t^{t+T} C_p(s,t)dt \qquad (E.2)$$

This distribution is computed separately over the suction and pressure surfaces. It is to be noted that the pressure coefficient is computed using the averaged value of static pressure along the inflow boundary and the axial velocity far upstream the stator :

$$C_p(s,t) = \frac{2(p(x_s,y_s,t) - p_\infty)}{\rho U_\infty^2} = 2(p(x_s,y_s,t) - p_\infty) \qquad (E.3)$$

E.3. RMS distributions

For a deterministic unsteadiness, the RMS distribution of the stator blade (pressure) loading along the chord is computed as :

$$\breve{C}_p(s) = \sqrt{\frac{1}{T}\int_t^{t+T} (C_p(s,t) - \bar{C}_p(s))dt} \qquad (E.4)$$

This distribution is computed separately over the suction and pressure surfaces. In addition, the RMS distribution of the flow vorticity across a vertical plane passing through the stator blade trailing edge plane is used :

$$\breve{\omega}(y_o) = \sqrt{\frac{1}{T}\int_t^{t+T} (\omega(x_o,y_o,t) - \bar{\omega}(x_o,y_o))dt} \qquad (E.5)$$

E.4. Spectral Distributions

The *amplitude spectrum* is the ensemble of coefficients in the timewise Fourier series expansion of some flowfield variable at a given point. For instance, the amplitude spectrum distribution of the blade loading along the chord is defined as:

$$\mathcal{C}_k(s) = \frac{1}{T}\int_t^{t+T} C_p(s,t)e^{2ik\pi t/T}dt \qquad (E.6)$$

The amplitude spectrum distribution of the vorticity fluctuation on the trailing edge plane is also defined as :

$$\mathcal{W}_k(y_o) = \frac{1}{T}\int_t^{t+T} \omega(x_o,y_o,t)e^{2ik\pi t/T}dt \qquad (E.7)$$

E.6. Global unsteadiness indexes

A *global unsteadiness index* is the space integral of a given RMS distribution over a specified region of the computational domain. The global unsteadiness index provides a rough but simple metric for the intensity of the fluctuations in this region. It is useful for rapid comparisons and as a constraint in the flow control optimization programs. The following global unsteadiness indexes are used :

(1) Pressure unsteadiness index on the suction surface :

$$\check{C}_{p,SS} = \int_0^1 \check{C}_{p,SS}(s)ds \qquad (E.8)$$

(2) Pressure unsteadiness index on the pressure surface :

$$\check{C}_{p,PS} = \int_0^1 \check{C}_{p,PS}(s)ds \qquad (E.9)$$

(3) Discharge plane unsteadiness index over the suction surface :

$$\check{W}_{SS} = \frac{2}{S}\int_{y_{te}}^{y_{te}+0.5S} \tilde{\omega}(y_o)dy_o \qquad (E.10)$$

(4) Discharge plane unsteadiness index over the pressure surface :

$$\check{W}_{PS} = \frac{2}{S}\int_{y_{te}-0.5S}^{y_{te}} \tilde{\omega}(y_o)dy_o \qquad (E.11)$$

(4) Discharge plane unsteadiness index local to the trailing edge surface :

$$\check{W}_{TE} = \frac{1}{2\delta}\int_{y_{te}-\delta}^{y_{te}+\delta} \tilde{\omega}(y_o)dy_o \qquad (E.12)$$

FIGURES

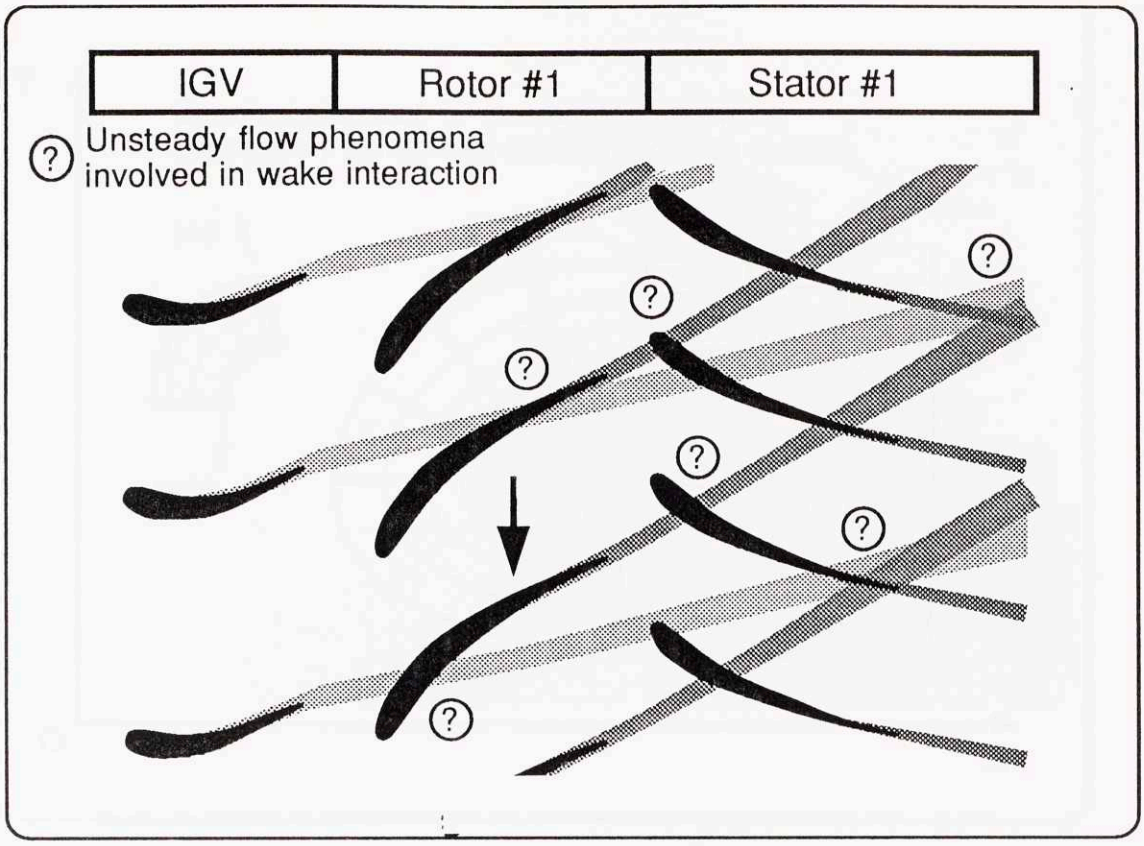

Fig.1.1. Two-dimensional representation of the wake interaction between blade rows.

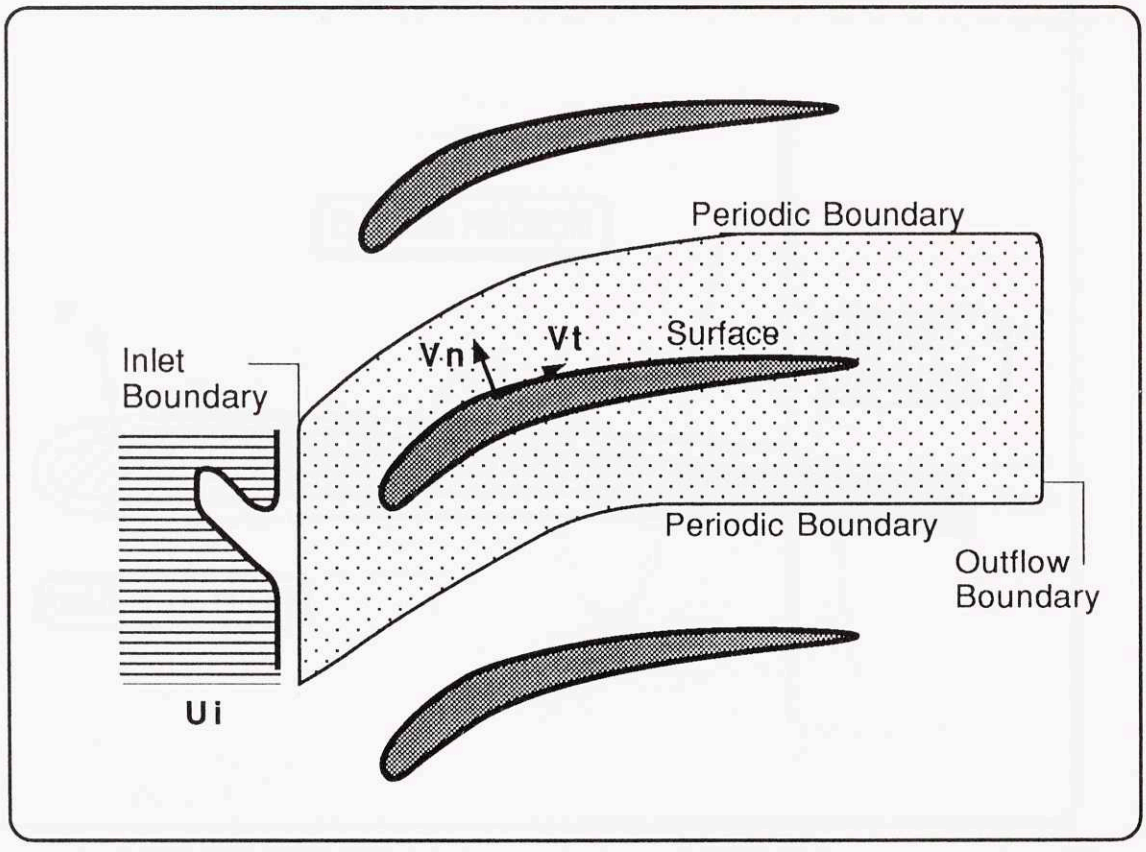

Fig.1.2. Computational domain, B.C., and representation of the rotor wakes.

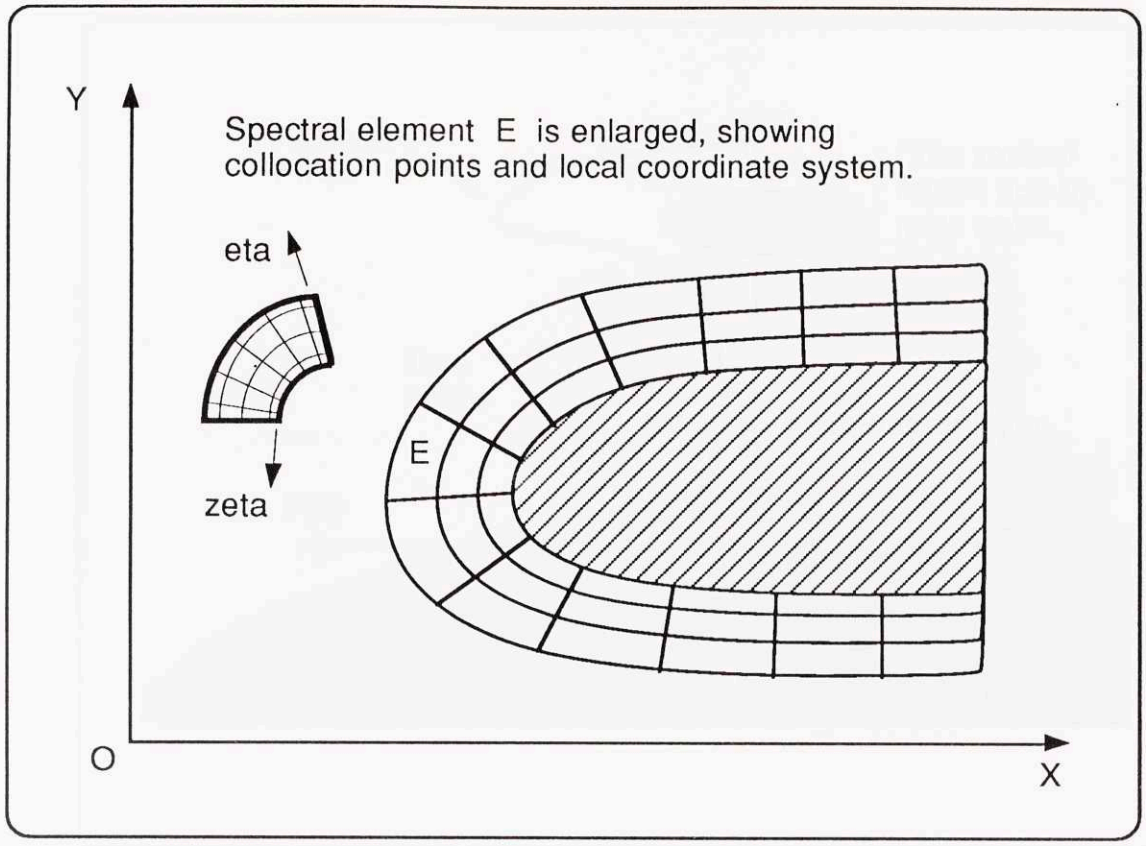

Fig.2.1. Discretization of the computational domain into spectral elements.

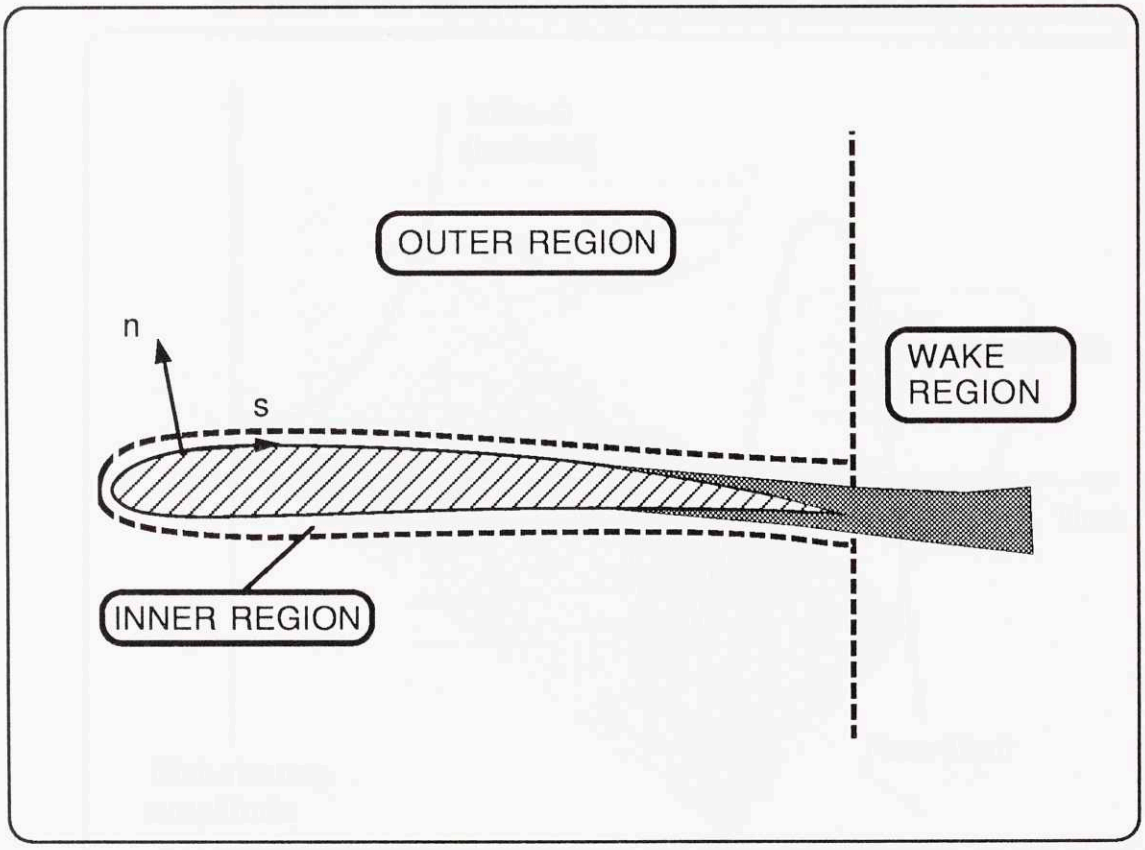

Fig.2.2. Division of the flowfield into three regions for the Baldwin-Lomax model.

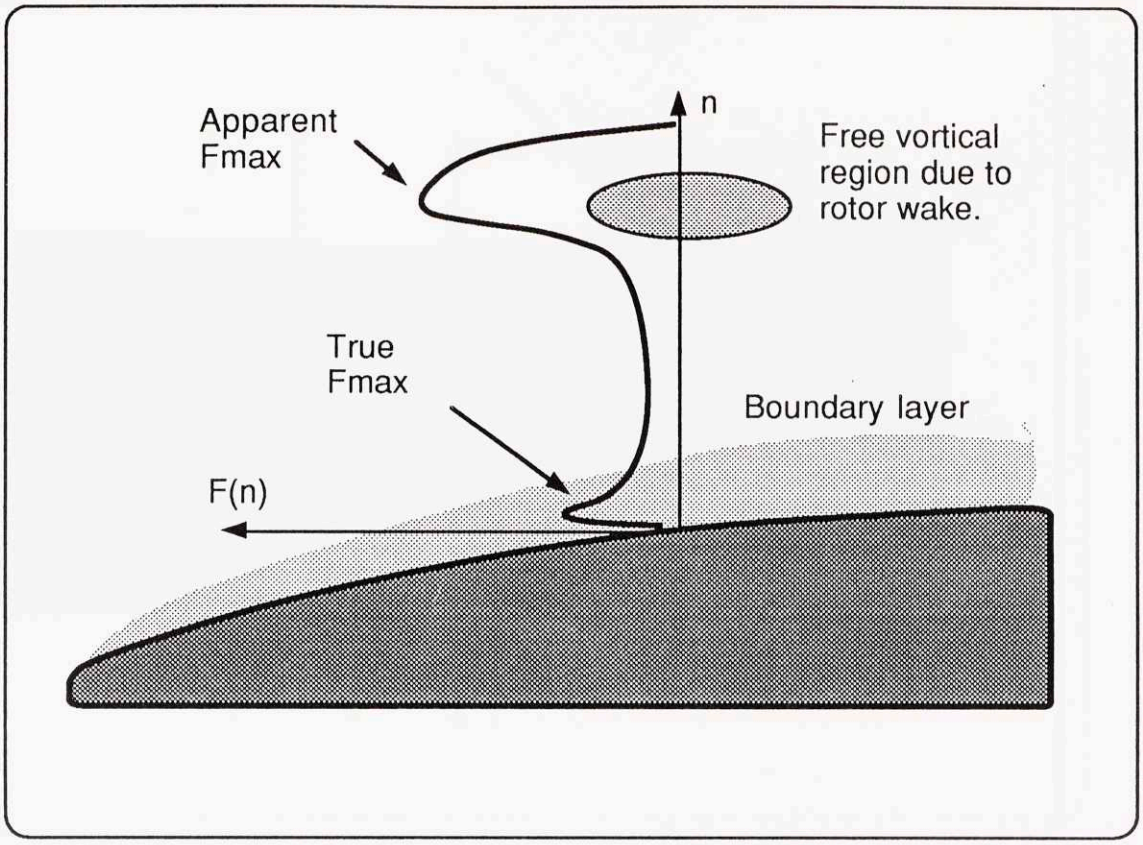

Fig.2.3. In presence of free vortical disturbances over the blade surface, the original formulation of the Baldwin-Lomax model may overestimate y_{max} and F_{max}.

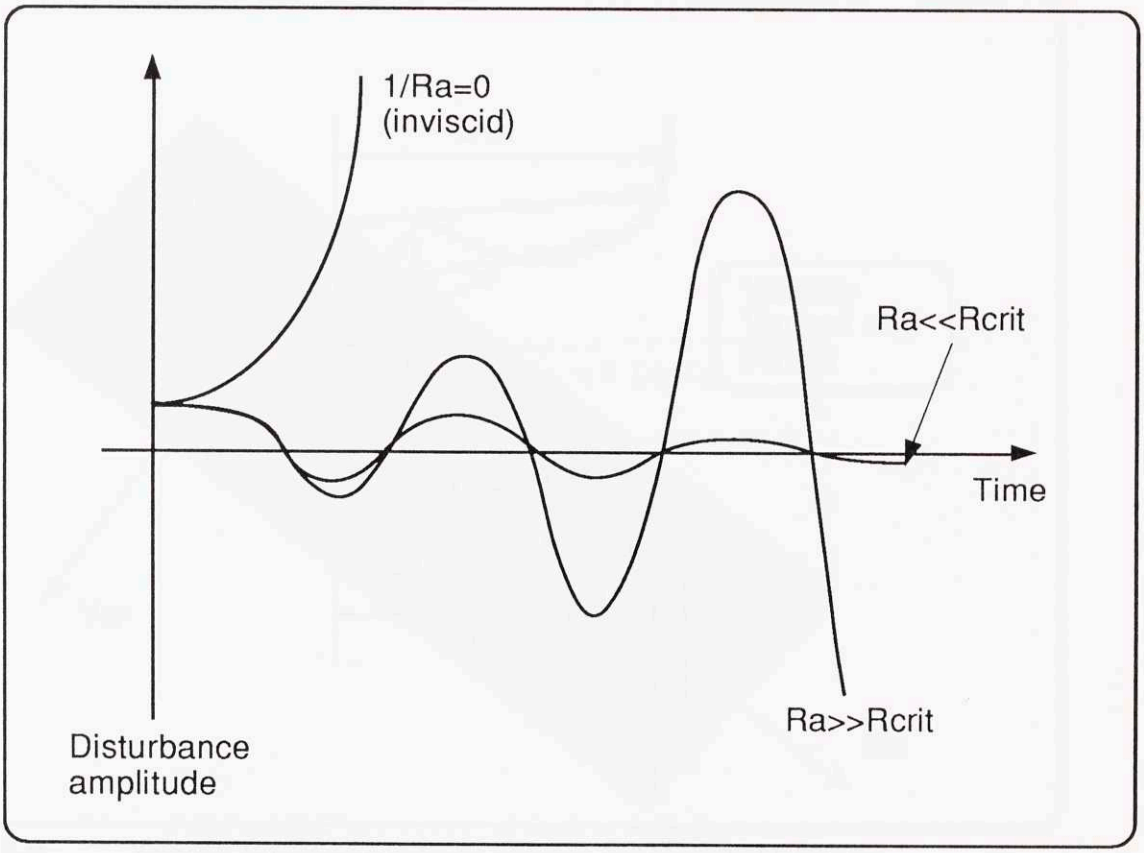

Fig.2.4. Behavior of the linearized solution for various values of the artificial viscosity parameter R_a (Illustrative).

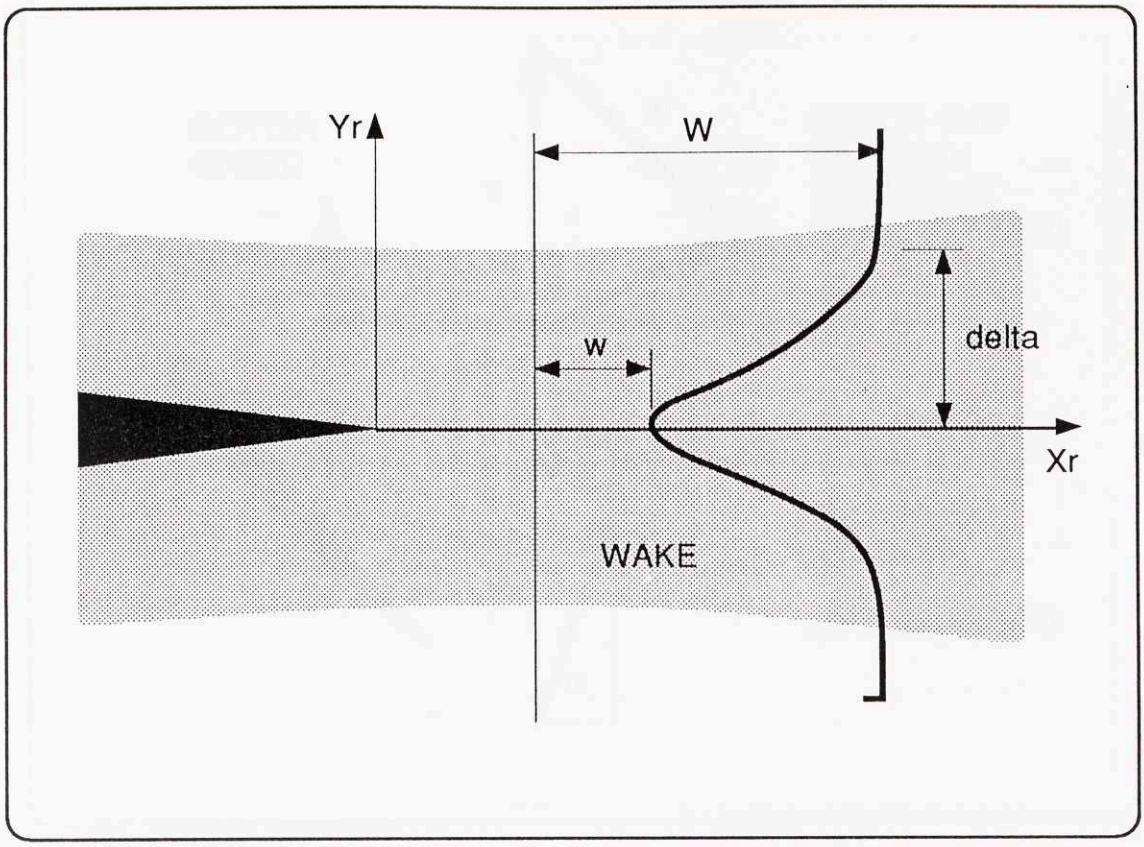

Fig.2.5. Velocity profile of the rotor wake in the rotating frame.

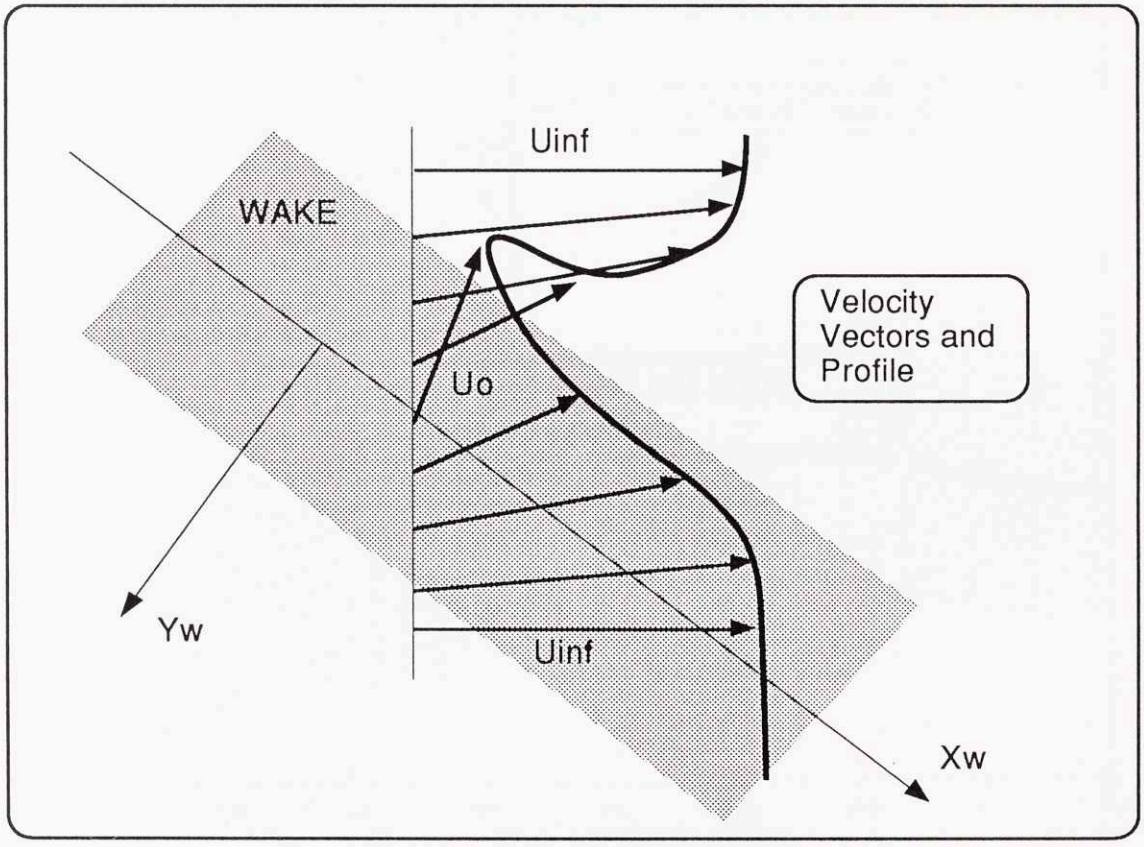

Fig.2.6. Velocity profile of the rotor wake in the stationary frame.

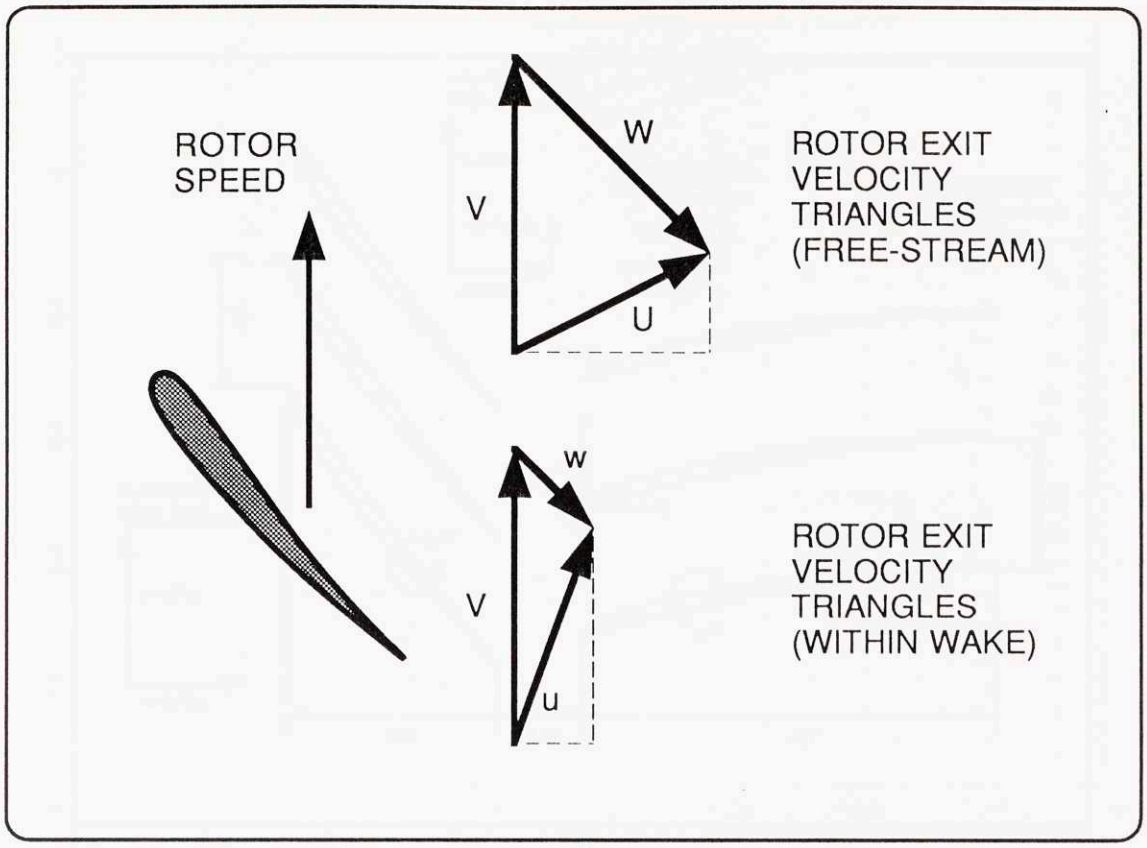

Fig.2.7. Velocity triangles in a compressor/pump environment.

This space has been left blank intentionally

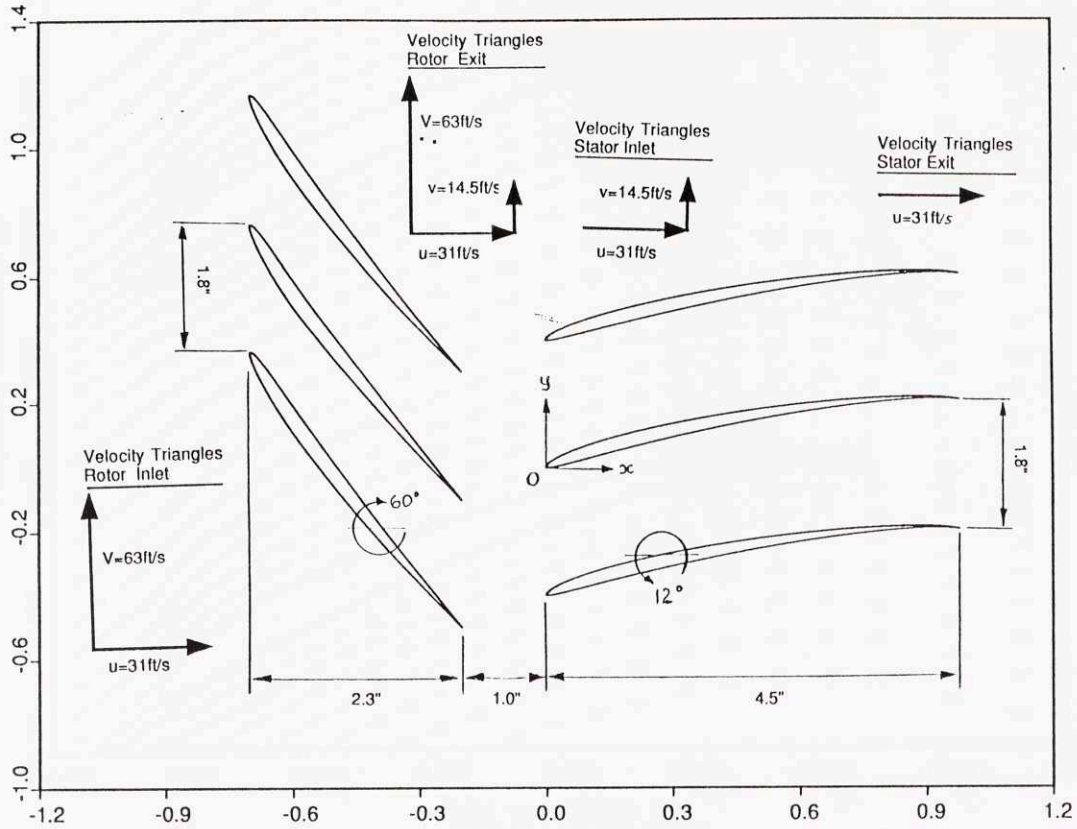

Fig.3.1. Rotor/stator configuration used in this work.

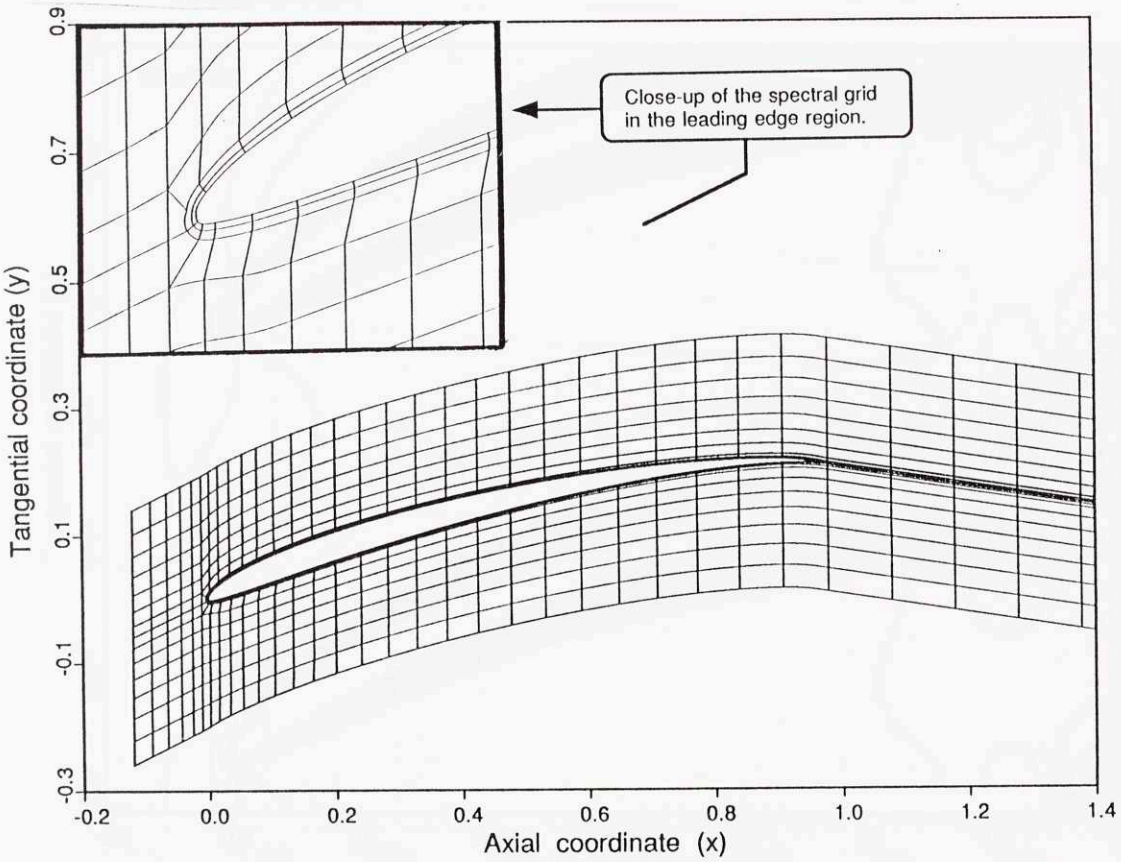

Fig.3.2. Spectral-element grid used in the laminar calculations (580 elements, Re=10,000).

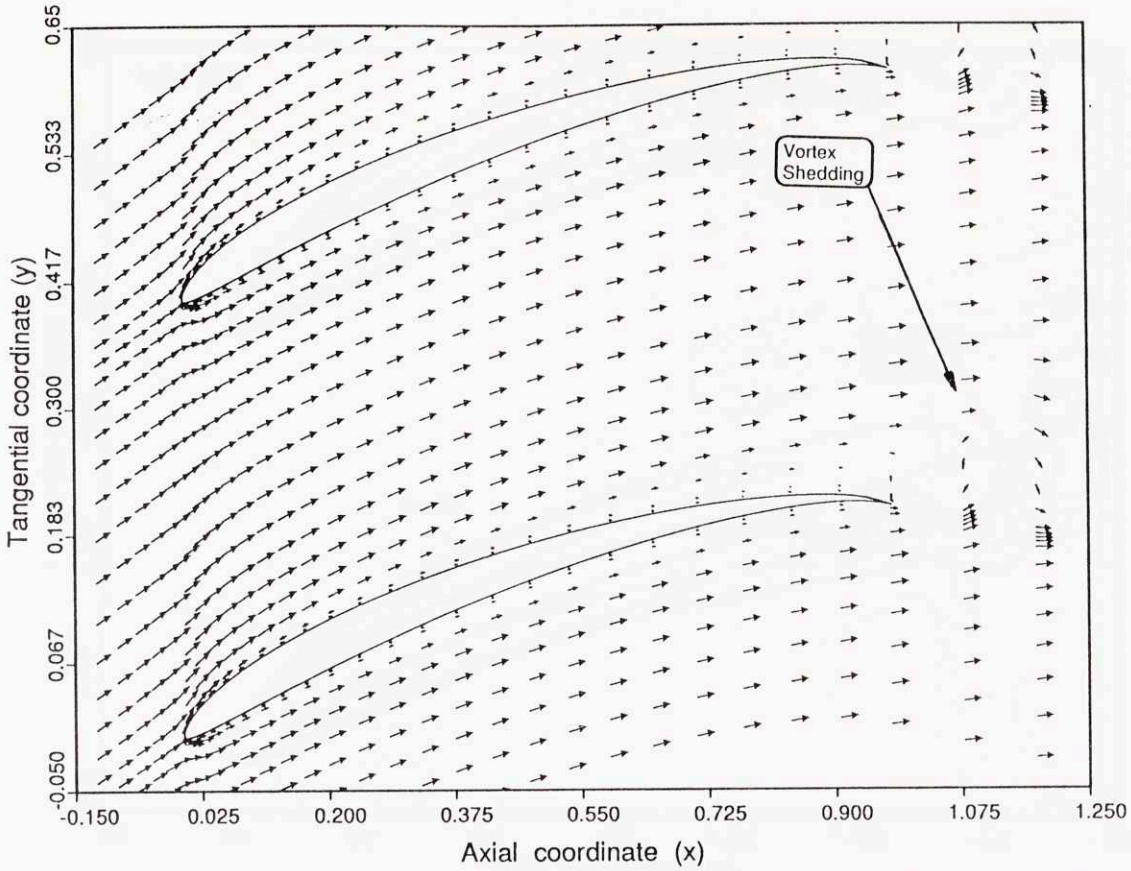

Fig.3.3. Computed velocity vectors in the stator passage. Undisturbed laminar flow (Re=10,000).

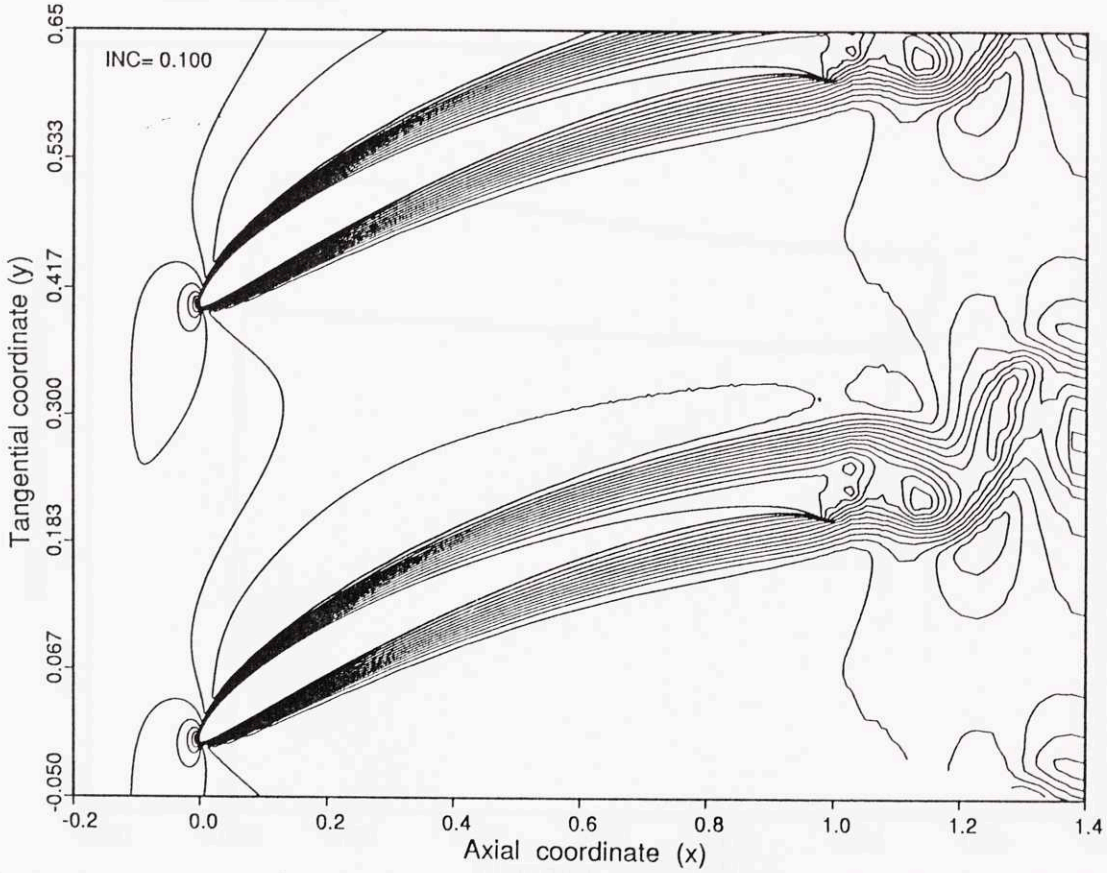

Fig.3.4. Computed velocity contours in the stator passage. Undisturbed laminar flow (Re=10,000).

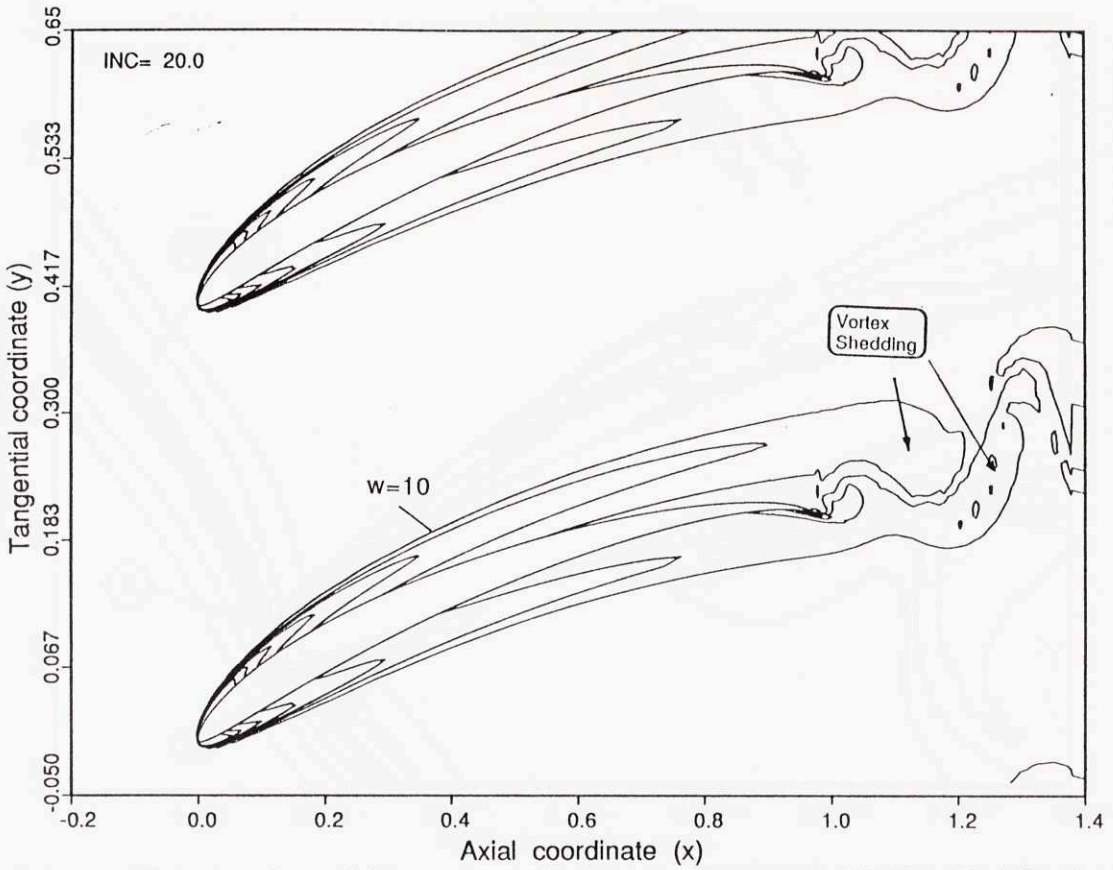

Fig.3.5. Computed vorticity contours in the stator passage. Undisturbed laminar flow (Re=10,000).

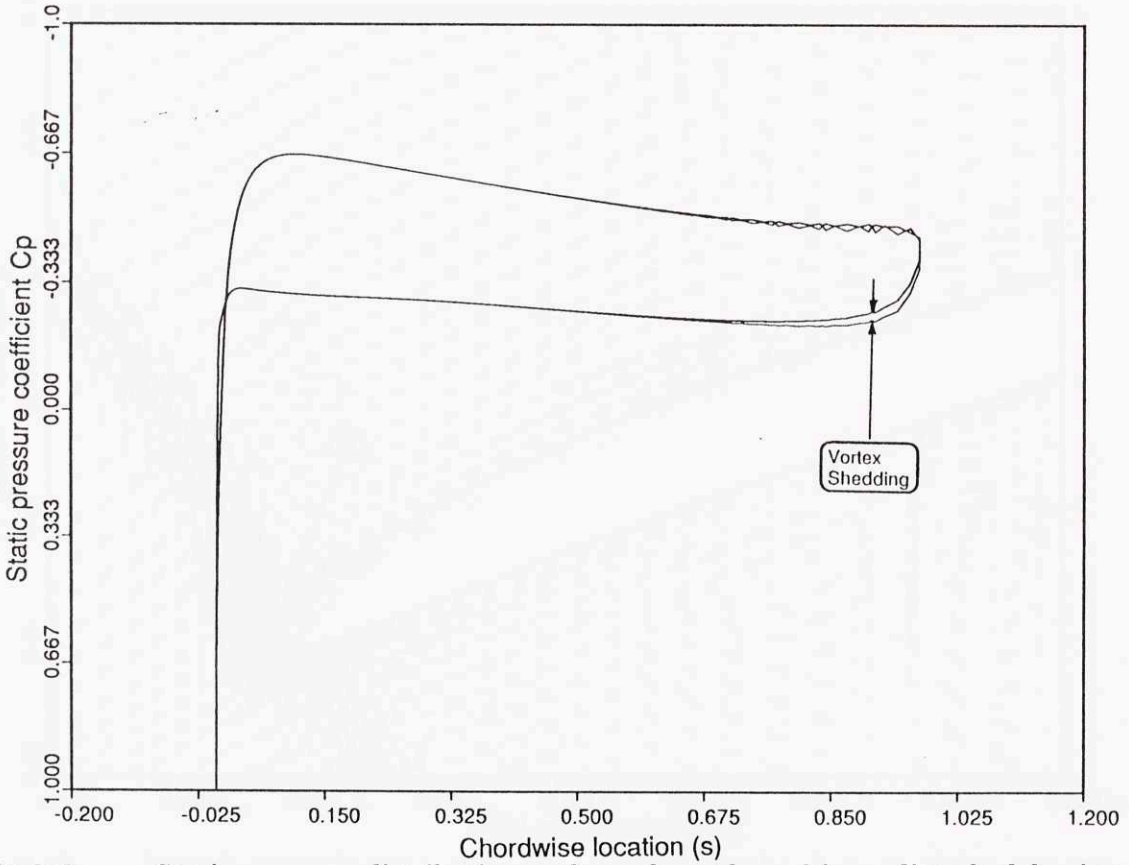

Fig.3.6. Static pressure distribution and envelope thereof in undisturbed laminar flow (Re=10,000).

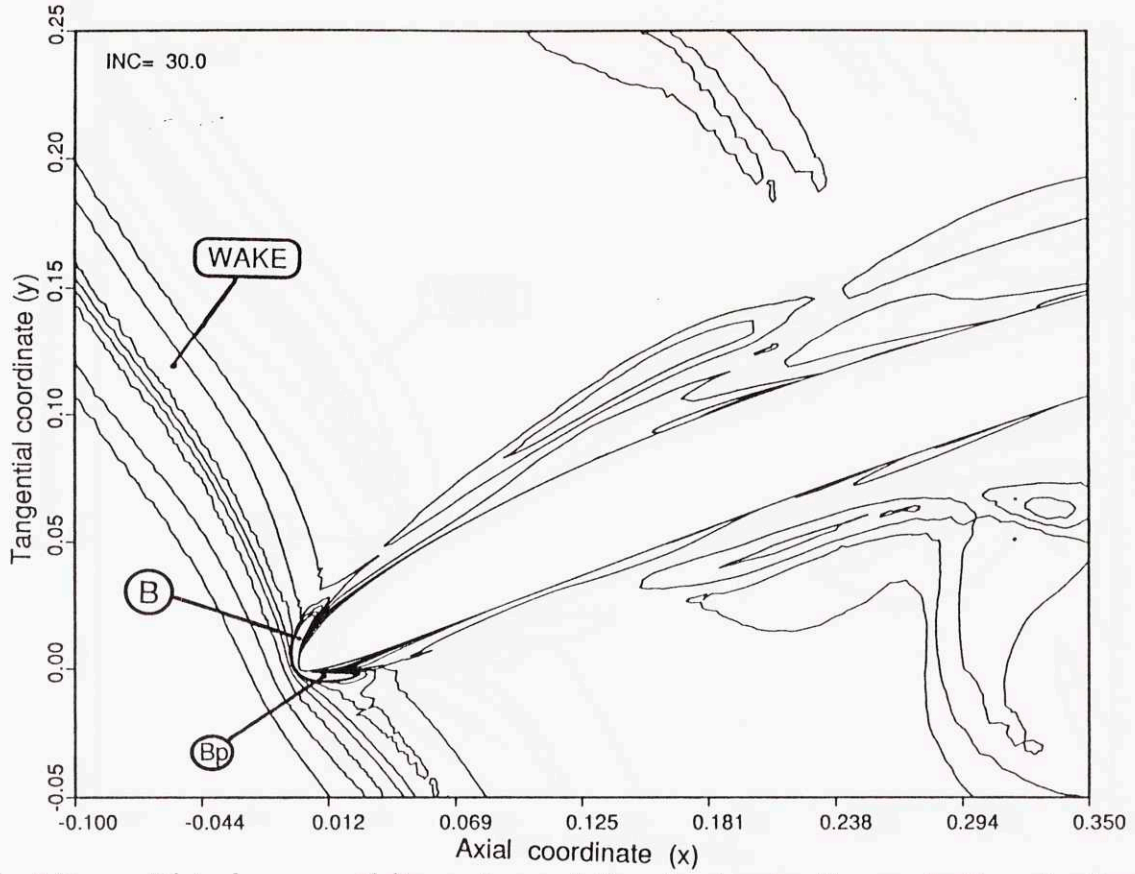

Fig.3.7a. Disturbance vorticity contours at time t_0, showing the production of a B-region at the leading edge by the wake.

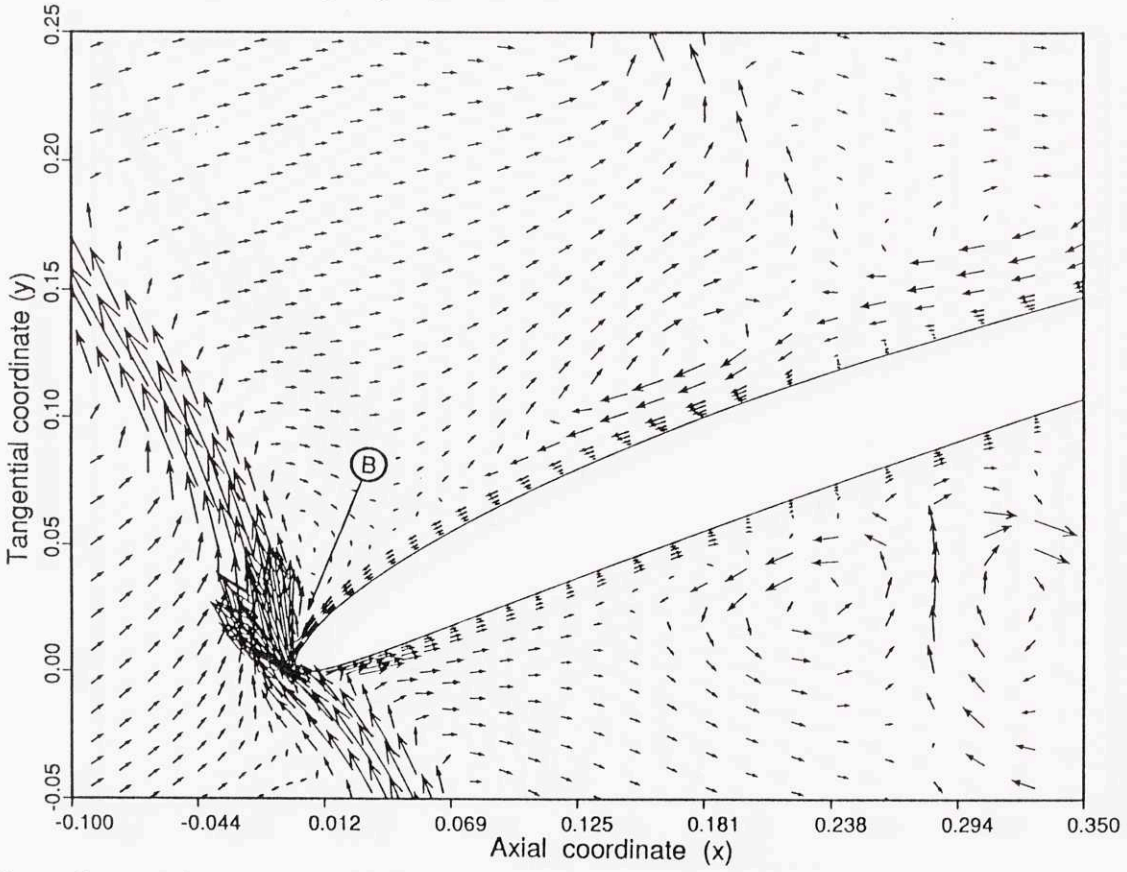

Fig.3.7b. Disturbance velocity vectors corresponding to the above vorticity contours.

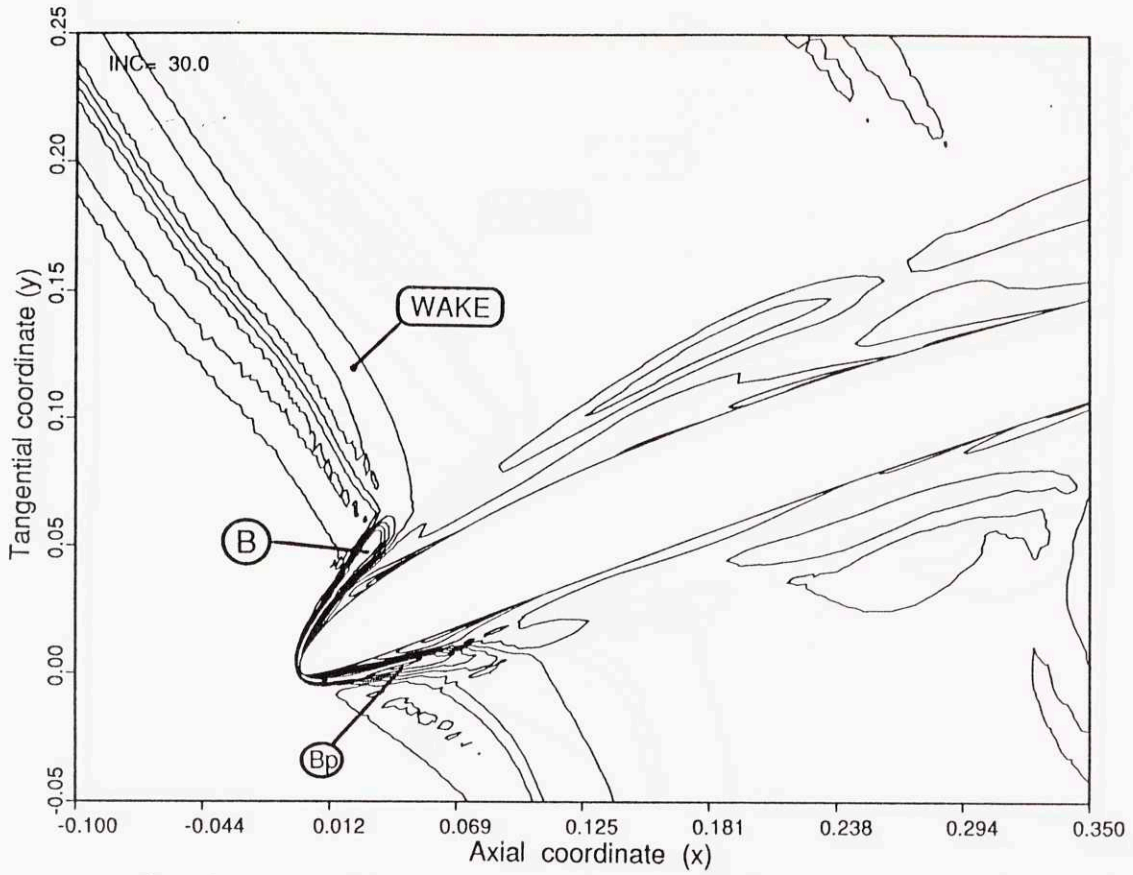

Fig.3.7c. Disturbance vorticity contours at time $t_0 + 0.2T$, showing the production of a B-region at the leading edge by the wake.

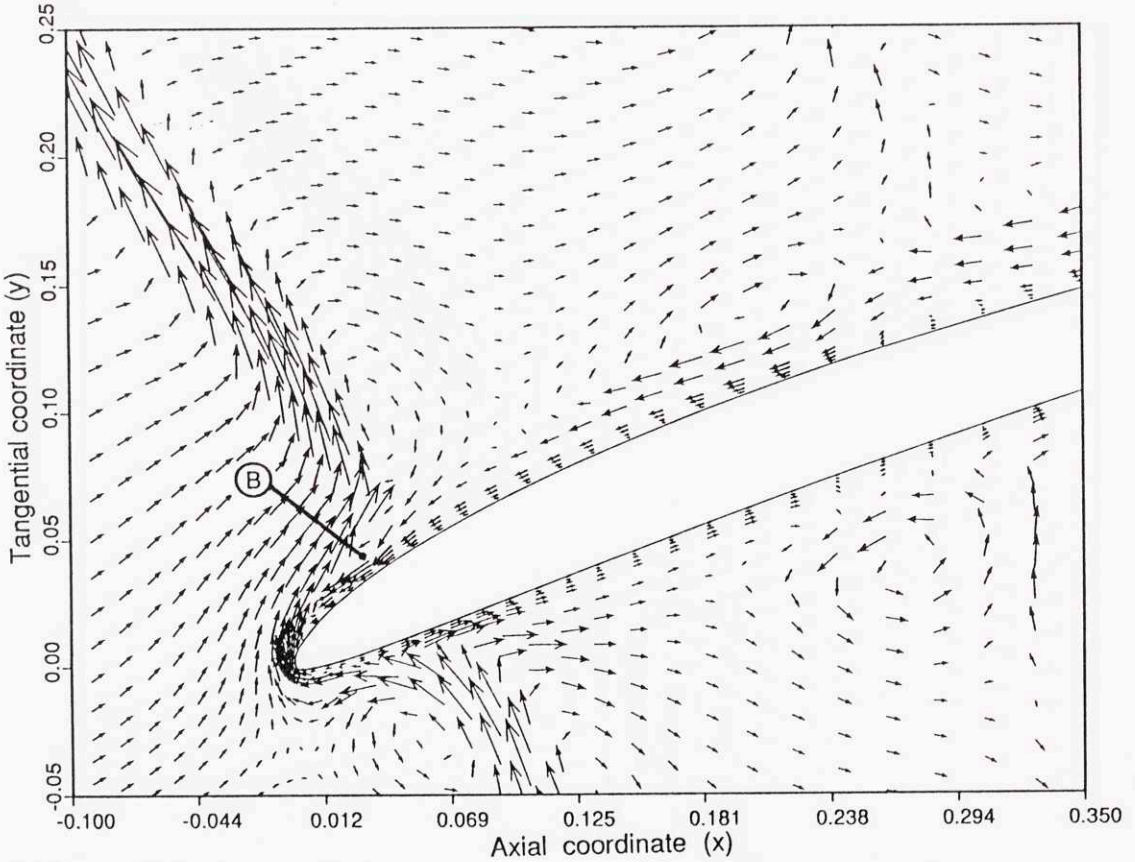

Fig.3.7d. Disturbance velocity vectors corresponding to the above vorticity contours.

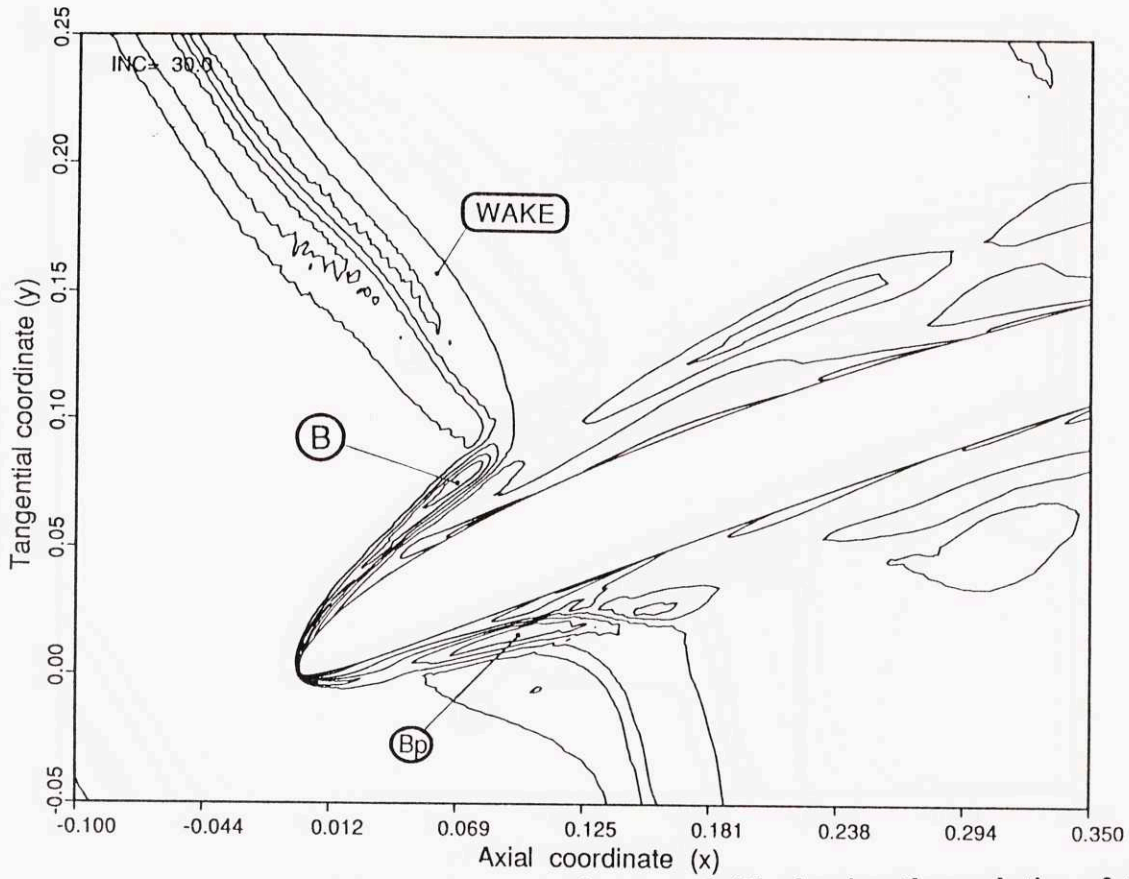

Fig.3.7e. Disturbance vorticity contours at time $t_0 + 0.4T$, showing the evolution of the B-region into a B-vortex.

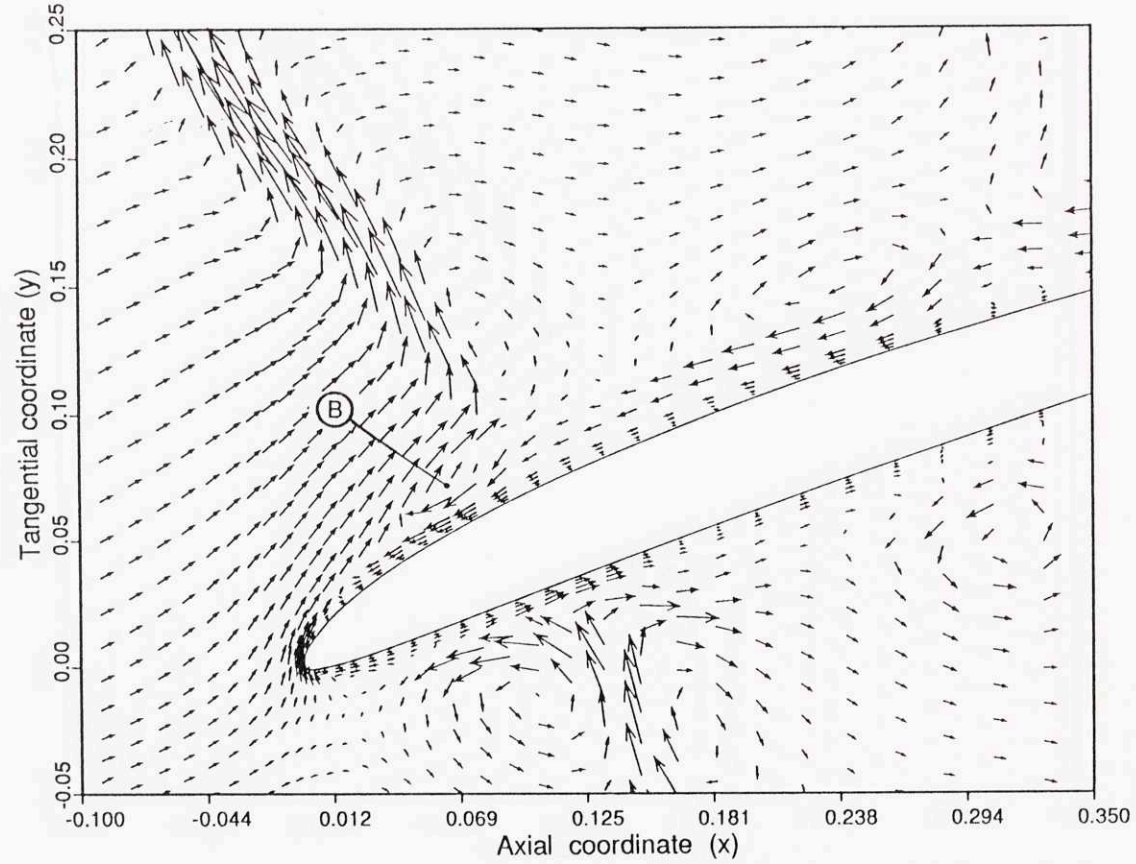

Fig.3.7f. Disturbance velocity vectors corresponding to the above vorticity contours.

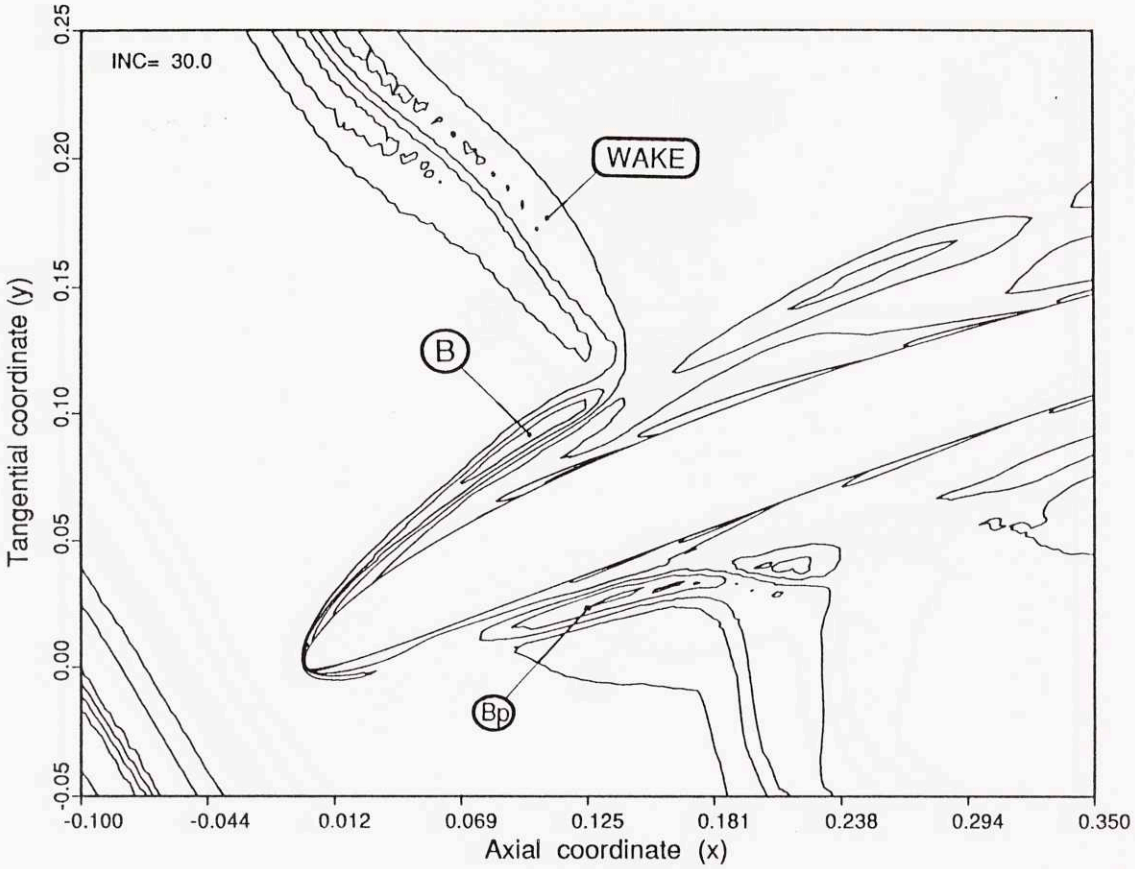

Fig.3.7g. Disturbance vorticity contours at time $t_0 + 0.6T$, showing the evolution of the B-region into a B-vortex.

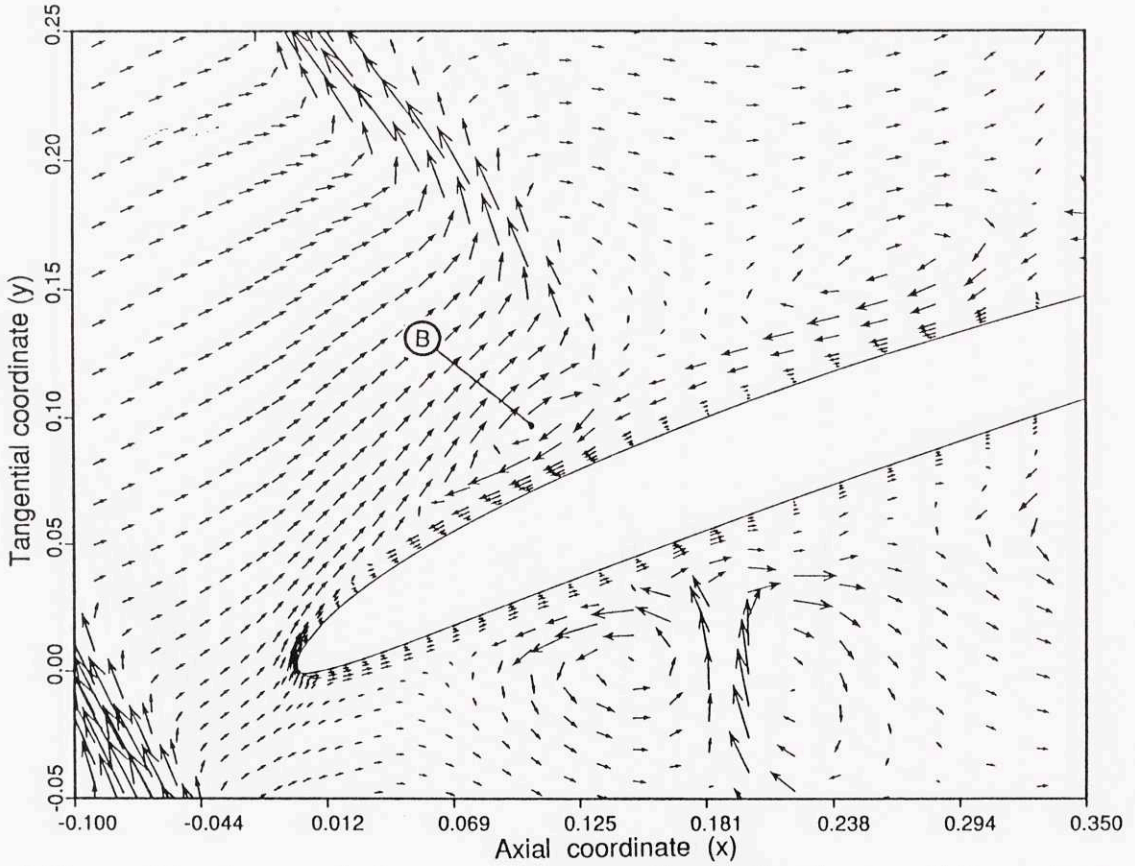

Fig.3.7h. Disturbance velocity vectors corresponding to the above vorticity contours.

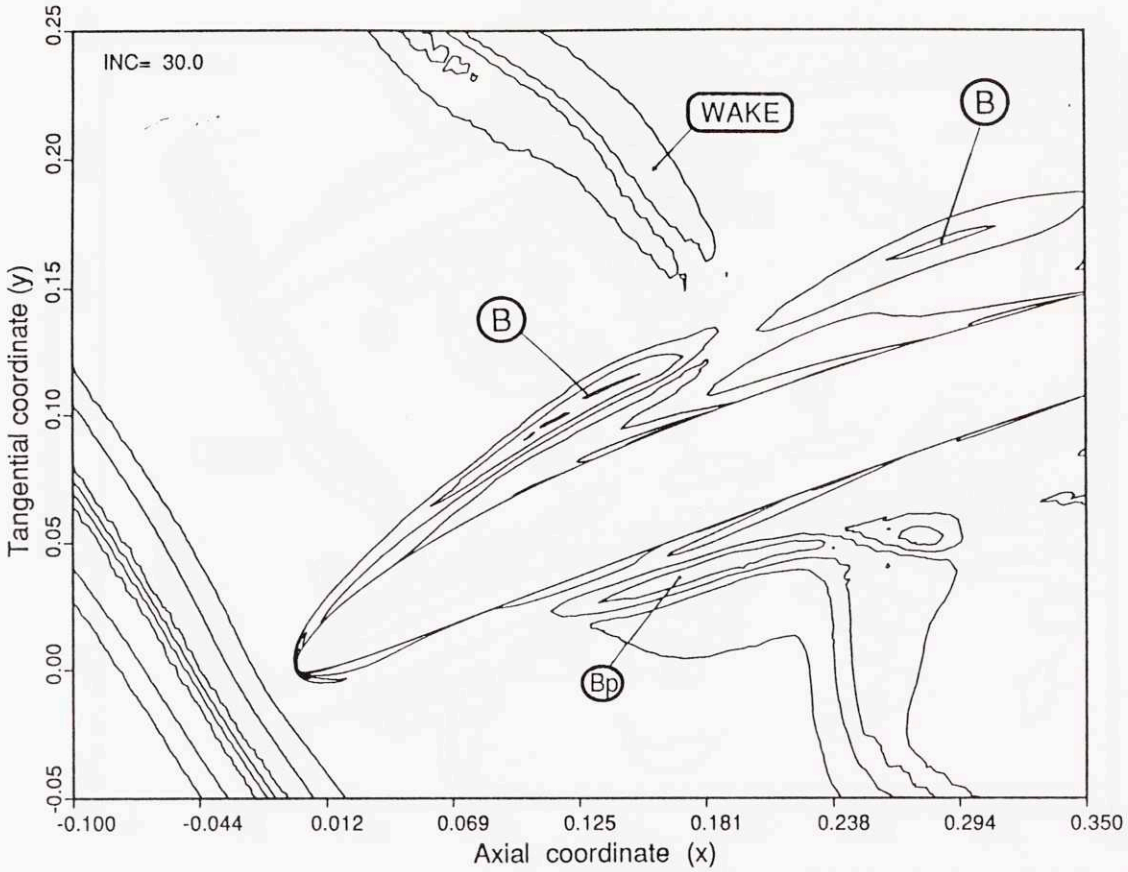

Fig.3.7i. Disturbance vorticity contours at time $t_0 + 0.8T$, showing the evolution of the B-region into a B-vortex.

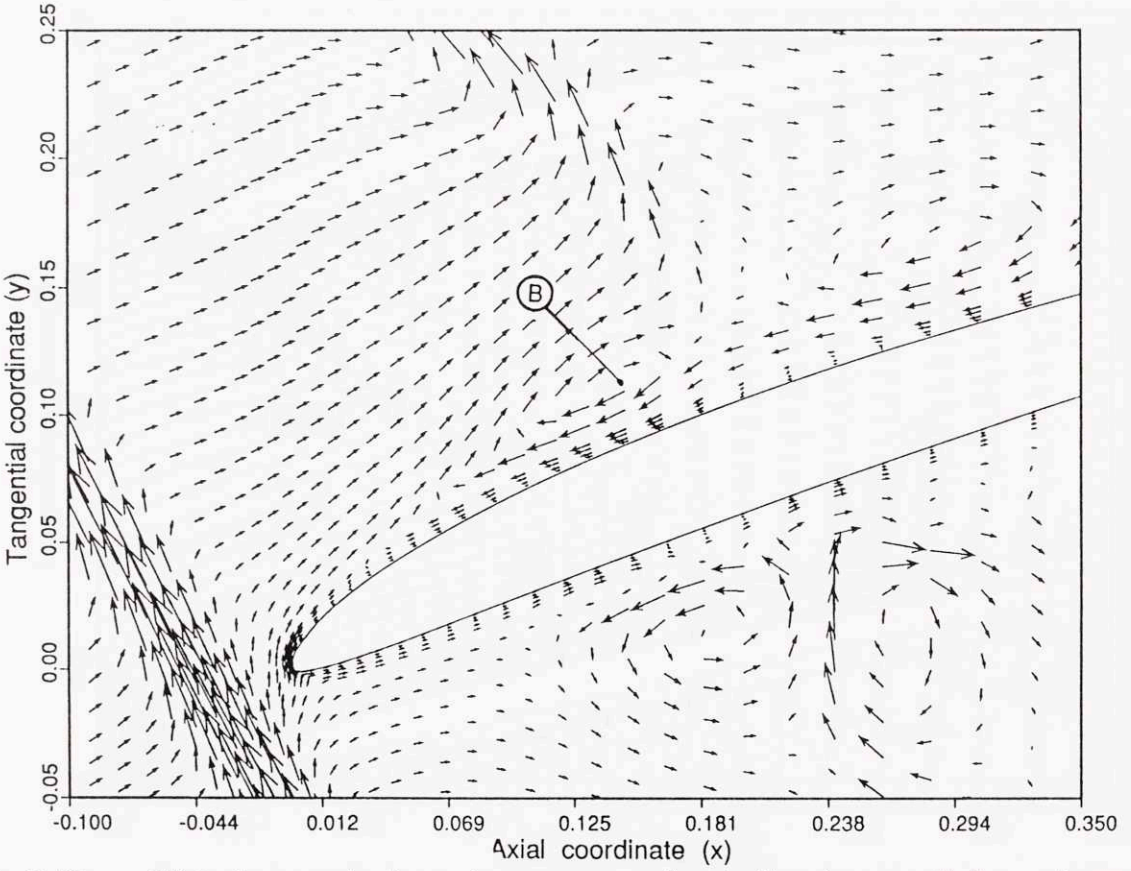

Fig.3.7j. Disturbance velocity vectors corresponding to the above vorticity contours.

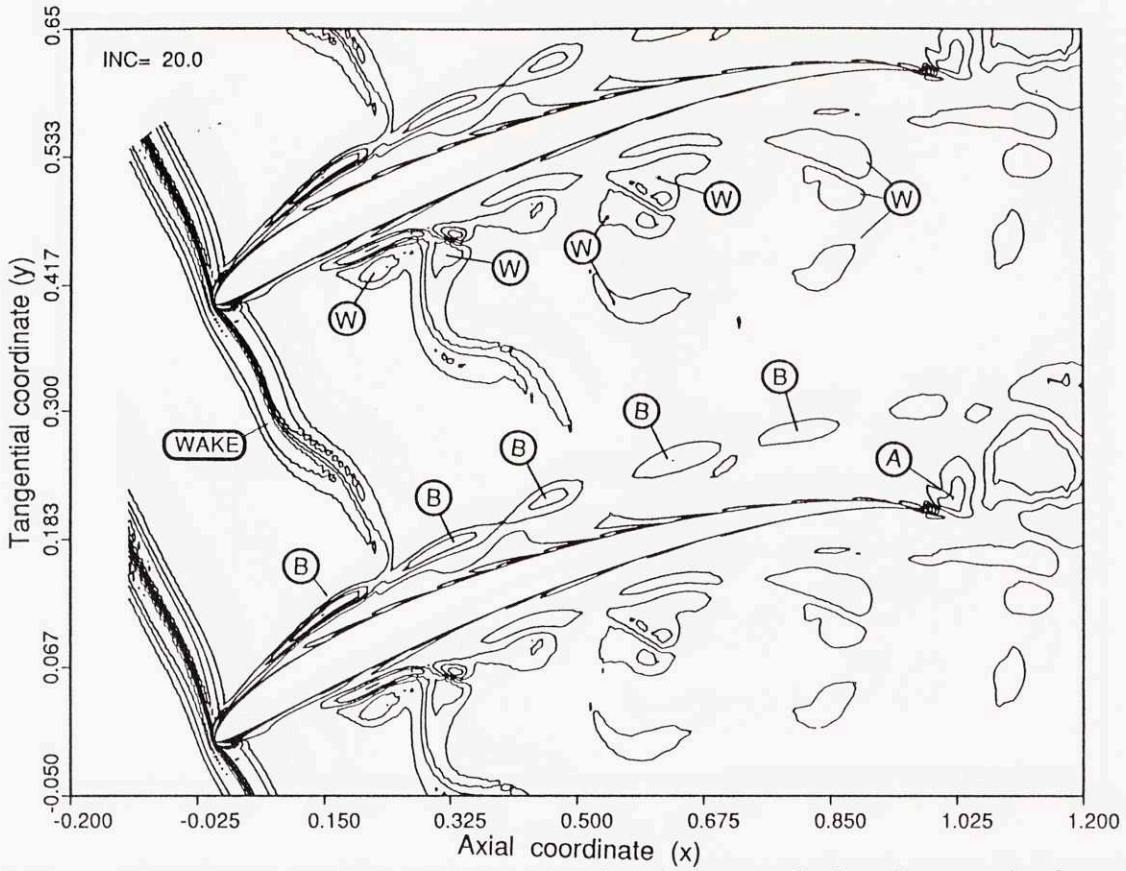

Fig.3.8a. Disturbance vorticity contours showing the unsteady flow features in the stator passage at time t_0.

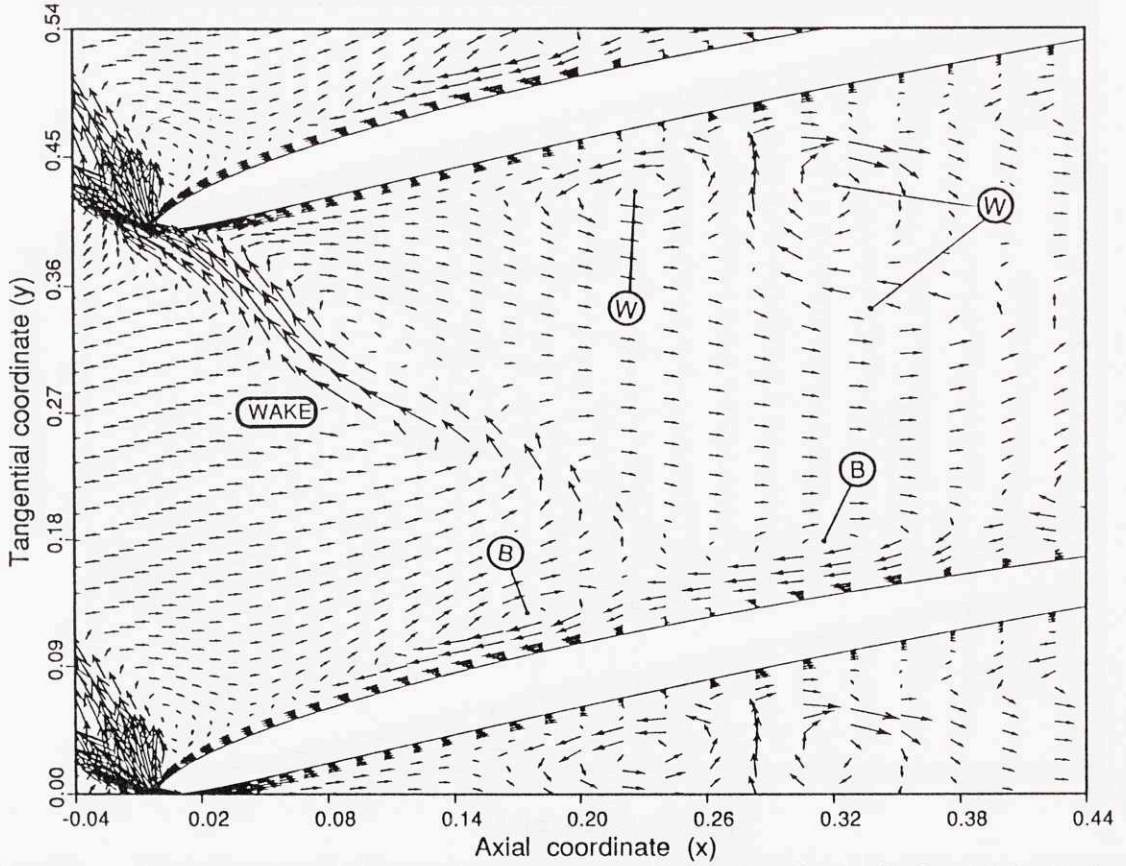

Fig.3.8b. Disturbance velocity vectors at time t_0, showing the evolution of the wake into counter-rotating vortices.

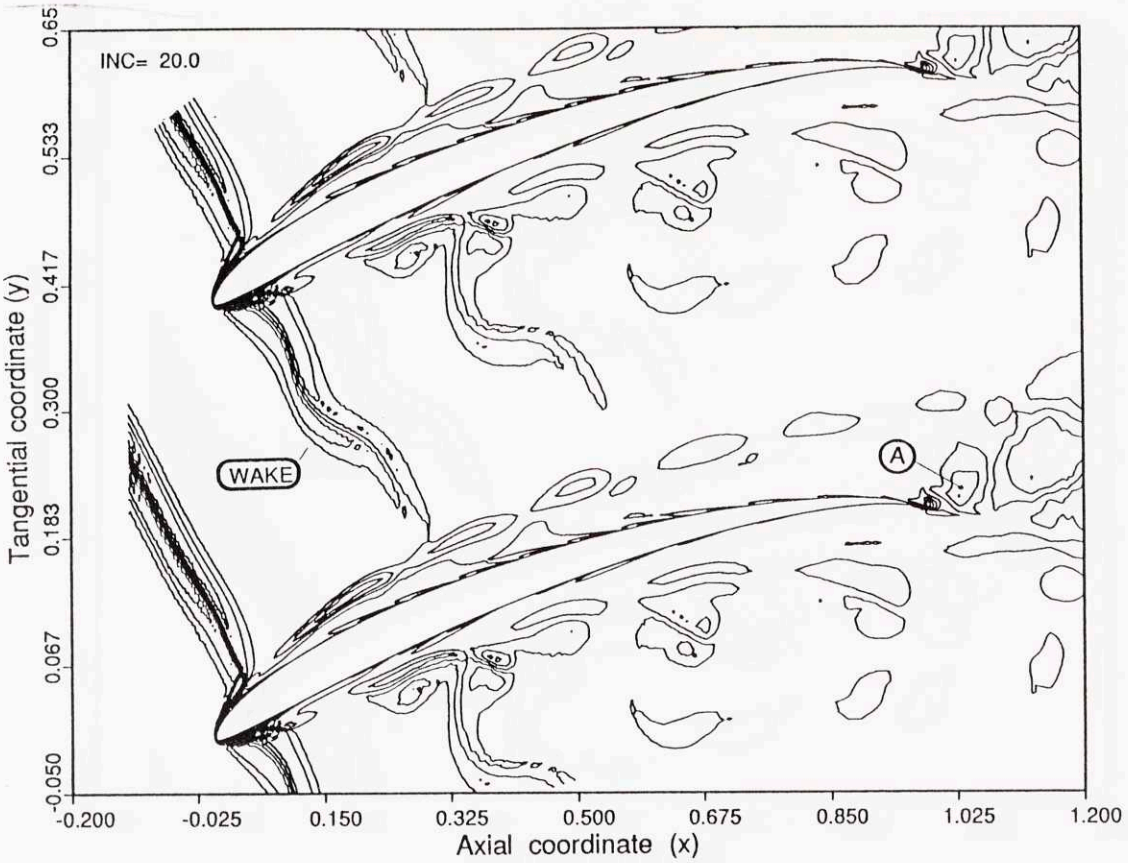

Fig.3.8c. Disturbance vorticity contours showing the unsteady flow features in the stator passage at time $t_0 + 0.2T$.

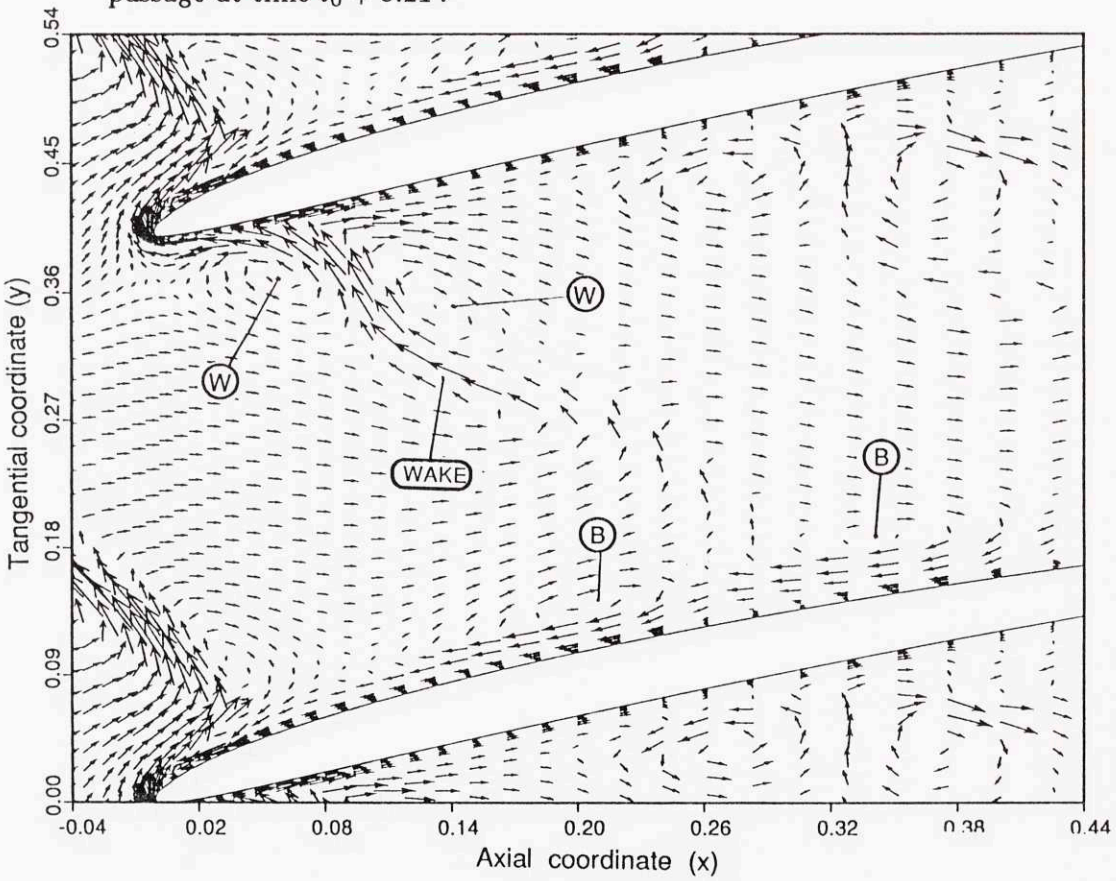

Fig.3.8d. Disturbance velocity vectors at time $t_0 + 0.2T$, showing the evolution of the wake into counter-rotating vortices.

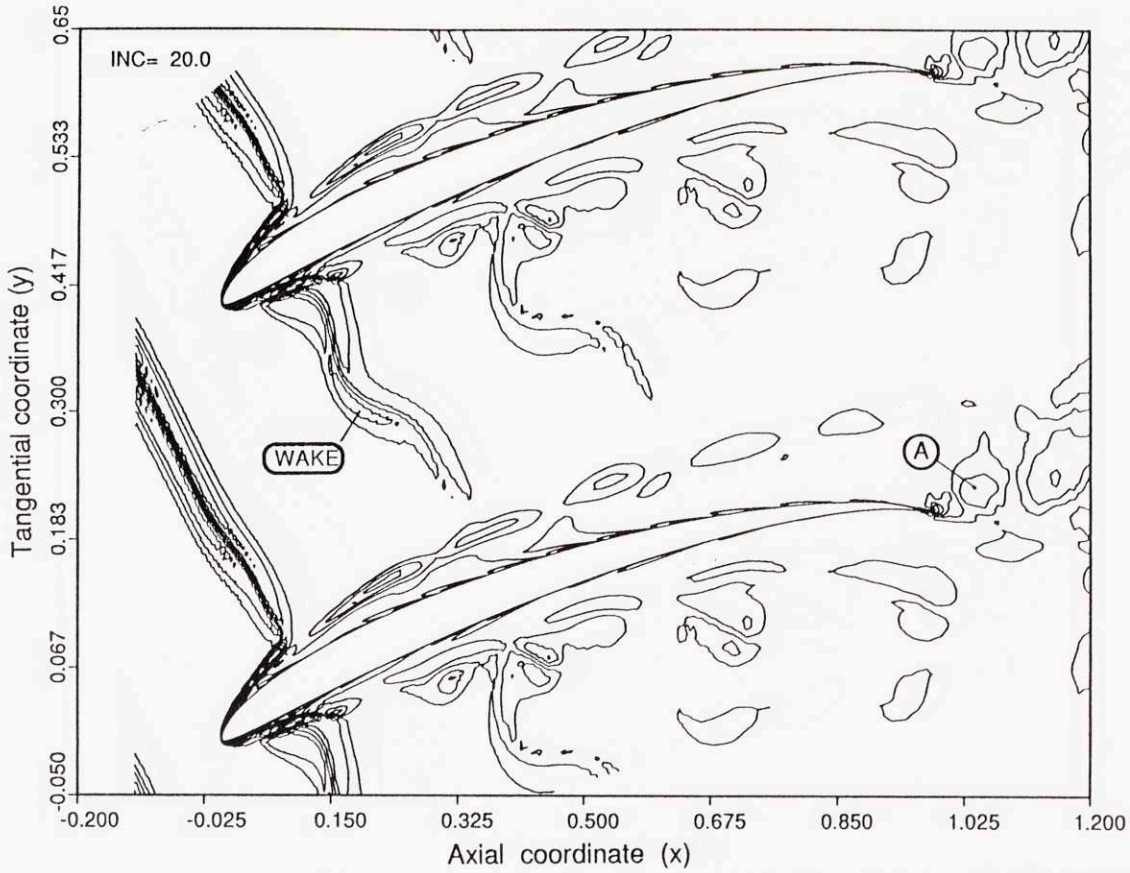

Fig.3.8e. Disturbance vorticity contours showing the unsteady flow features in the stator passage at time $t_0 + 0.4T$.

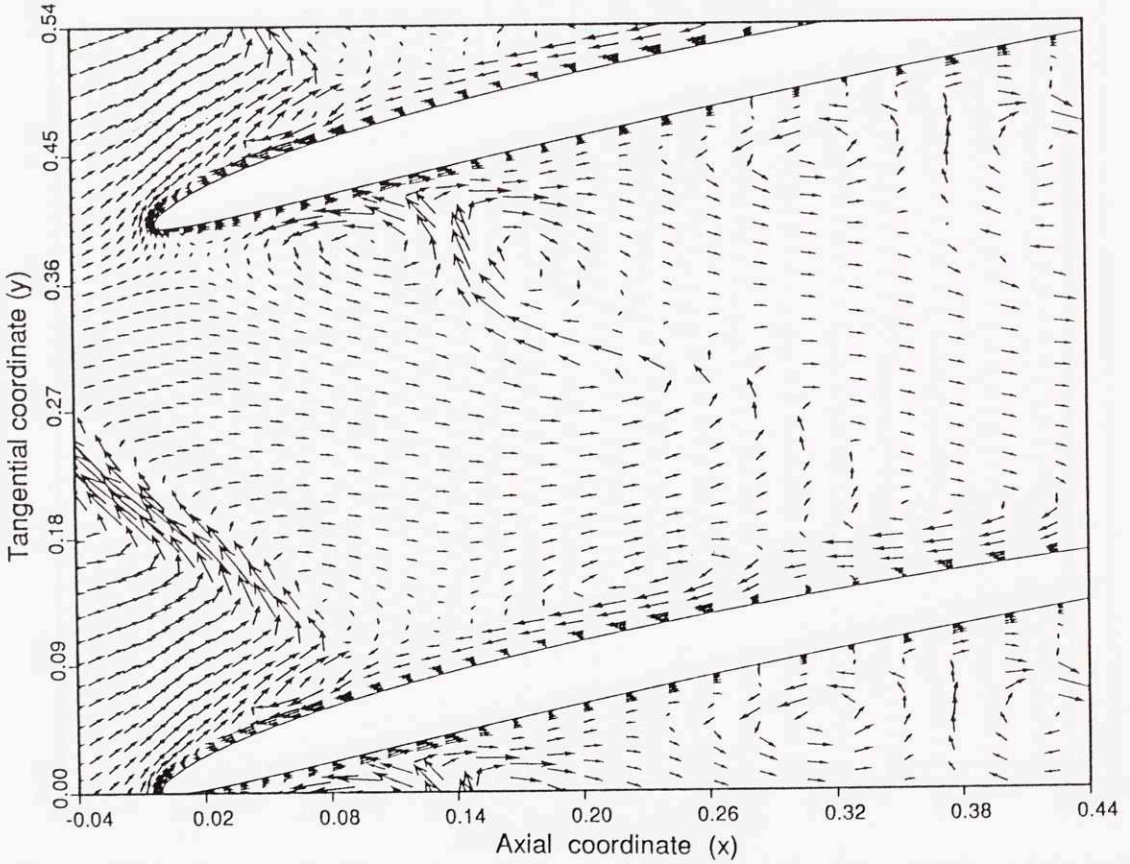

Fig.3.8f. Disturbance velocity vectors at time $t_0 + 0.4T$, showing the evolution of the wake into counter-rotating vortices.

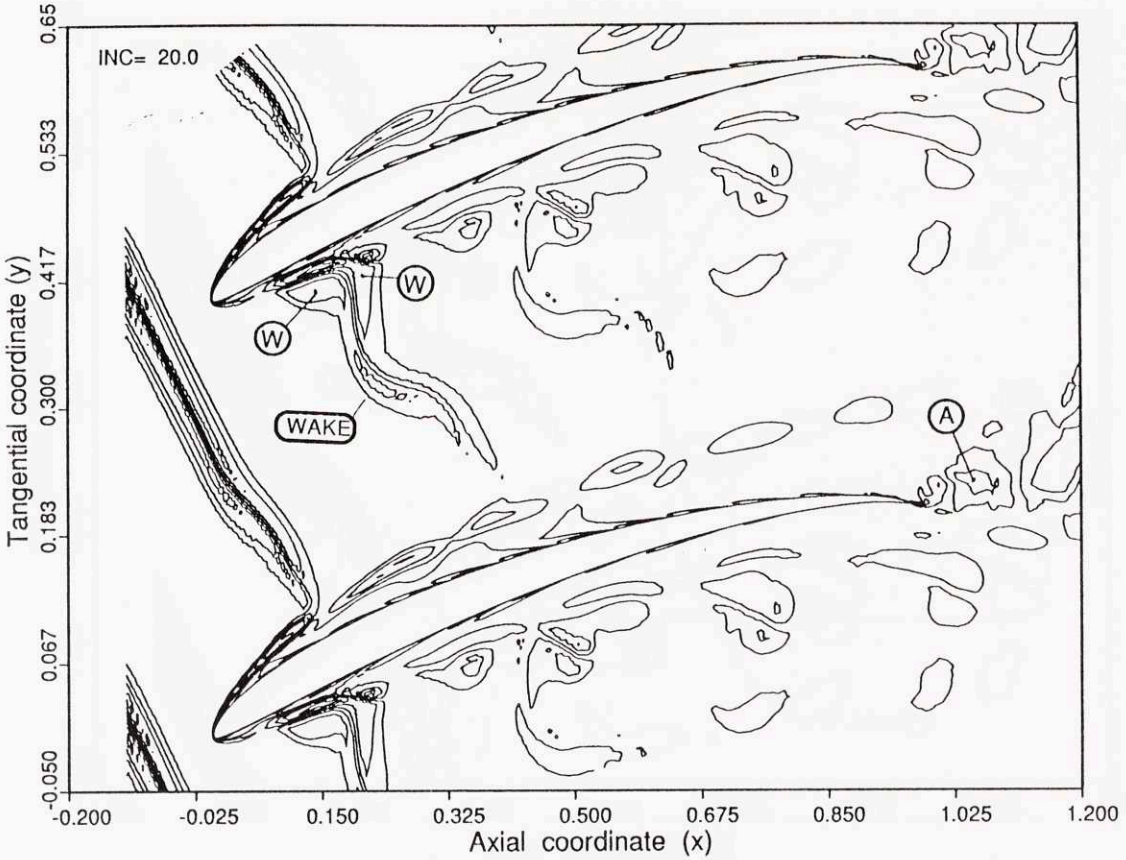

Fig.3.8g. Disturbance vorticity contours showing the unsteady flow features in the stator passage at time $t_0 + 0.6T$.

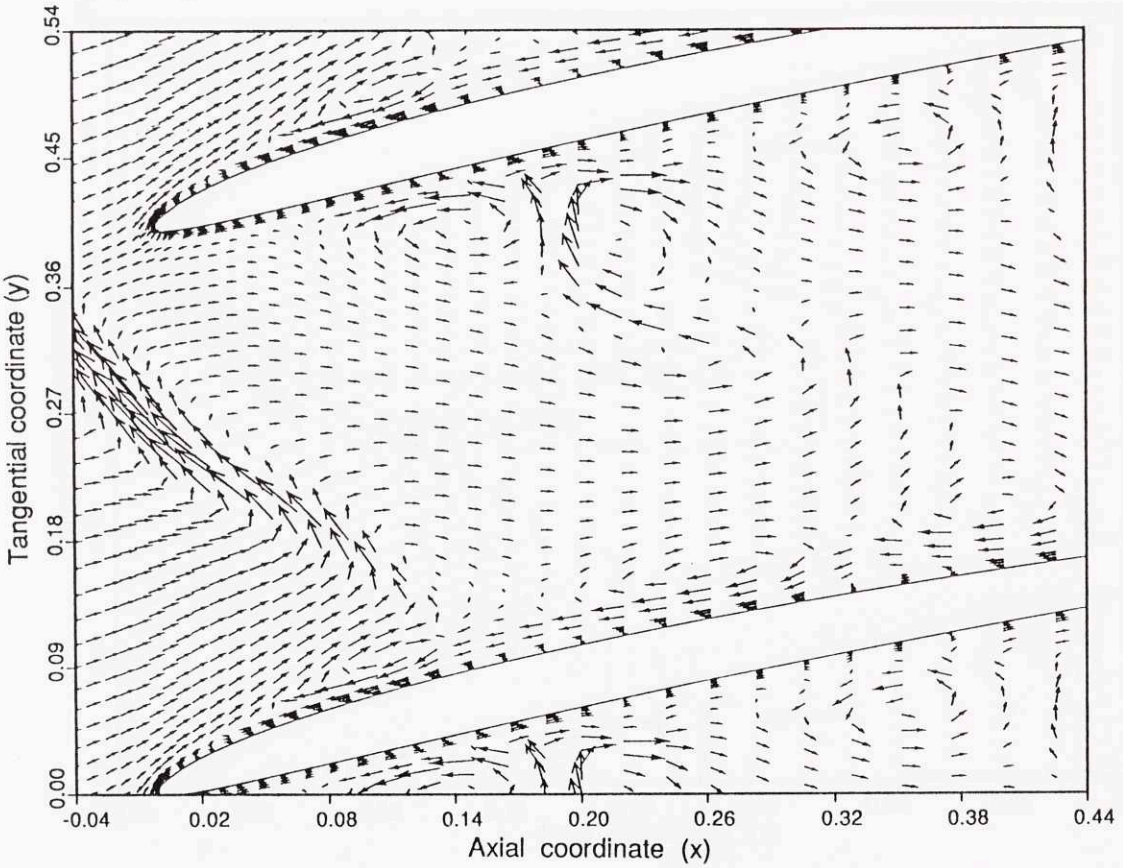

Fig.3.8h. Disturbance velocity vectors at time $t_0 + 0.6T$, showing the evolution of the wake into counter-rotating vortices.

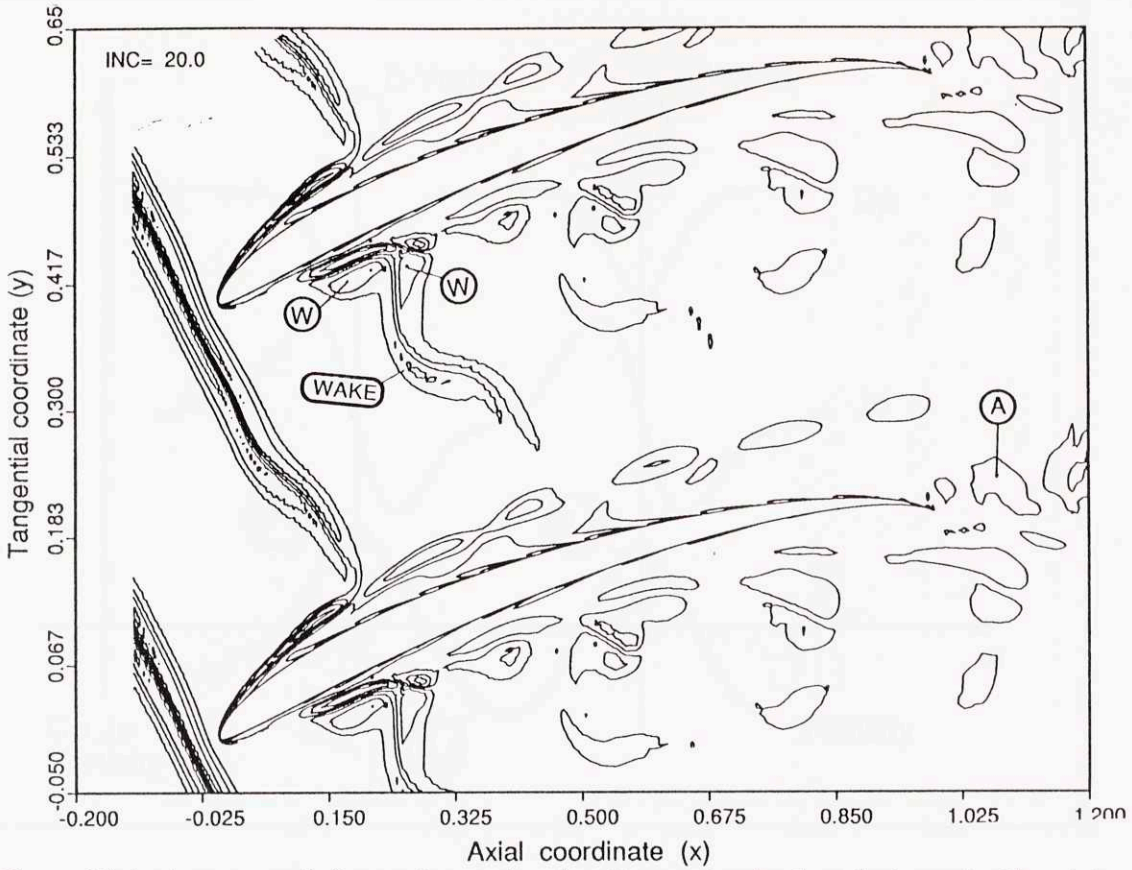

Fig.3.8i. Disturbance vorticity contours showing the unsteady flow features in the stator passage at time $t_0 + 0.8T$.

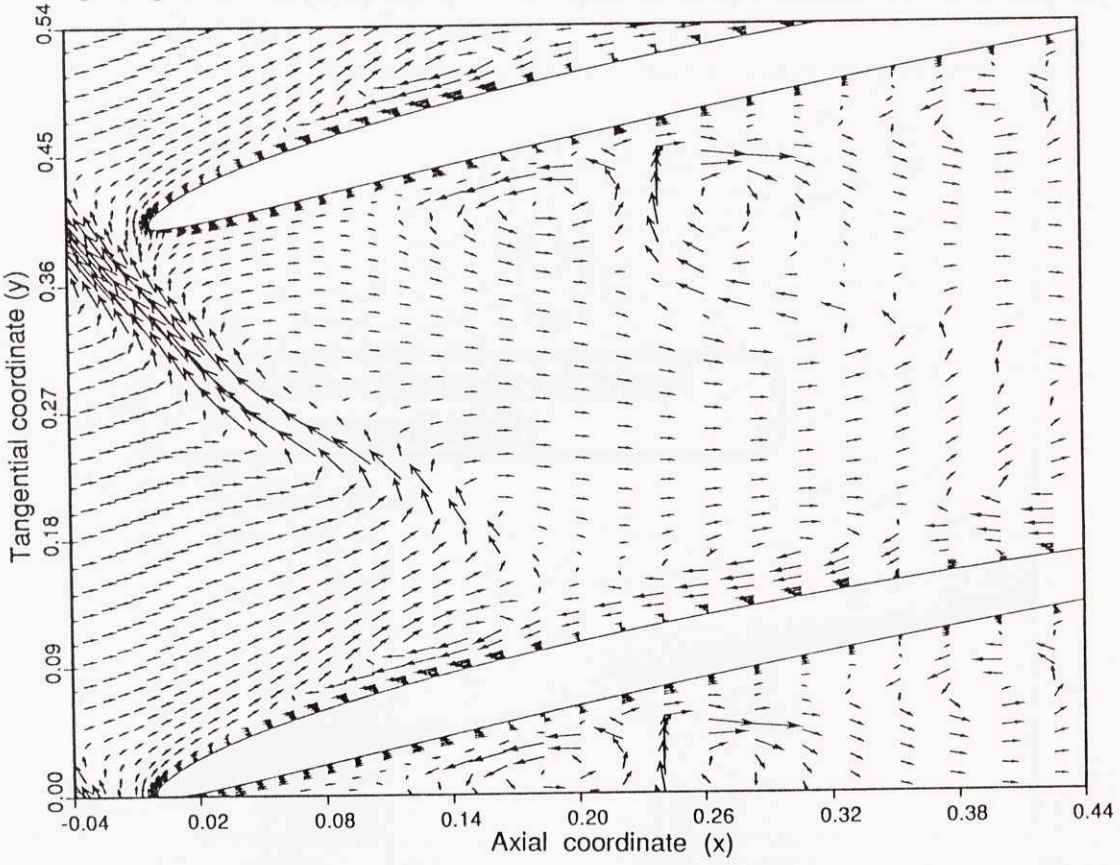

Fig.3.8j. Disturbance velocity vectors at time $t_0 + 0.8T$, showing the evolution of the wake into counter-rotating vortices.

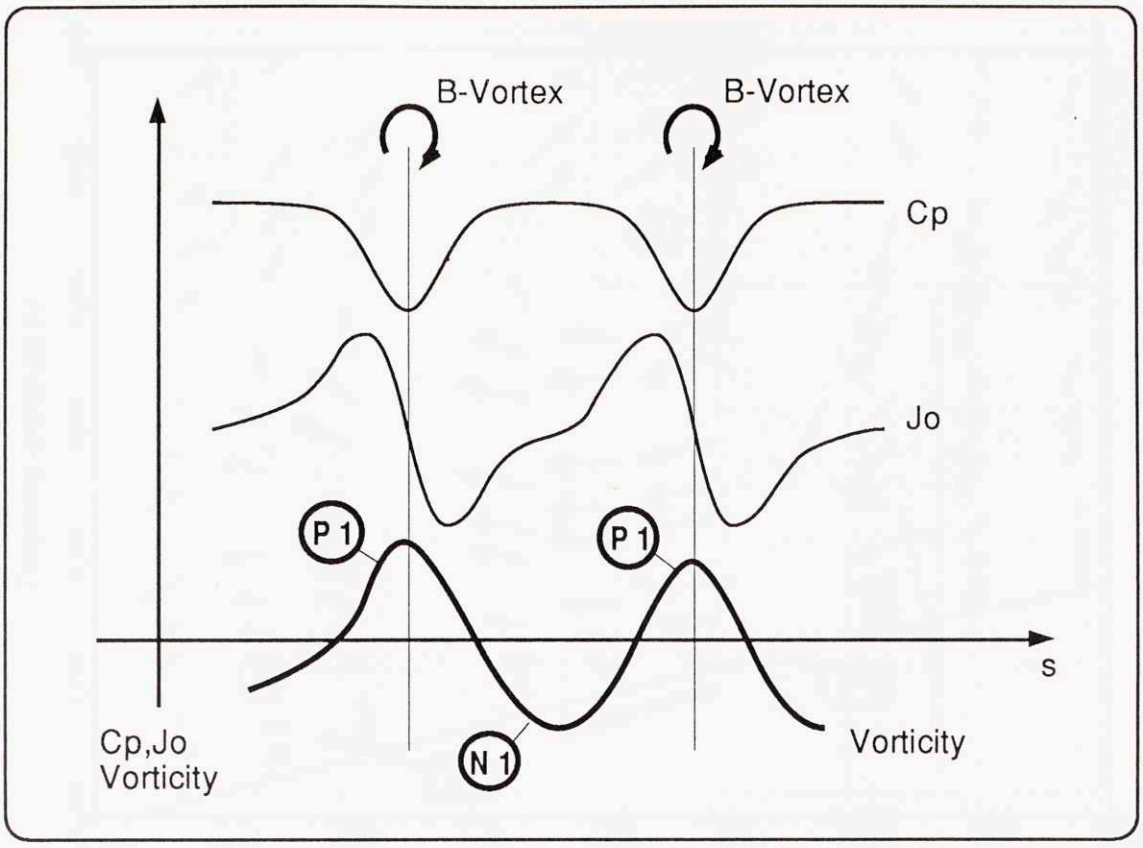

Fig.3.9. Illustration of the mechanism for production of P1 and N1 vortical boundary layer disturbances by the row of B-vortices.

This space has been left blank intentionally

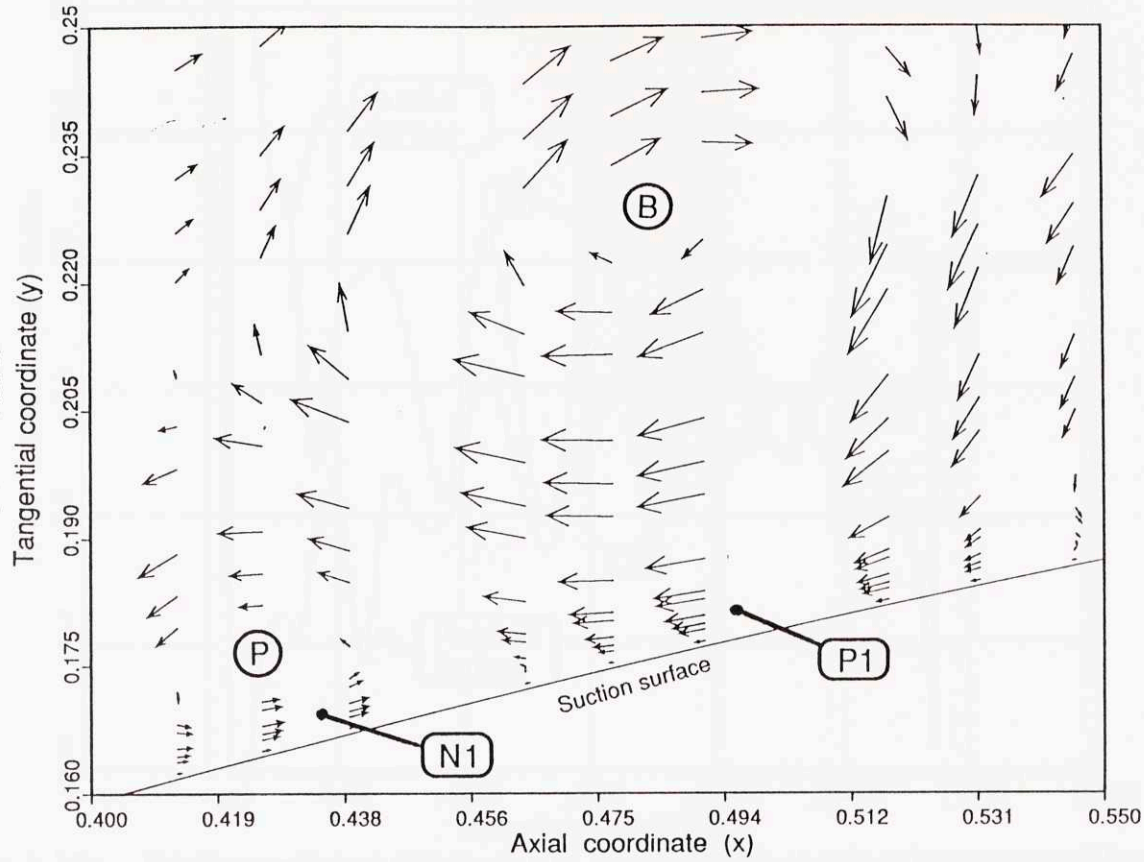

Fig.3.10. Close-up of the disturbance velocity contours in the proximity of a B-vortex and the suction surface, showing (1) a region of reverse disturbance flow and (2) a small P-vortex.

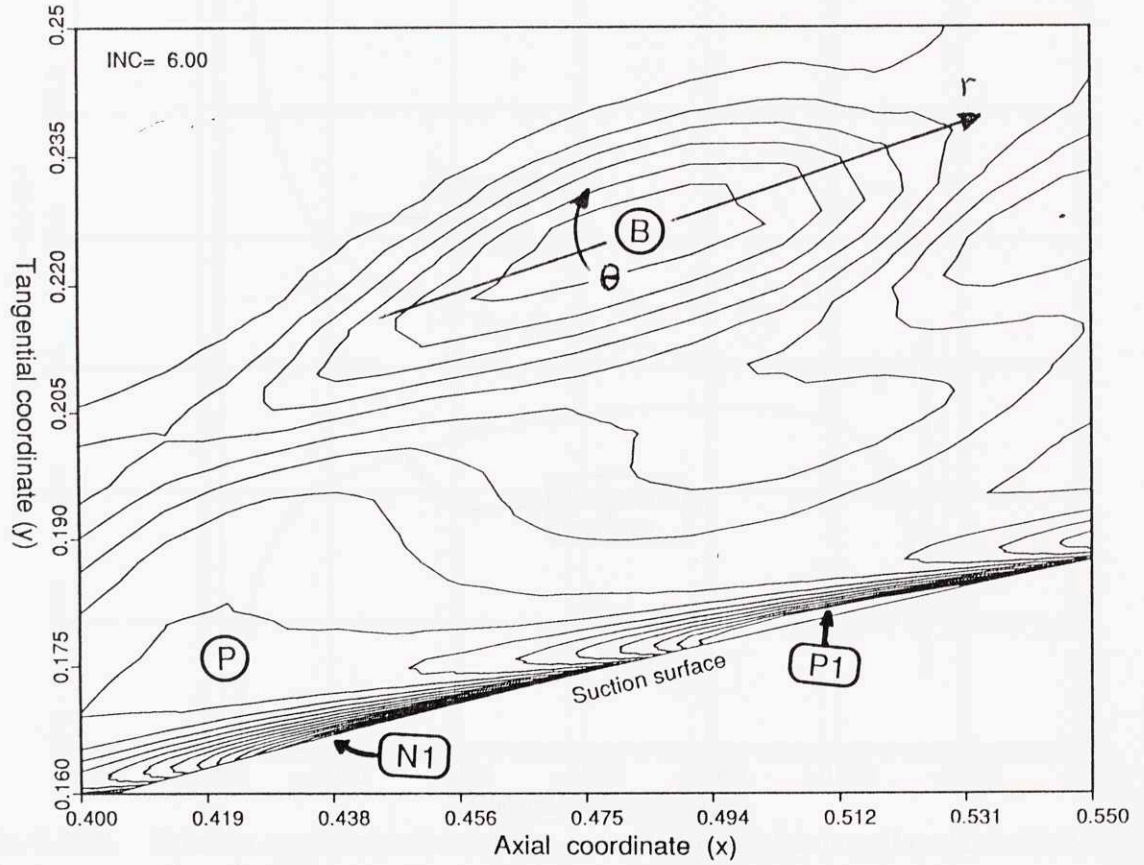

Fig.3.11. Disturbance vorticity contours, corresponding to the above disturbance velocity contours, showing (1) a P1 vortical region and (2) a N1 vortical region.

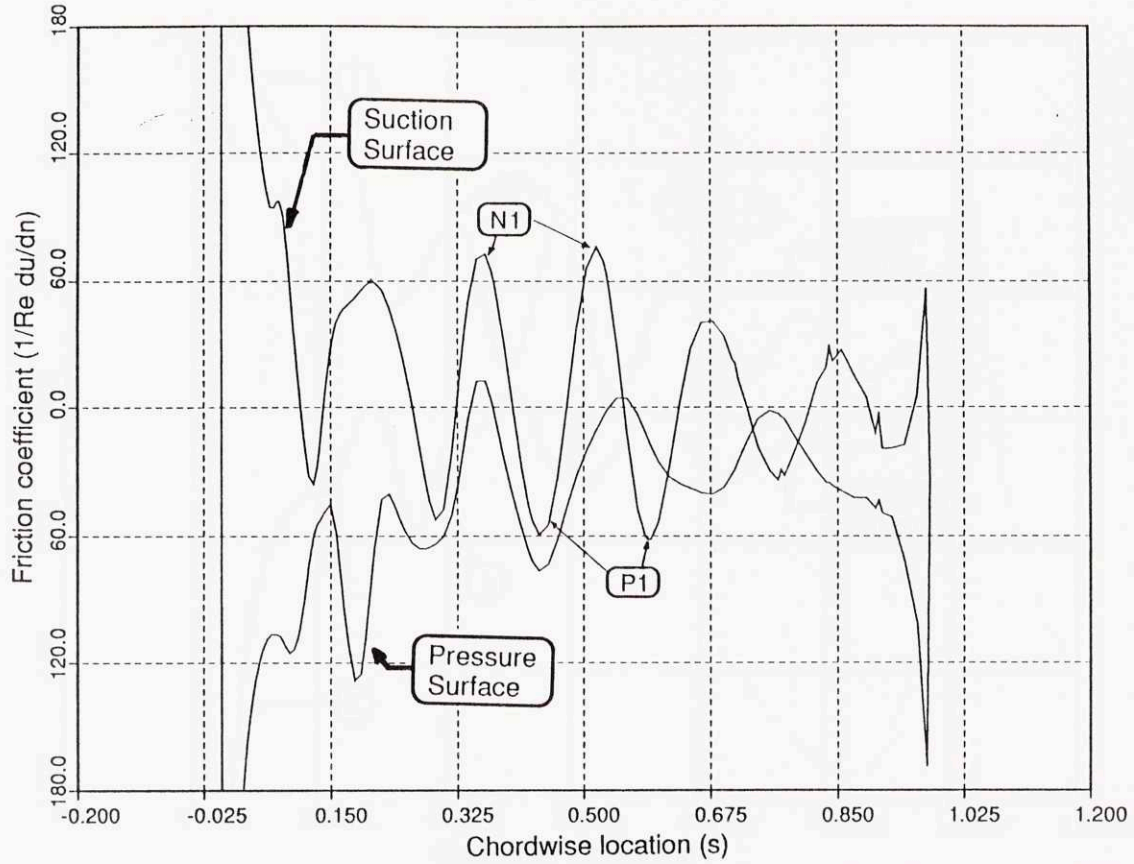

Fig.3.12a. Friction coefficient distribution at time $t_0 + 0.6T$, showing the presence of fluctuations due to the moving opposite-sign P1 and N1 disturbance vortical regions.

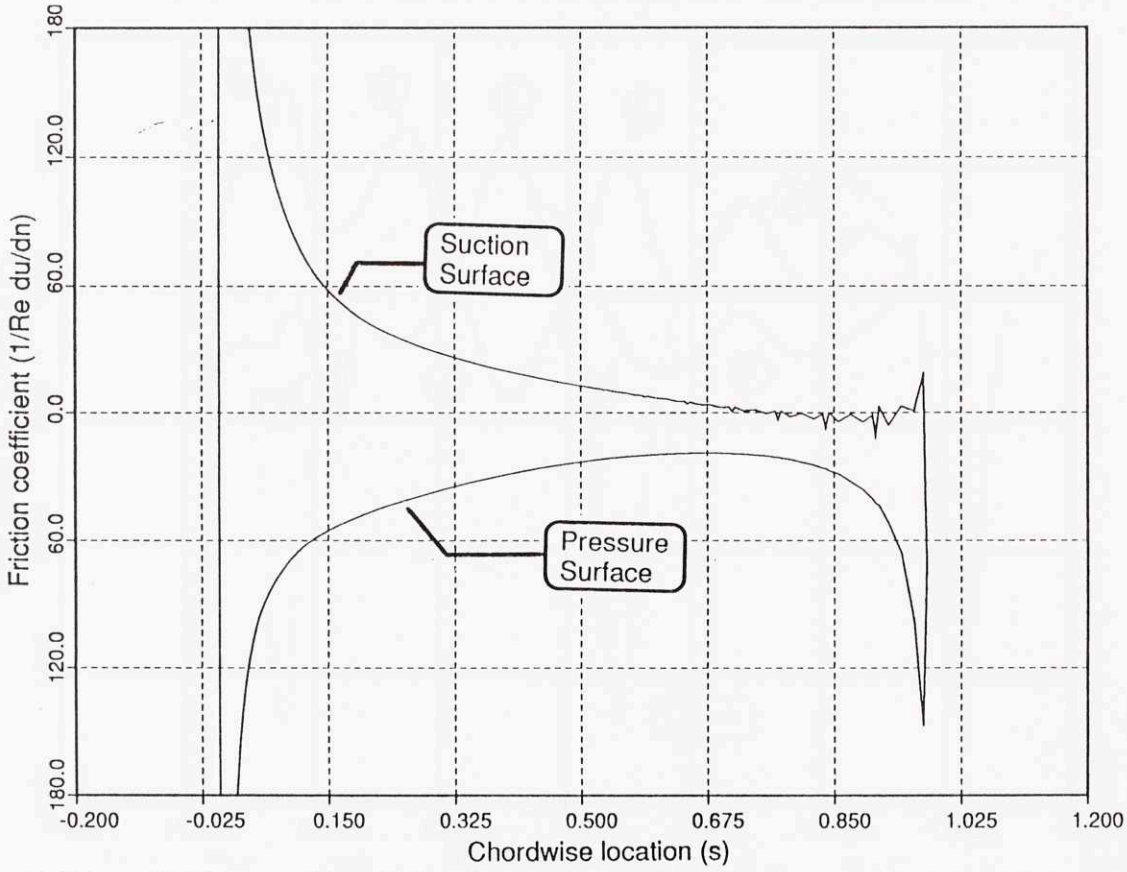

Fig.3.12b. Friction coefficient distribution in undisturbed laminar flow (Re=10,000). This figure is for comparison with Figure 3.12a.

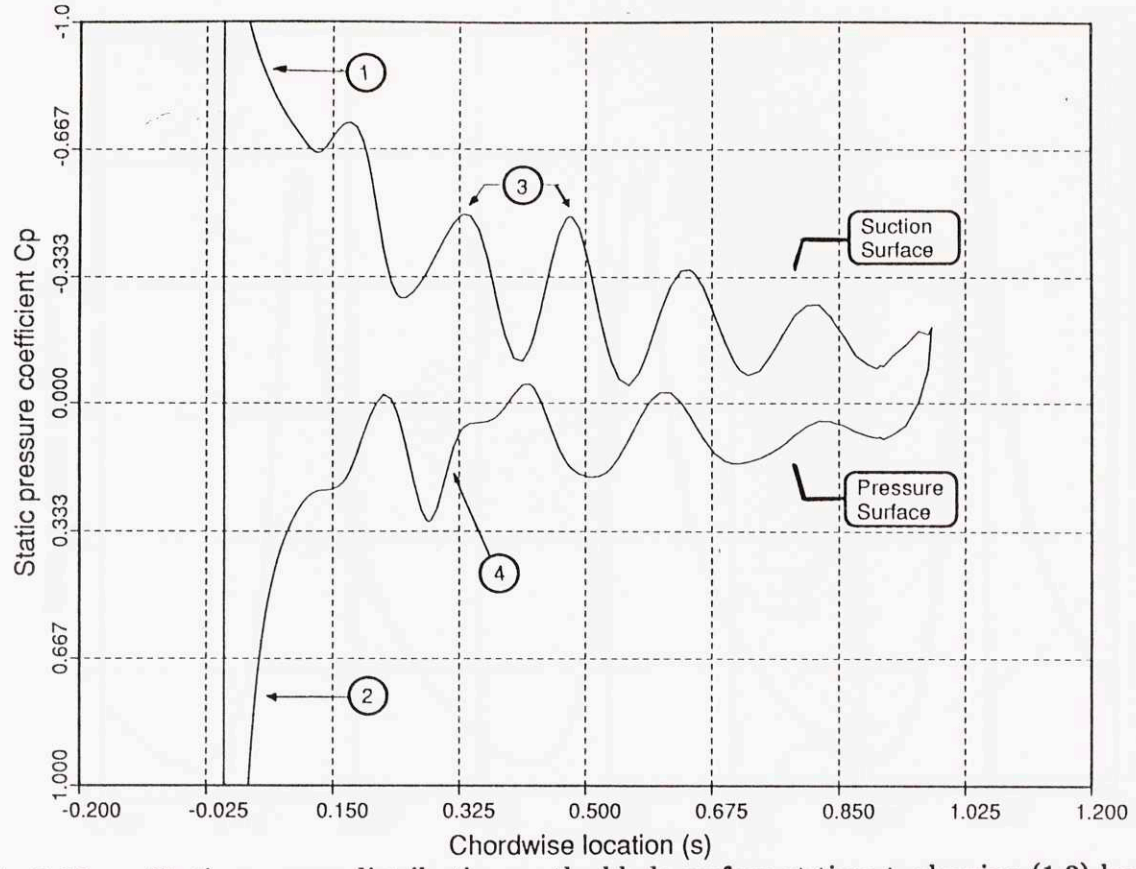

Fig.3.13a. Static pressure distribution on the blade surface at time t_0 showing (1,2) leading edge pulses, (3) S.S. depressions, and (4) P.S. disturbances.

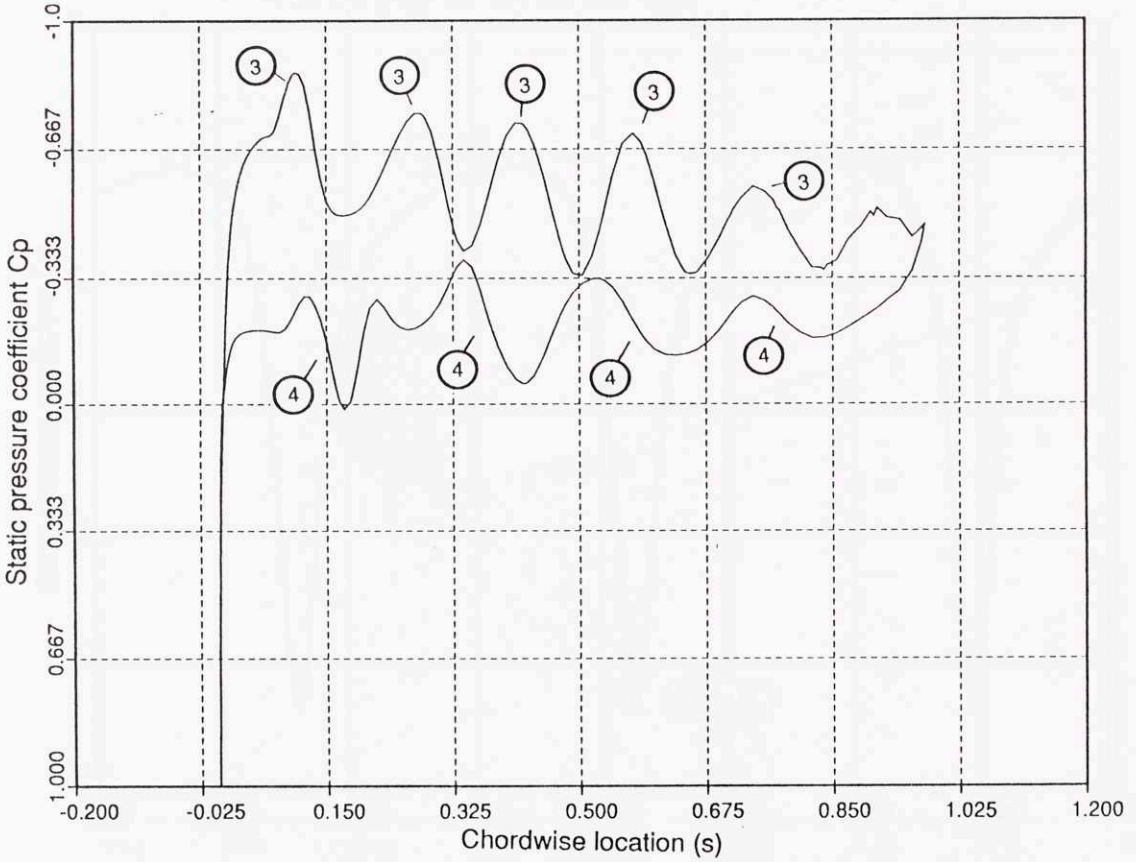

Fig.3.13b. Static pressure distribution on the blade surface at time $t_0 + 0.6T$ showing (3) suction surface depressions, and (4) pressure surface disturbances.

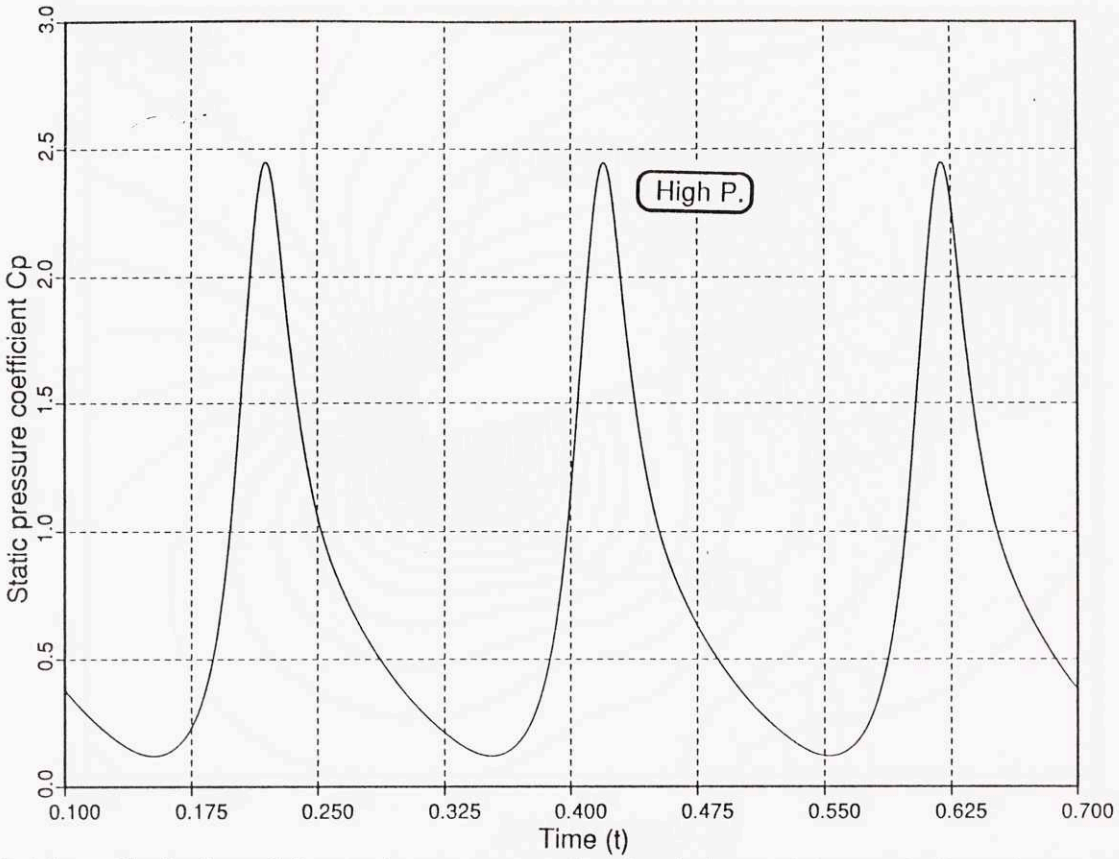

Fig.3.14a. Evolution of the static pressure at the chordwise position x=0.02 on the pressure surface of the leading edge, showing the positive pressure pulse.

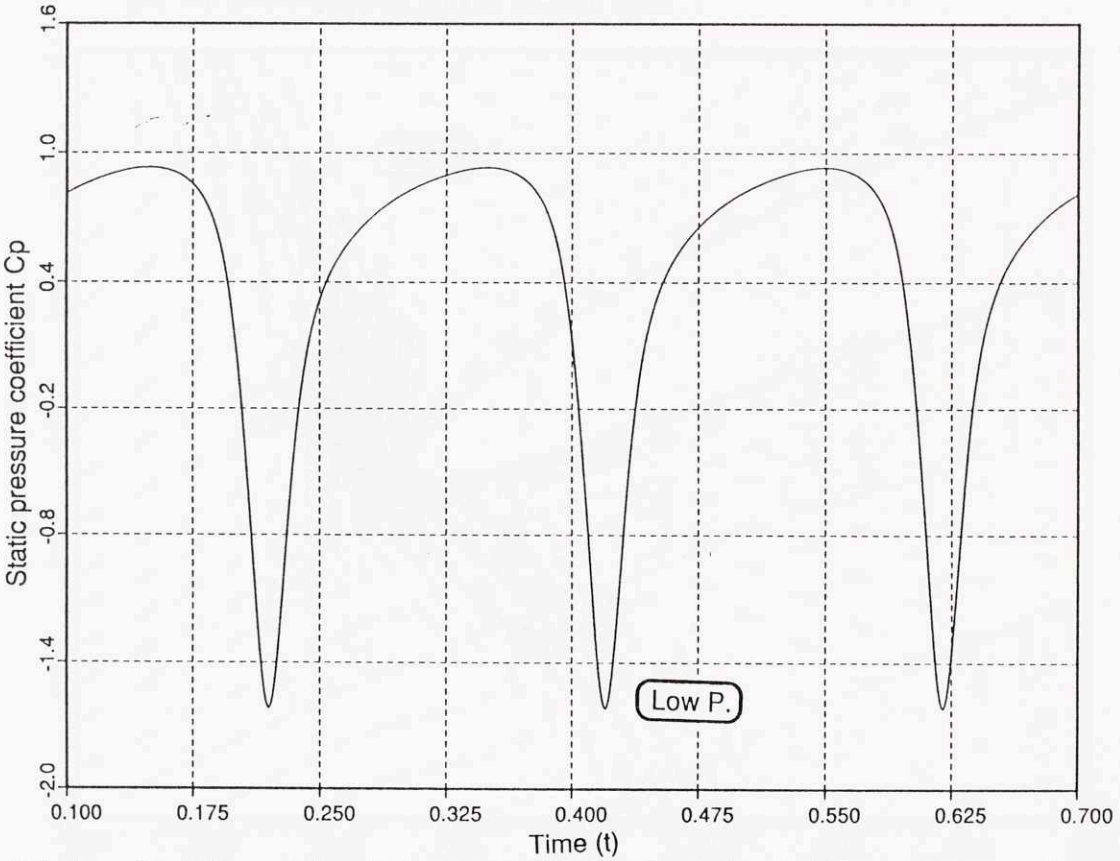

Fig.3.14b. Evolution of the static pressure at the chordwise position x=0.015 on the suction surface of the leading edge, showing the negative pressure pulse.

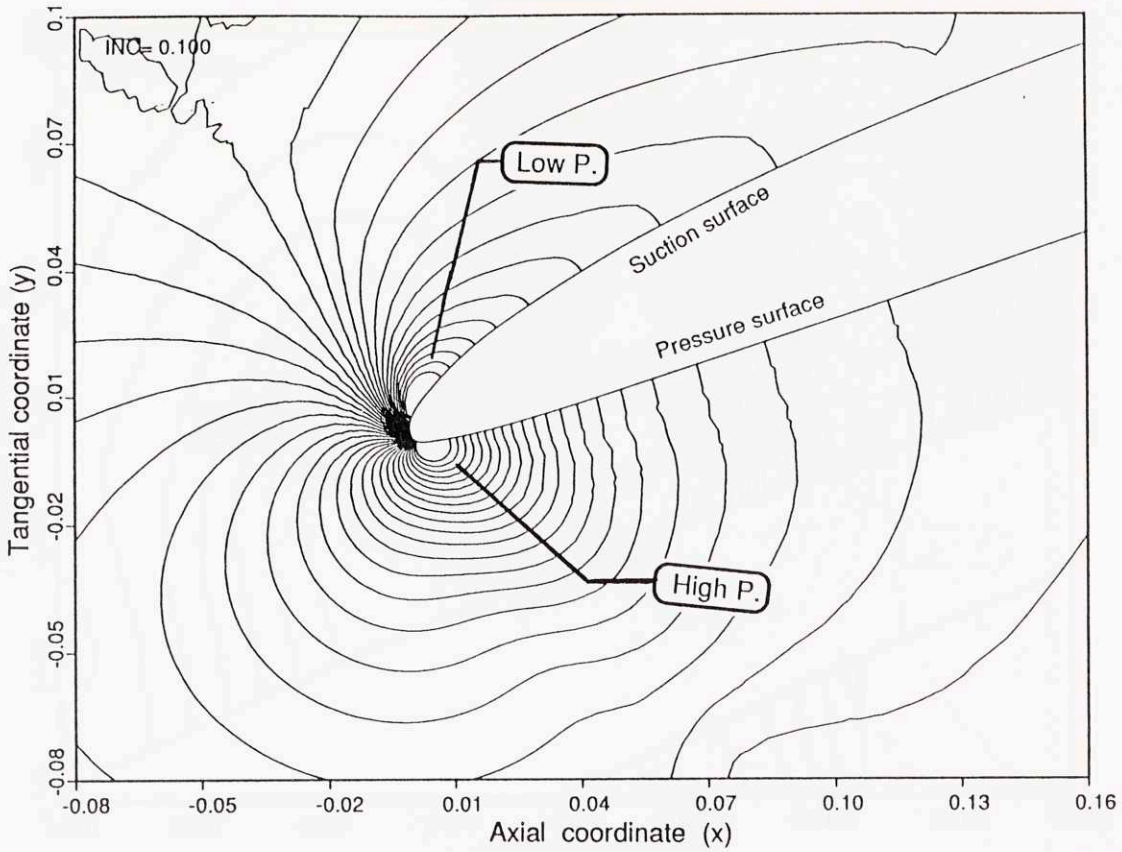

Fig.3.15a. Static pressure contours in the leading edge region upon wake interception (time t_0), showing the production of (1) high pressure peak on the pressure side; and (2) low pressure peak on the suction side.

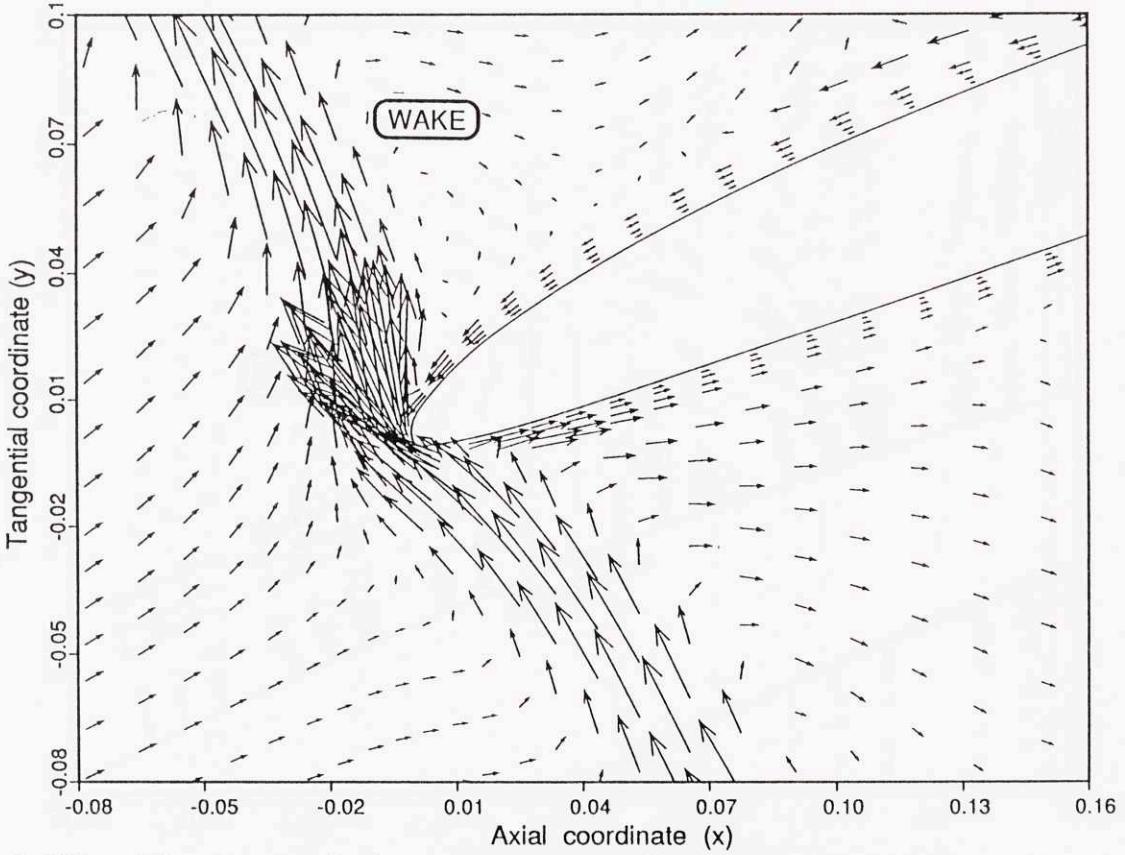

Fig.3.15b. Disturbance velocity vectors corresponding to the above pressure field.

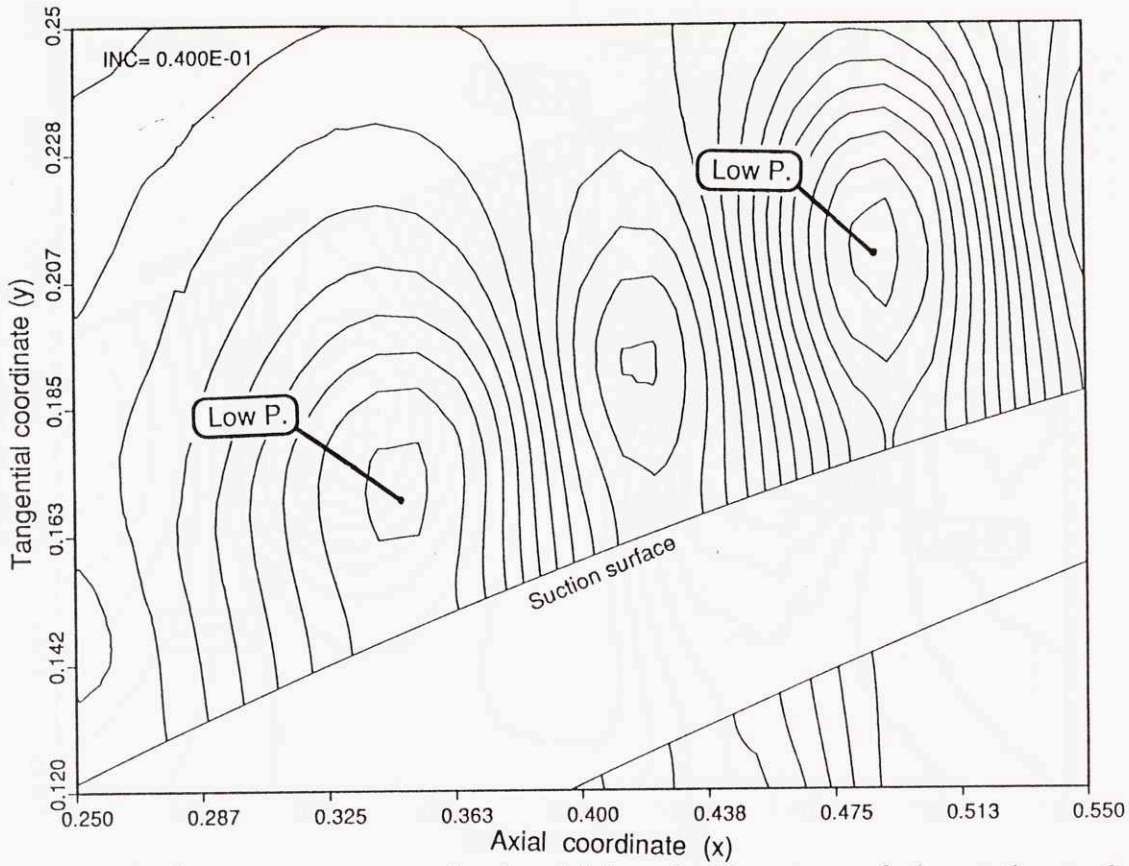

Fig.3.16a. Static pressure contours in the vicinity of a B-vortex and the suction surface. The low-pressure region in the vortex core is perceived as a moving low-pressure disturbance on the suction surface.

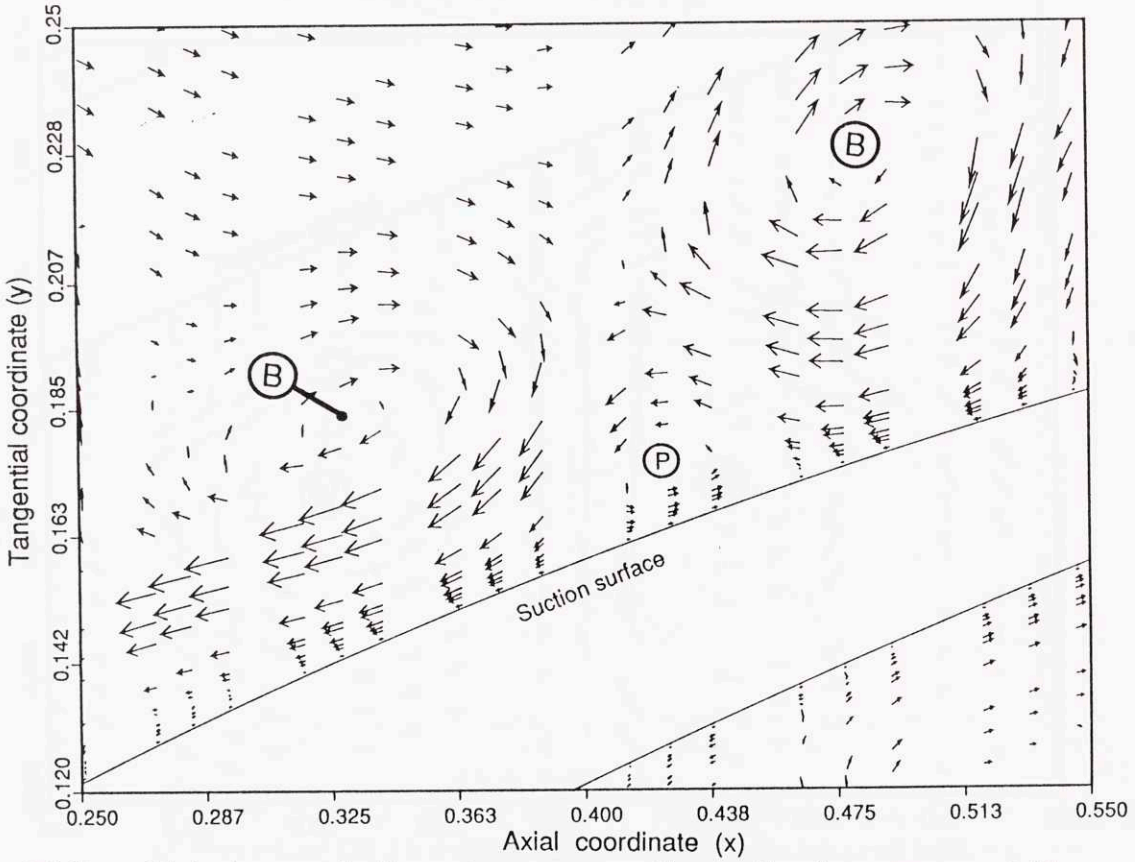

Fig.3.16b. Disturbance velocity vectors corresponding to the above pressure field.

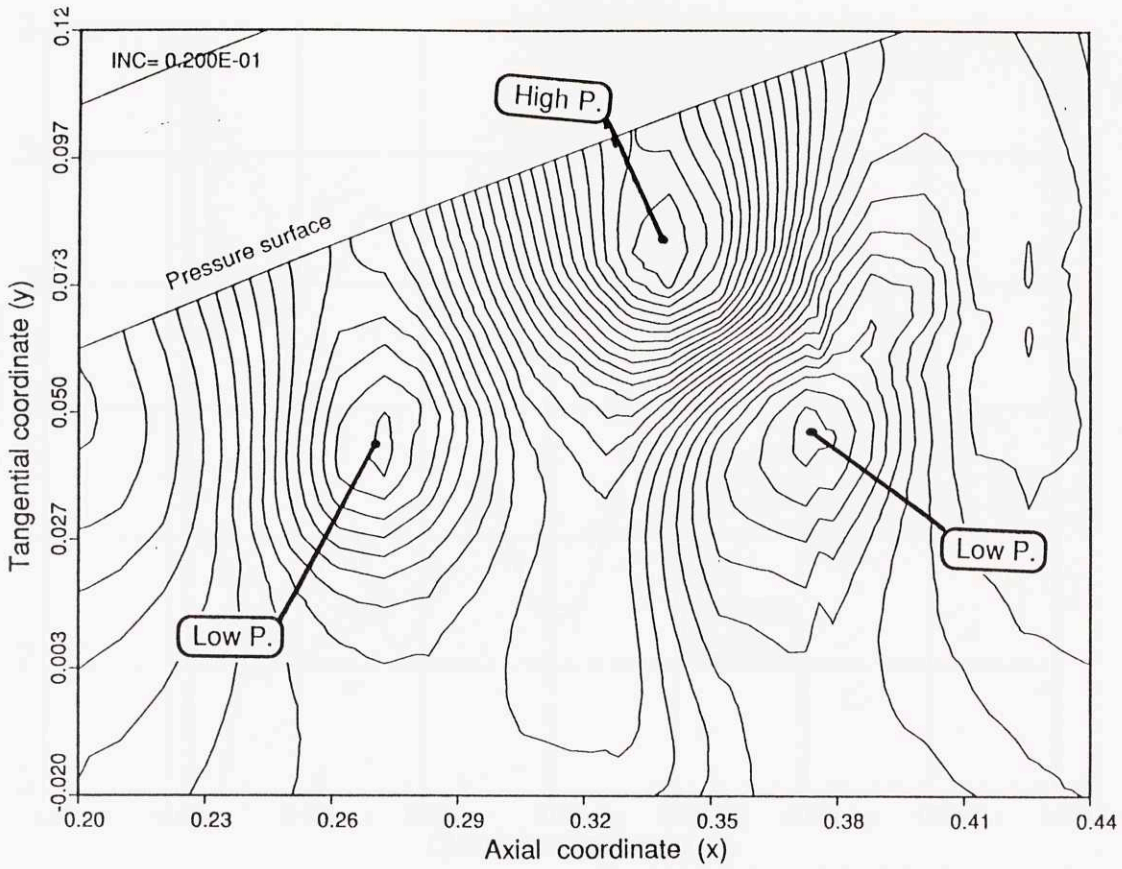

Fig.3.17a. Static pressure contours in the vicinity of a system of counterrotating wake vortices and the pressure surface, showing (1) low-pressure regions associated to the vortex cores; and (2) high-pressure region associated to stagnation flow.

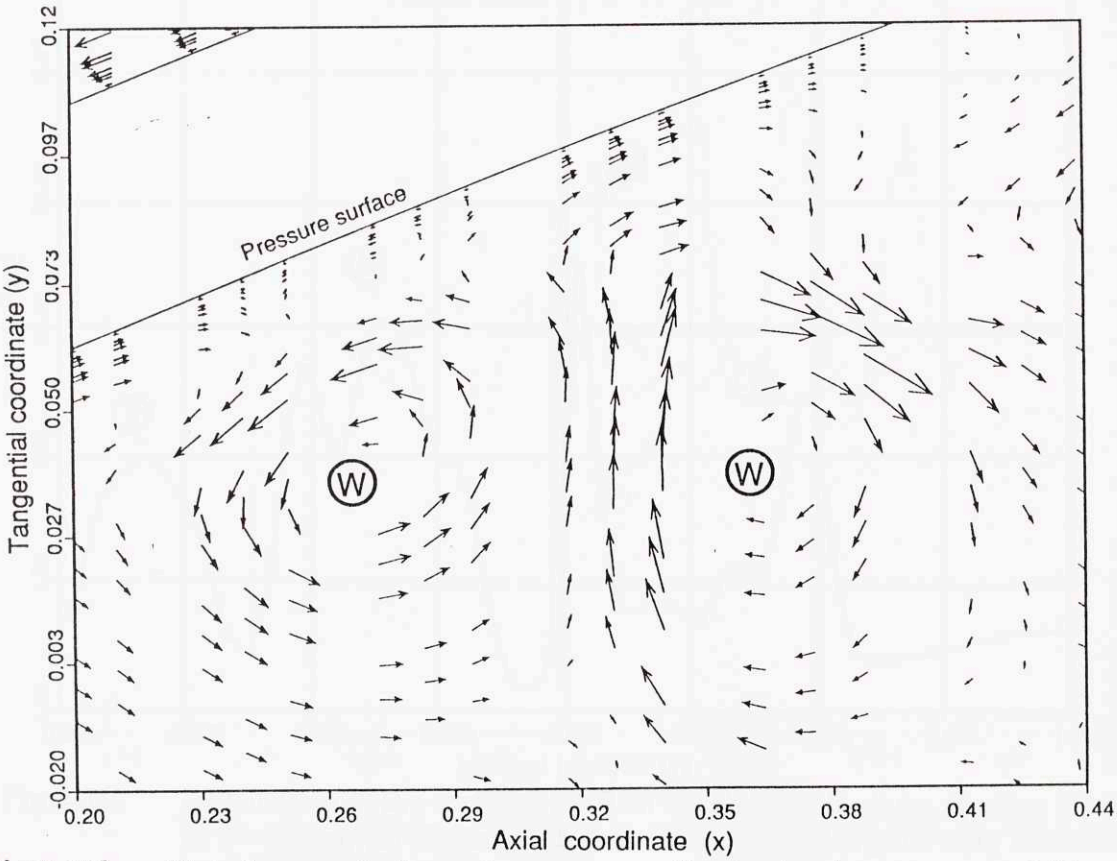

Fig.3.17b. Disturbance velocity vectors corresponding to the above pressure field.

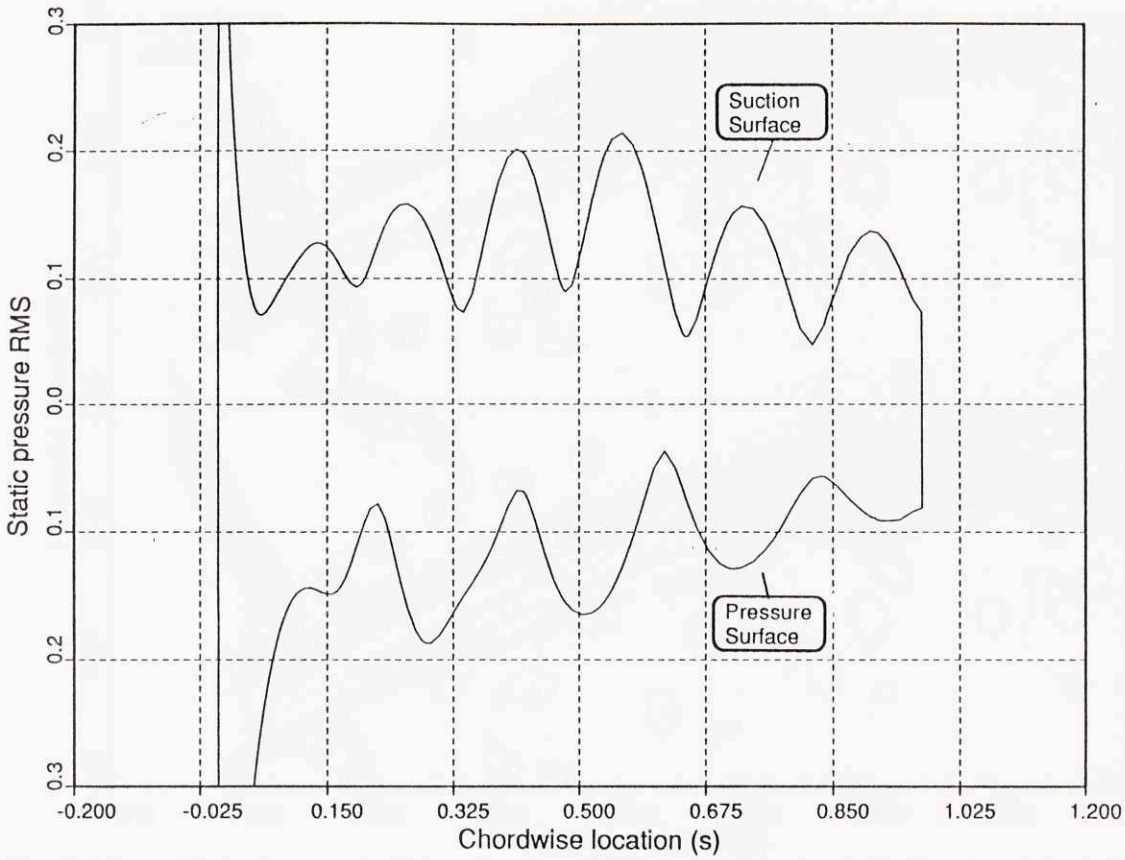

Fig.3.18. Distribution of the static pressure RMS on the blade surface.

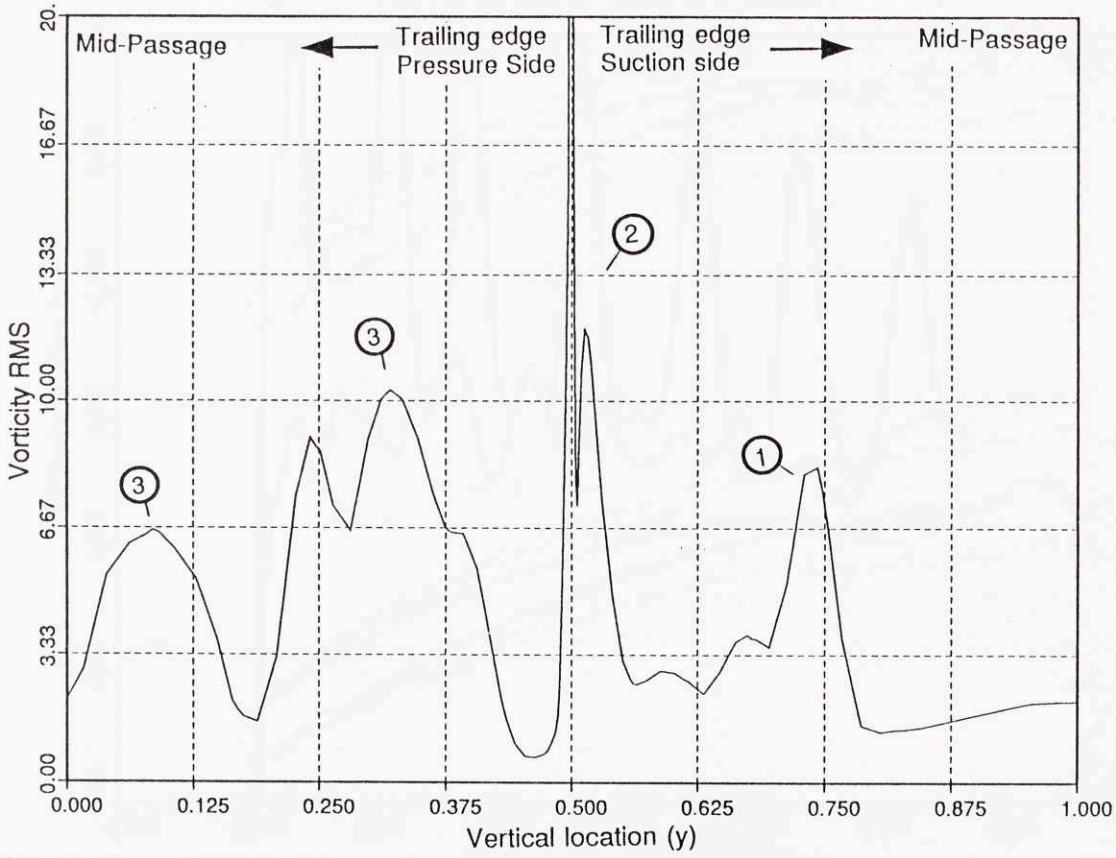

Fig.3.19. Distribution of the vorticity RMS on the stator exit plane, showing (1) discharge of B-vortices; (2) discharge of A-vortices; (3) discharge of wake vortices.

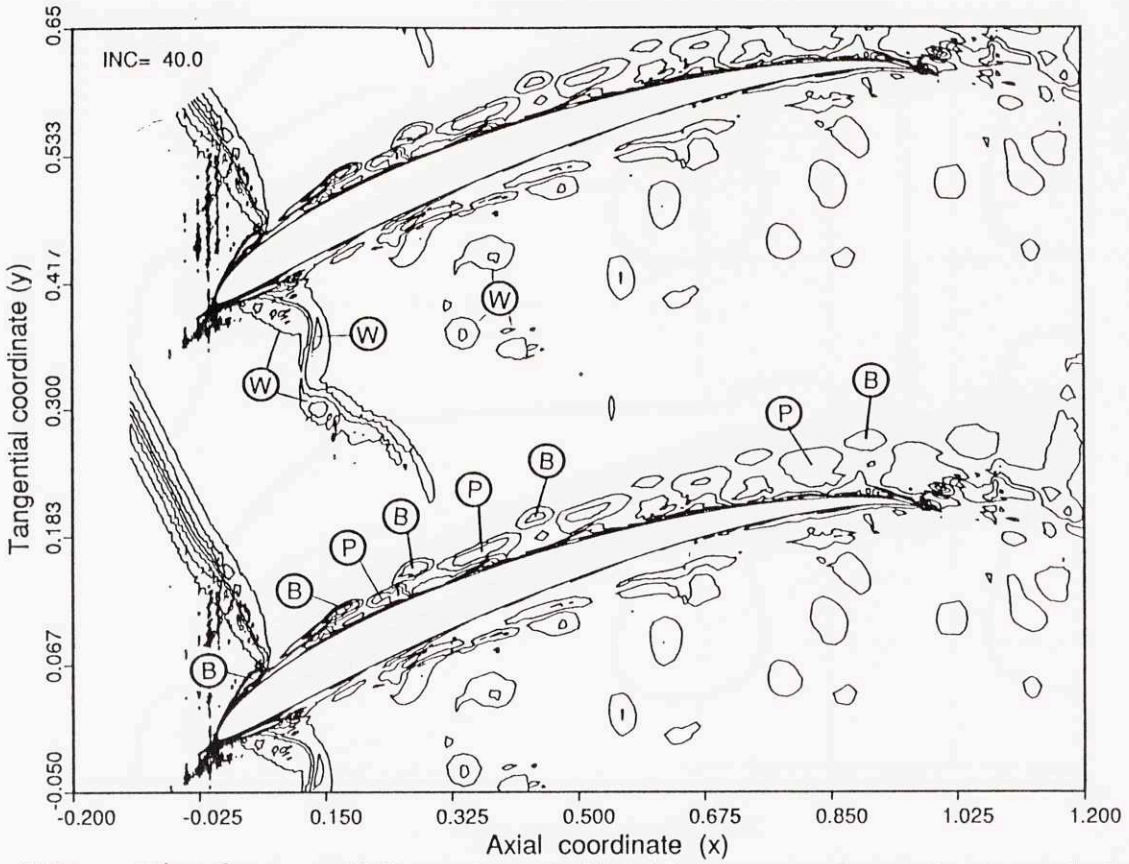

Fig.3.20. Disturbance vorticity contours in the stator passage from a laminar calculation at a Reynolds number of 40,000 (time $t_0 + 0.6T$).

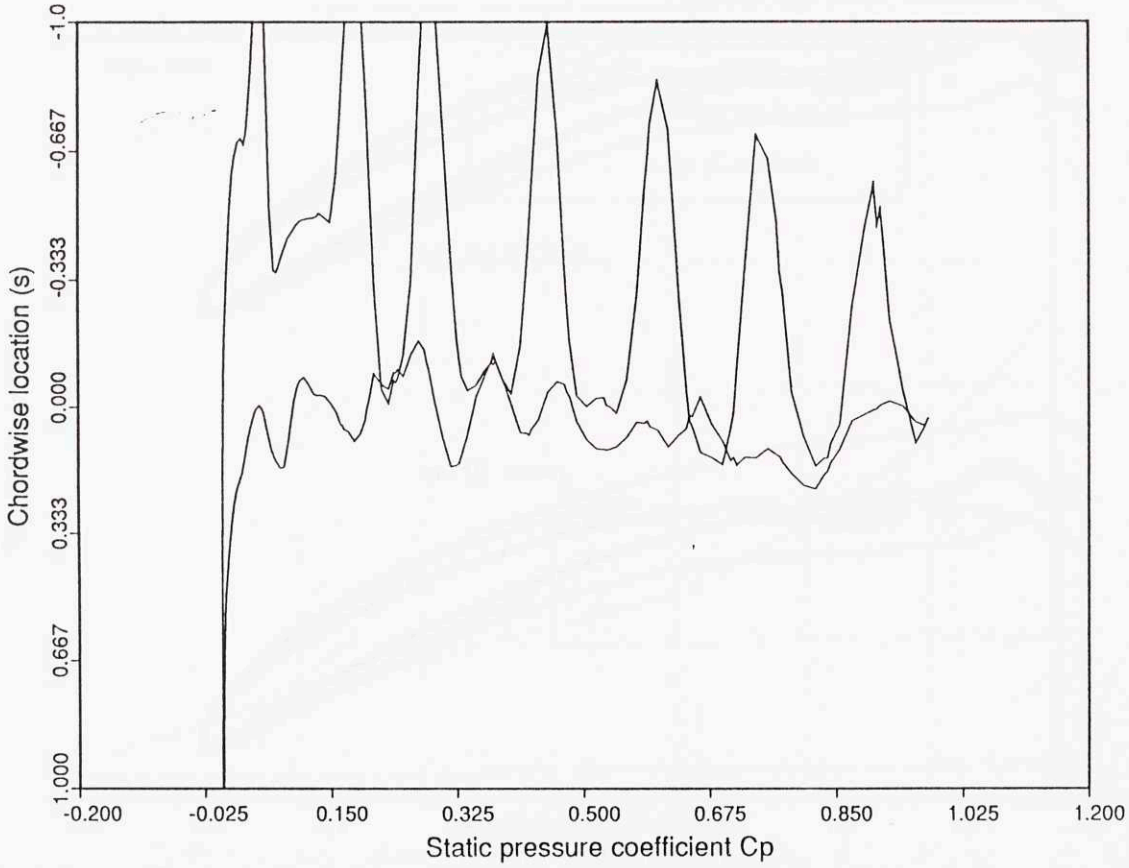

Fig.3.21. Static pressure distribution from a laminar calculation at a Reynolds number of 40,000 (time $t_0 + 0.6T$).

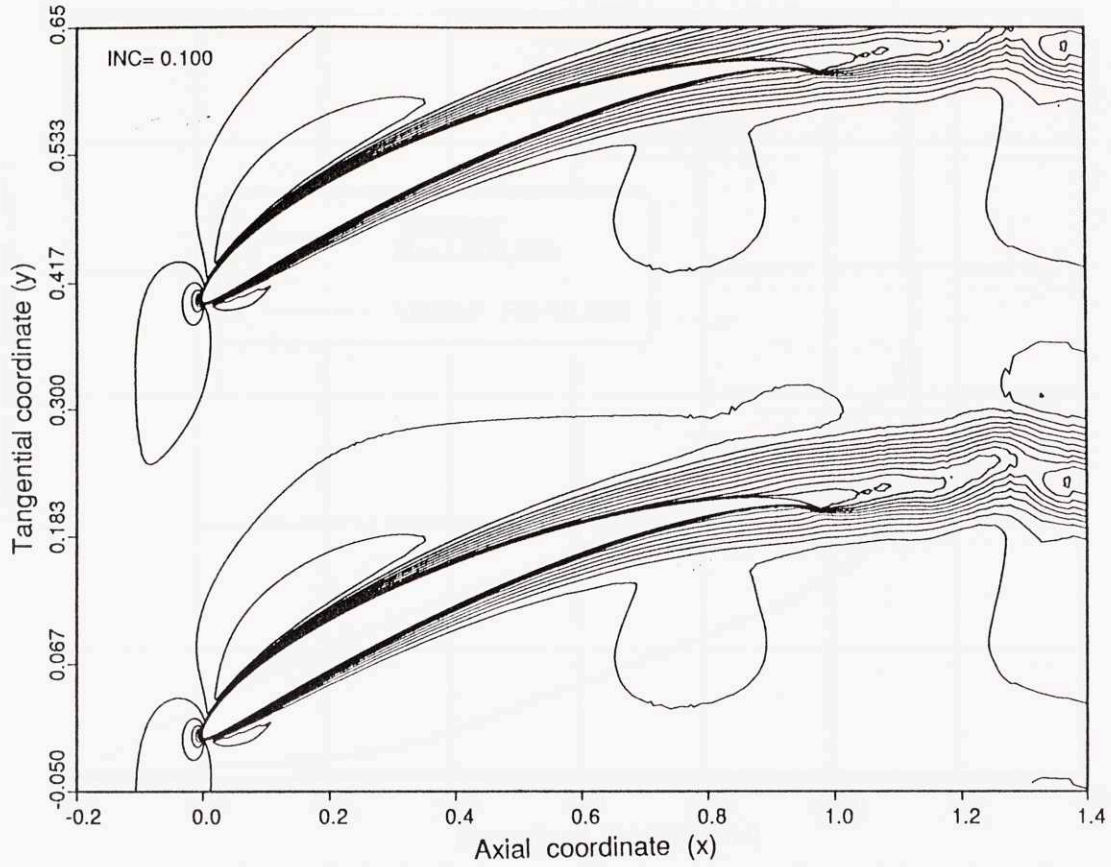

Fig.4.1. Computed velocity contours in the stator passage. Undisturbed turbulent flow (Re=1,000,000).

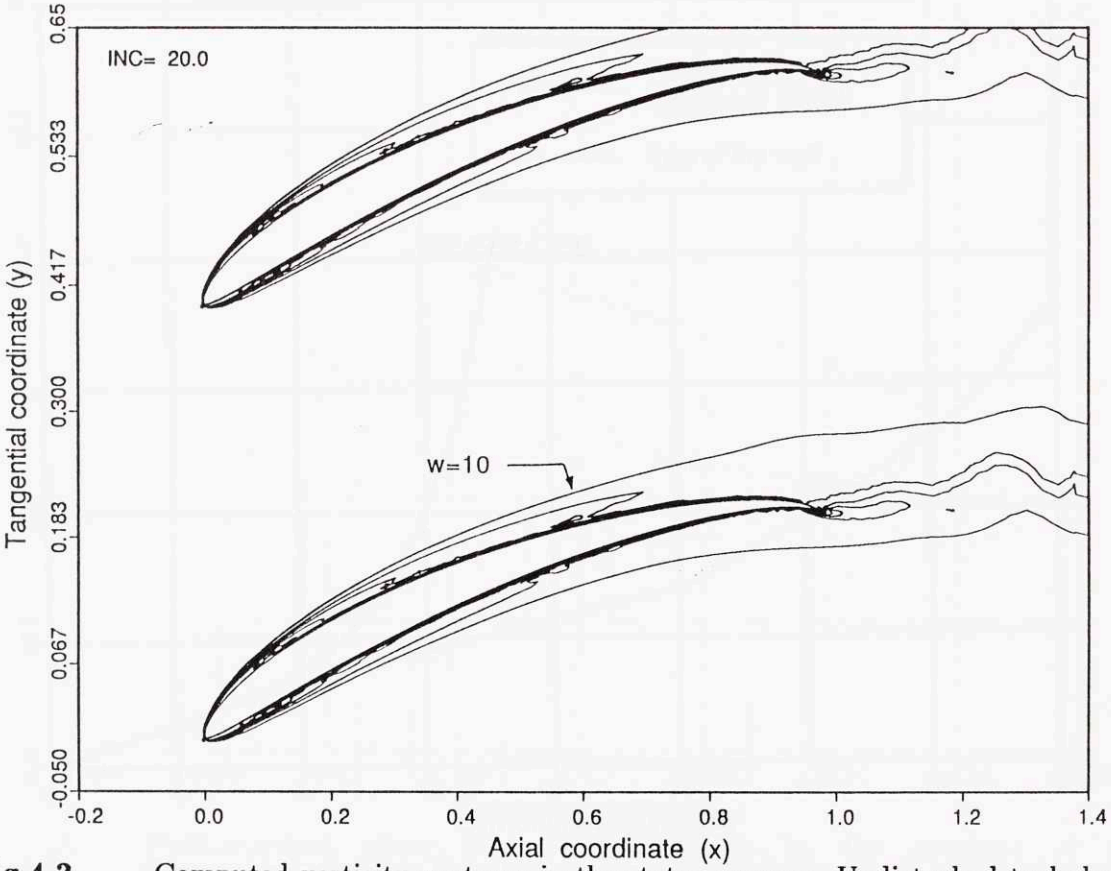

Fig.4.2. Computed vorticity contours in the stator passage. Undisturbed turbulent flow (Re=1,000,000).

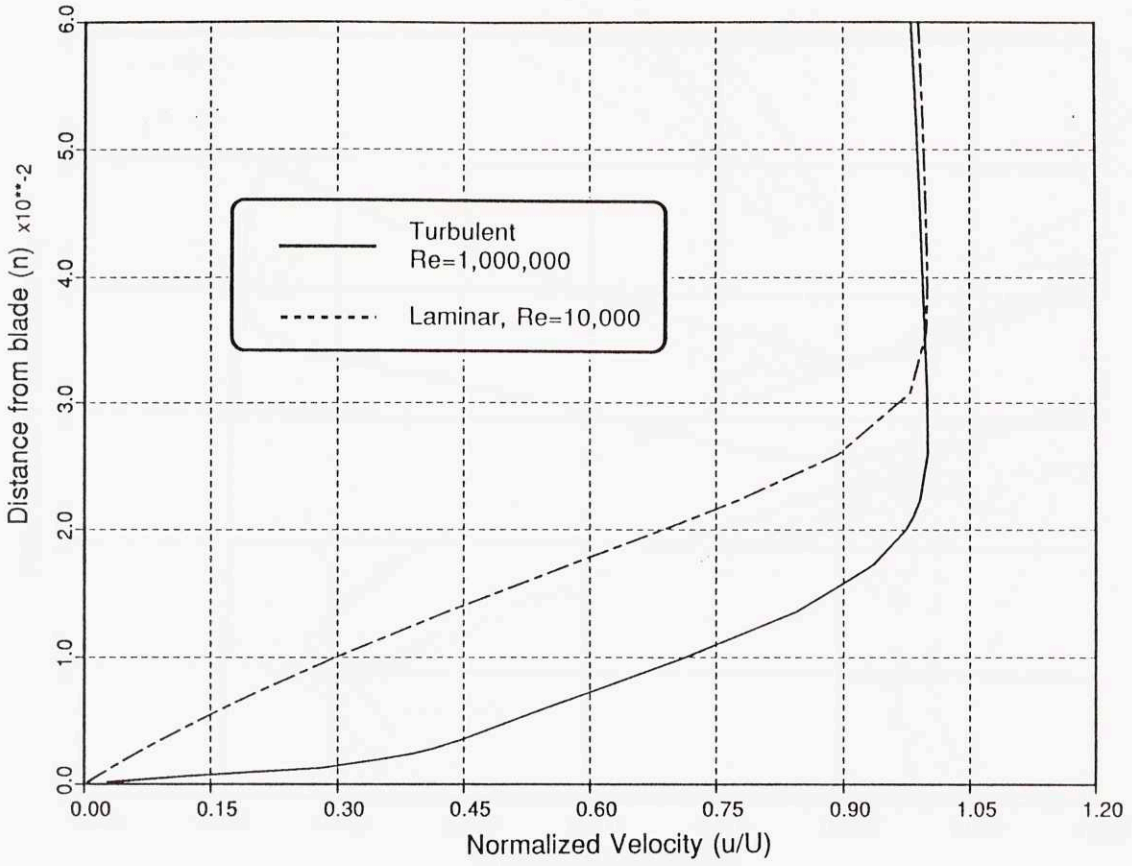

Fig.4.3. Comparison of the velocity profile in the suction surface boundary layer (x=0.25c), between undisturbed turbulent and laminar flows.

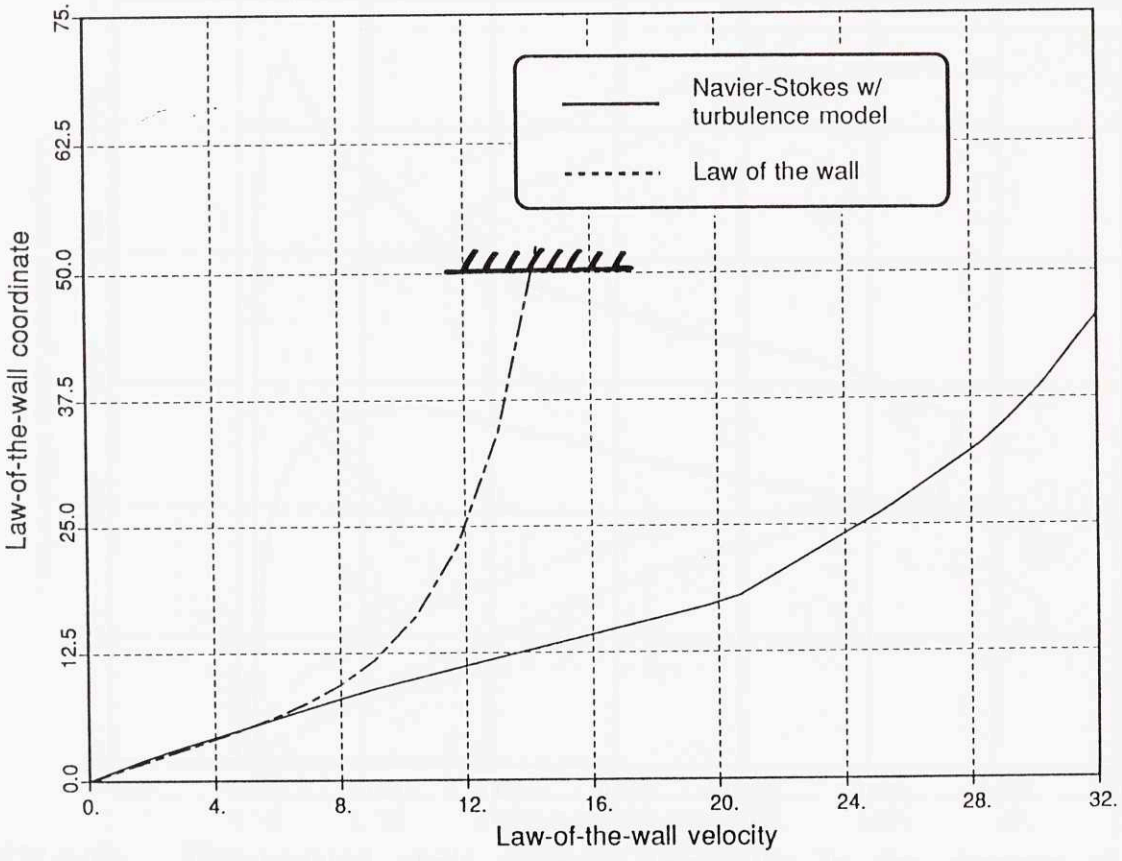

Fig.4.4. Comparison of the undisturbed computed velocity profile in the suction surface boundary layer (x=0.25c) and the law-of-the-wall.

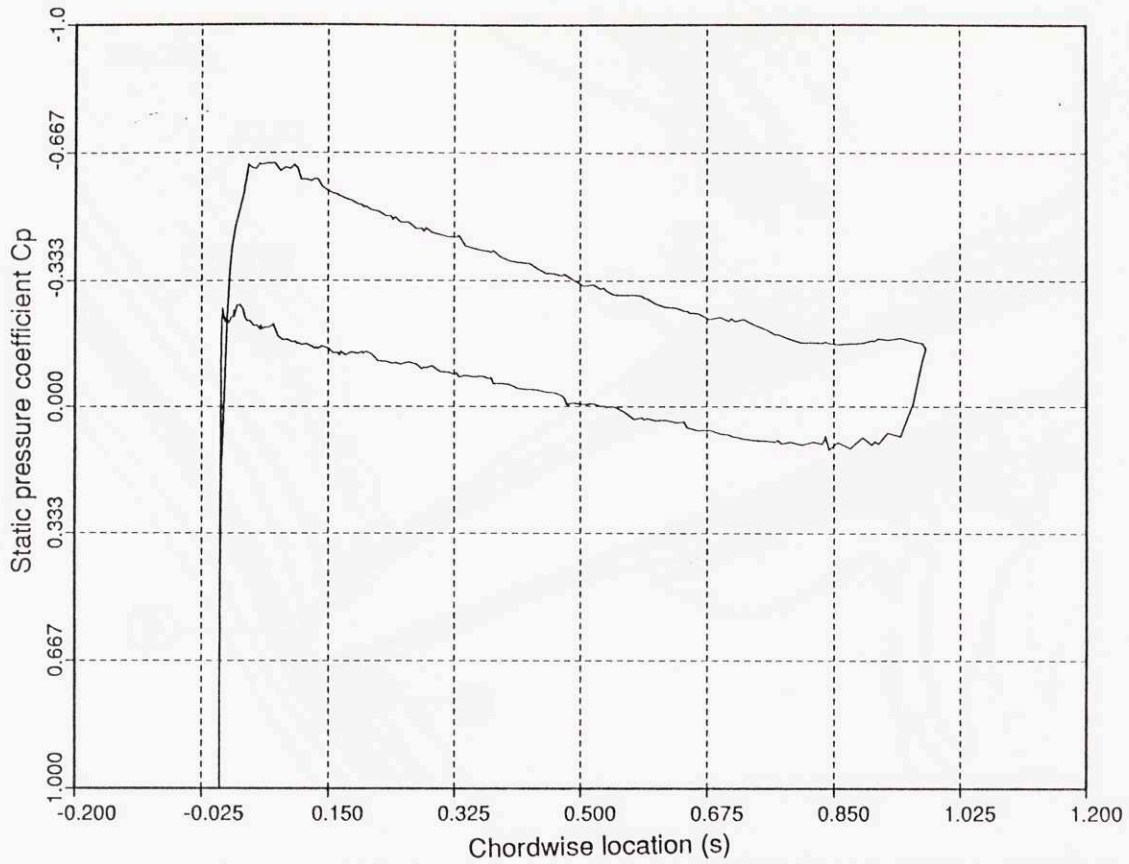

Fig.4.5a. Static pressure distribution in undisturbed turbulent flow (Re=1,000,000).

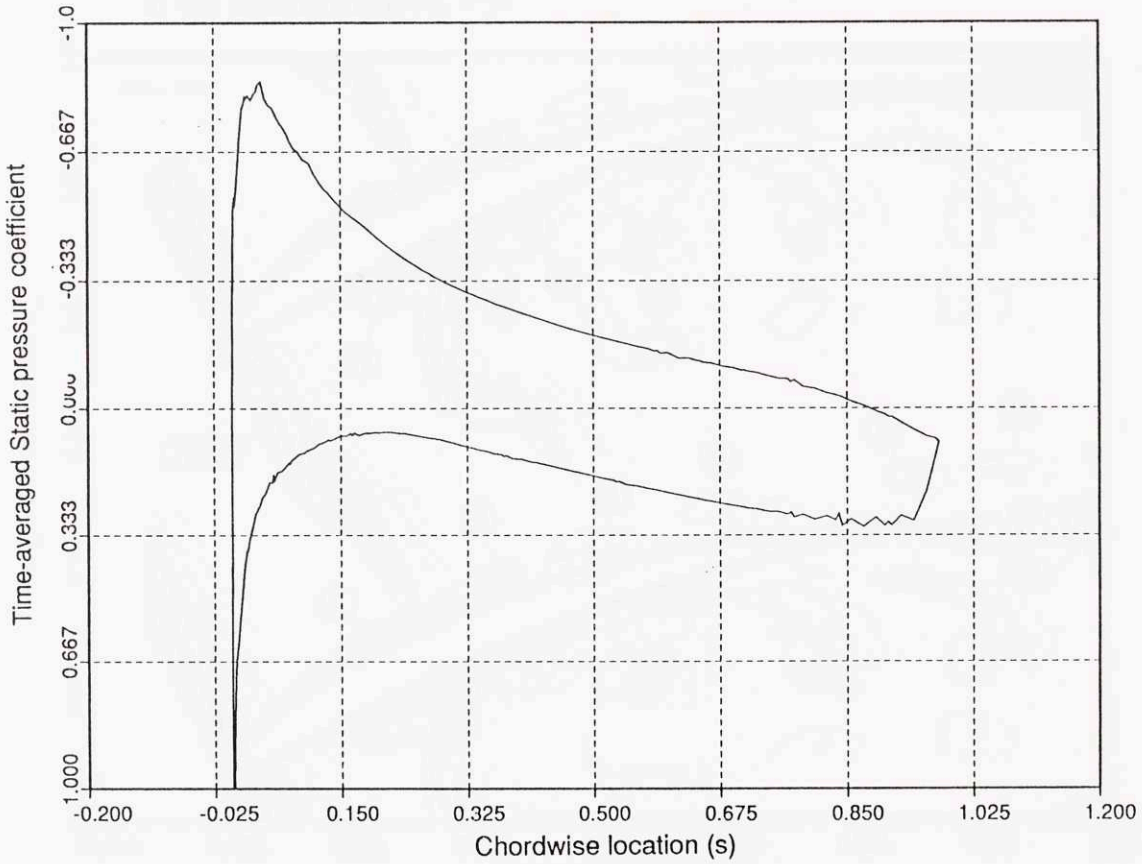

Fig.4.5b. Time-averaged static pressure distribution in the presence of wakes (Re=1,000,000).

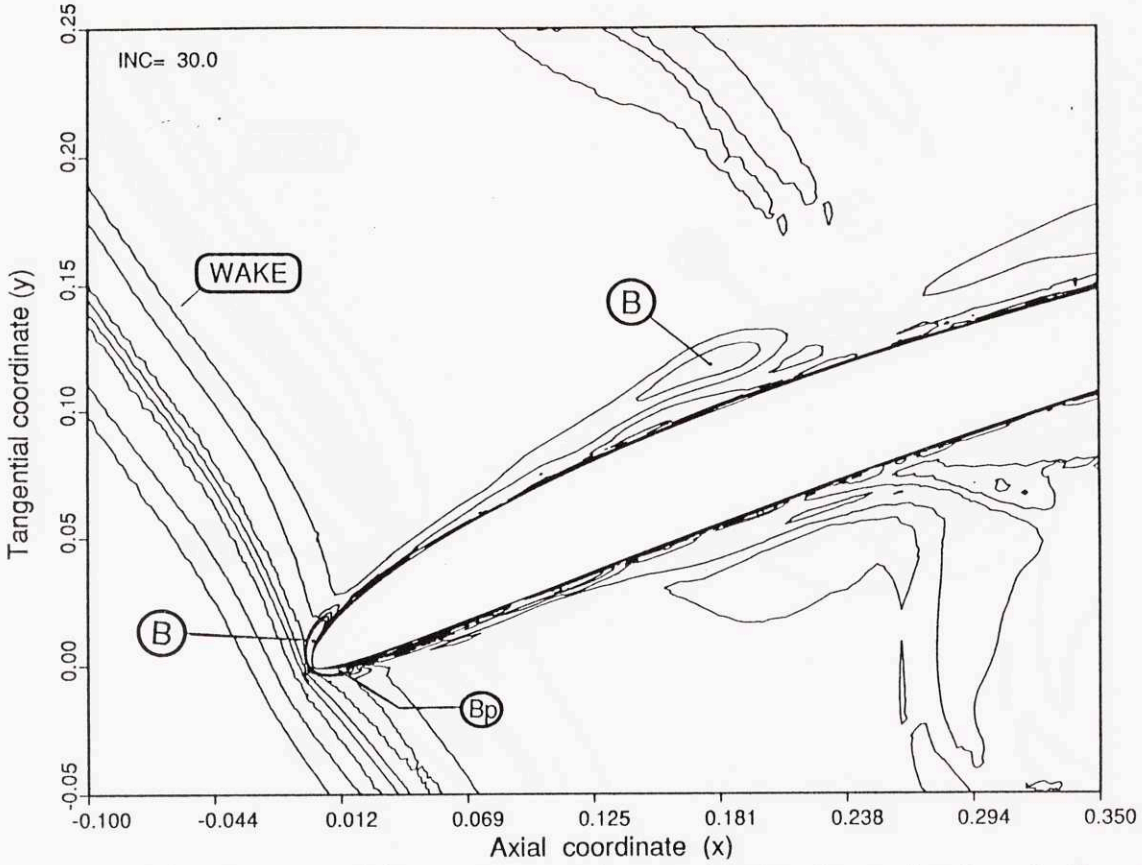

Fig.4.6a. Disturbance vorticity contours at time t_0, showing the production of a B-vortex at the leading edge.

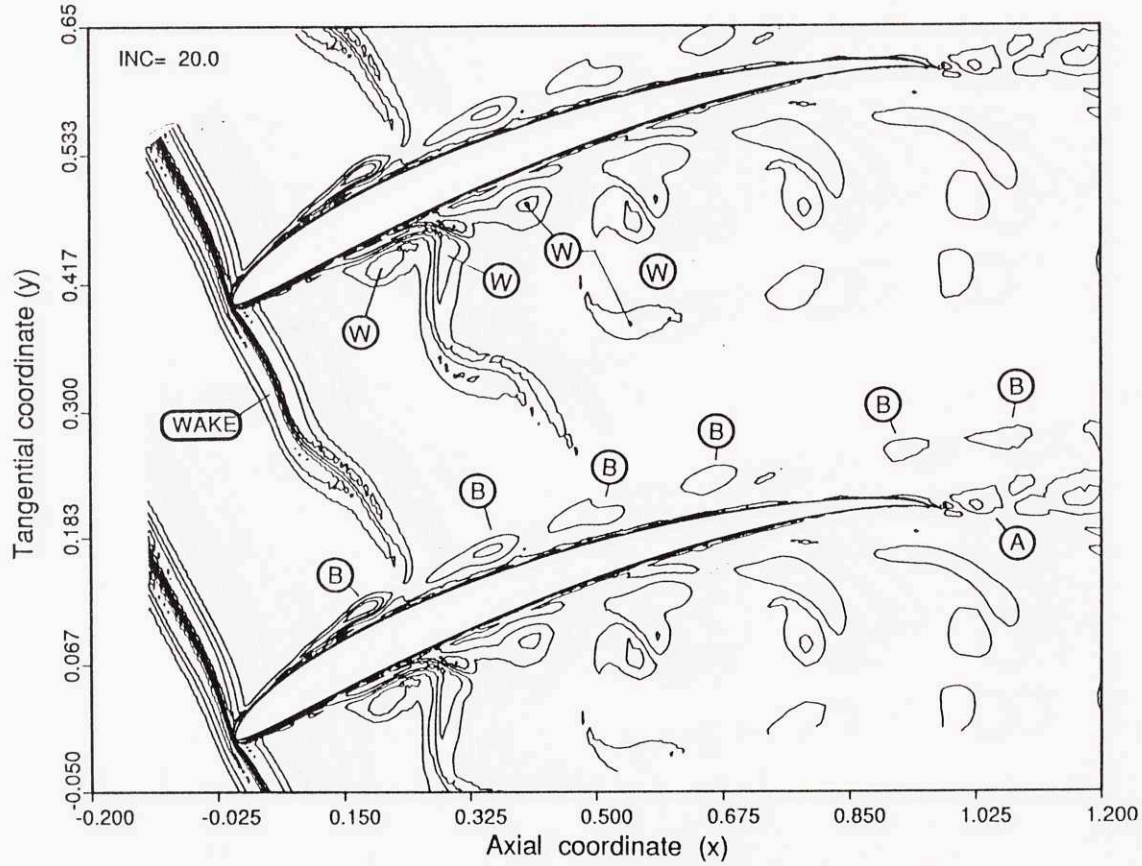

Fig.4.6b. Disturbance vorticity contours showing the unsteady flow features in the stator passage at time $t = t_0$.

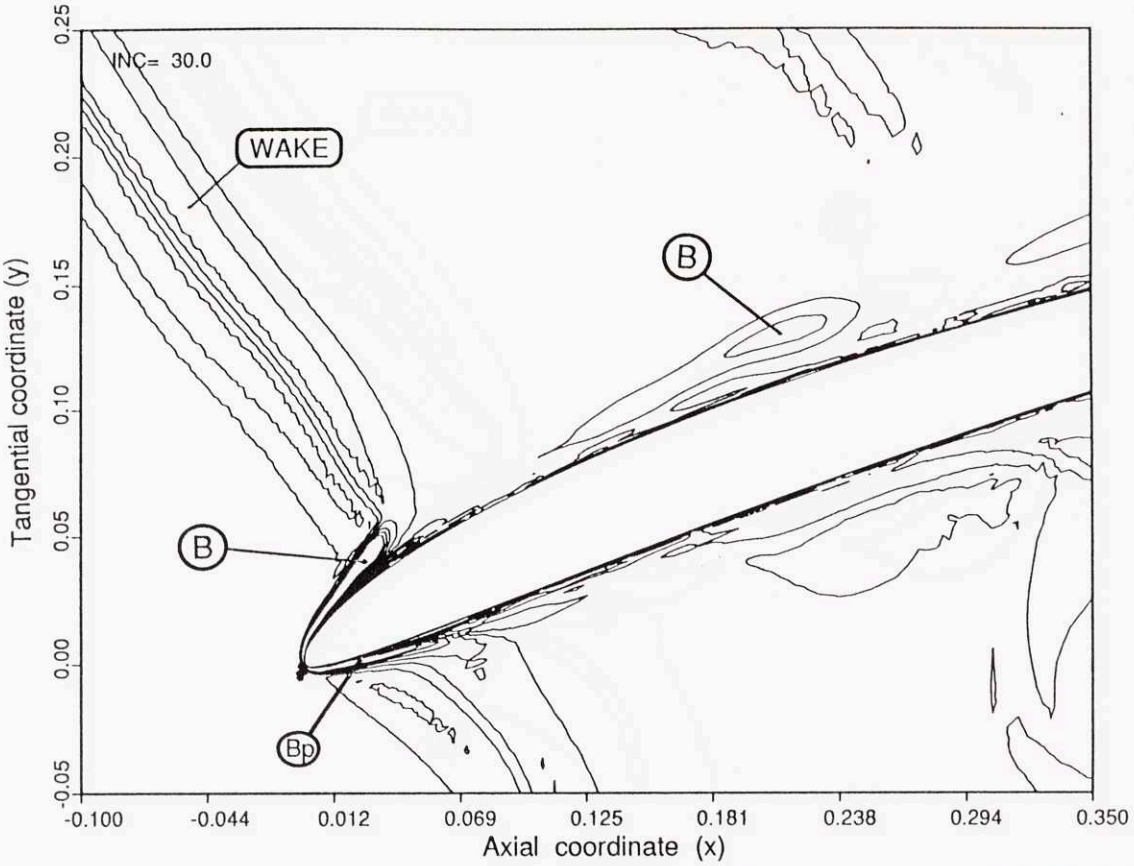

Fig.4.6c. Disturbance vorticity contours at time $t_0 + 0.2T$, showing the production of a B-vortex at the leading edge.

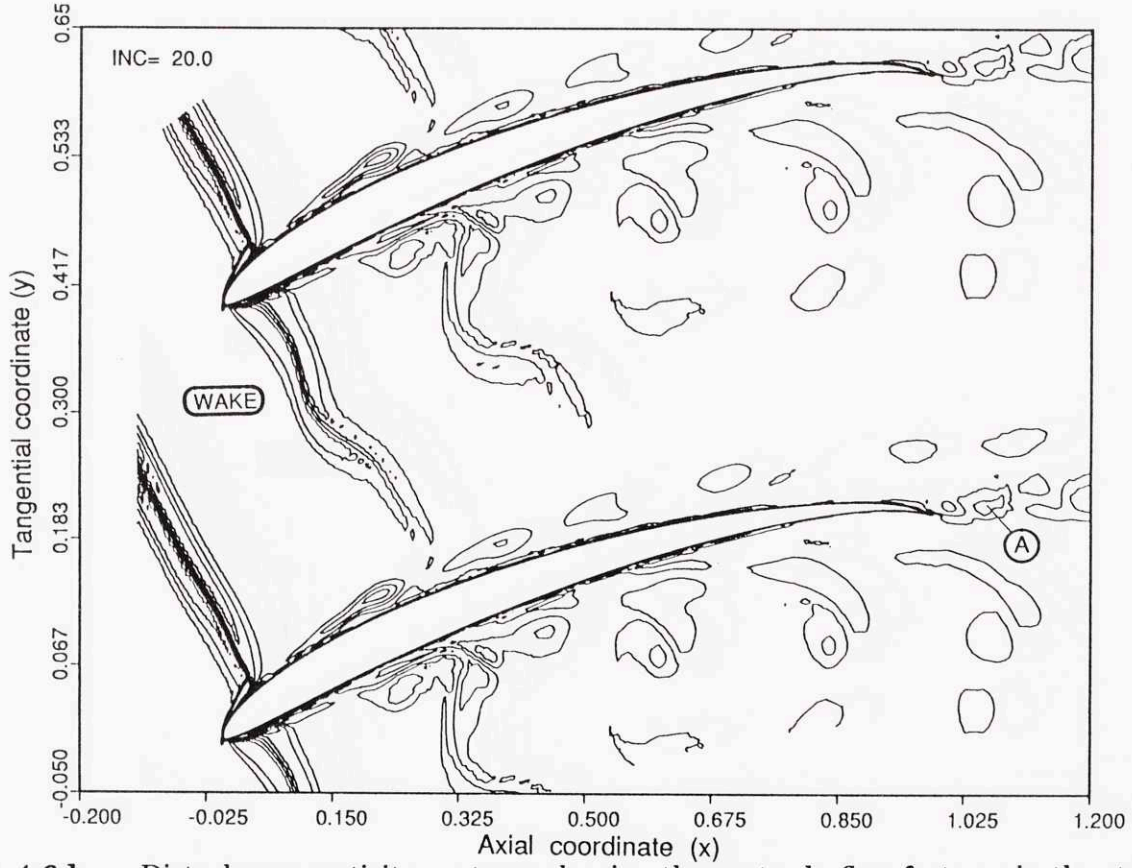

Fig.4.6d. Disturbance vorticity contours showing the unsteady flow features in the stator passage at time $t = t_0 + 0.2T$.

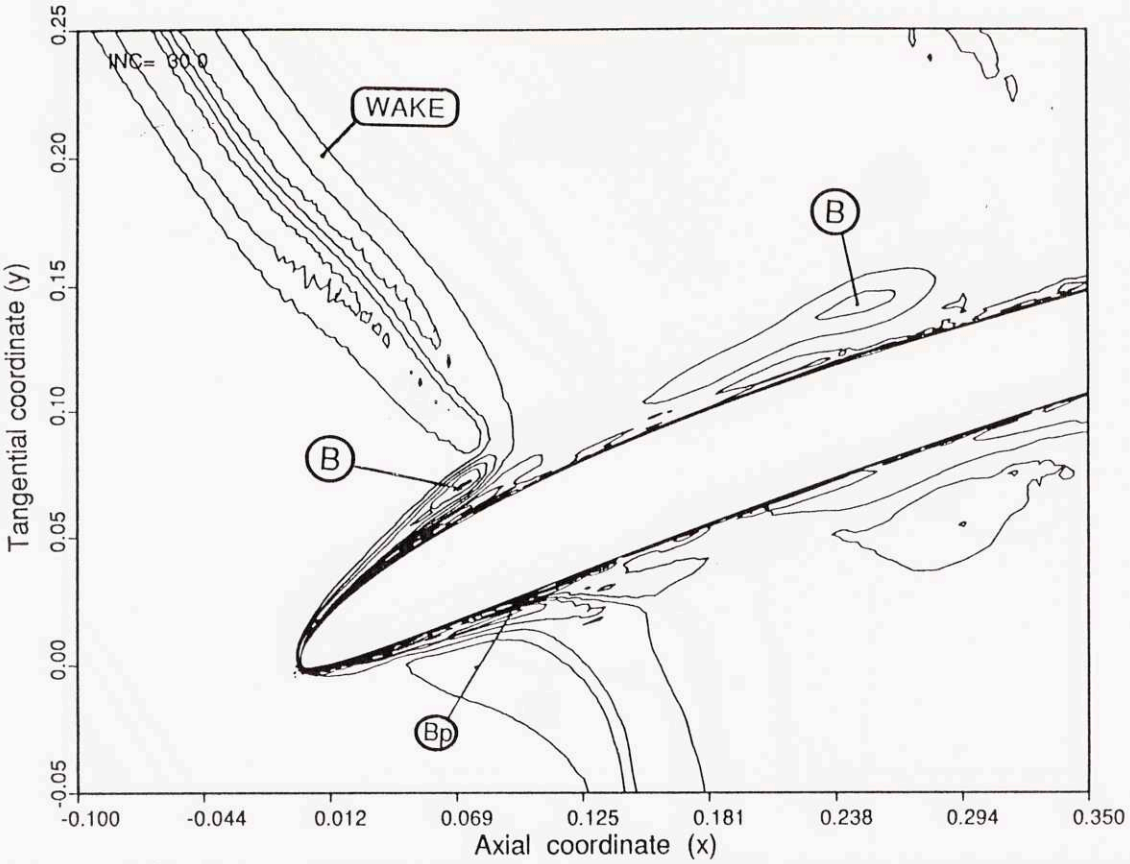

Fig.4.6e. Disturbance vorticity contours at time $t_0 + 0.4T$, showing the production of a B-vortex at the leading edge.

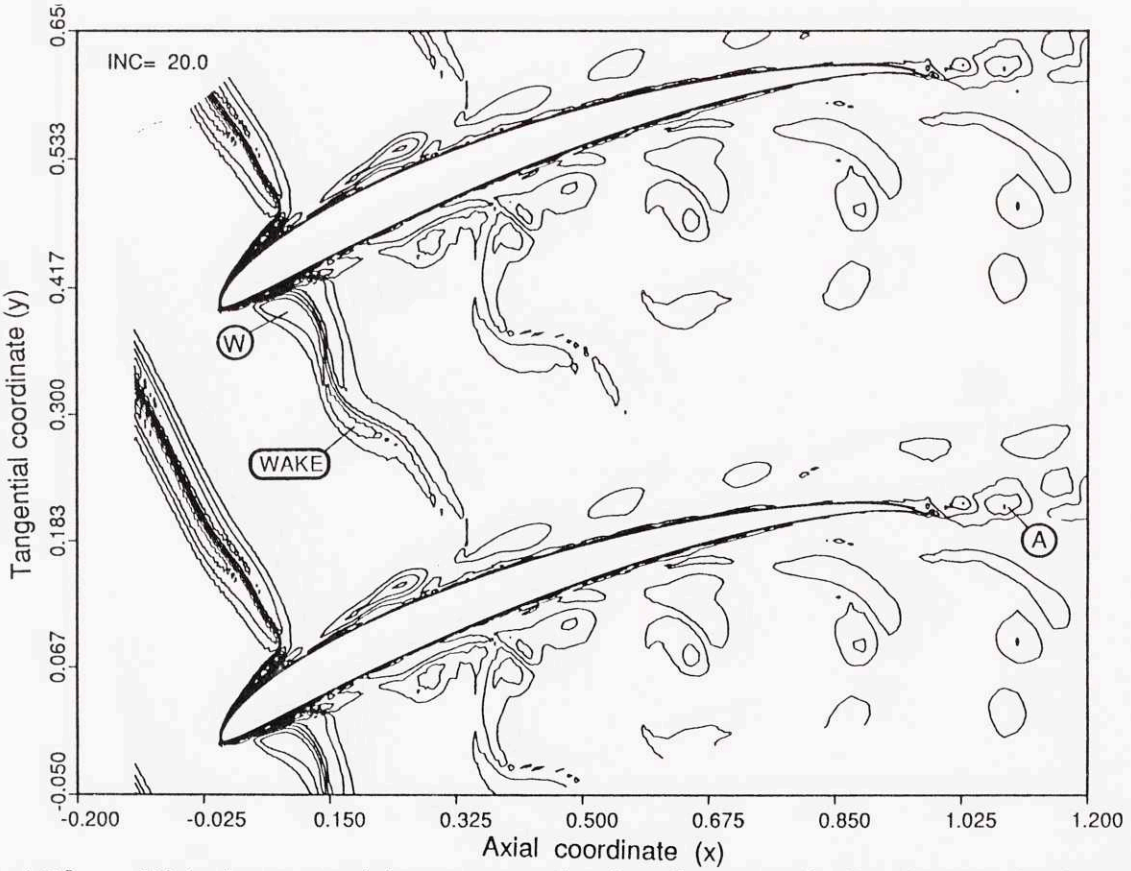

Fig.4.6f. Disturbance vorticity contours showing the unsteady flow features in the stator passage at time $t = t_0 + 0.4T$.

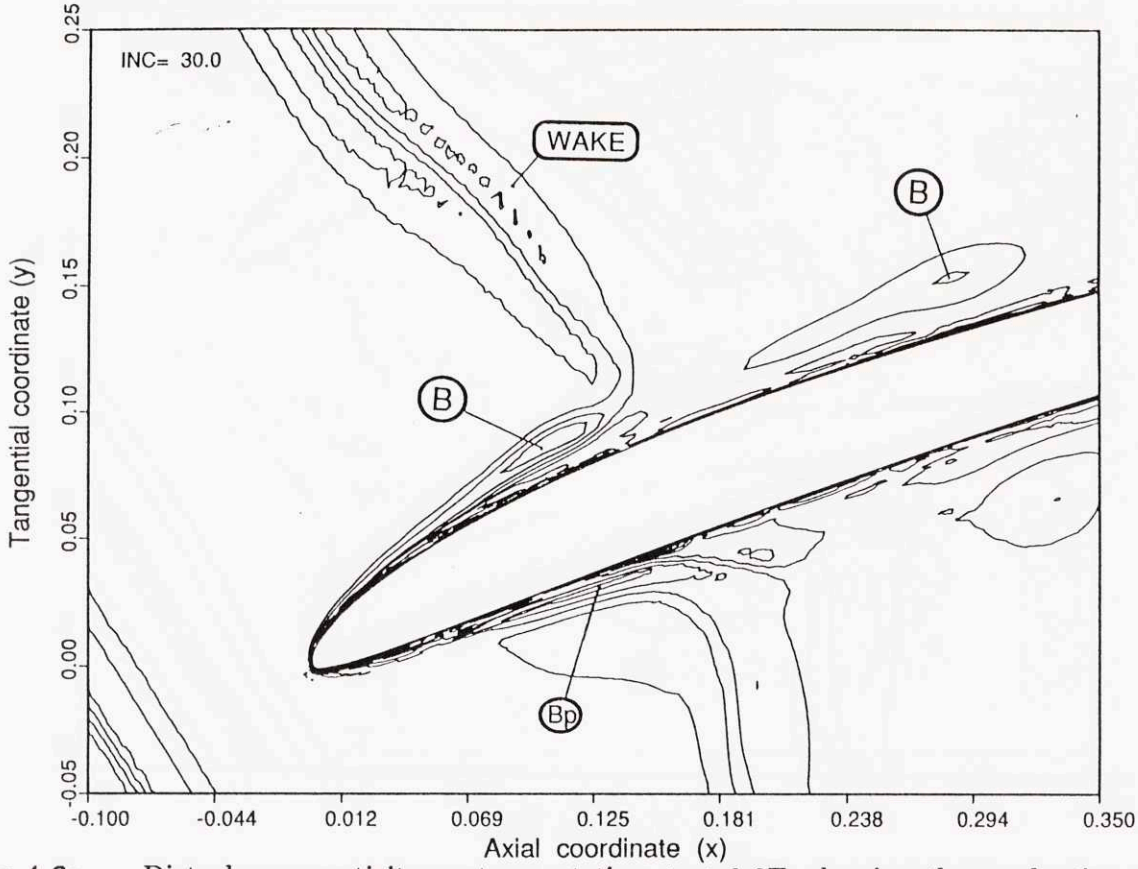

Fig.4.6g. Disturbance vorticity contours at time $t_0 + 0.6T$, showing the production of a B-vortex at the leading edge.

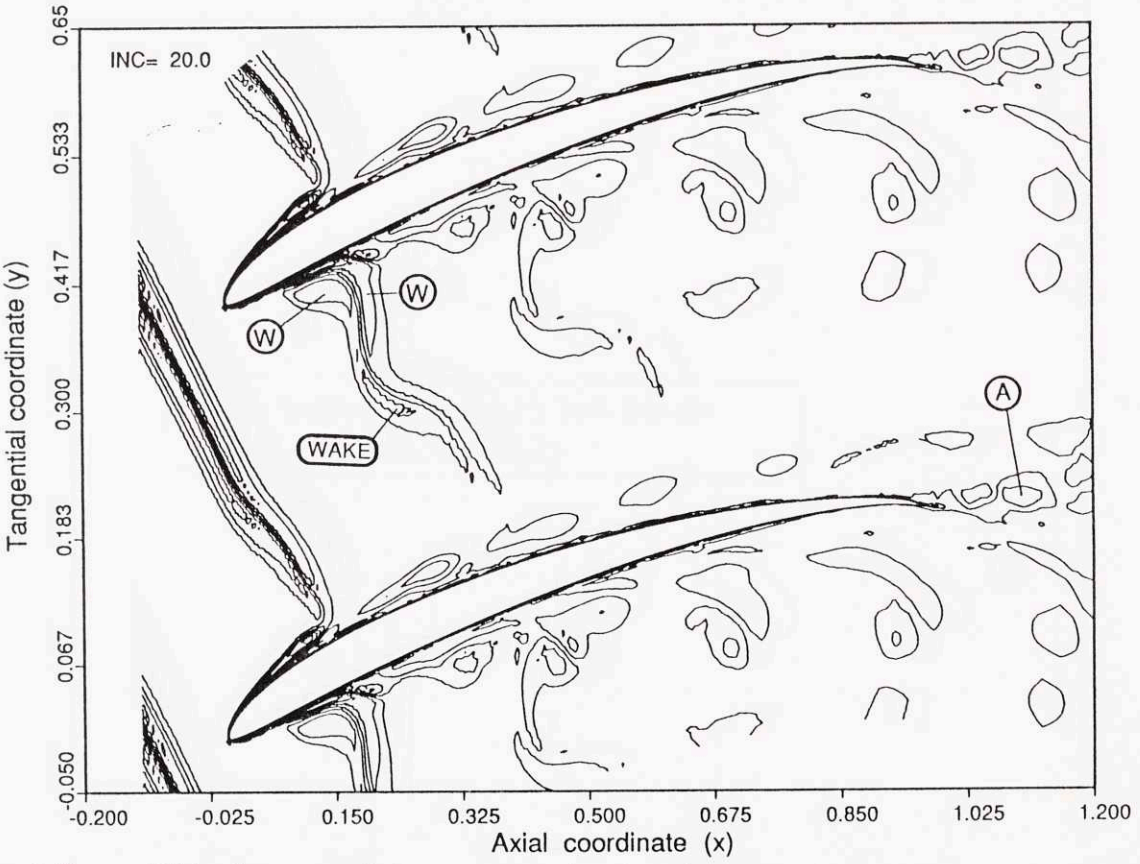

Fig.4.6h. Disturbance vorticity contours showing the unsteady flow features in the stator passage at time $t = t_0 + 0.6T$.

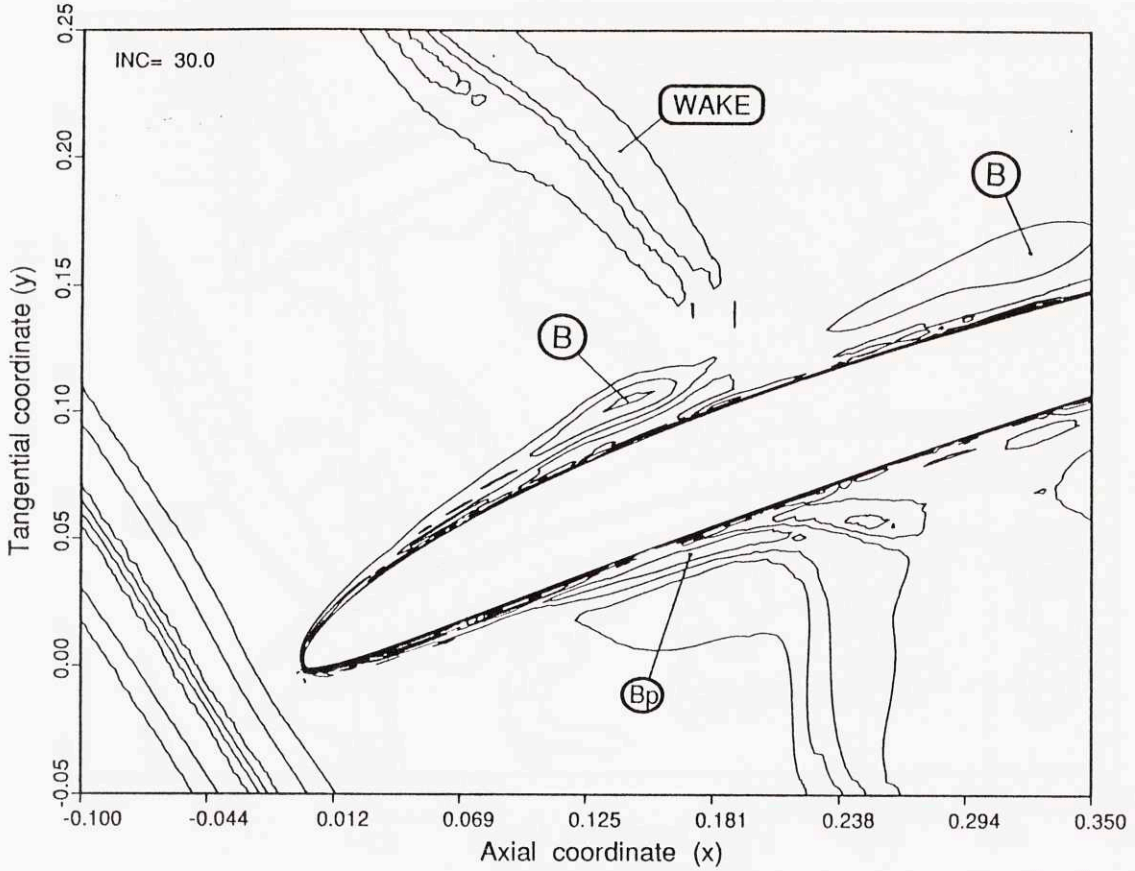

Fig.4.6i. Disturbance vorticity contours at time $t_0 + 0.8T$, showing the production of a B-vortex at the leading edge.

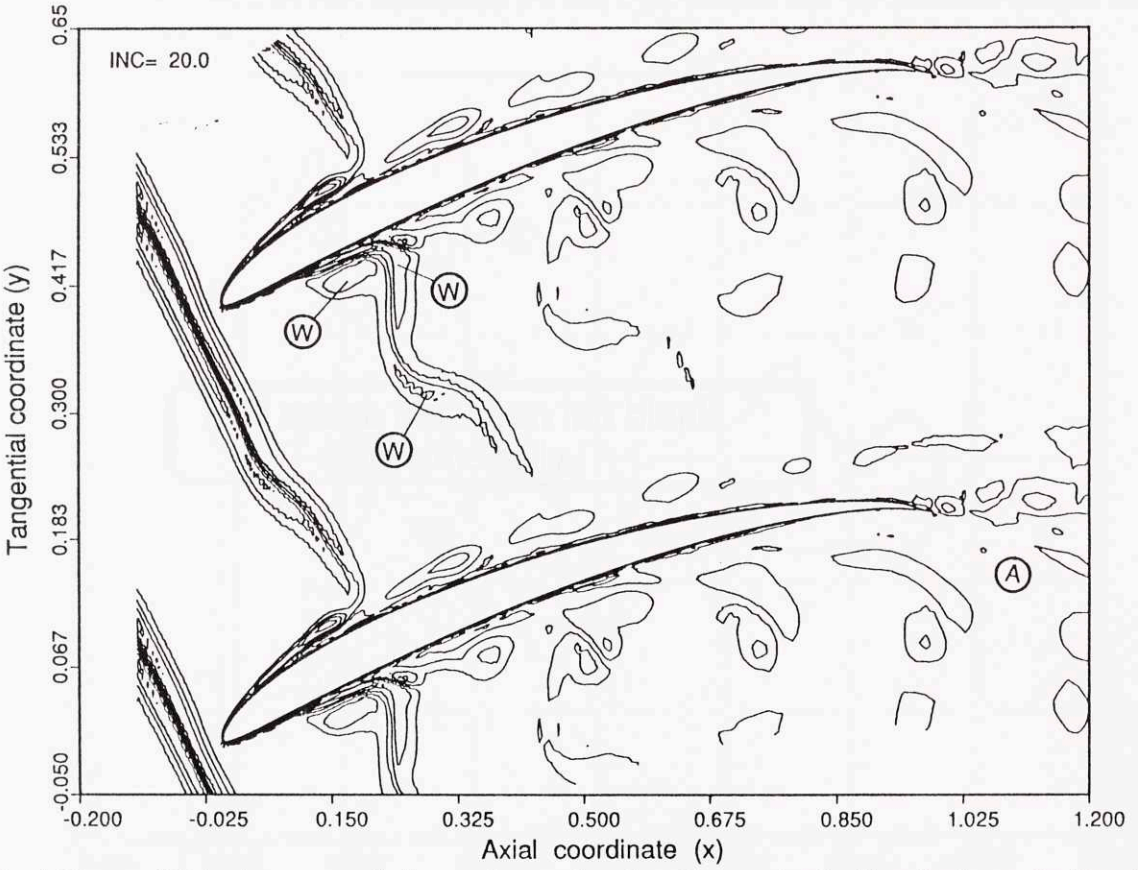

Fig.4.6j. Disturbance vorticity contours showing the unsteady flow features in the stator passage at time $t = t_0 + 0.8T$.

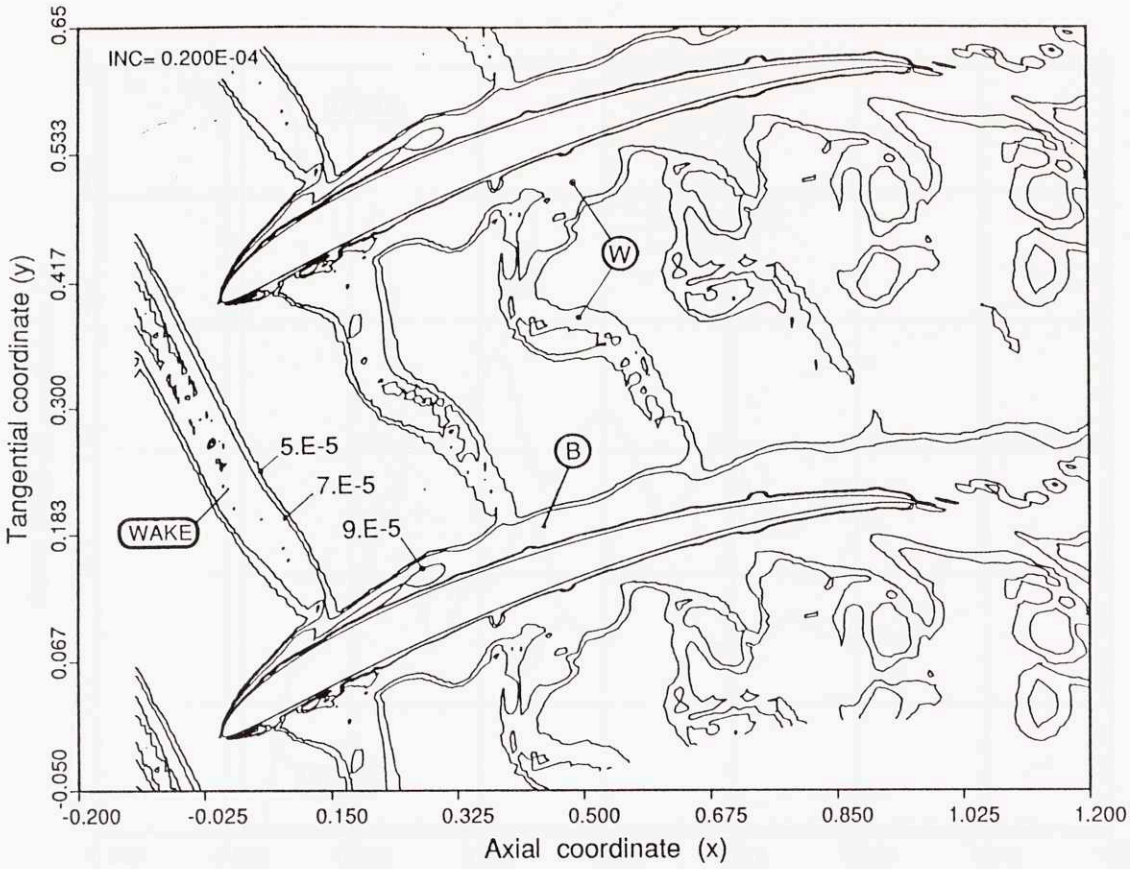

Fig.4.7. Eddy viscosity contours in the stator passage at time $t + 0.6T$ showing high diffusion rates inside the envelope of motion of the B-vortices.

This space has been left blank intentionally

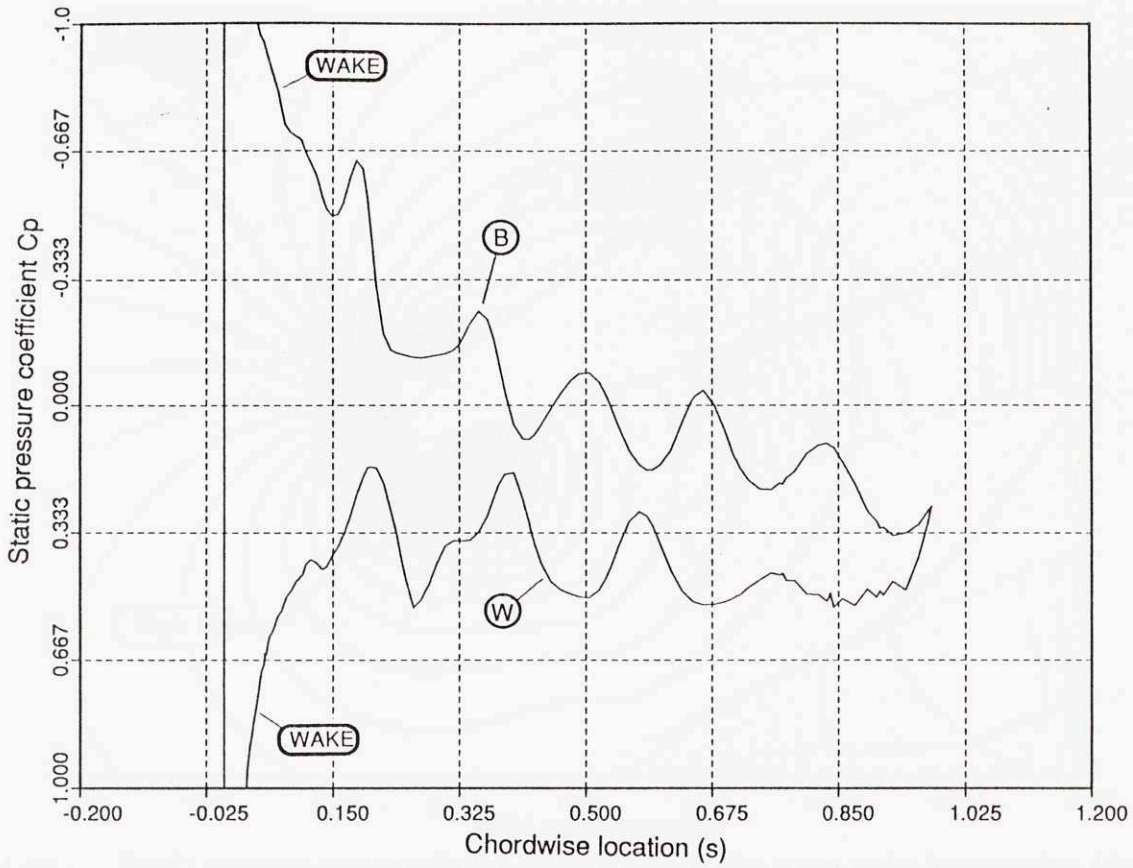

Fig.4.8a. Static pressure distribution on the blade surface at time t_0 showing (1,2) leading edge pulses, (3) suction surface depressions, and (4) pressure surface disturbances.

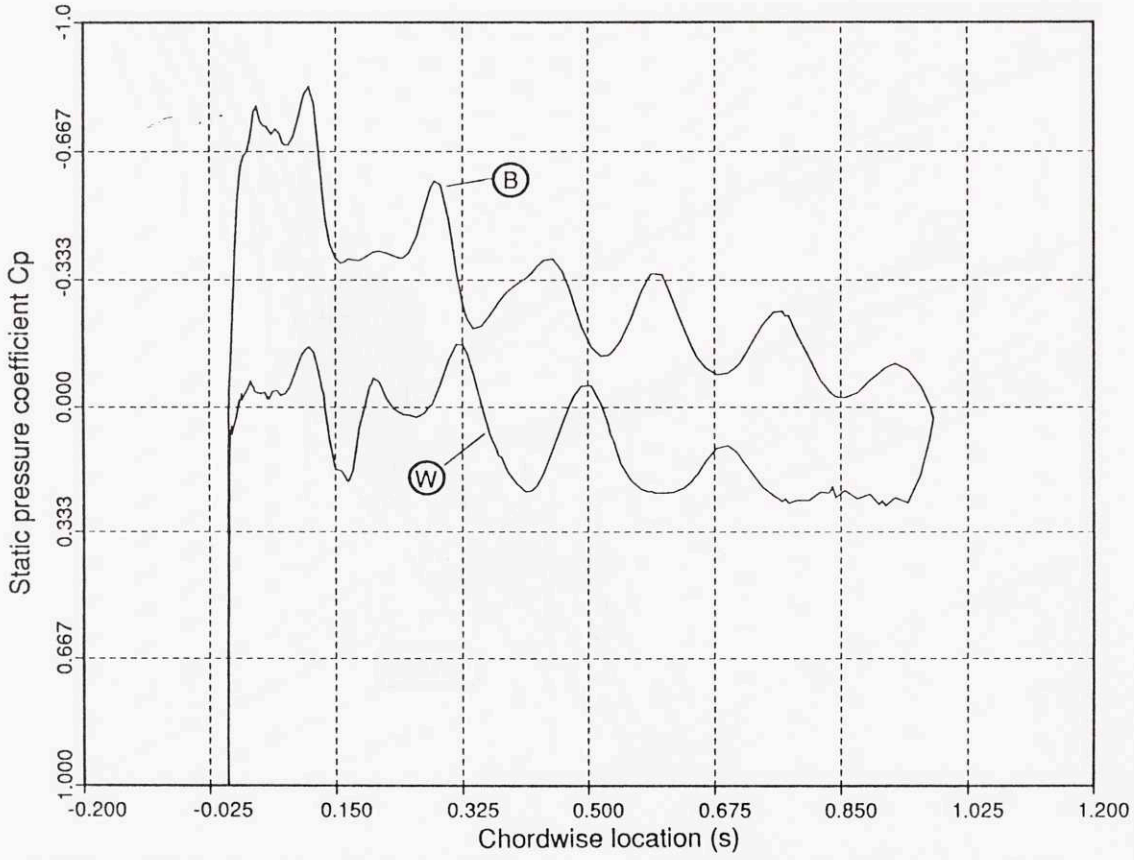

Fig.4.8b. Static pressure distribution on the blade surface at time $t_0 + 0.6T$ showing (3) suction surface depressions, and (4) pressure surface disturbances.

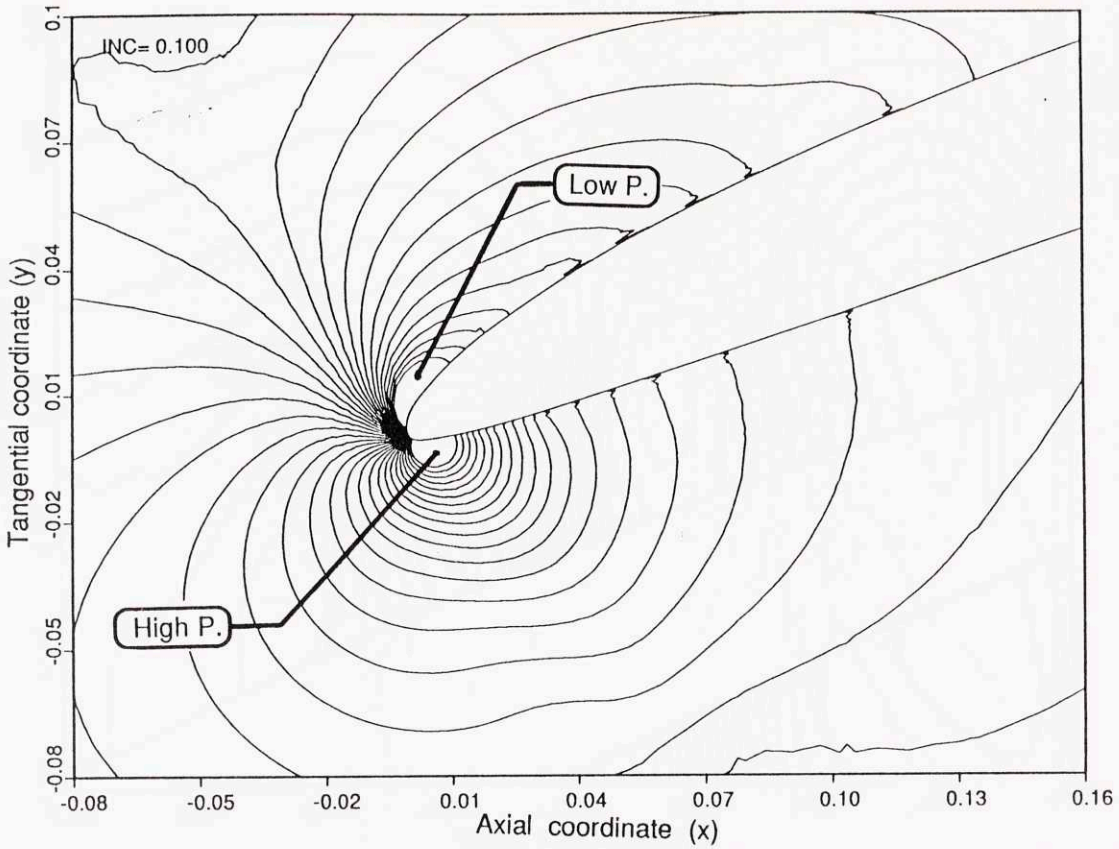

Fig.4.9a. Static pressure contours in the leading edge region upon wake interception (time t_0), showing the production of (1) high pressure peak on the pressure side; and (2) low pressure peak on the suction side.

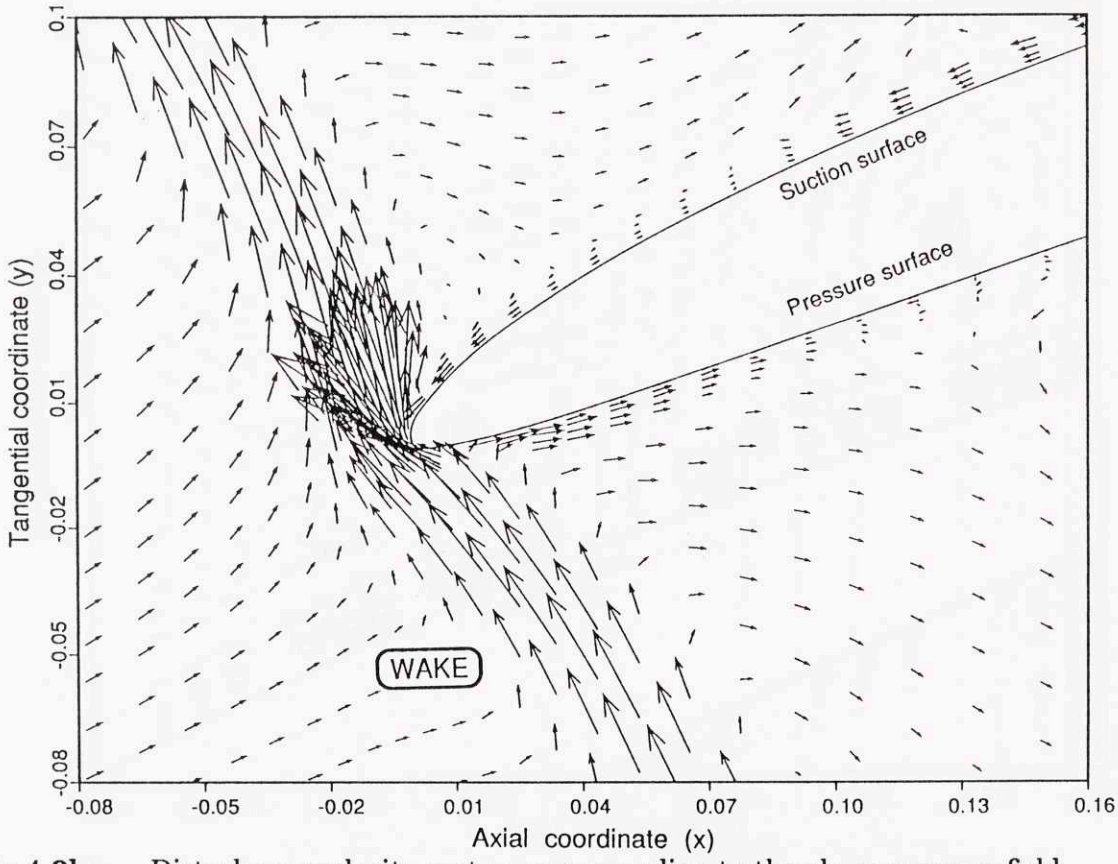

Fig.4.9b. Disturbance velocity vectors corresponding to the above pressure field.

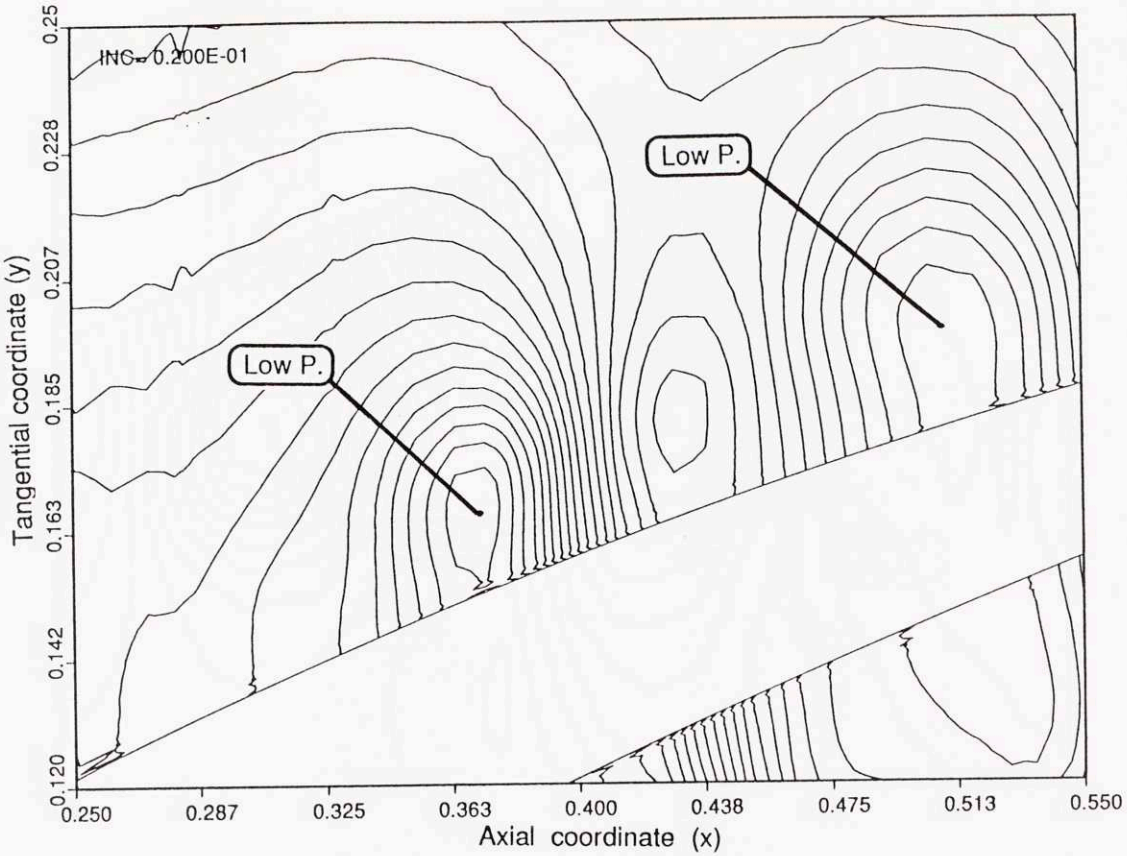

Fig.4.10a. Static pressure contours in the vicinity of a B-vortex and the suction surface. The low-pressure region in the vortex core is perceived as a moving low-pressure disturbance on the suction surface.

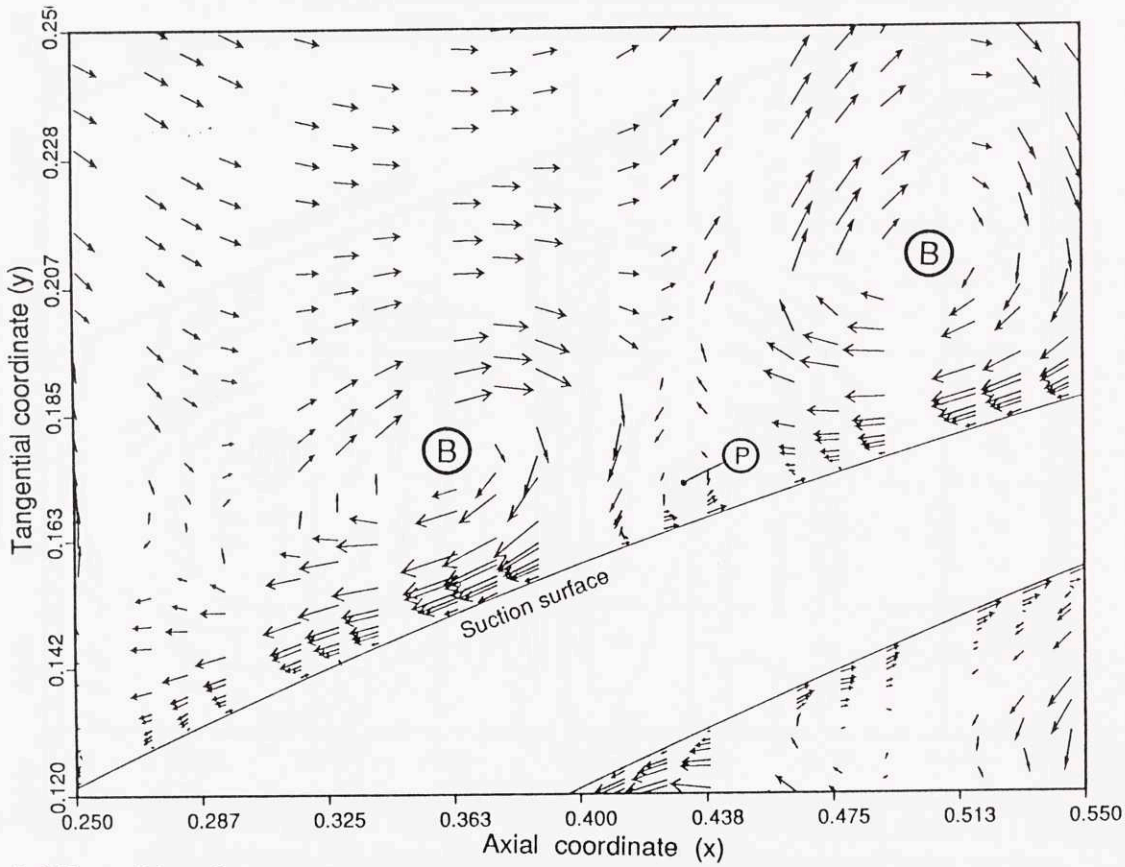

Fig.4.10b. Disturbance velocity vectors corresponding to the above pressure field.

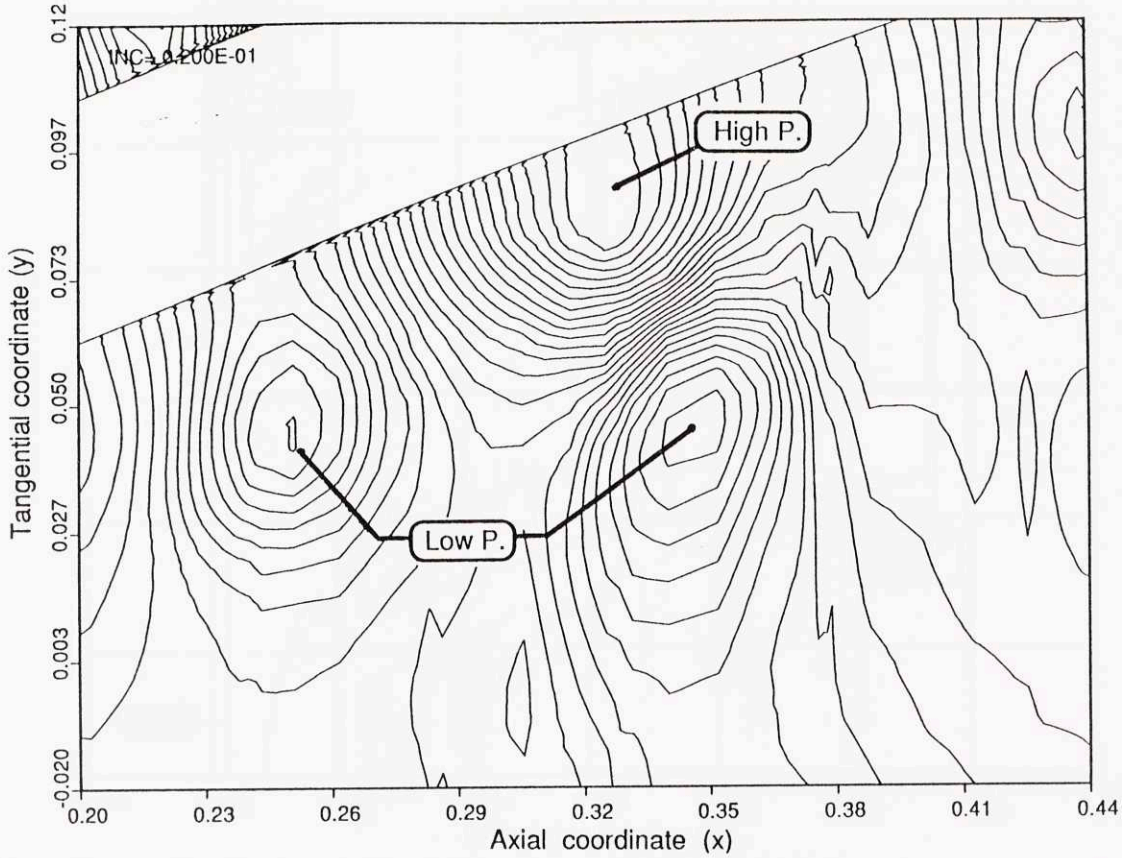

Fig.4.11a. Static pressure contours in the vicinity of a system of counterrotating wake vortices and the pressure surface, showing (1) low-pressure regions associated to the vortex cores; and (2) high-pressure region associated to stagnation flow.

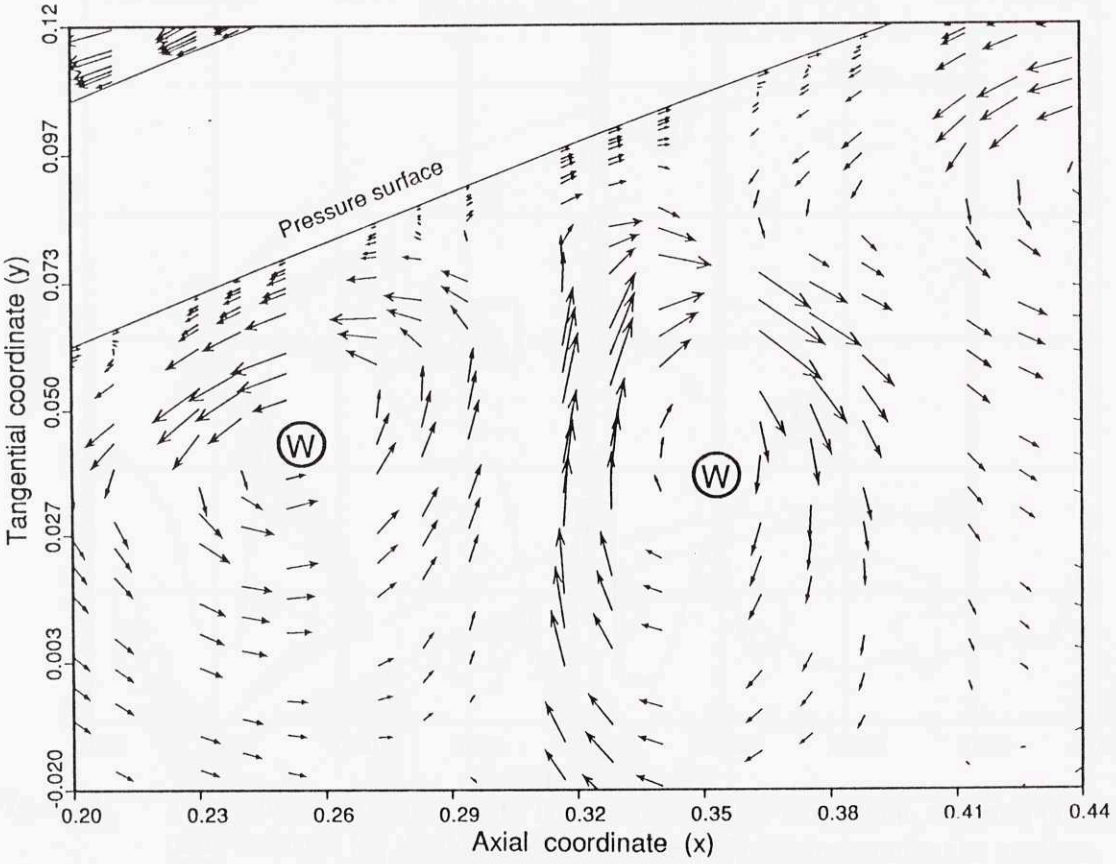

Fig.4.11b. Disturbance velocity vectors corresponding to the above pressure field.

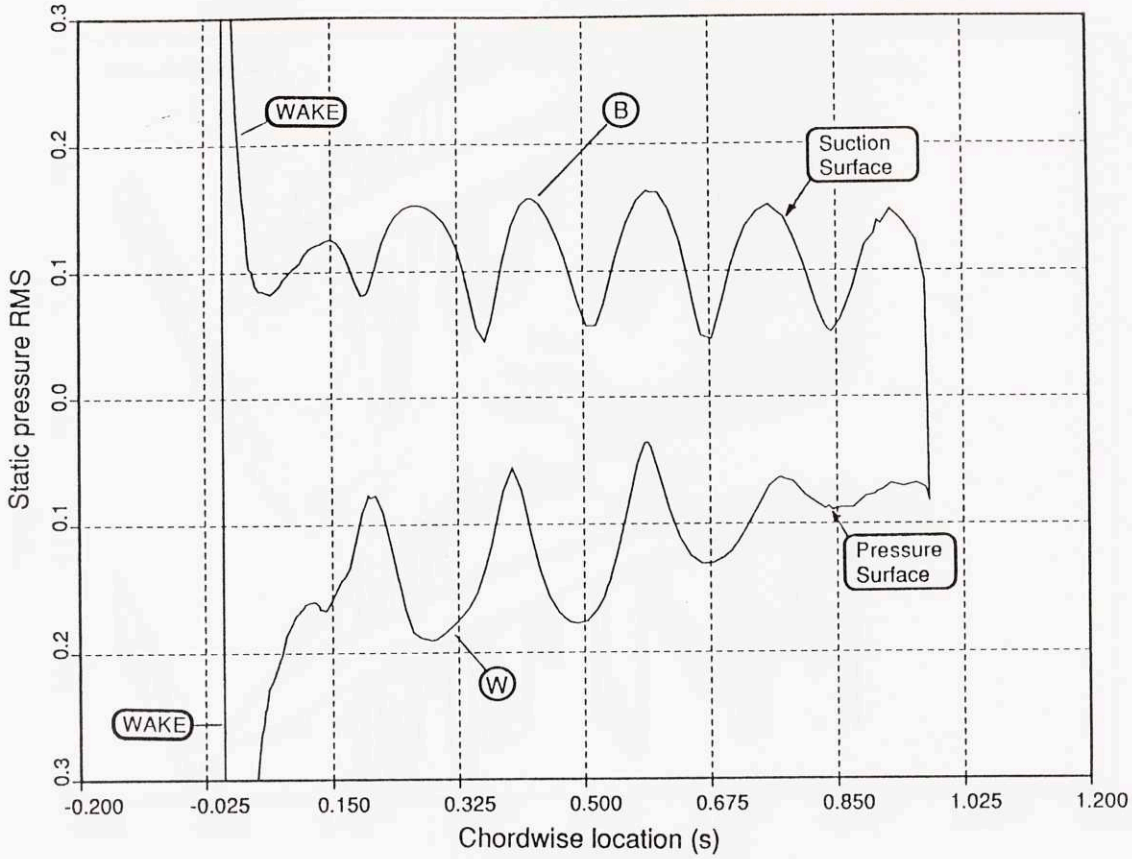

Fig.4.12. Distribution of the static pressure RMS on the blade surface.

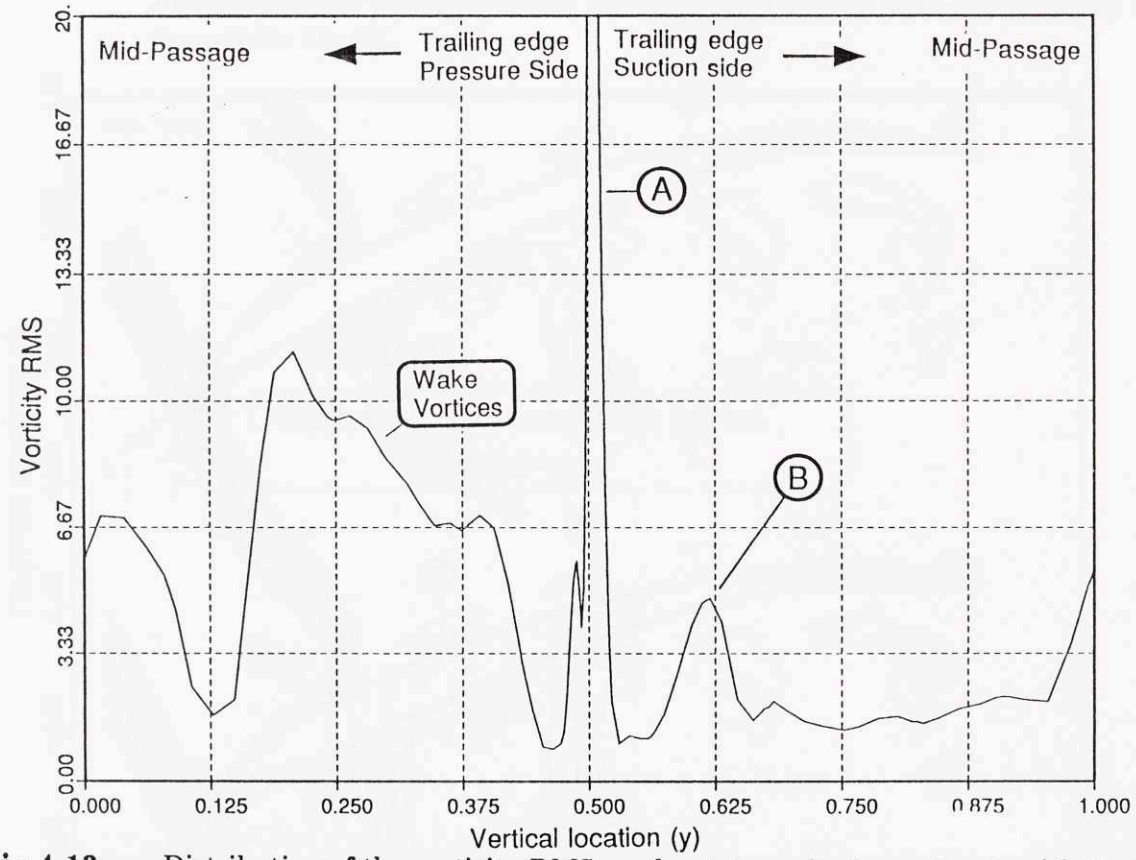

Fig.4.13. Distribution of the vorticity RMS on the stator exit plane, showing (1) discharge of B-vortices; (2) discharge of A-vortices; (3) discharge of wake vortices.

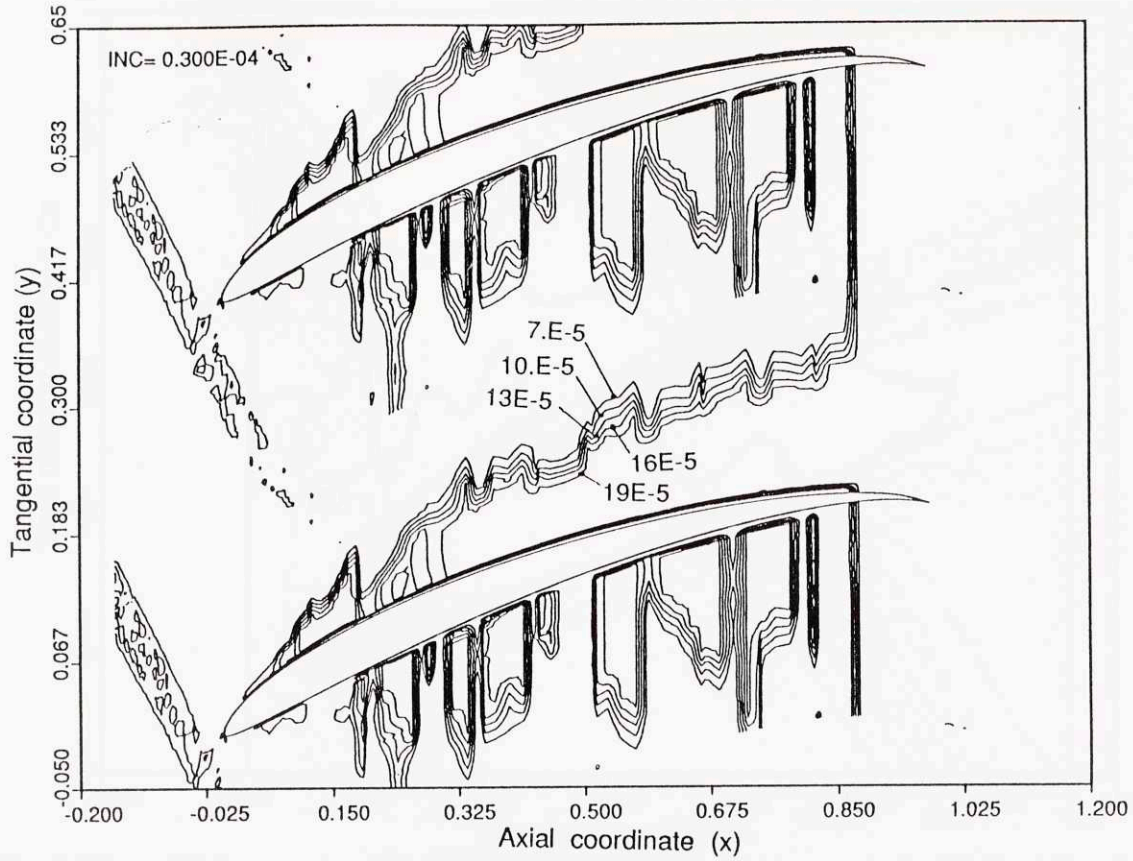

Fig.4.14. Eddy viscosity contours in the stator passage using the original (non-modified) Baldwin-Lomax model, showing diffusion rates about three times larger than those from Fig.4.7.

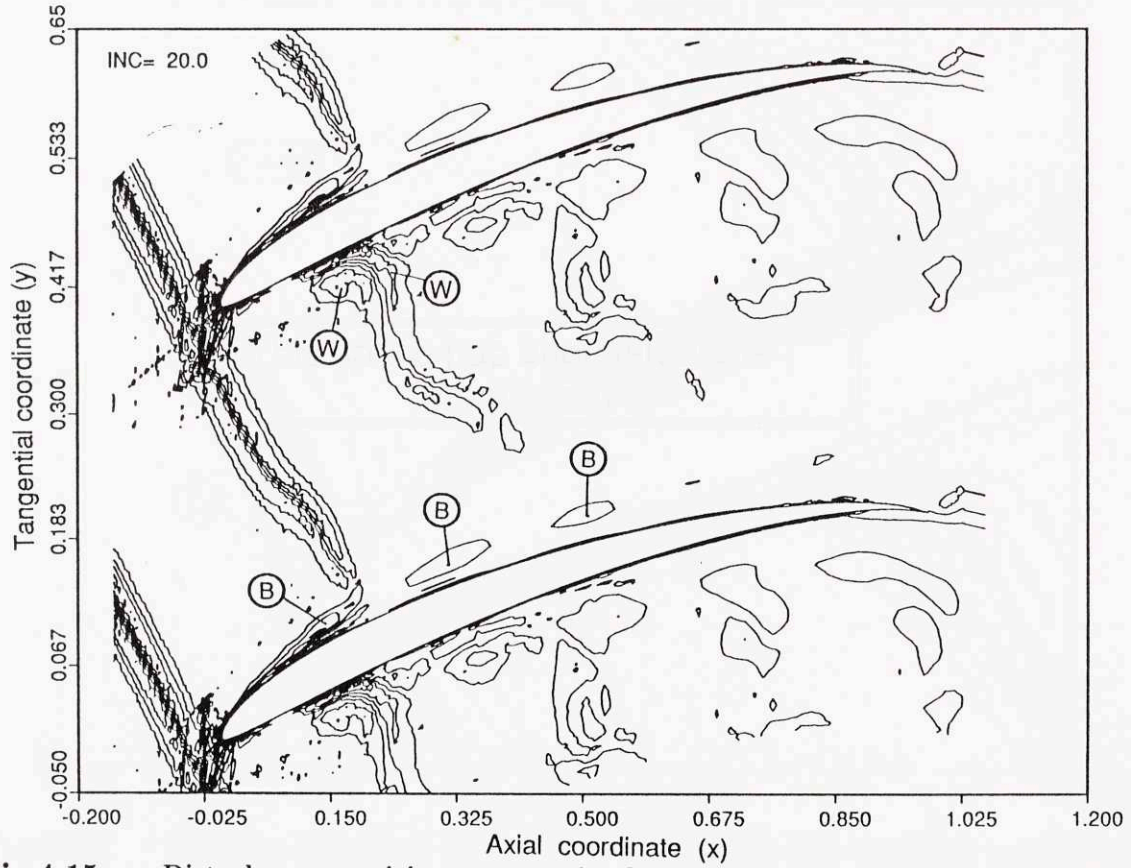

Fig.4.15. Disturbance vorticity contours in the stator passage computed with the eddy viscosity distribution from Fig.4.14. Note the rapid dissipation of the vortices.

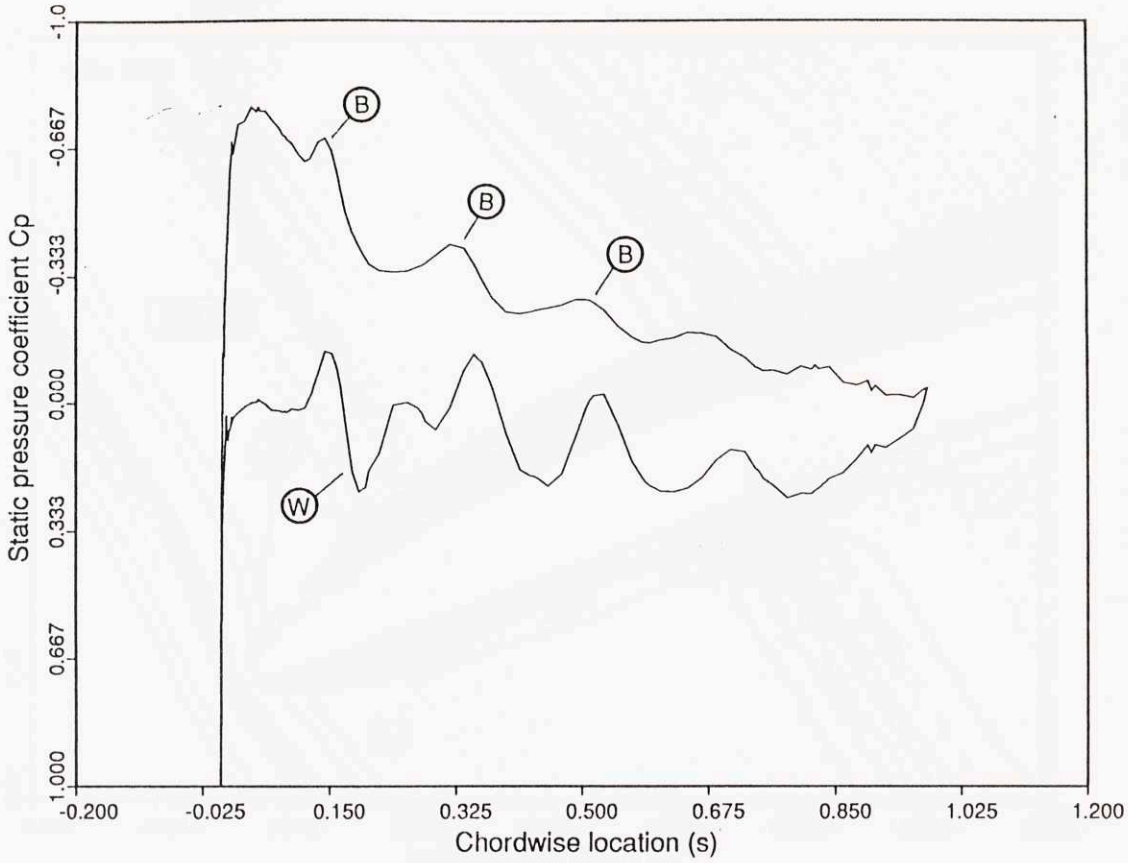

Fig.4.16. Static pressure distribution on the blade surface computed with the eddy viscosity distribution from Fig.4.14.

This space has been left blank intentionally

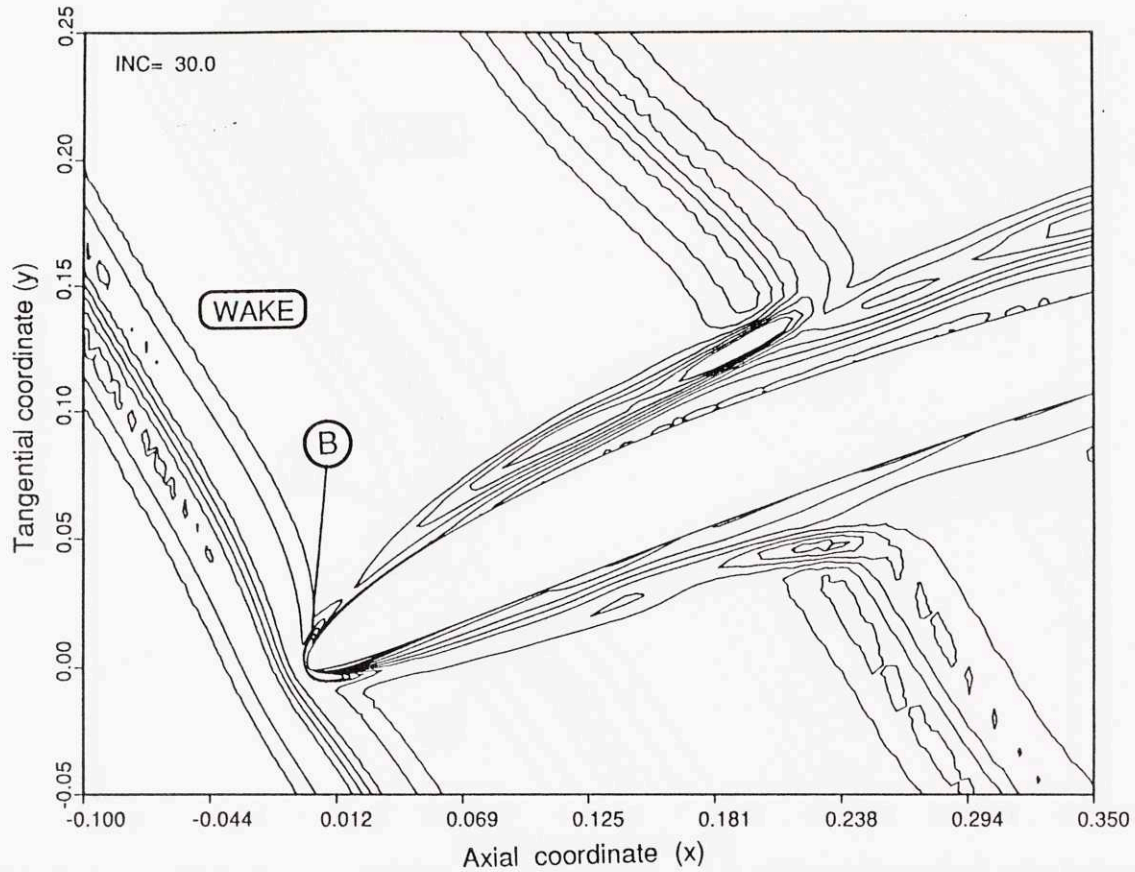

Fig.5.1a. Disturbance vorticity contours at time t_0 from linearized calculations with laminar base flow at Re=10,000.

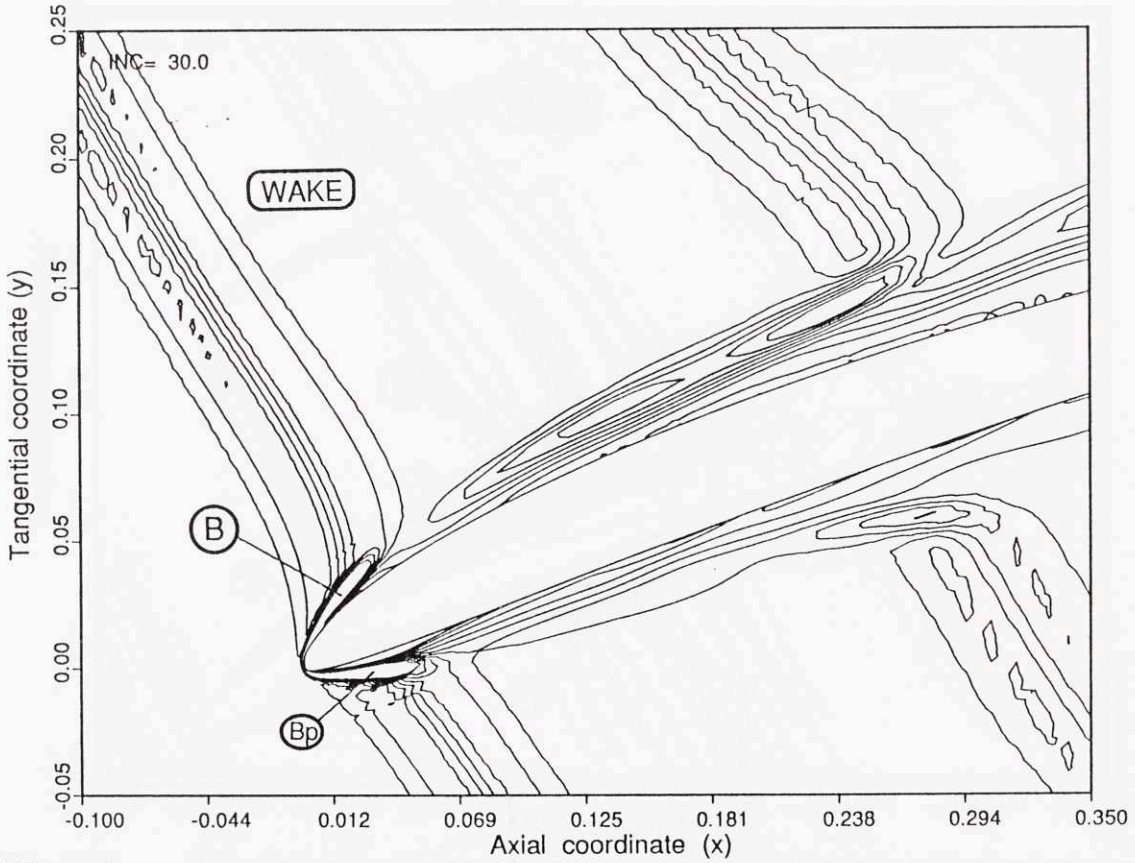

Fig.5.1b. Disturbance vorticity contours at time $t_0 + 0.2T$ from linearized calculations with laminar base flow at Re=10,000.

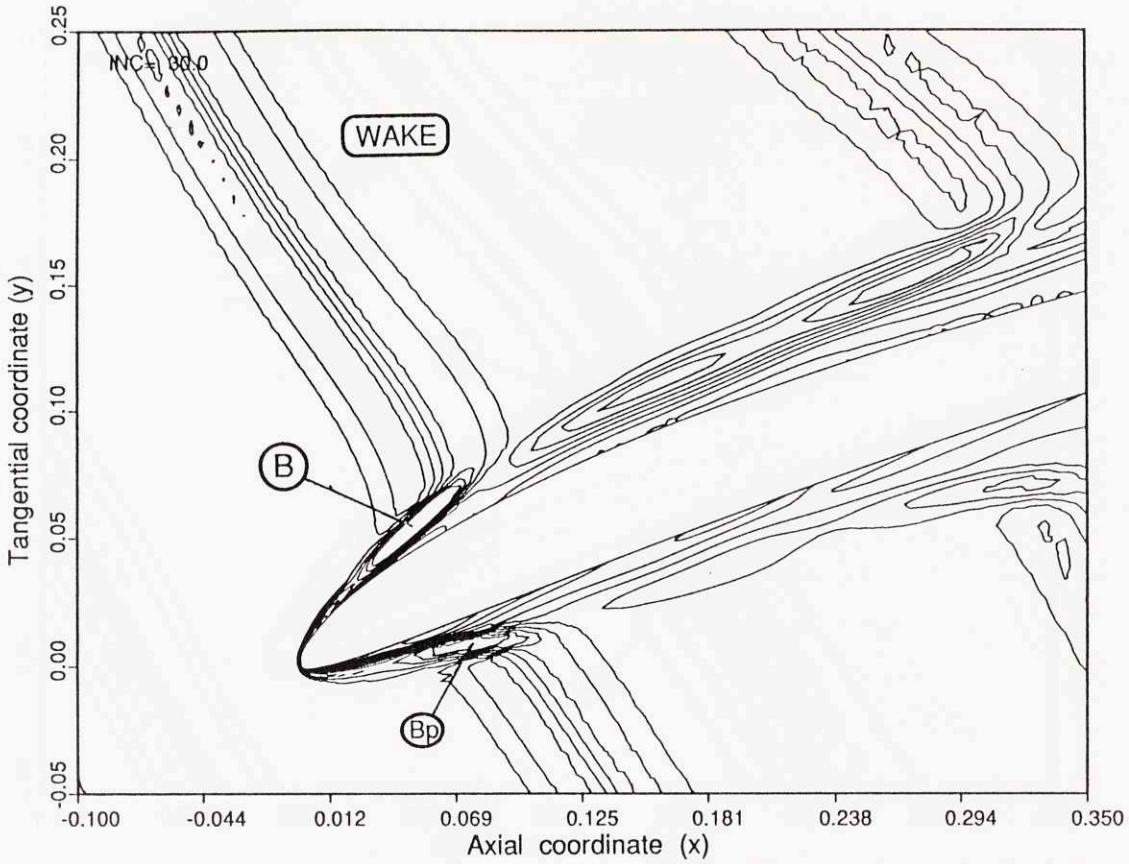

Fig.5.1c. Disturbance vorticity contours at time $t_0+0.4T$ from linearized calculations with laminar base flow at Re=10,000.

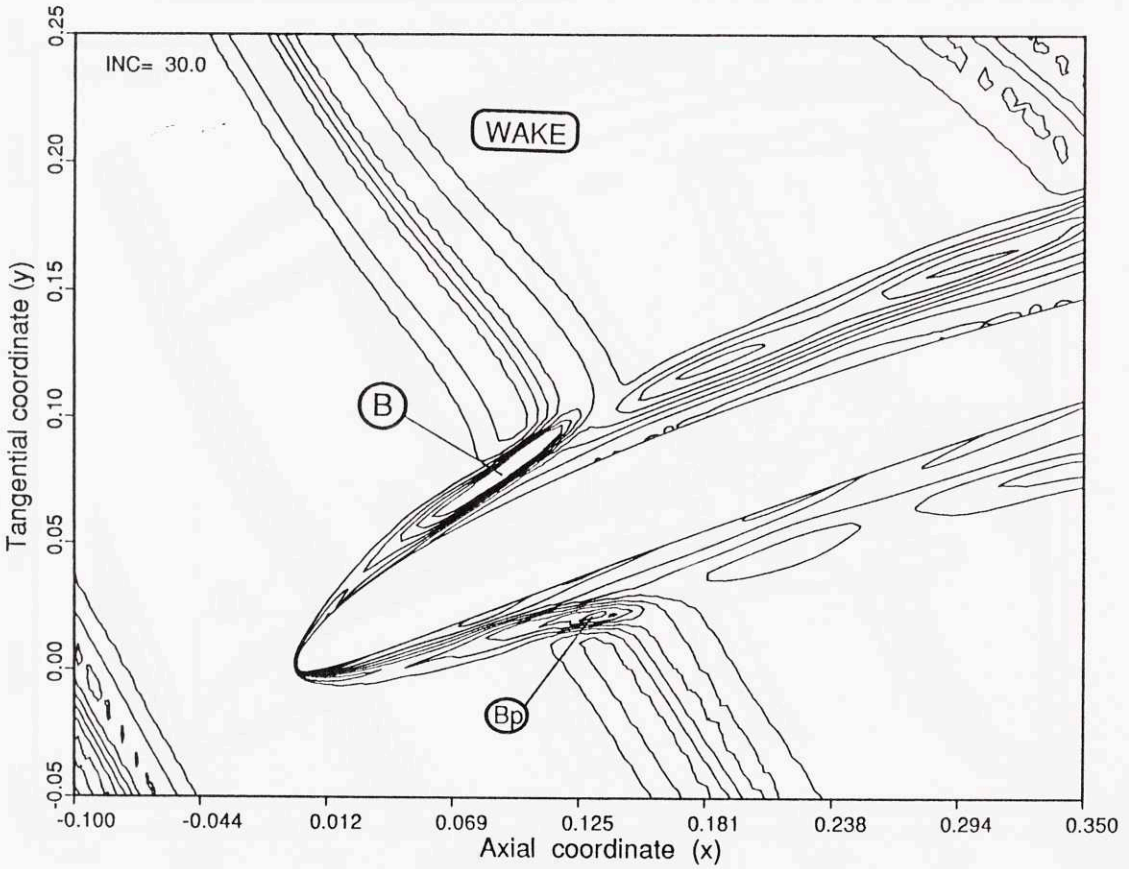

Fig.5.1d. Disturbance vorticity contours at time $t_0+0.6T$ from linearized calculations with laminar base flow at Re=10,000.

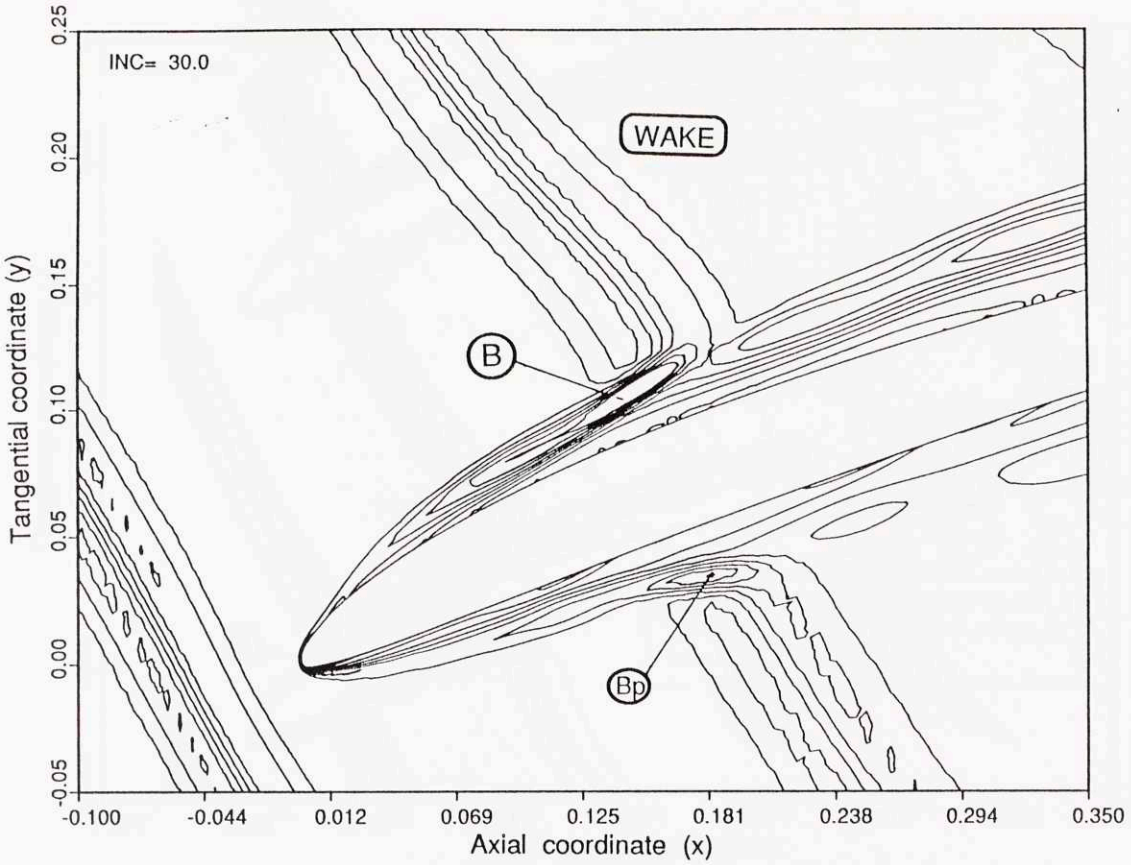

Fig.5.1e. Disturbance vorticity contours at time $t_0+0.8T$ from linearized calculations with laminar base flow at Re=10,000.

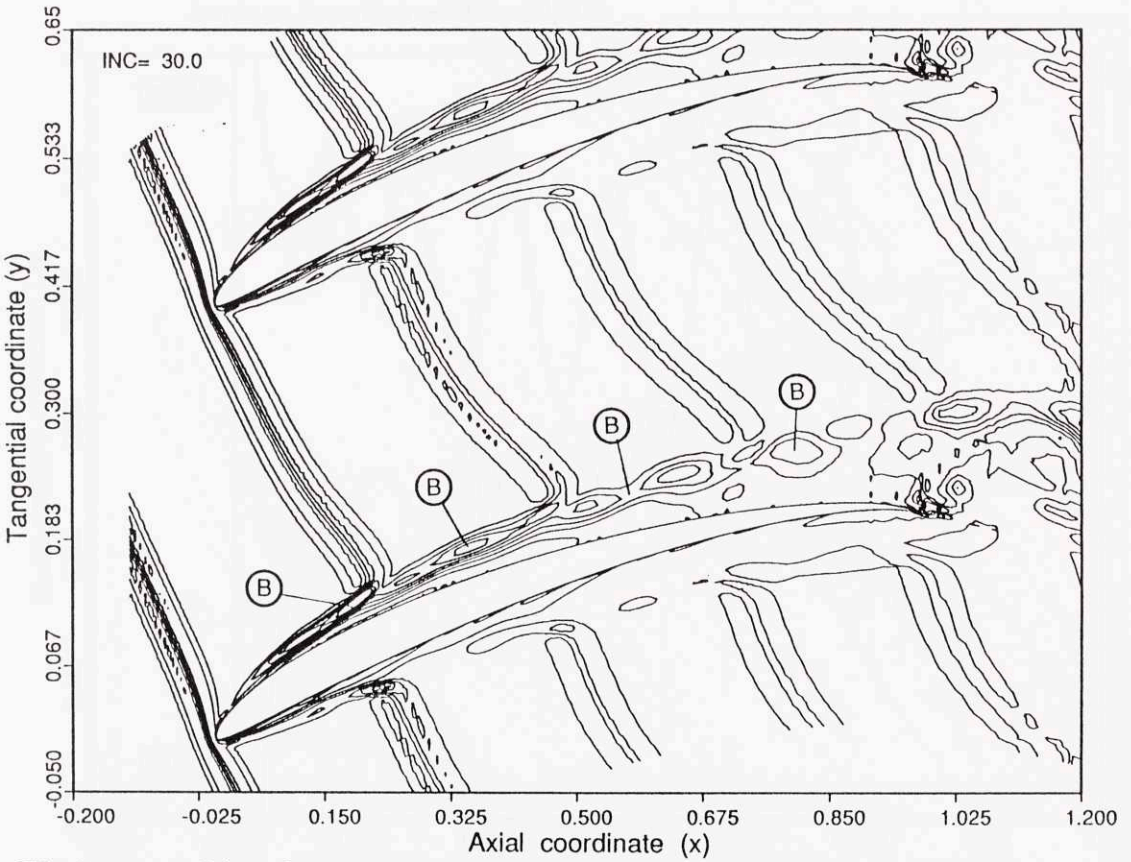

Fig.5.2a. Disturbance vorticity contours in the passage at time t_0, showing the absence of wake migration and wake vortices. Linearized calculations with a laminar base flow at Re=10,000.

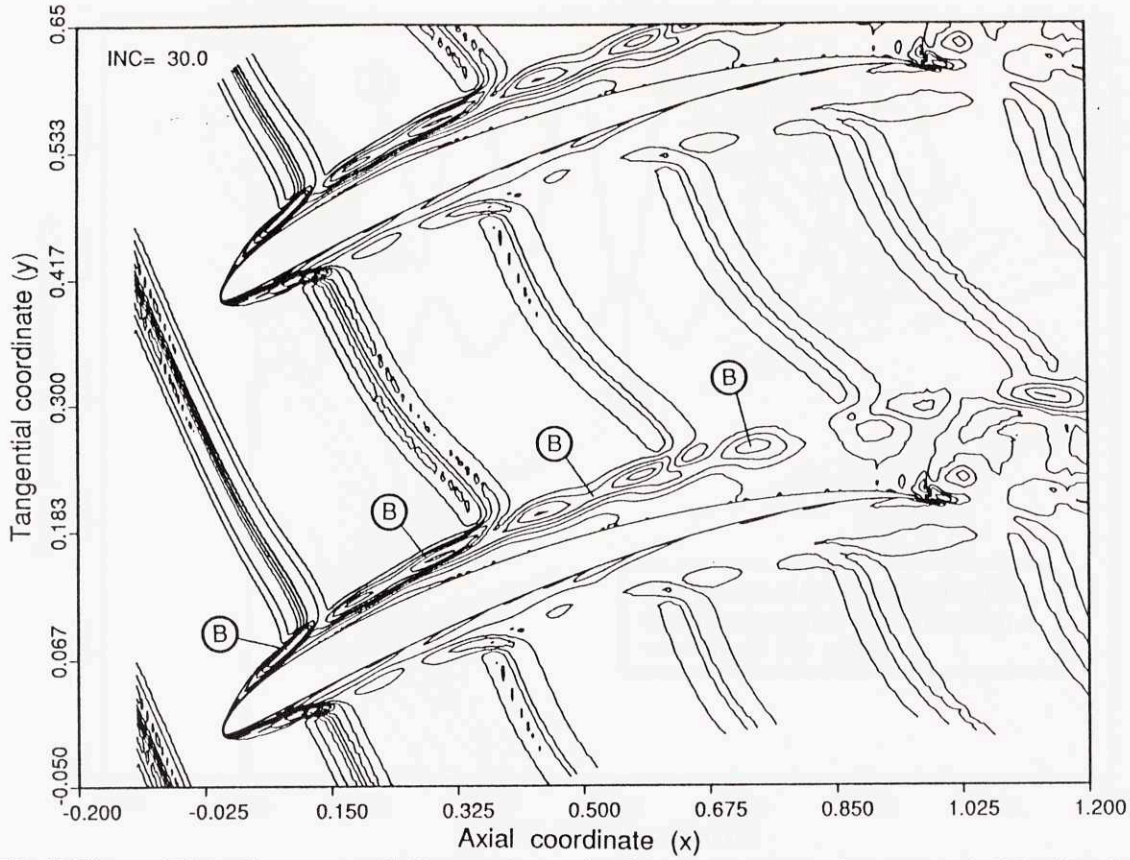

Fig.5.2b. Disturbance vorticity contours in the passage at time $t_0 + 0.6T$, showing the absence of wake migration and wake vortices. Linearized calculations with a laminar base flow at Re=10,000.

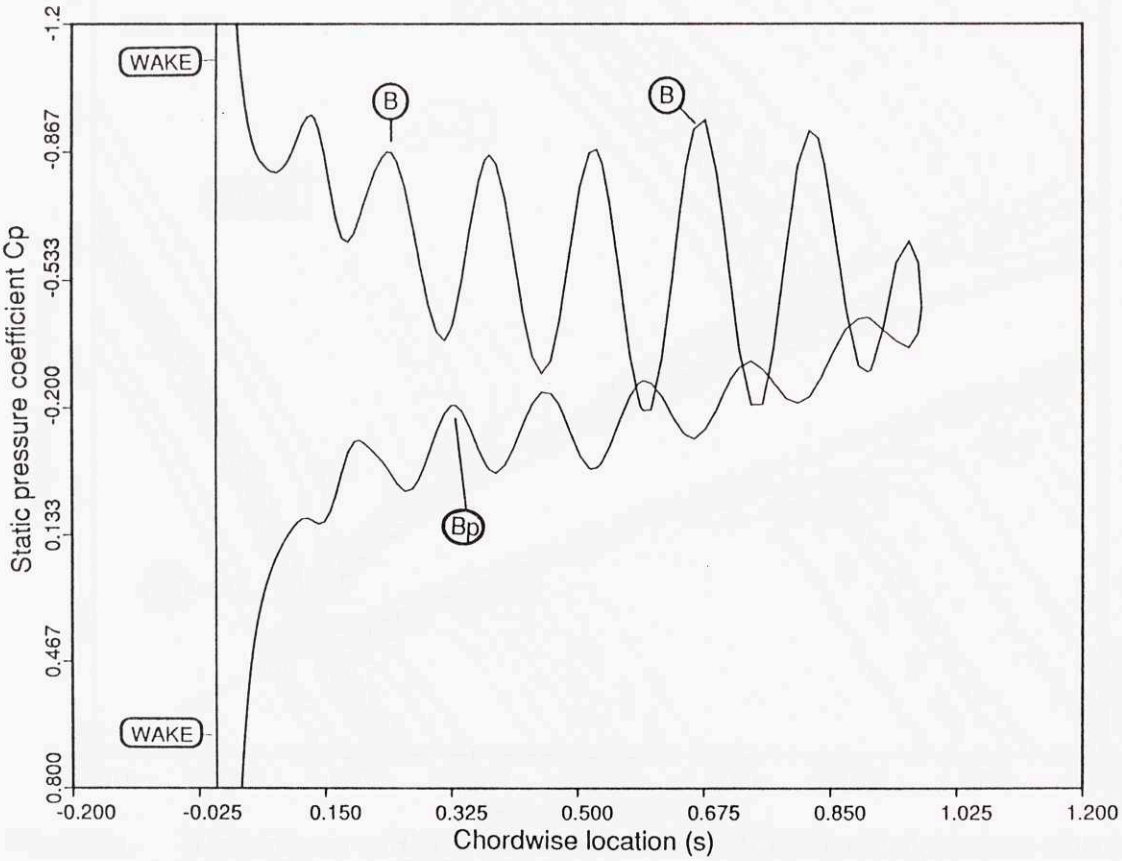

Fig.5.3a. Static pressure distribution on the blade surface at time t_0 from the linearized calculations with a laminar base flow at Re=10,000.

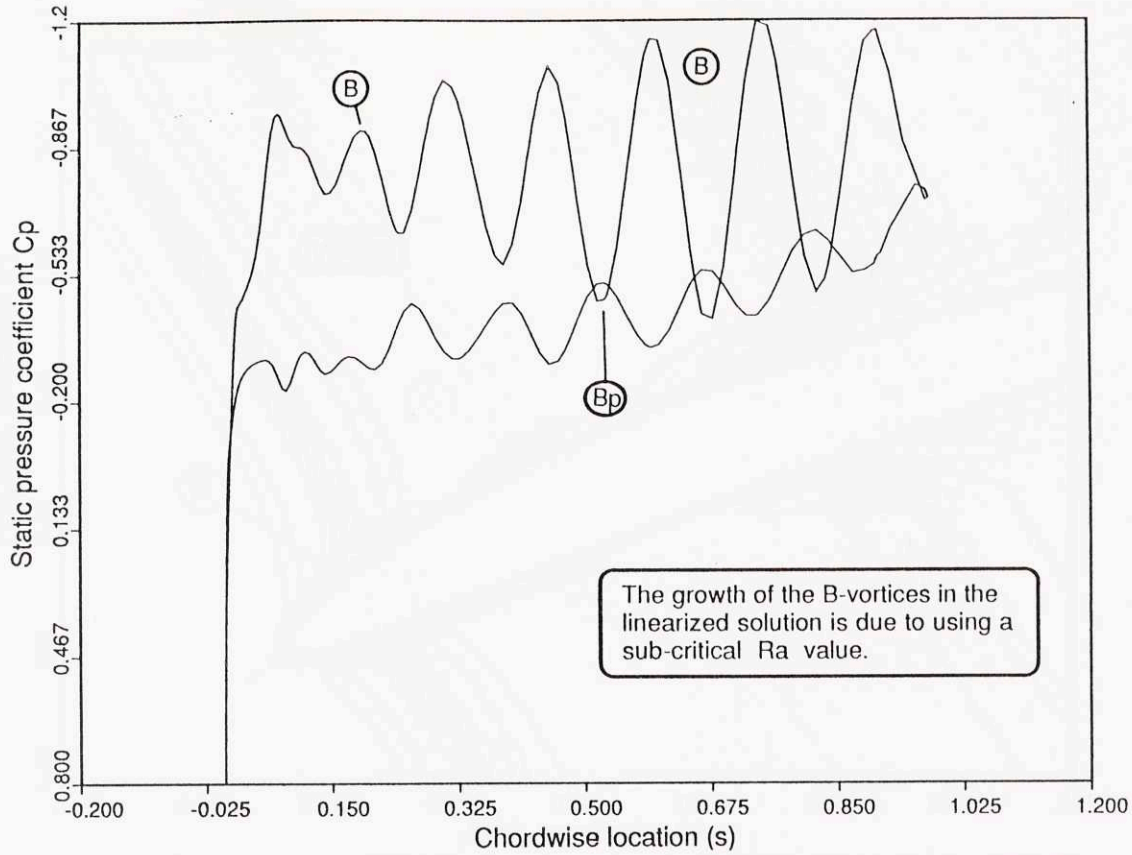

Fig.5.3b. Static pressure distribution on the blade surface at time $t_0 + 0.6T$ from the linearized calculations with a laminar base flow at Re=10,000.

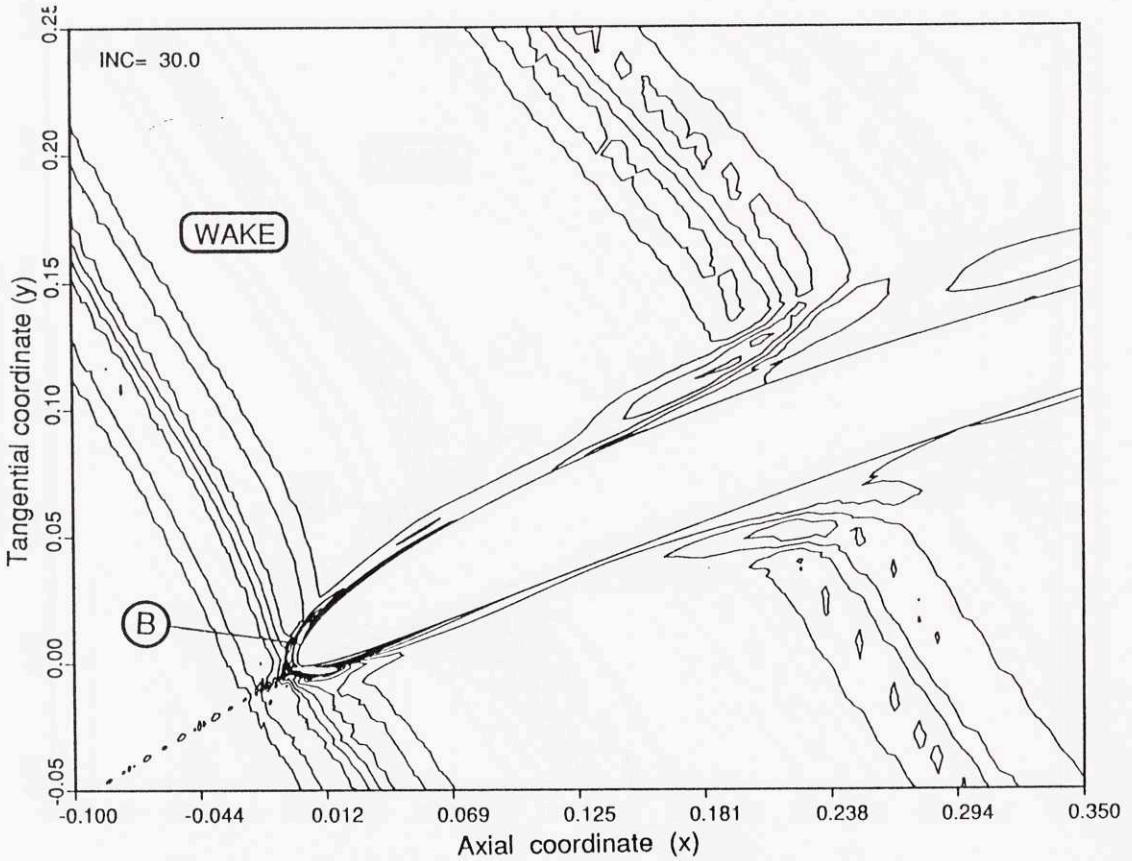

Fig.5.4a. Disturbance vorticity contours at time t_0. Linearized calculations with turbulent base flow at Re=1,000,000.

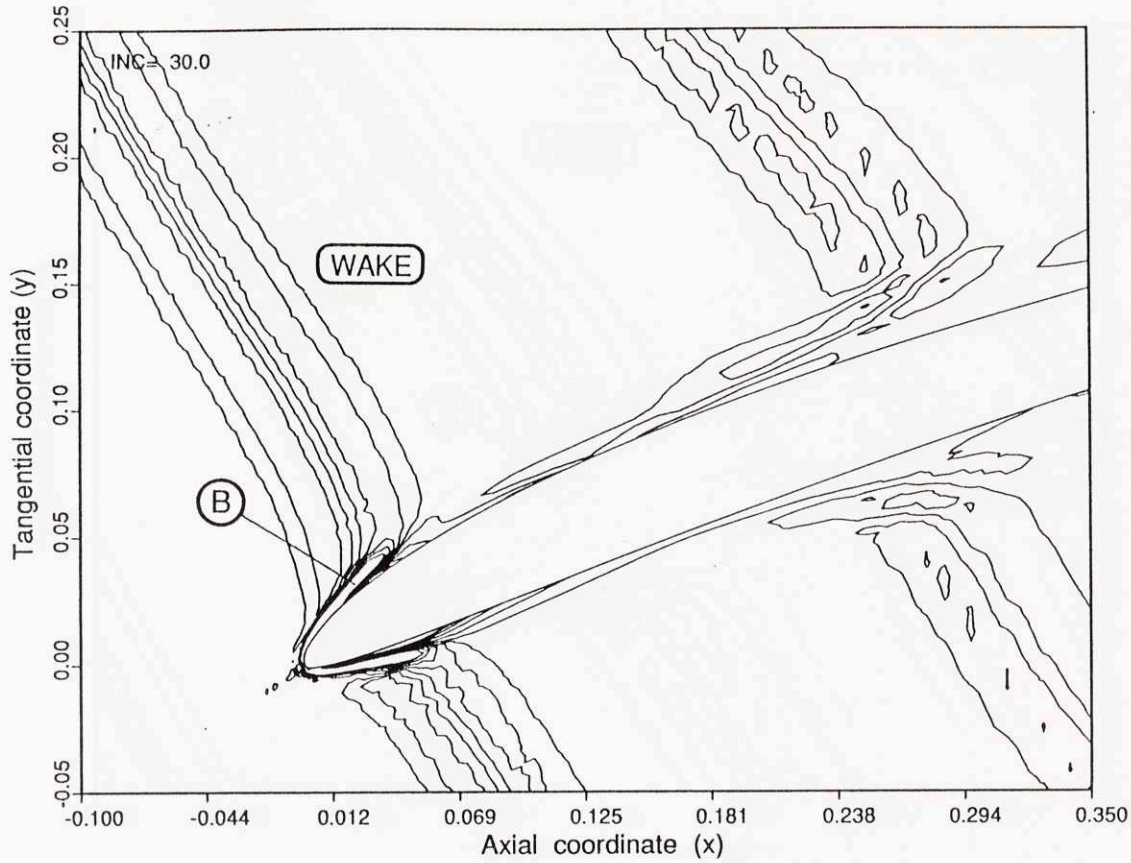

Fig.5.4b. Disturbance vorticity contours at time $t_0 + 0.2T$. Linearized calculations with turbulent base flow at Re=1,000,000.

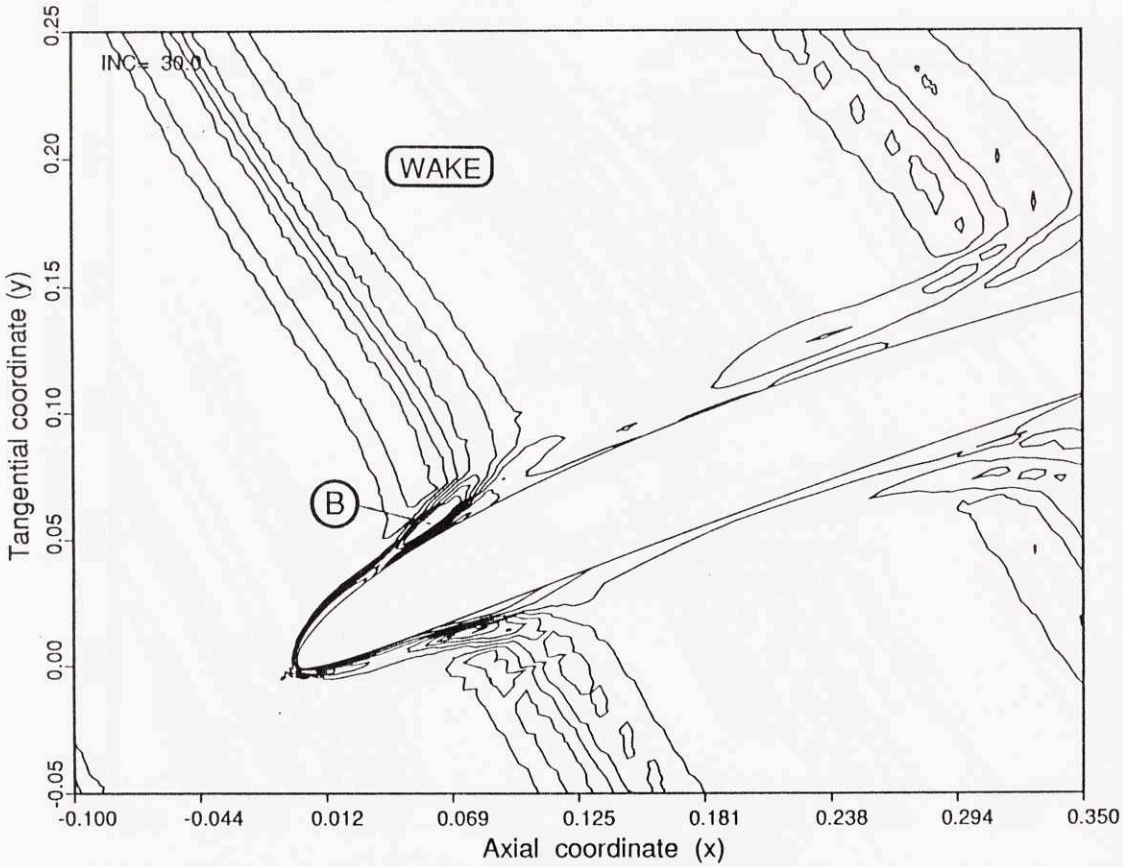

Fig.5.4c. Disturbance vorticity contours at time $t_0 + 0.4T$. Linearized calculations with turbulent base flow at Re=1,000,000.

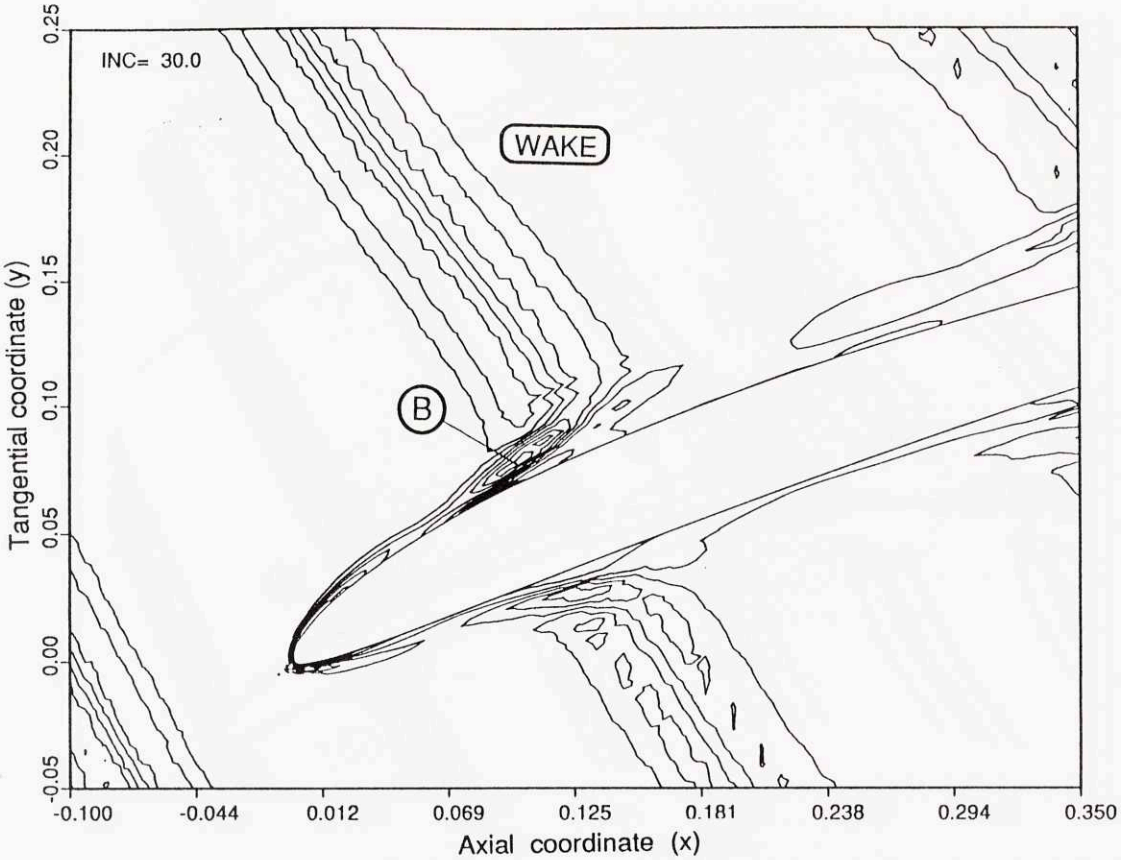

Fig.5.4d. Disturbance vorticity contours at time $t_0 + 0.6T$. Linearized calculations with turbulent base flow at Re=1,000,000.

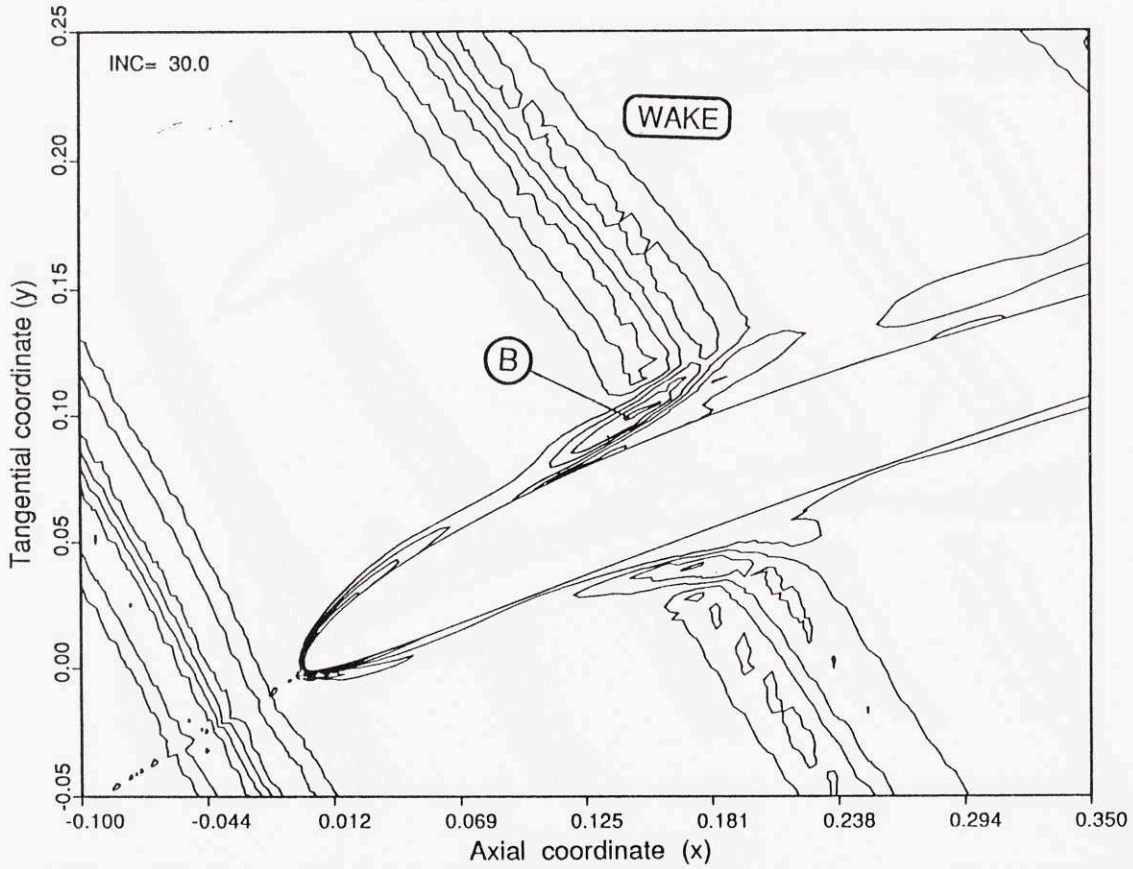

Fig.5.4e. Disturbance vorticity contours at time $t_0 + 0.8T$. Linearized calculations with turbulent base flow at Re=1,000,000.

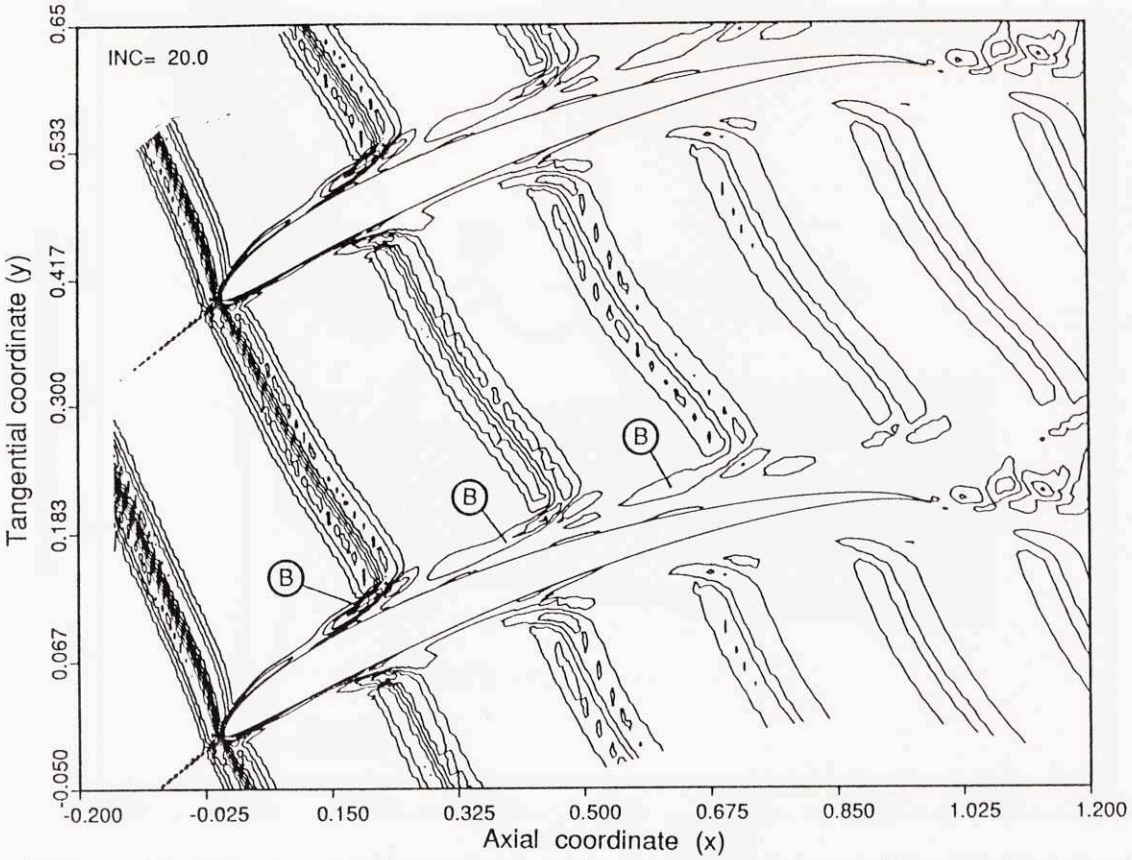

Fig.5.5a. Disturbance vorticity contours in the passage at time t_0. Linearized calculations with a turbulent base flow at Re=1,000,000.

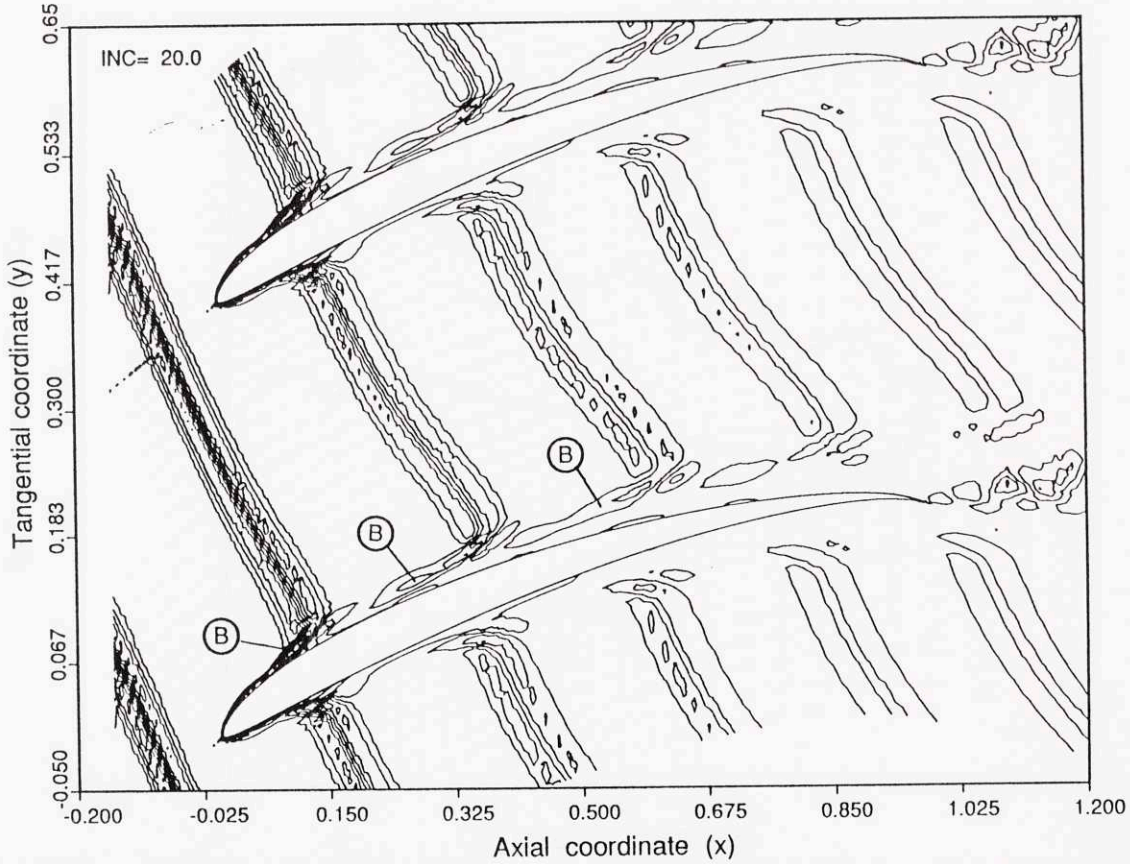

Fig.5.5b. Disturbance vorticity contours in the passage at time $t_0 + 0.6T$. Linearized calculations with a turbulent base flow at Re=1,000,000.

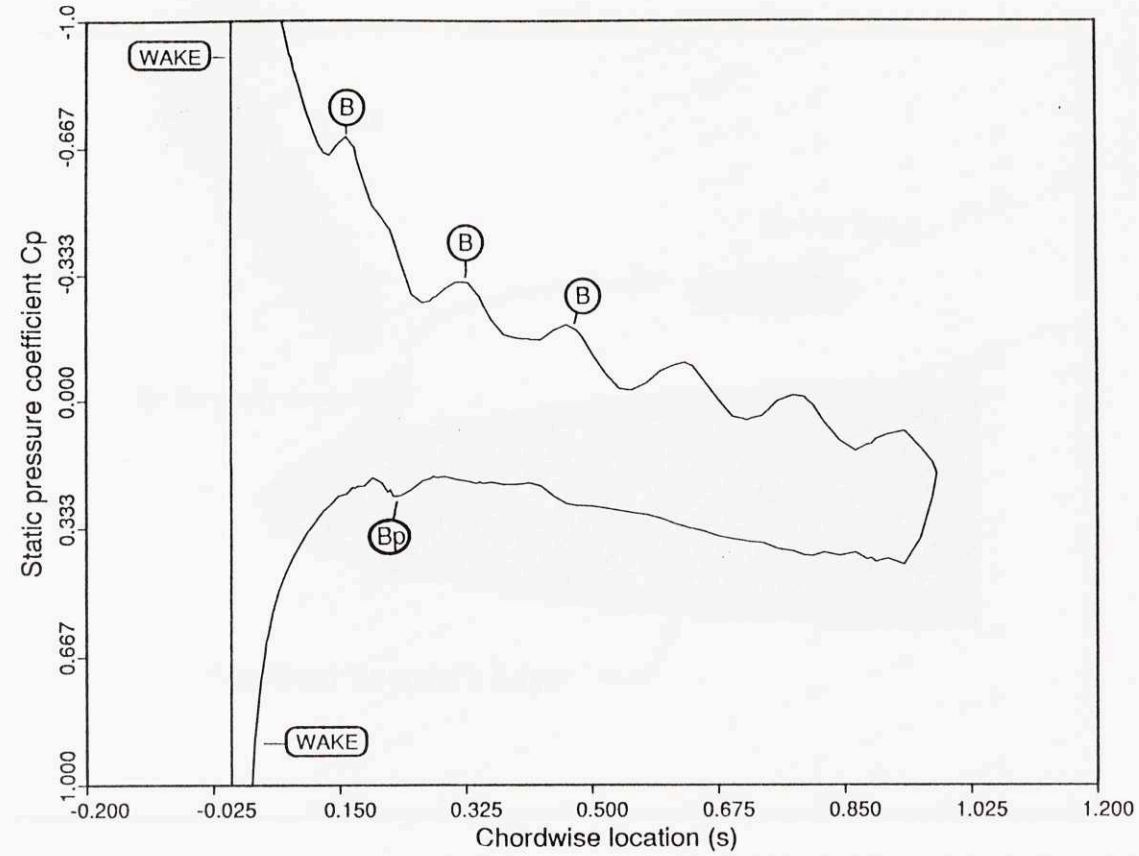

Fig.5.6a. Static pressure distribution on the blade surface at time t_0 from the linearized calculations with a turbulent base flow at Re=1,000,000.

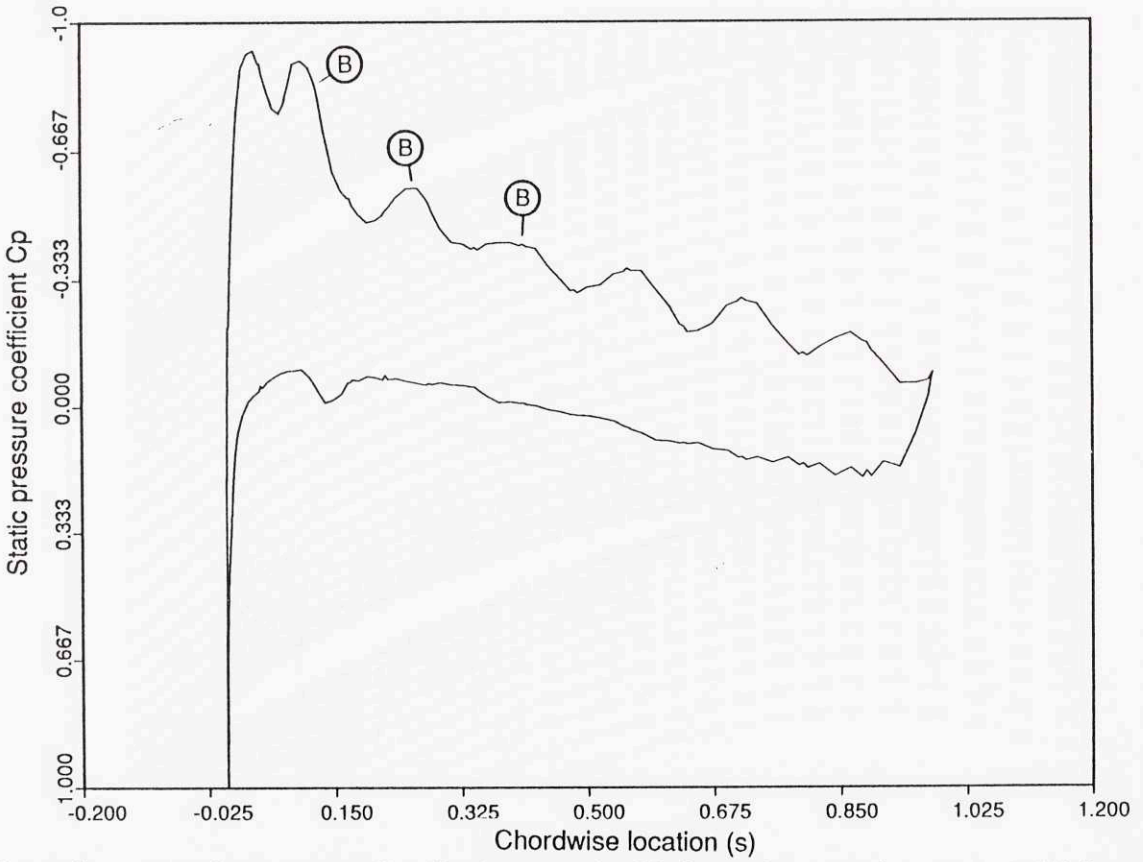

Fig.5.6b. Static pressure distribution on the blade surface at time $t_0 + 0.6T$ from the linearized calculations with a turbulent base flow at Re=1,000,000.

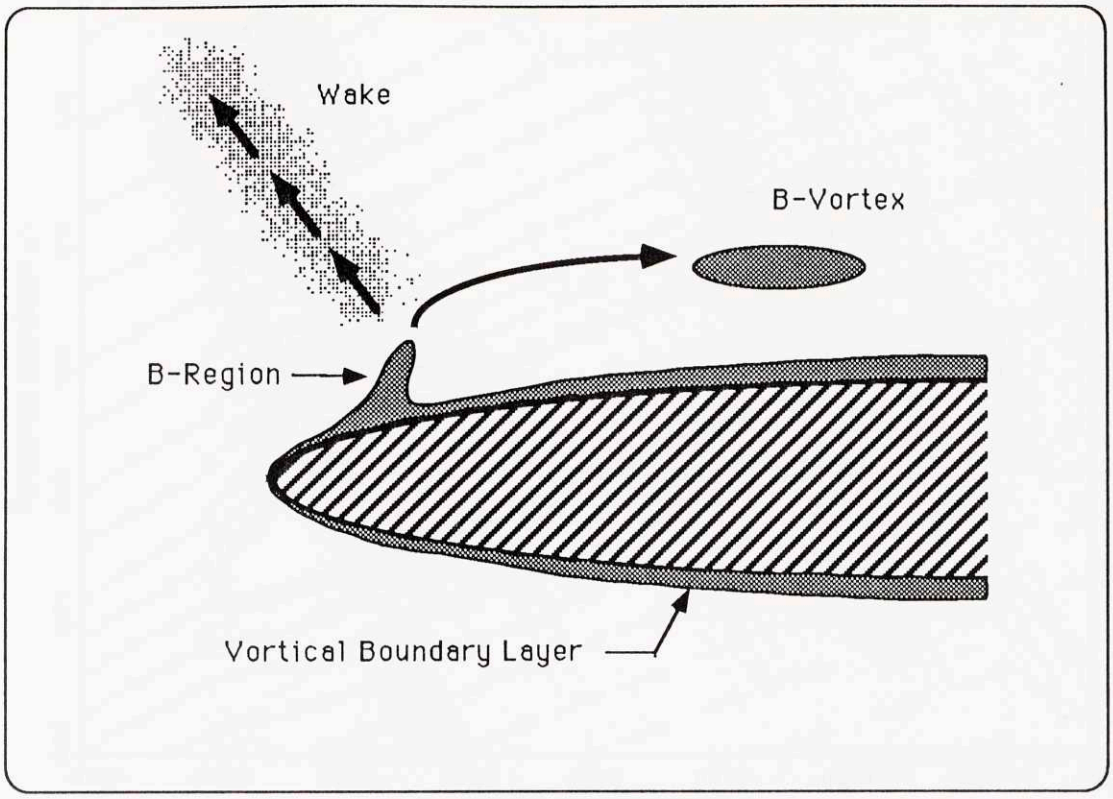

Fig.5.7. Schematic representation of the B-vortex production involving a boundary layer distortion and detachment mechanism.

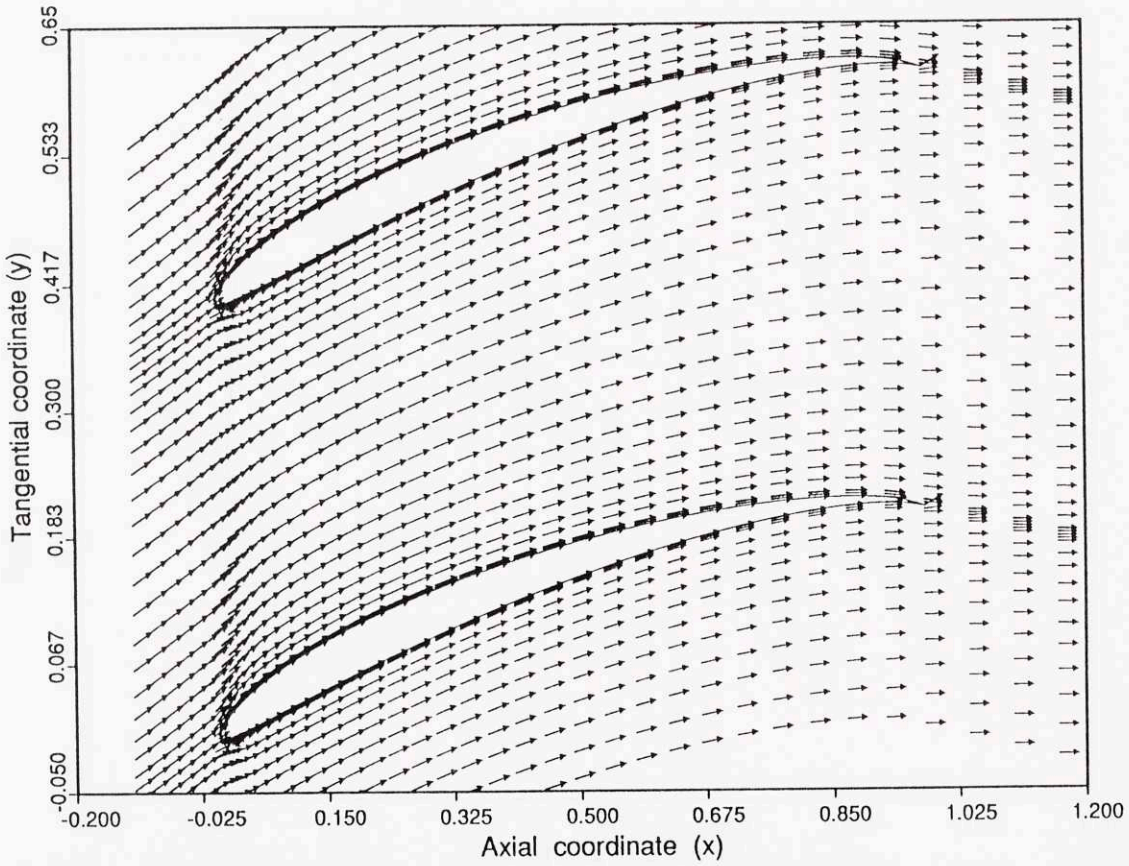

Fig.5.8a. Steady inviscid flow velocity vectors in the stator passage. Calculations using PCPANNEL code (McFarland [32]).

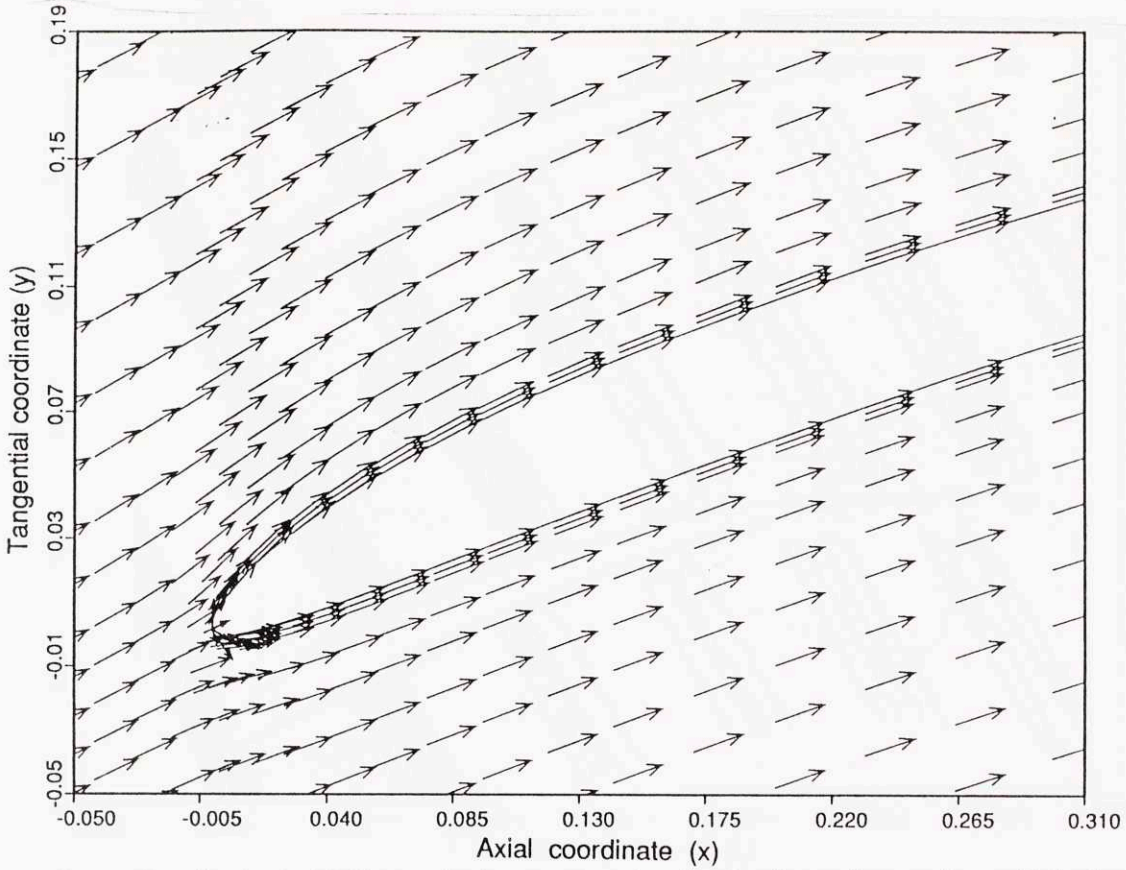

Fig.5.8b. Steady inviscid flow velocity vectors in the leading edge region. Calculations using PCPANNEL code (McFarland [32]). Note the absence of vortical B.S.

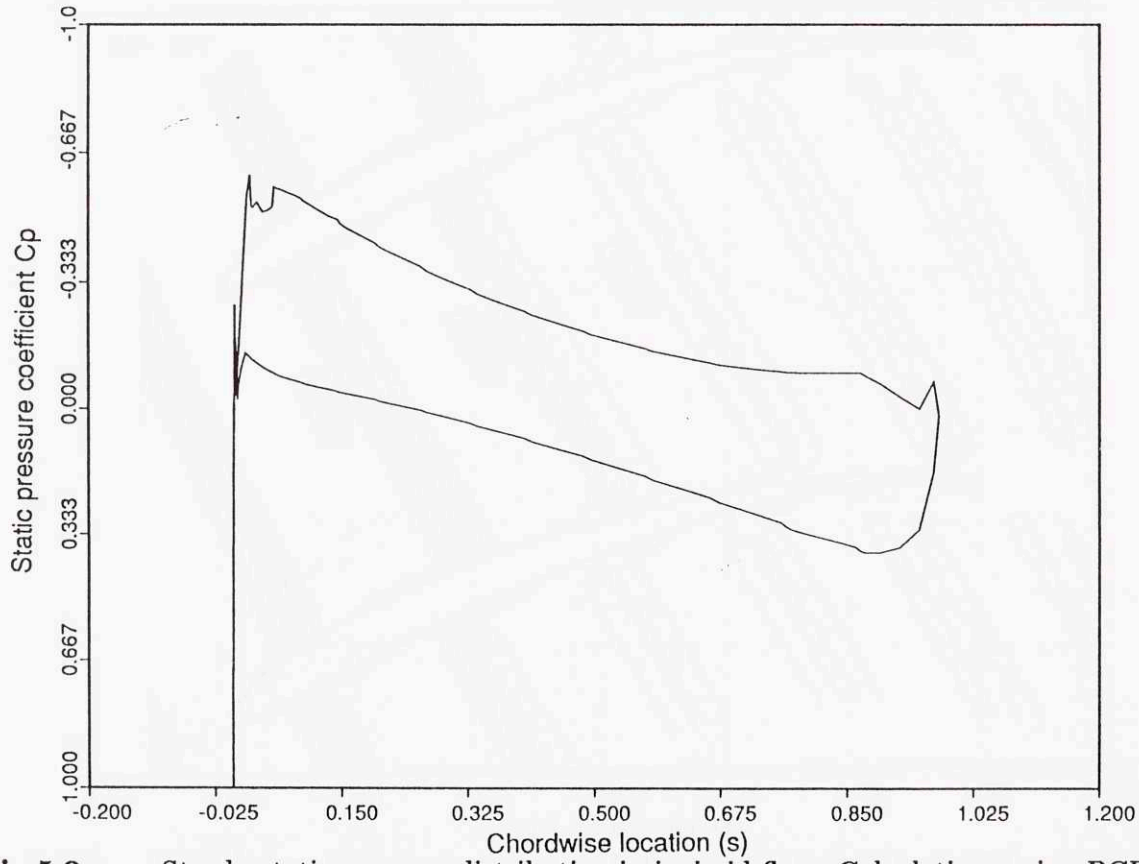

Fig.5.9. Steady static pressure distribution in inviscid flow. Calculations using PCPANNEL code (McFarland [32]).

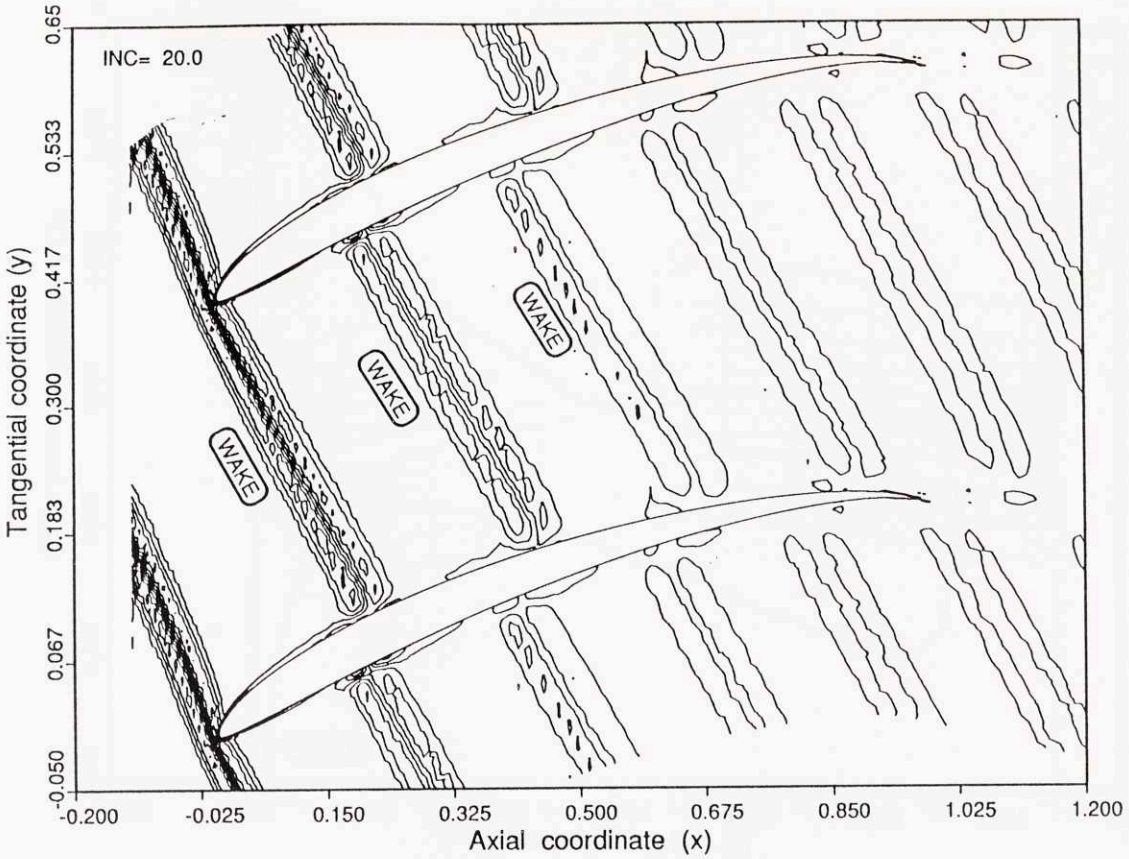

Fig.5.10a. Disturbance vorticity contours in the passage at time t_0. Linearized calculations with an inviscid base flow.

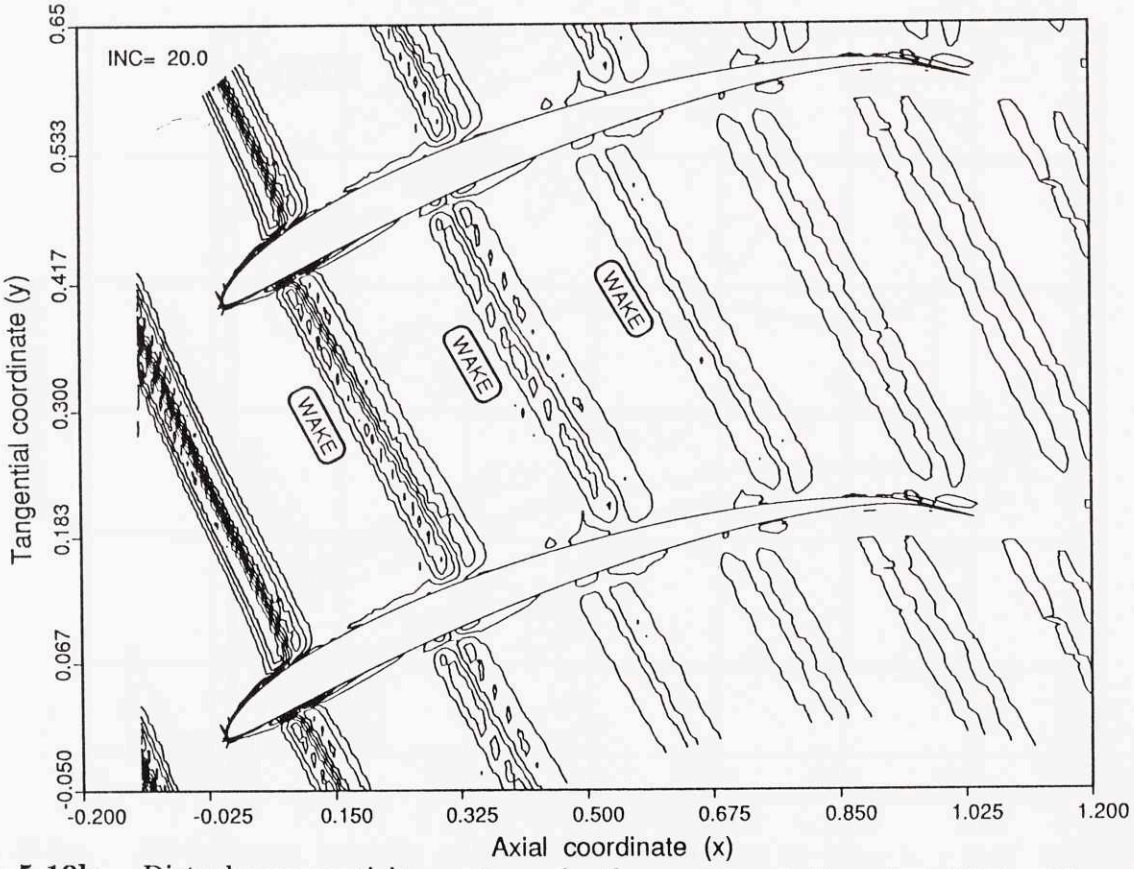

Fig.5.10b. Disturbance vorticity contours in the passage at time $t_0 + 0.6T$. Linearized calculations with an inviscid base flow.

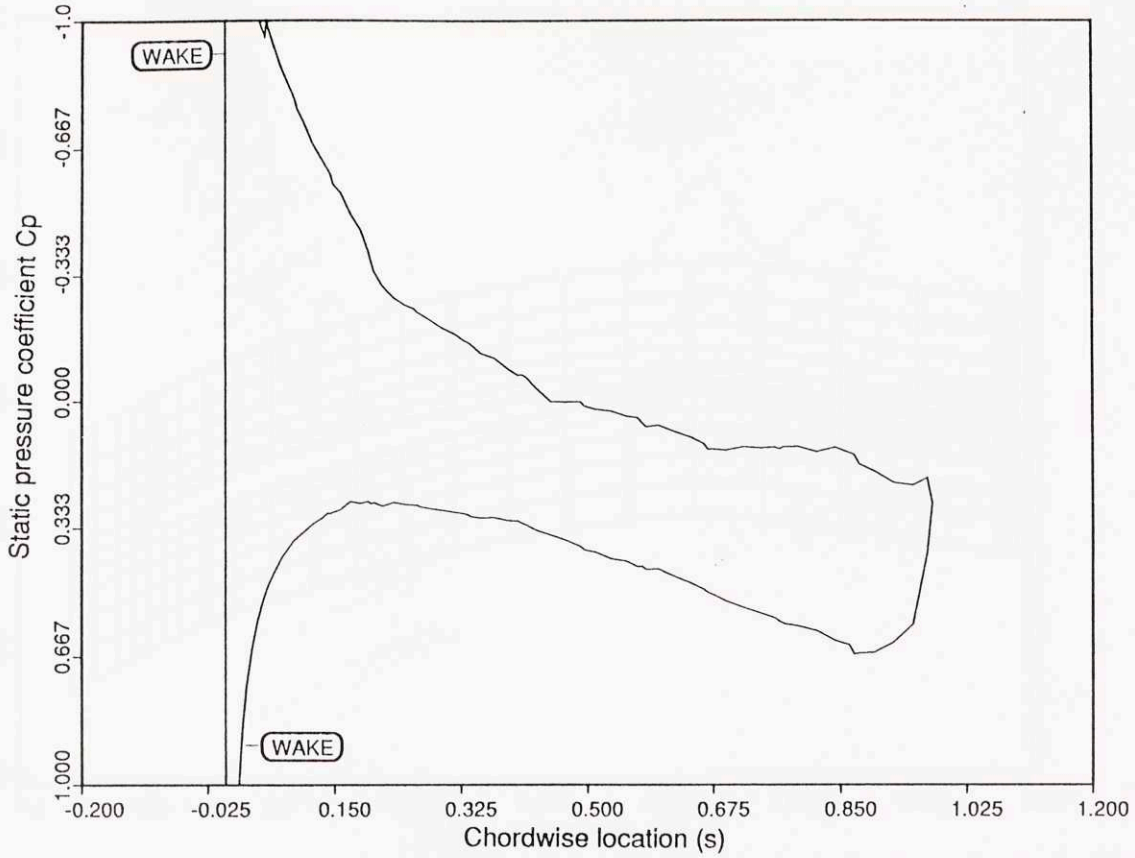

Fig.5.11 Static pressure distribution on the blade surface at time t_0 from the linearized calculations with an inviscid base flow.

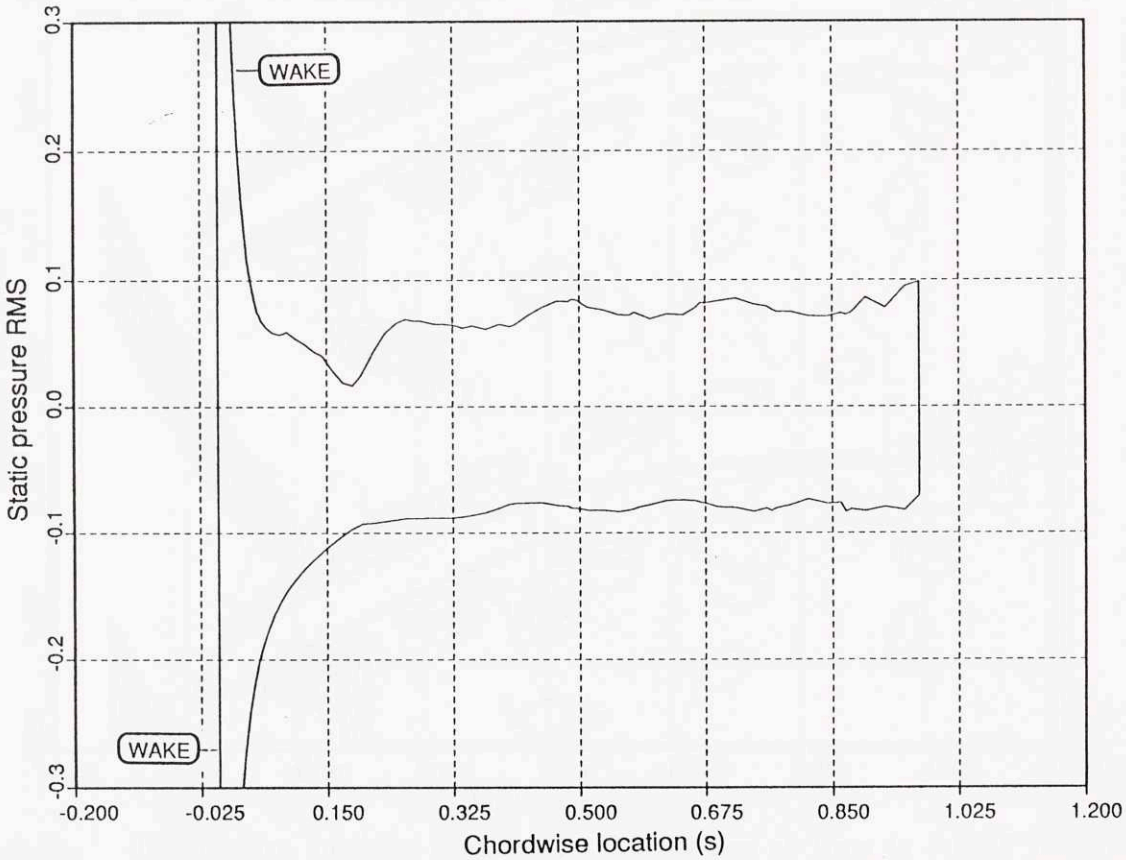

Fig.5.12. Distribution of the static pressure RMS on the blade surface from the linearized calculations with an inviscid base flow; showing flat, low RMS levels mainly due to potential effects.

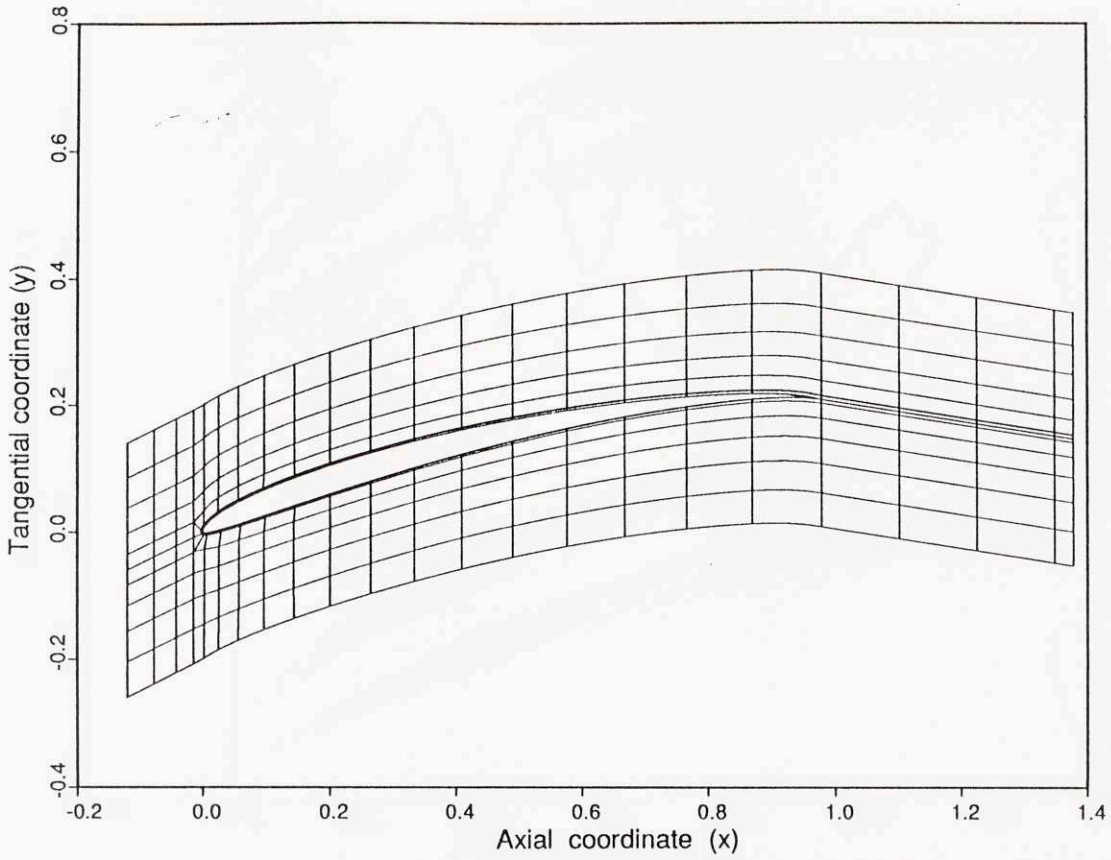

Fig.6.1. Spectral-element grid used in the parametric study (262 elements, Re=10,000).

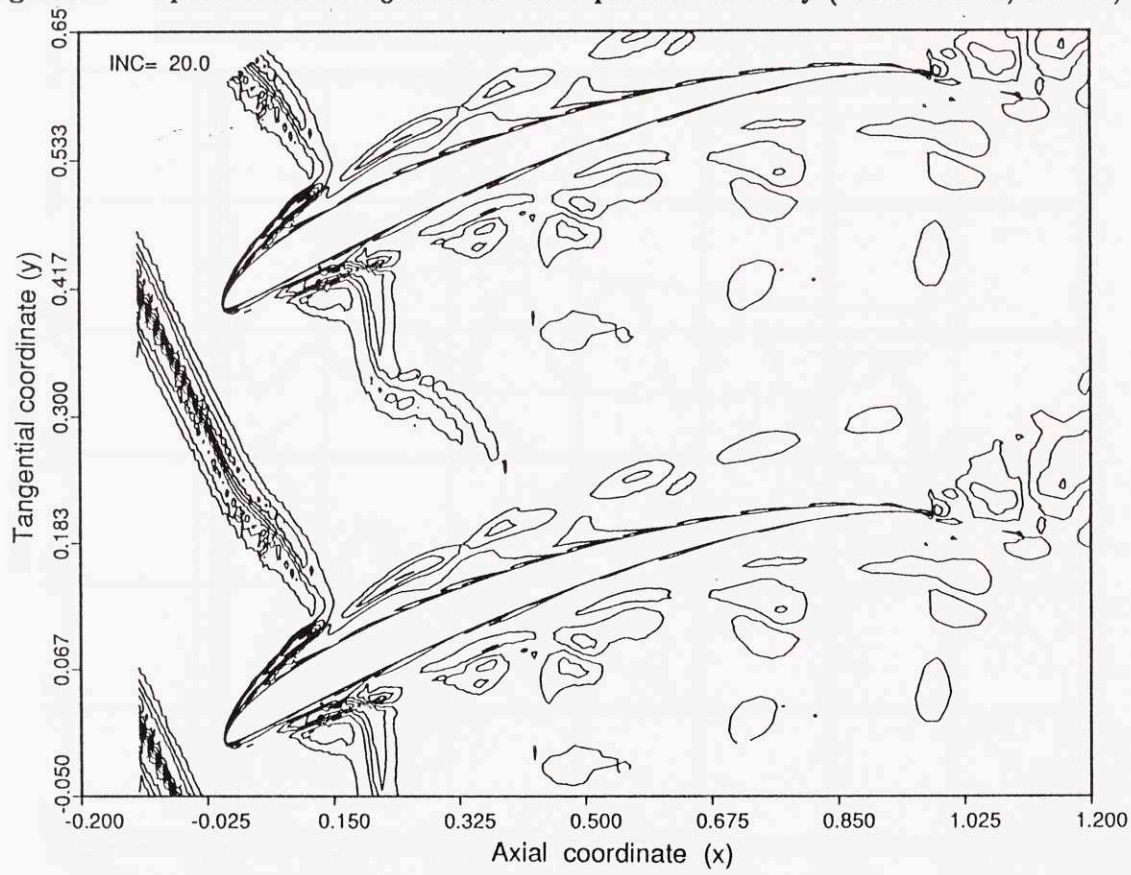

Fig.6.2a. Disturbance vorticity contours in the passage at time $t_0 + 0.6T$ from a re-calculated baseline flow with the 262 elements grid.

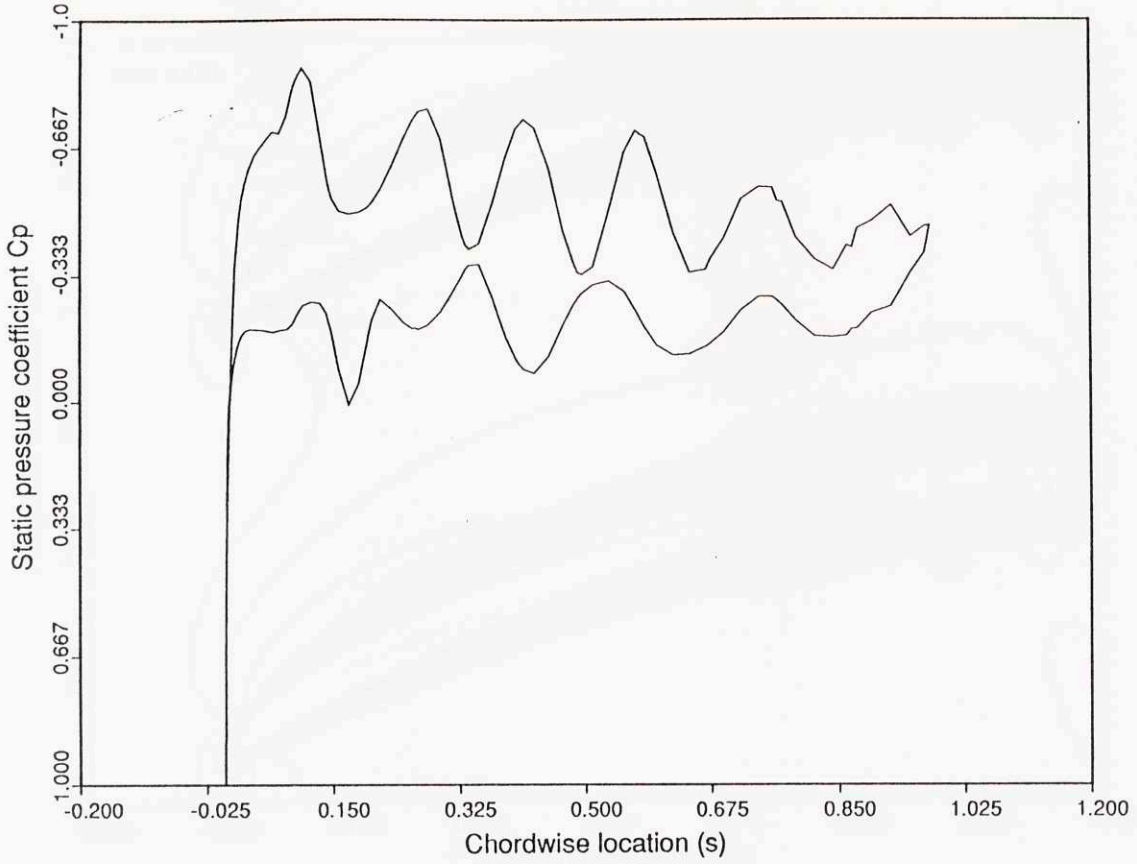

Fig.6.2b. Static pressure distribution on the blade surface at time $t_0 + 0.6T$ from a re-calculated baseline flow with the 262 elements grid.

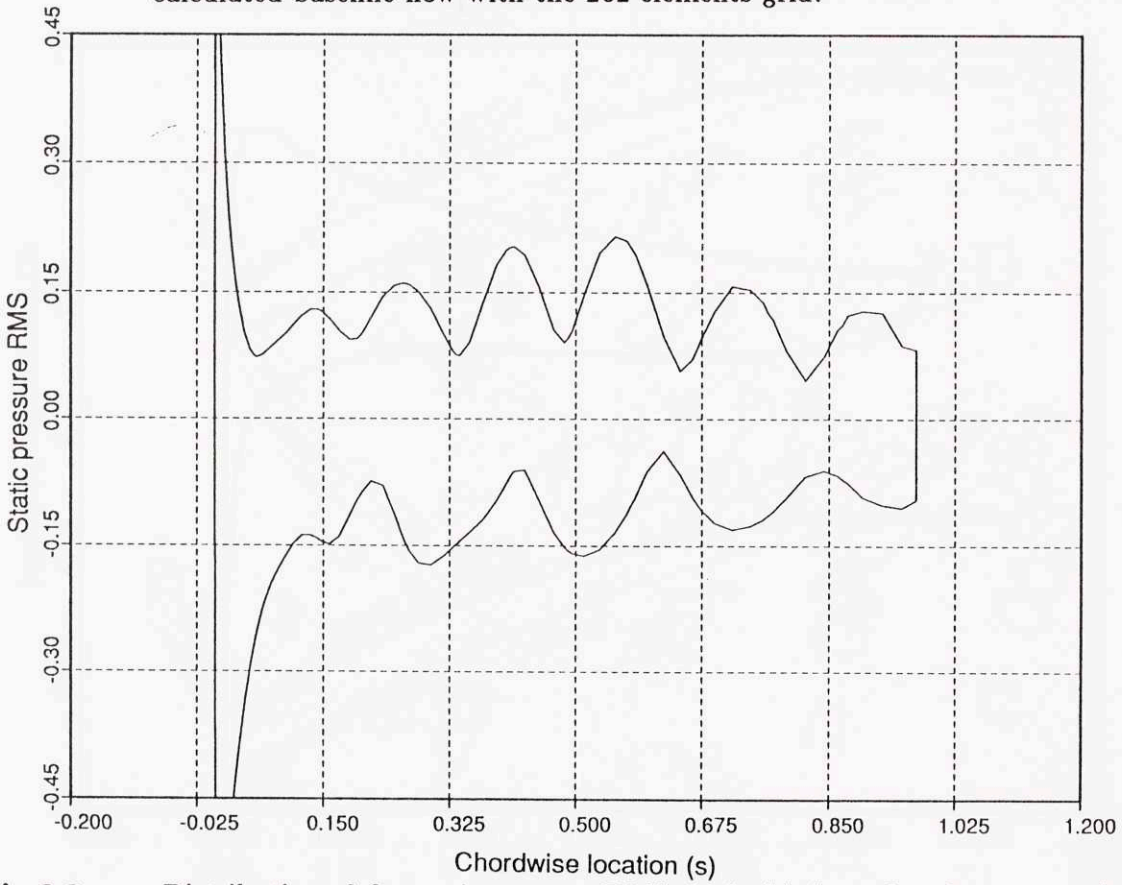

Fig.6.2c. Distribution of the static pressure RMS on the blade surface from a re-calculated baseline flow with the 262 elements grid.

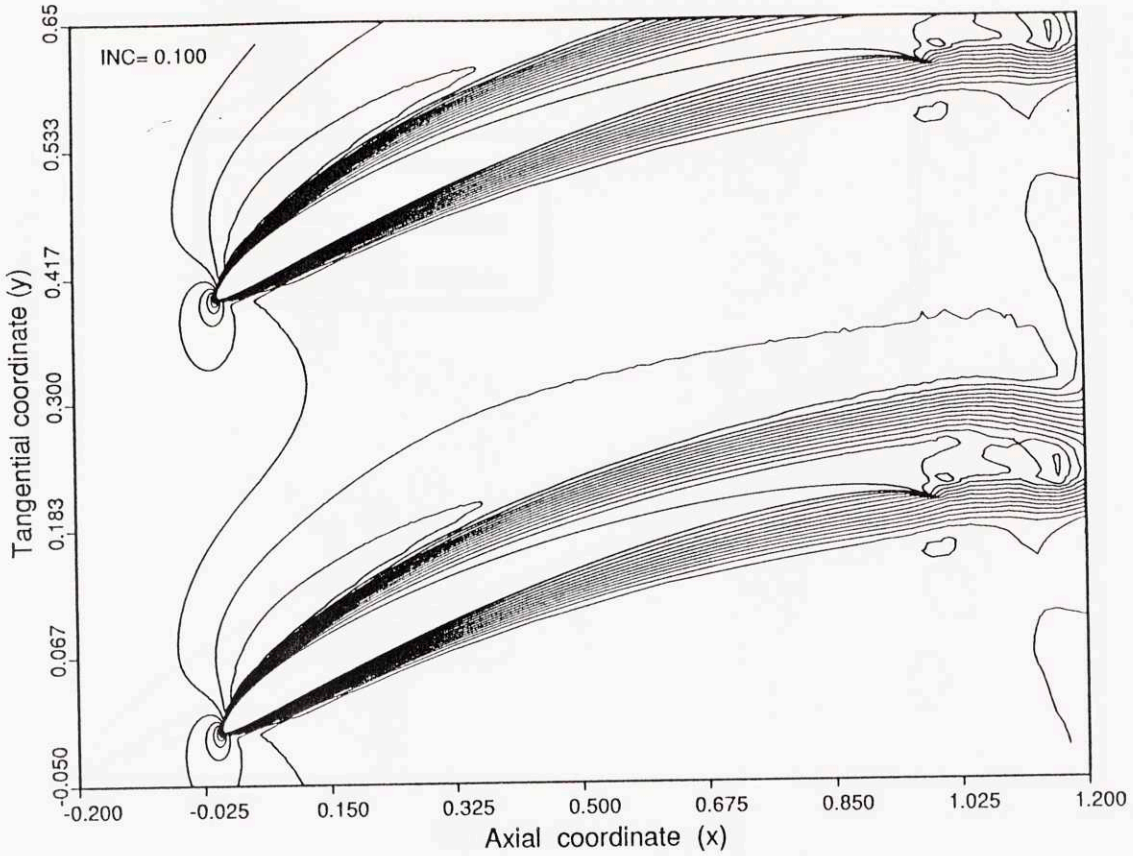

Fig.6.3. Computed velocity contours in the absence of wakes, for the case of 30 degrees inlet angle (high loading case).

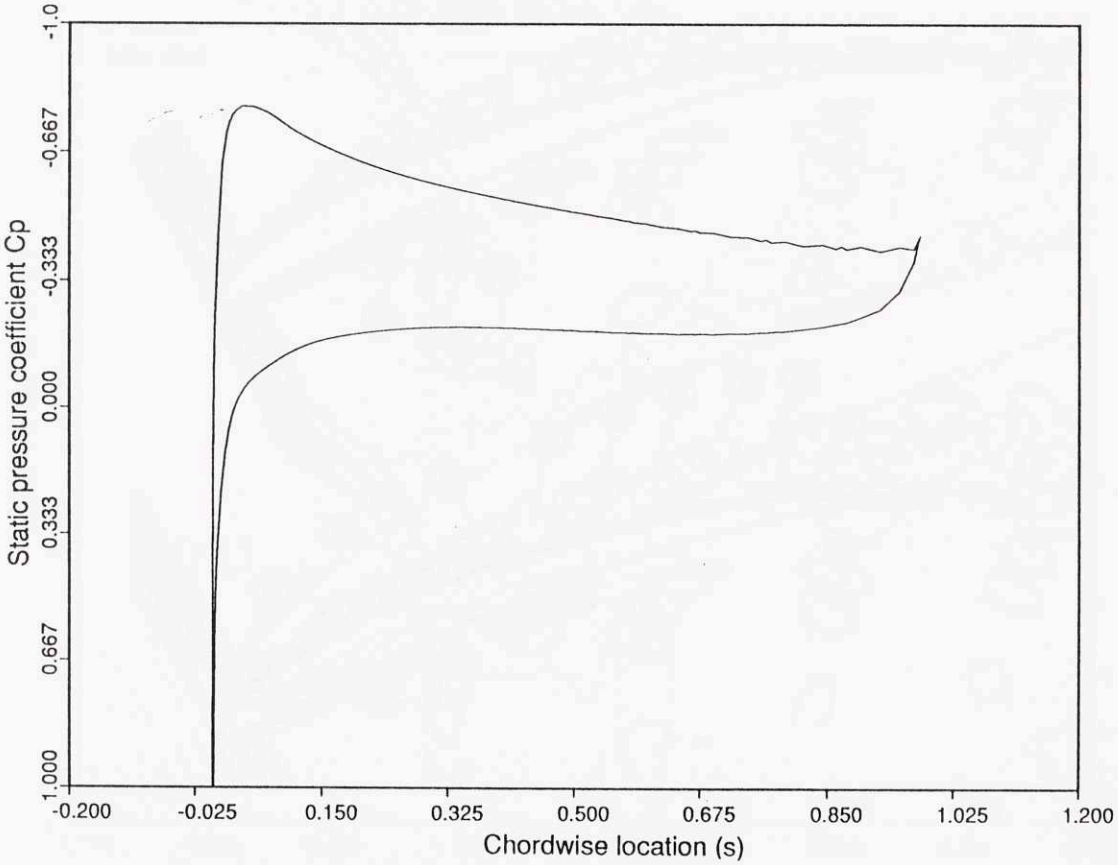

Fig.6.4. Static pressure distribution in the absence of wakes, for the case of 30 degrees inlet angle (high loading case).

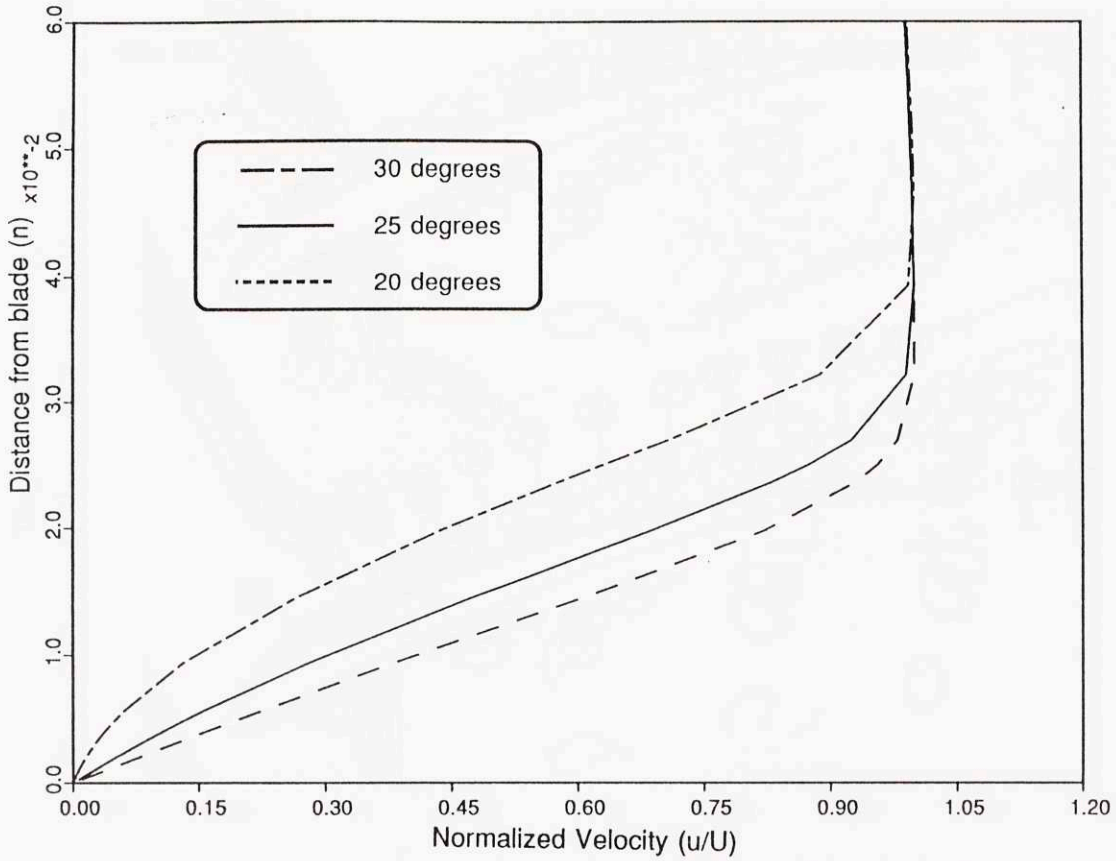

Fig.6.5. Velocity profiles in the suction surface boundary layer (x=0.25c) for three loading cases (i.e. three different inlet angles).

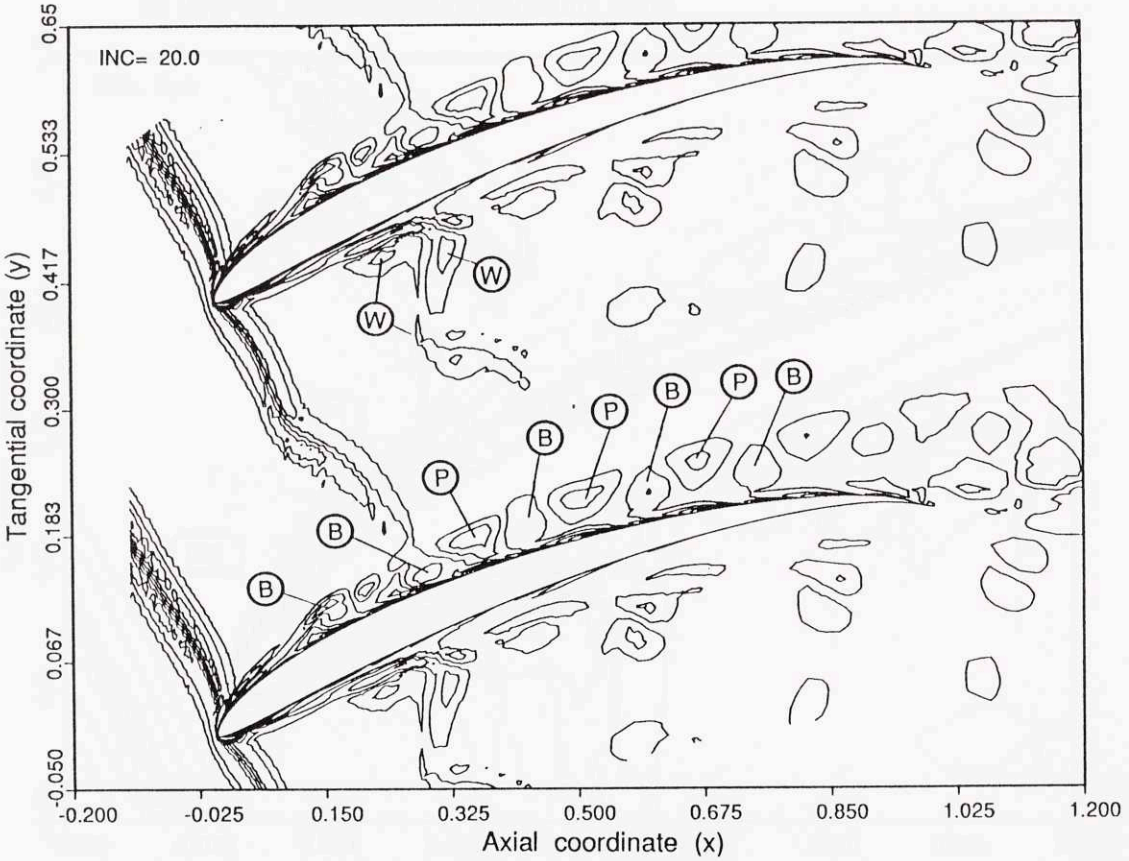

Fig.6.6a. Disturbance vorticity contours in the stator passage at time t_0, showing a vortex street of counter-rotating B- and P-vortices. Laminar calculation with 30 degrees inlet angle (high loading case).

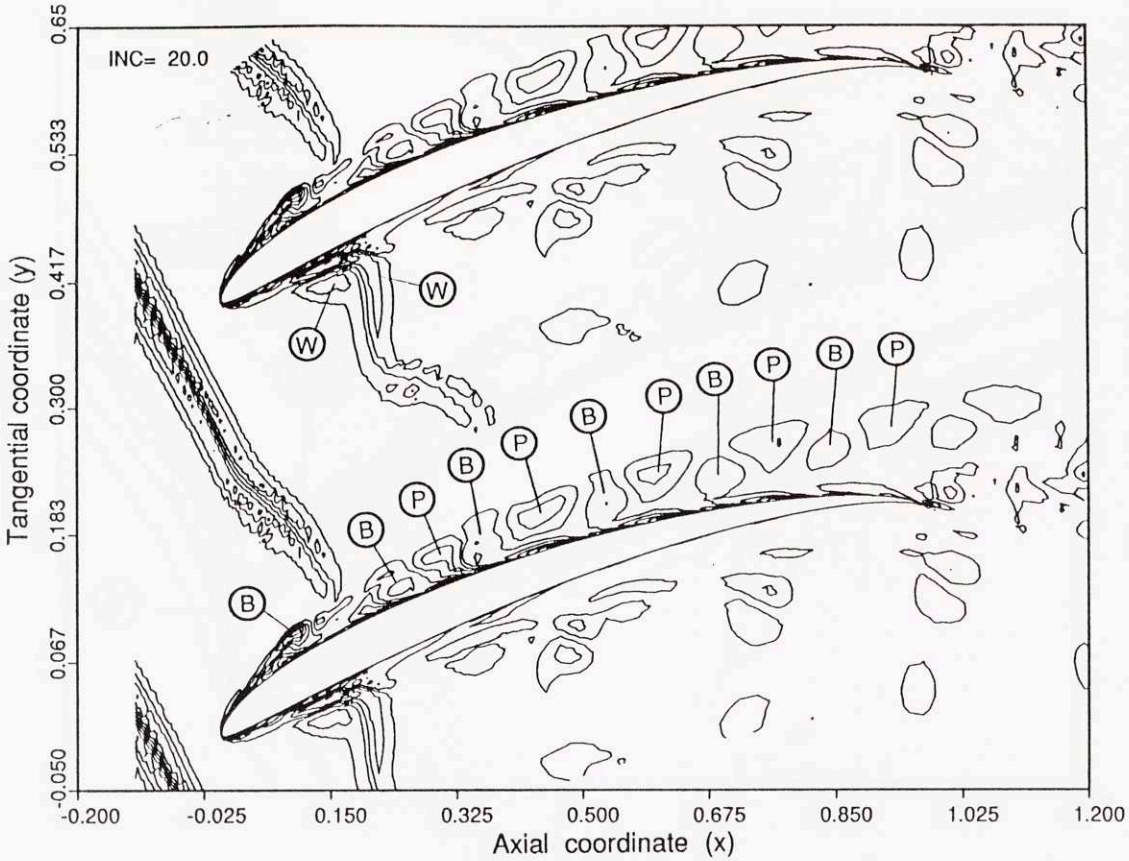

Fig.6.6b. Disturbance vorticity contours in the stator passage at time $t_0 + 0.6T$, showing a vortex street of counter-rotating B- and P-vortices. Laminar calculation with 30 degrees inlet angle (high loading case).

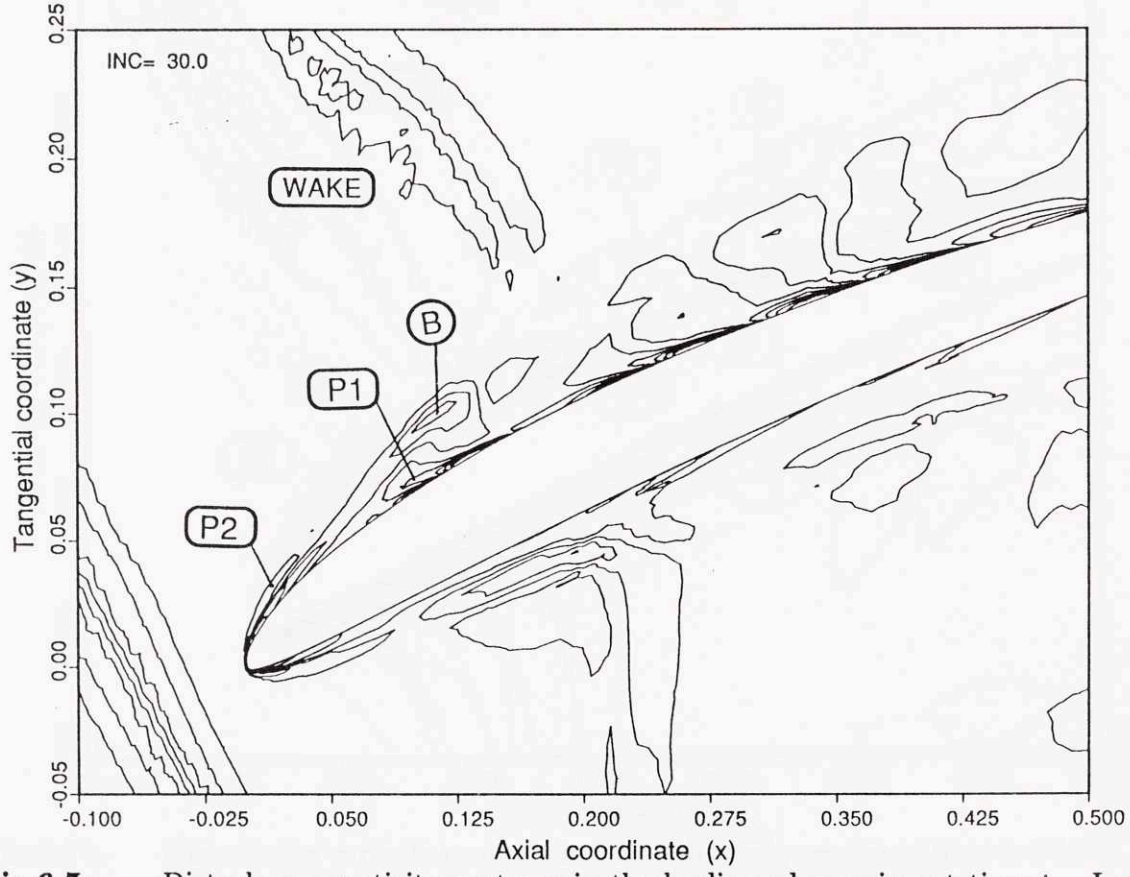

Fig.6.7a. Disturbance vorticity contours in the leading edge region at time t_0. Laminar calculation with 30 degrees inlet angle (high loading case).

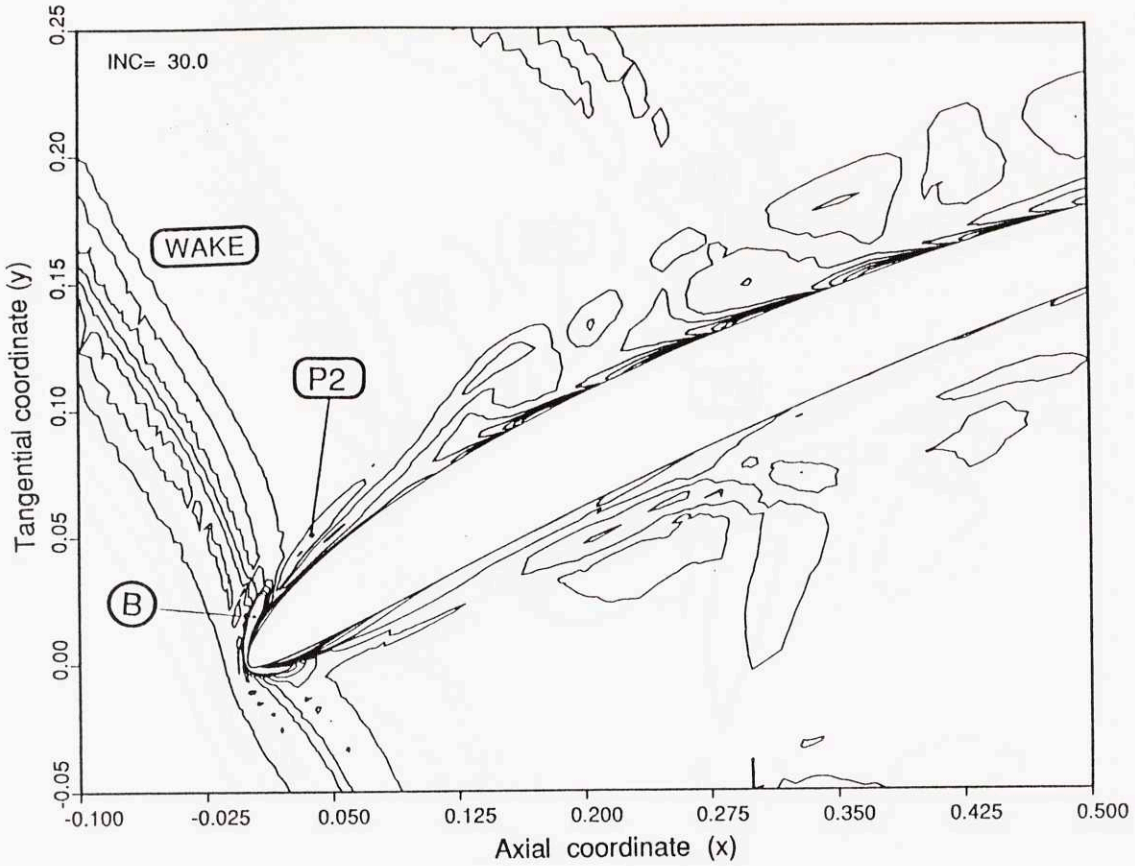

Fig.6.7b. Disturbance vorticity contours in the leading edge region at time $t_0+0.3T$. Laminar calculation with 30 degrees inlet angle (high loading case).

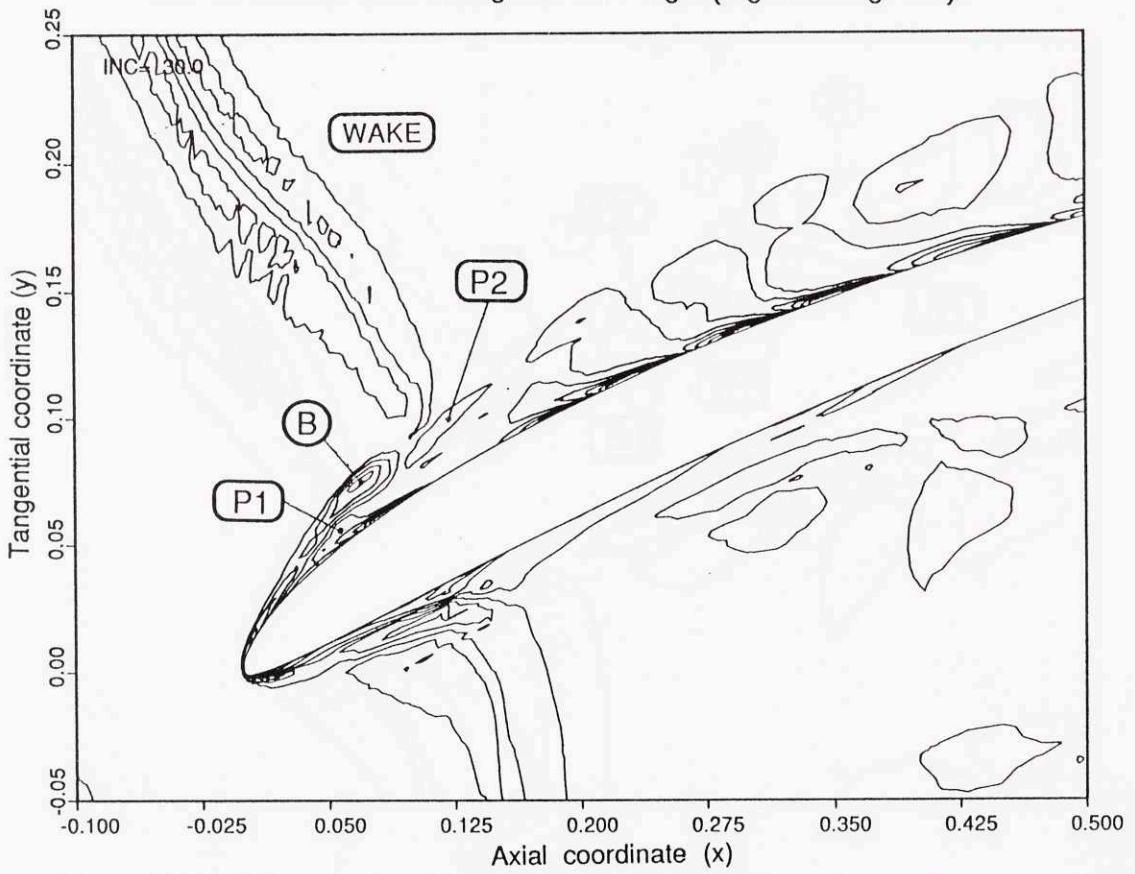

Fig.6.7c. Disturbance vorticity contours in the leading edge region at time $t_0+0.5T$. Laminar calculation with 30 degrees inlet angle (high loading case).

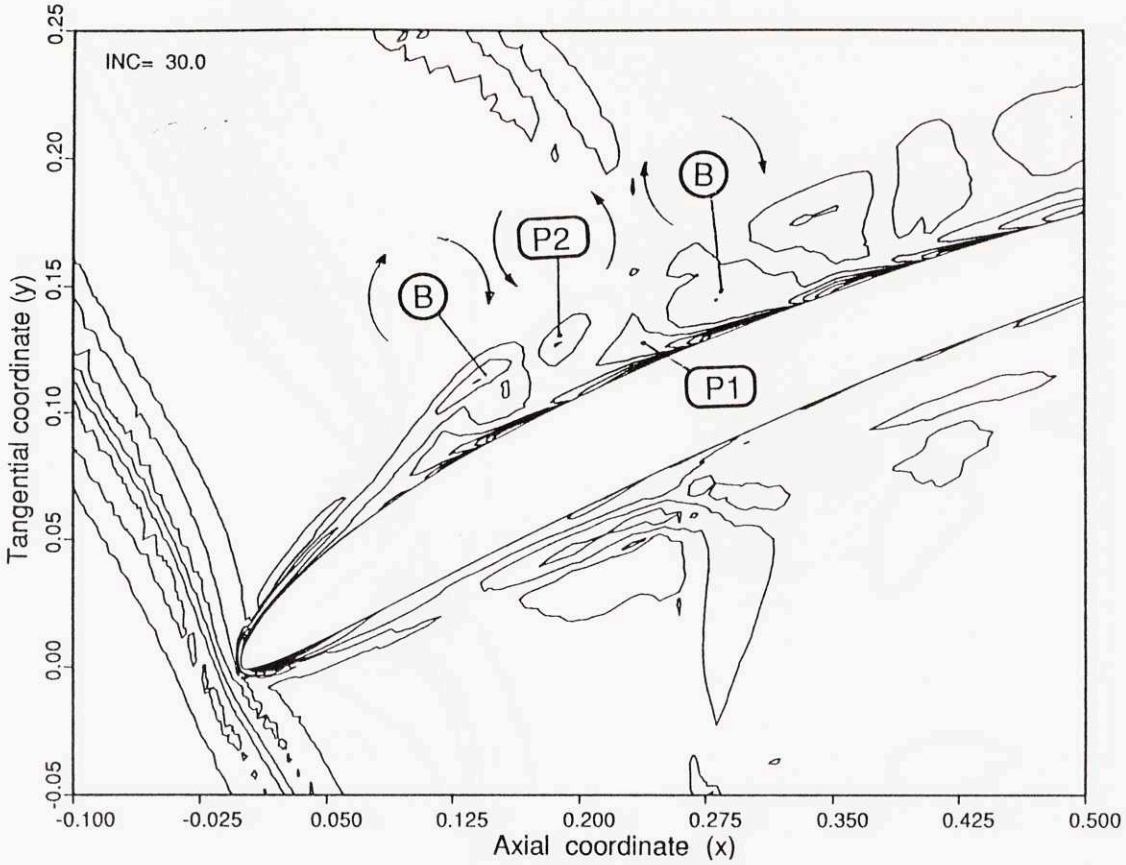

Fig.6.7d. Disturbance vorticity contours in the leading edge region at time $t_0 + 0.9T$. Laminar calculation with 30 degrees inlet angle (high loading case).

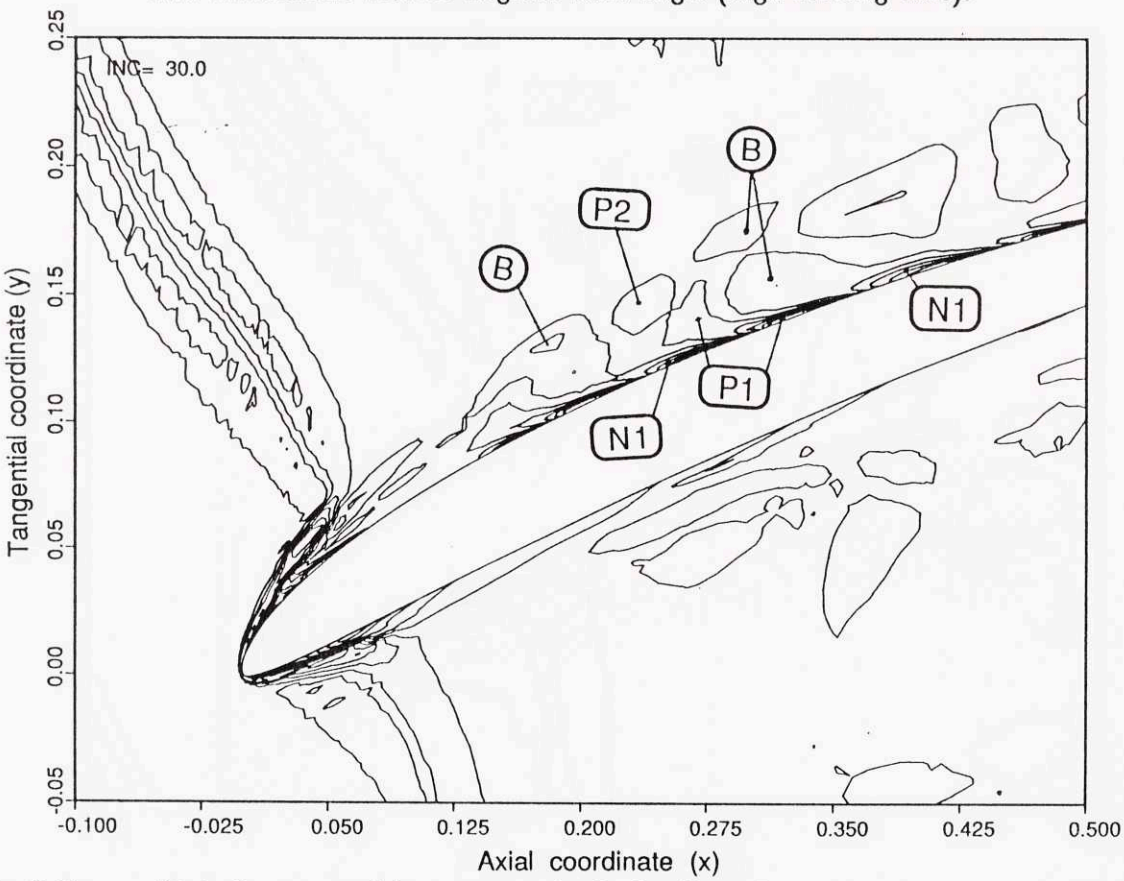

Fig.6.7e. Disturbance vorticity contours in the leading edge region at time $t_0 + 1.1T$. Laminar calculation with 30 degrees inlet angle (high loading case).

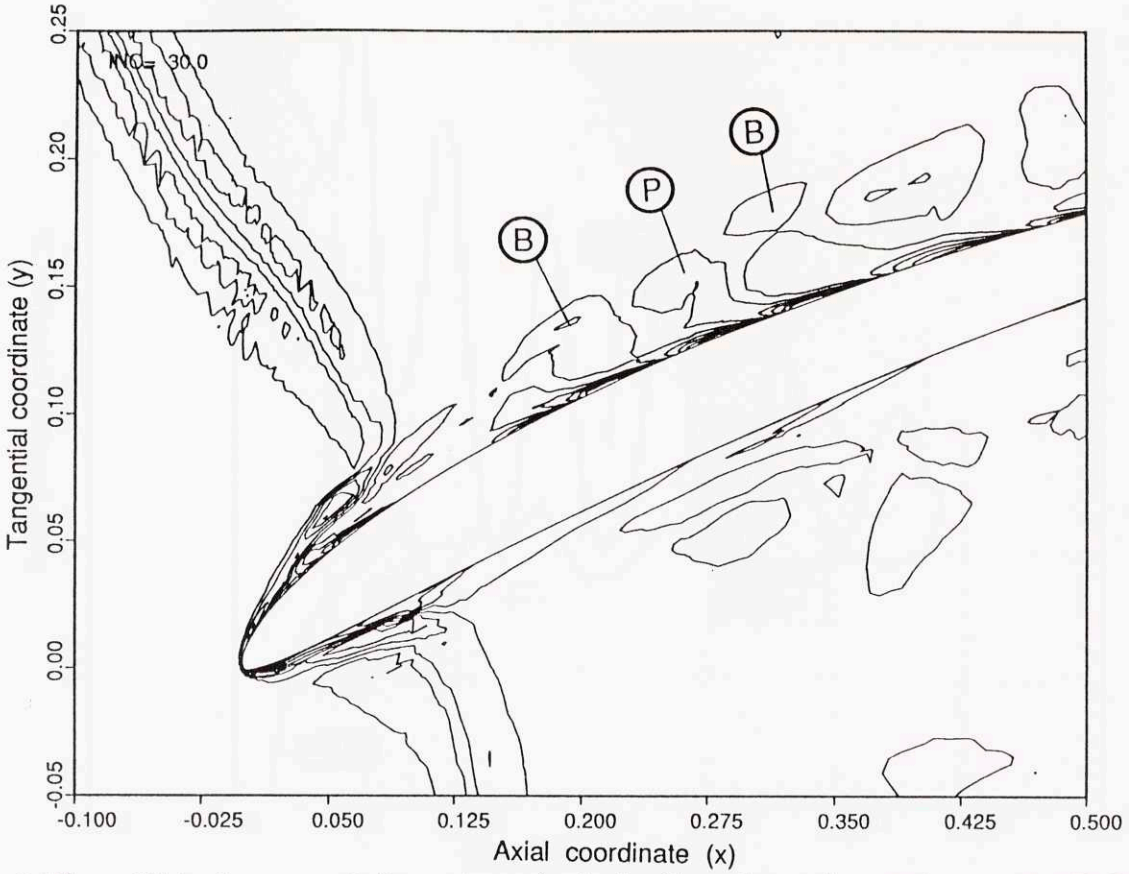

Fig.6.7f. Disturbance vorticity contours in the leading edge region at time $t_0 + 1.2T$. Laminar calculation with 30 degrees inlet angle (high loading case).

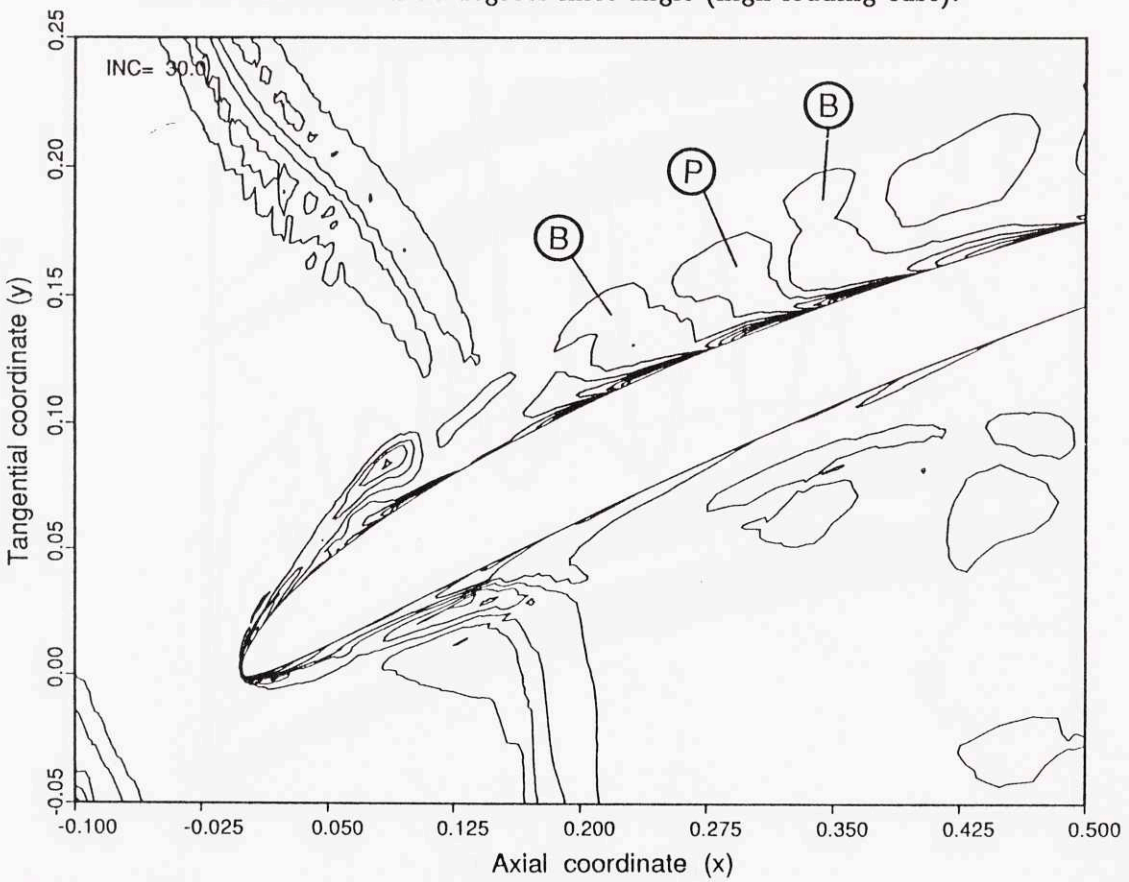

Fig.6.7g. Disturbance vorticity contours in the leading edge region at time $t_0 + 1.3T$. Laminar calculation with 30 degrees inlet angle (high loading case).

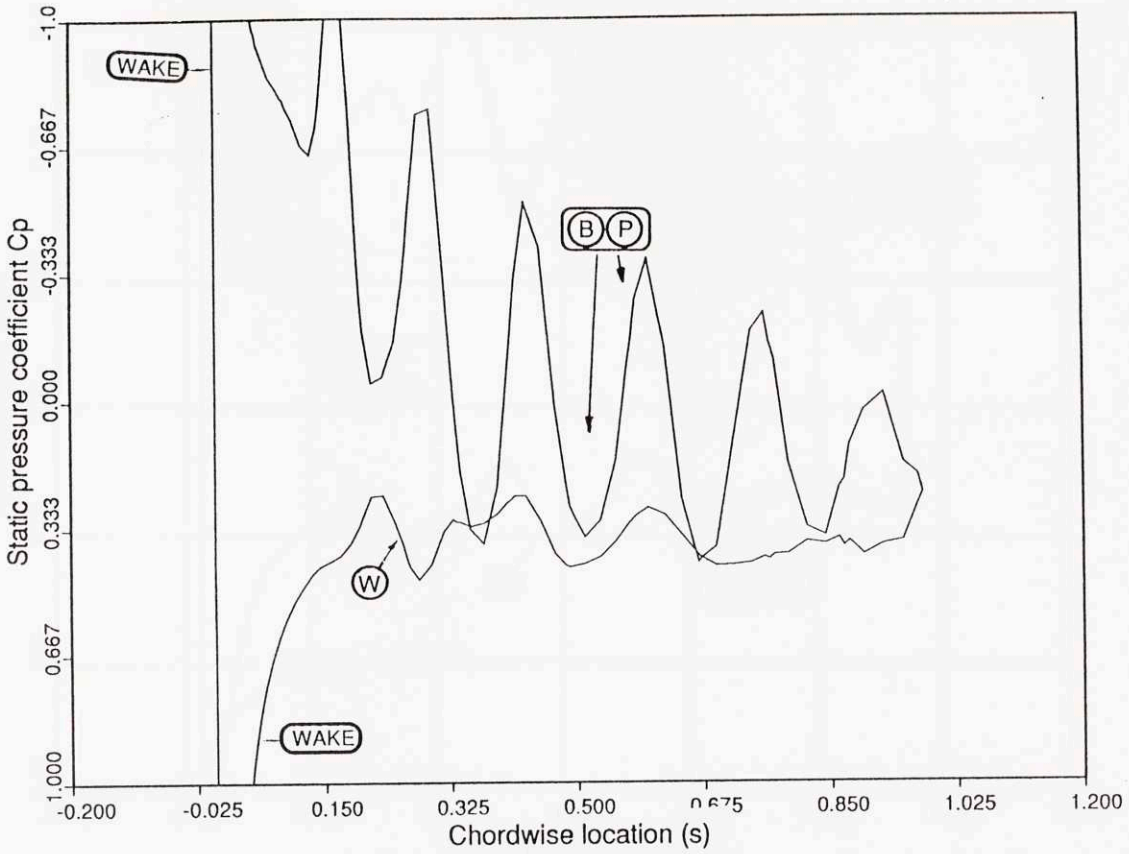

Fig.6.8a. Static pressure distribution on the blade surface at time t_0. Laminar calculation with 30 degrees inlet angle (high loading case).

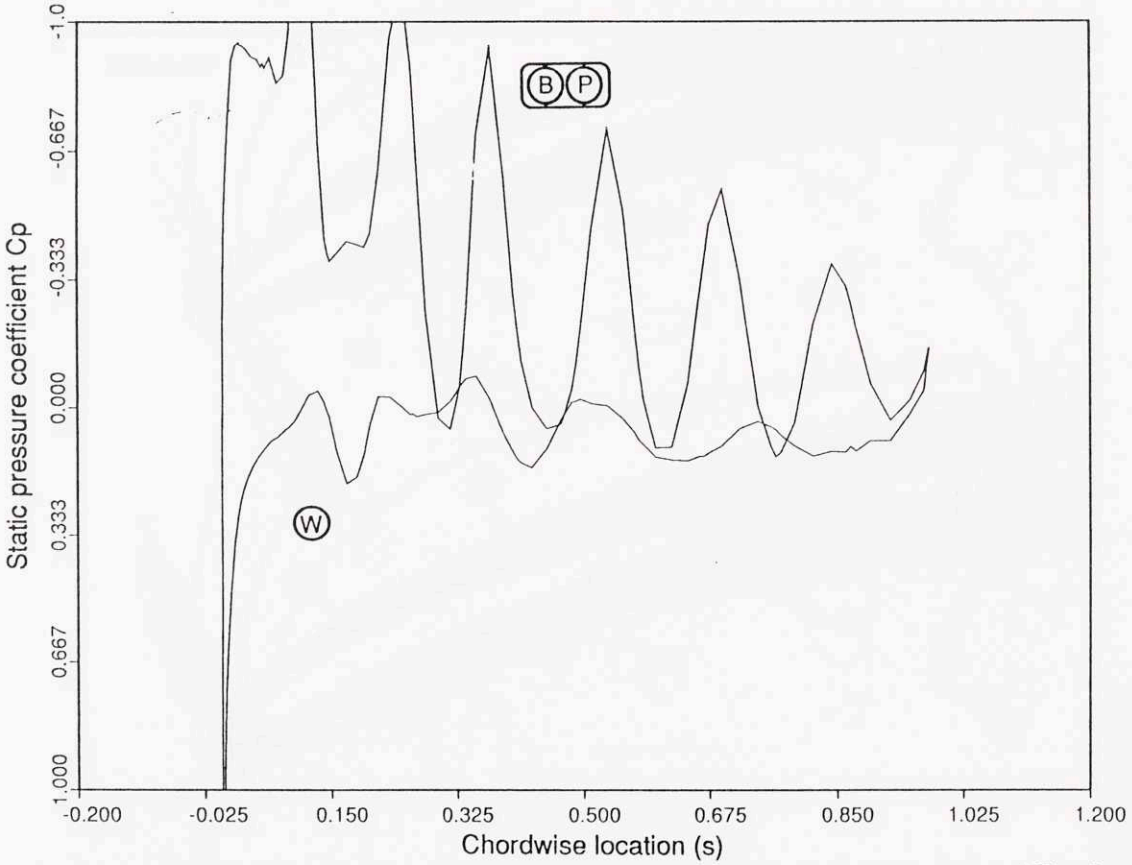

Fig.6.8b. Static pressure distribution on the blade surface at time $t_0 + 0.6T$. Laminar calculation with 30 degrees inlet angle (high loading case).

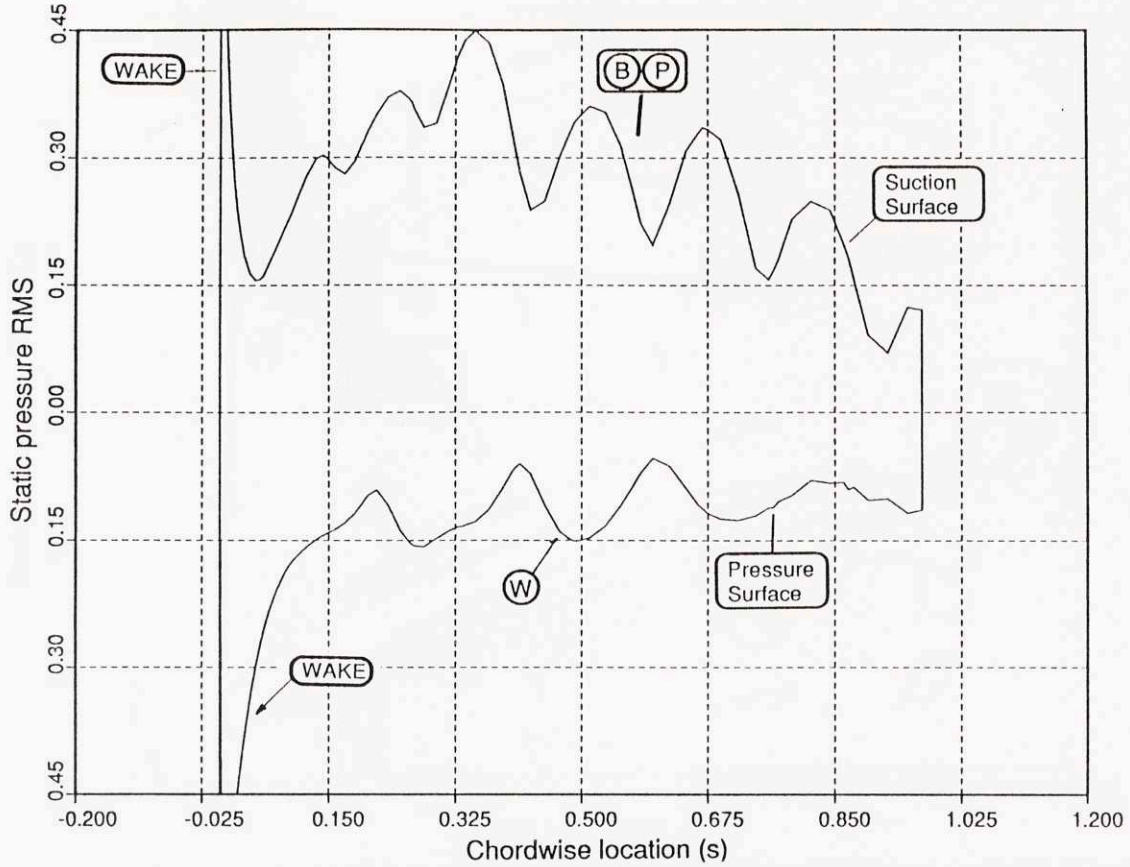

Fig.6.9. Distribution of the static pressure RMS on the blade surface from the calculation with 30 degrees inlet angle (high loading case).

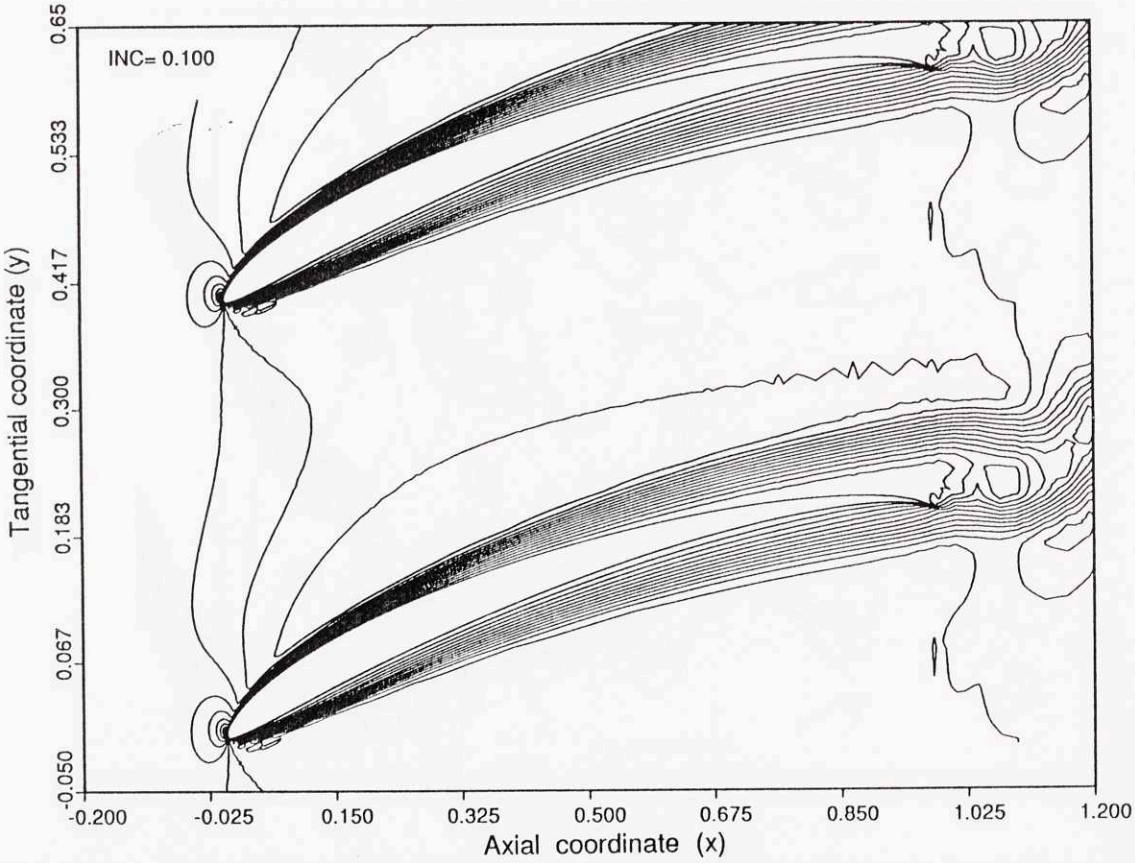

Fig.6.10. Computed velocity contours in the absence of wakes, for the case of 20 degrees inlet angle (low loading case).

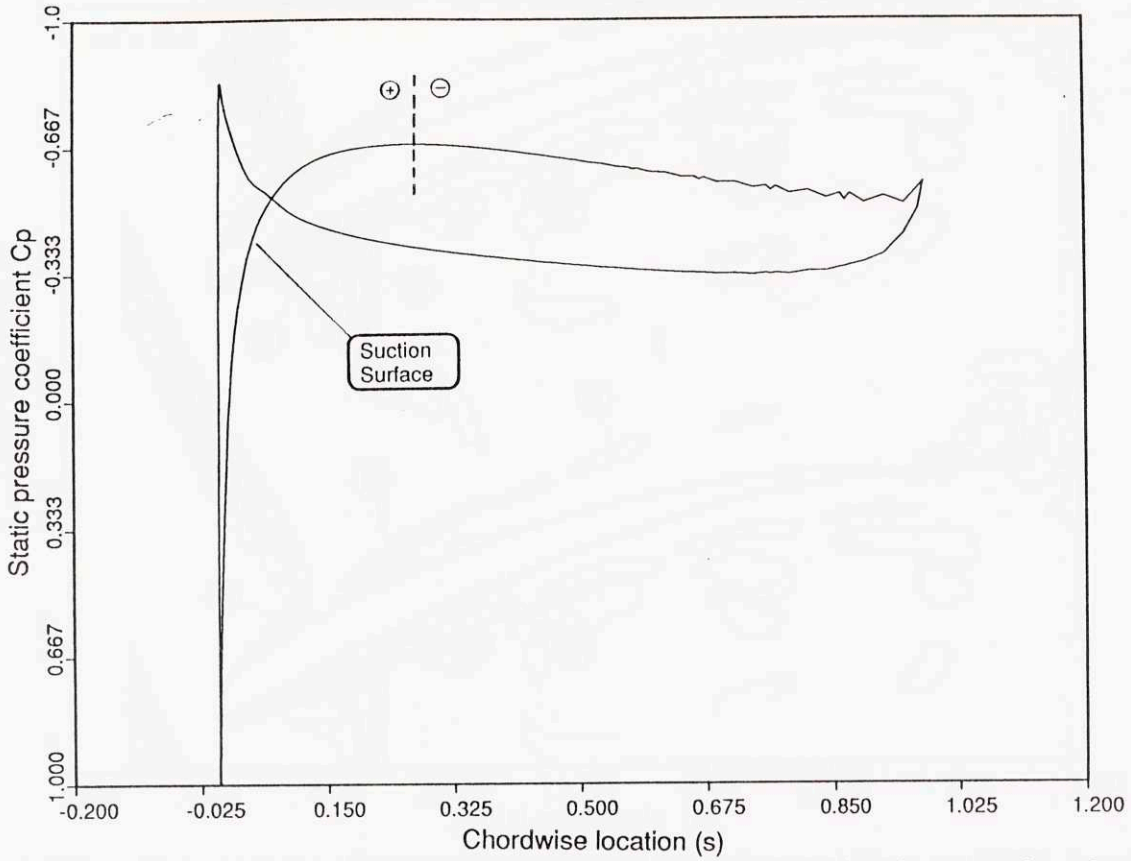

Fig.6.11. Static pressure distribution in the absence of wakes, for the case of 20 degrees inlet angle (low loading case).

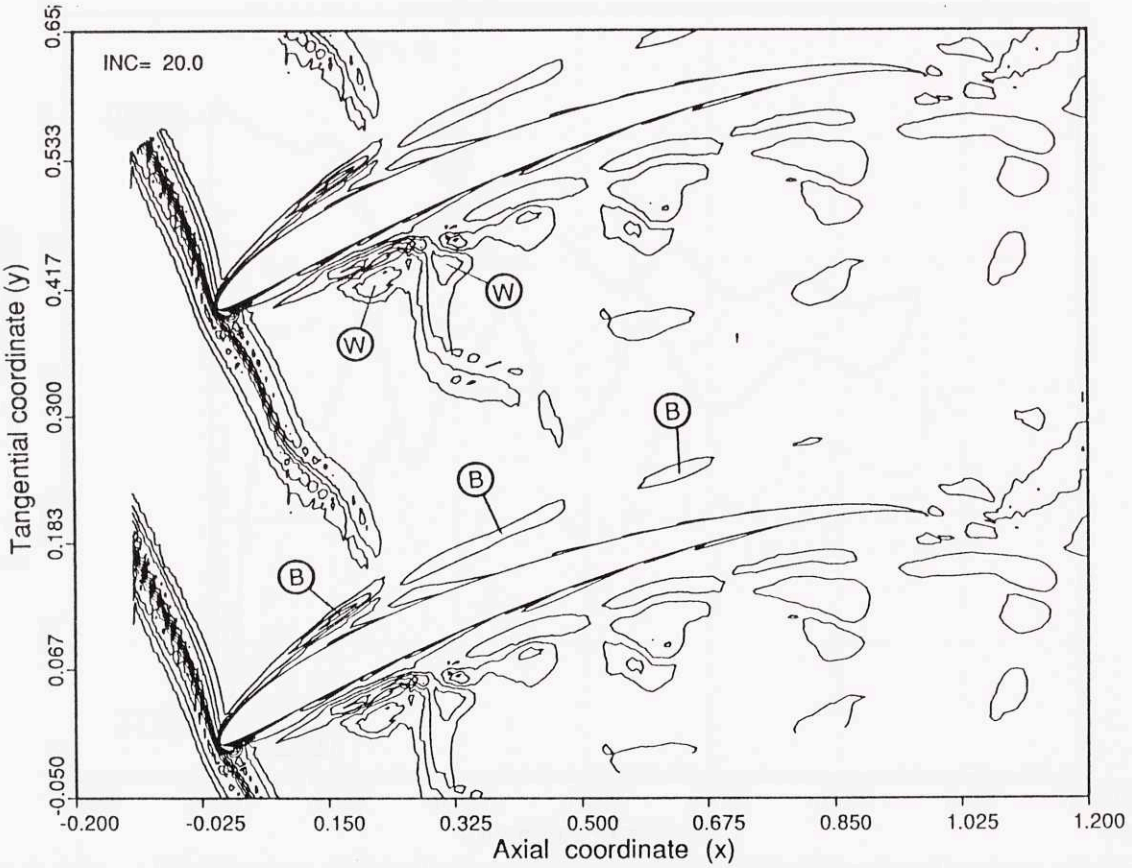

Fig.6.12a. Disturbance vorticity contours in the stator passage at time t_0. Laminar calculation with 20 degrees inlet angle (low loading case).

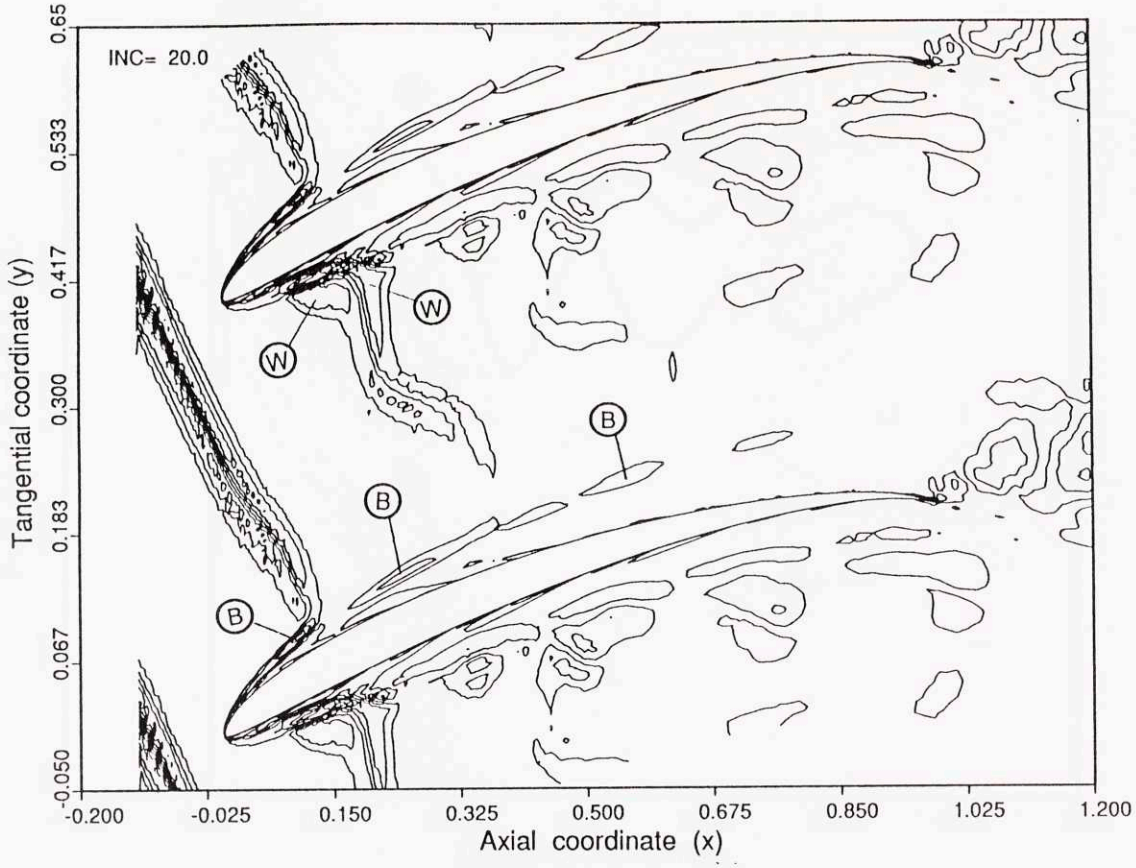

Fig.6.12b. Disturbance vorticity contours in the stator passage at time $t_0 + 0.6T$. Laminar calculation with 20 degrees inlet angle (low loading case).

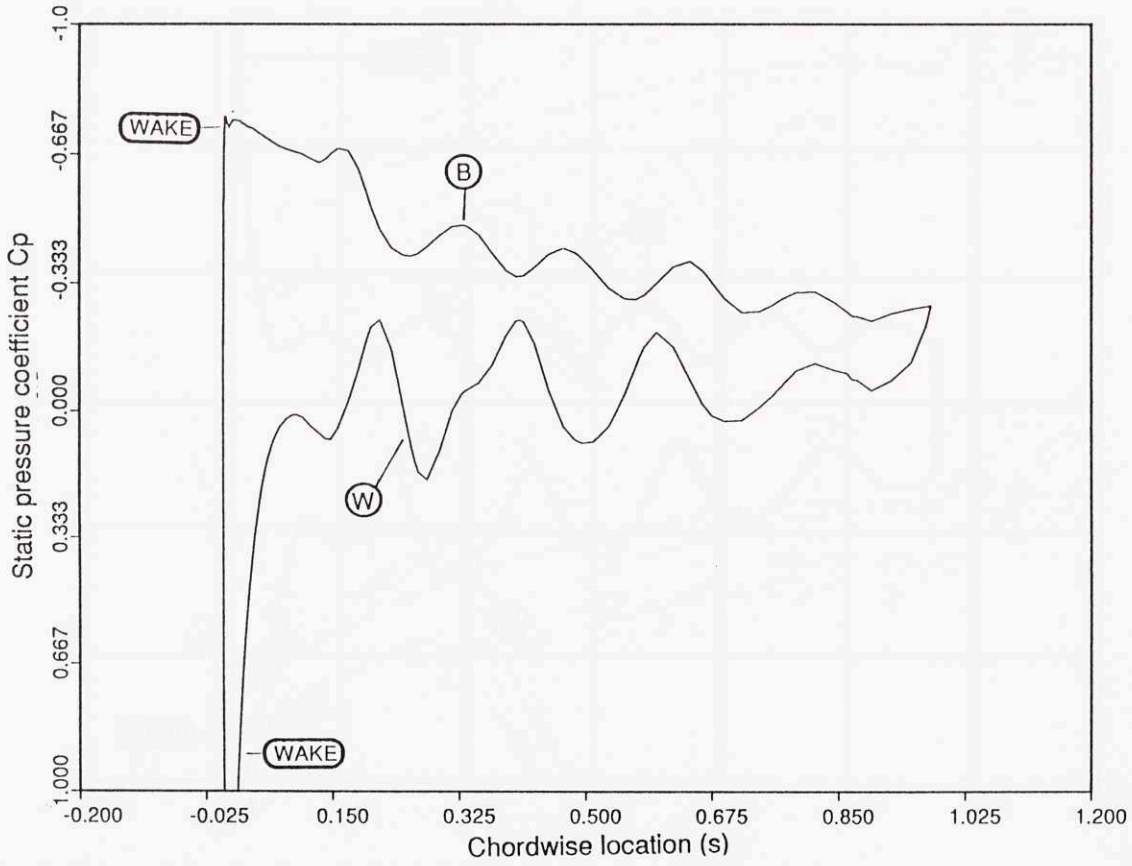

Fig.6.13a. Static pressure distribution on the blade surface at time t_0. Laminar calculation with 20 degrees inlet angle (low loading case).

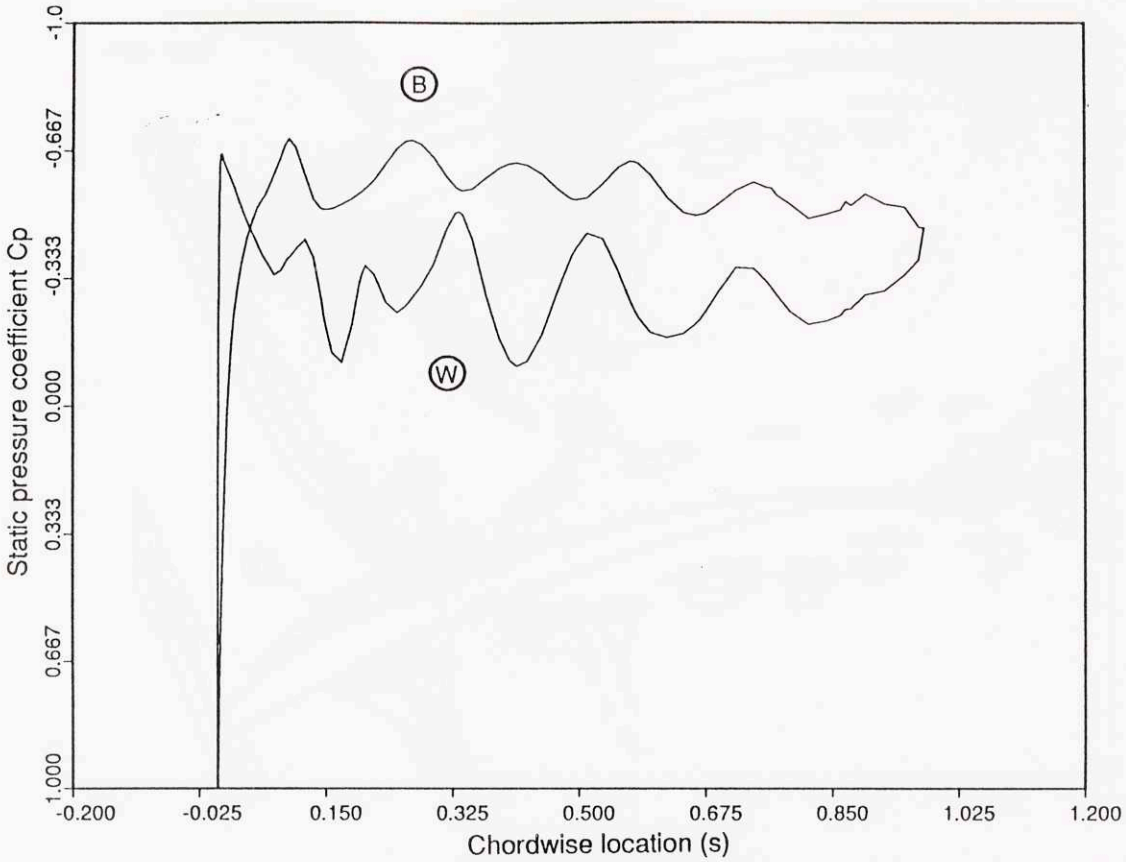

Fig.6.13b. Static pressure distribution on the blade surface at time $t_0 + 0.6T$. Laminar calculation with 20 degrees inlet angle (low loading case).

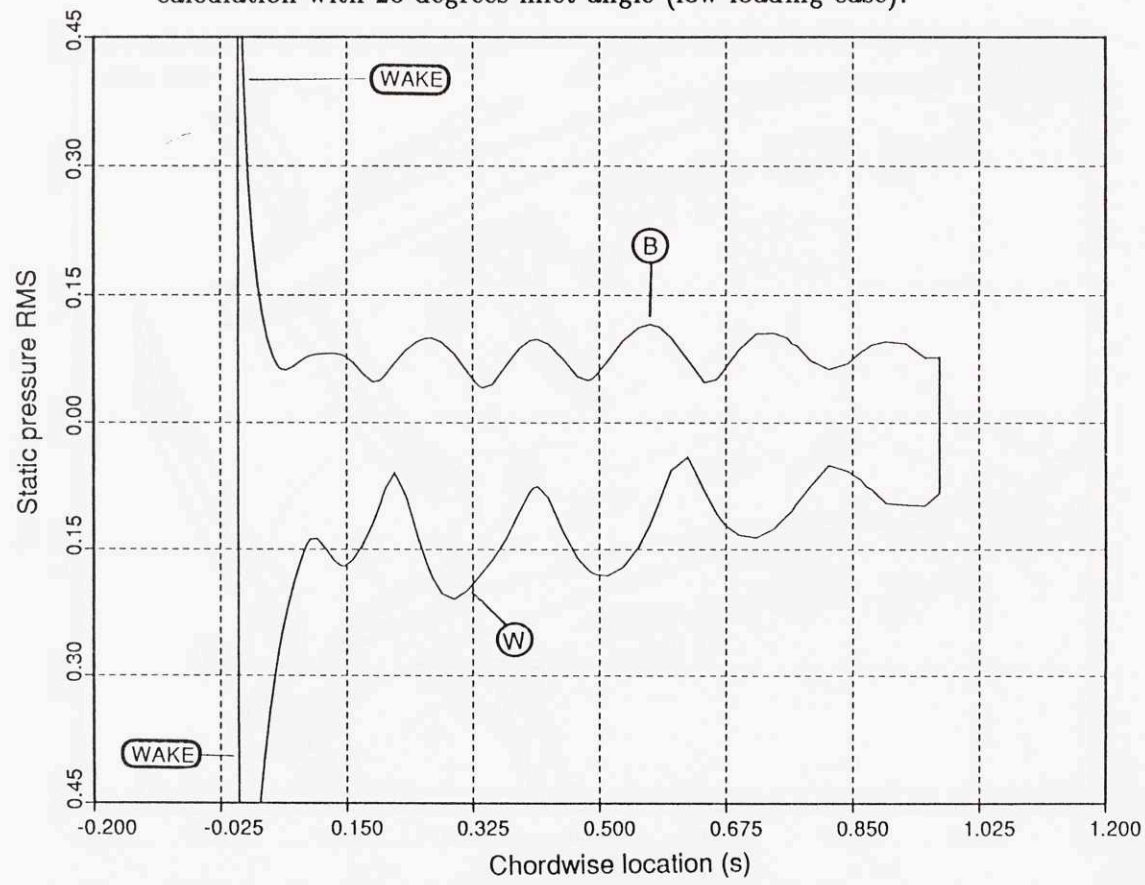

Fig.6.14. Distribution of the static pressure RMS on the blade surface from the calculation with 20 degrees inlet angle (low loading case).

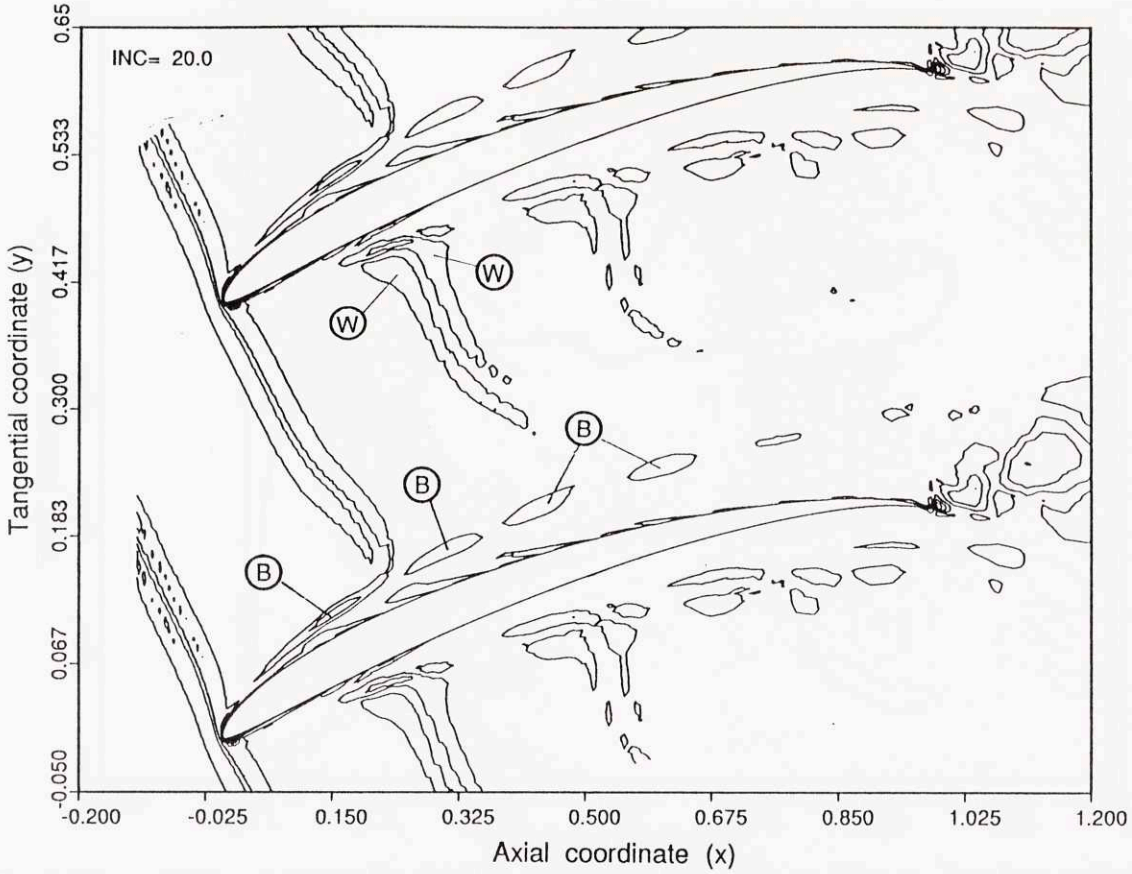

Fig.6.15a. Disturbance vorticity contours in the stator passage at time t_0. Laminar calculation with 30% wake velocity defect.

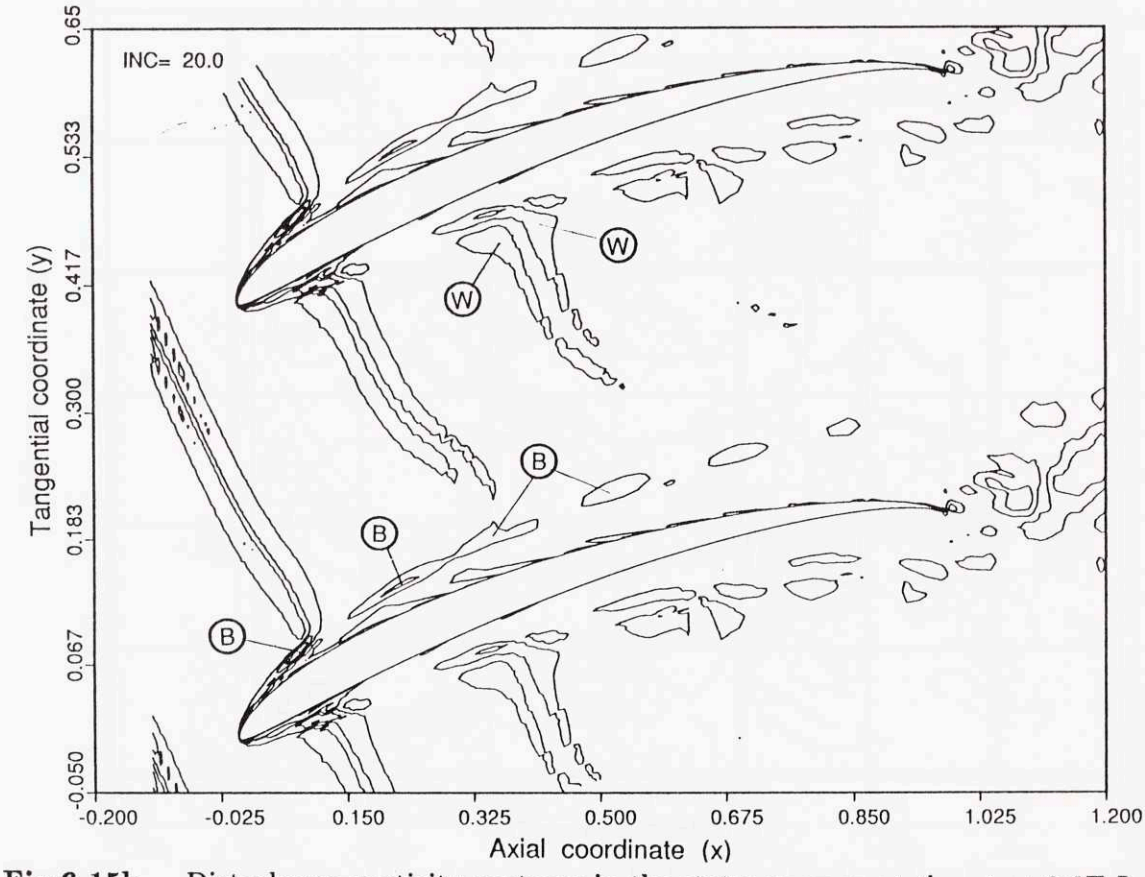

Fig.6.15b. Disturbance vorticity contours in the stator passage at time $t_0 + 0.6T$ Laminar calculation with 30% wake velocity defect.

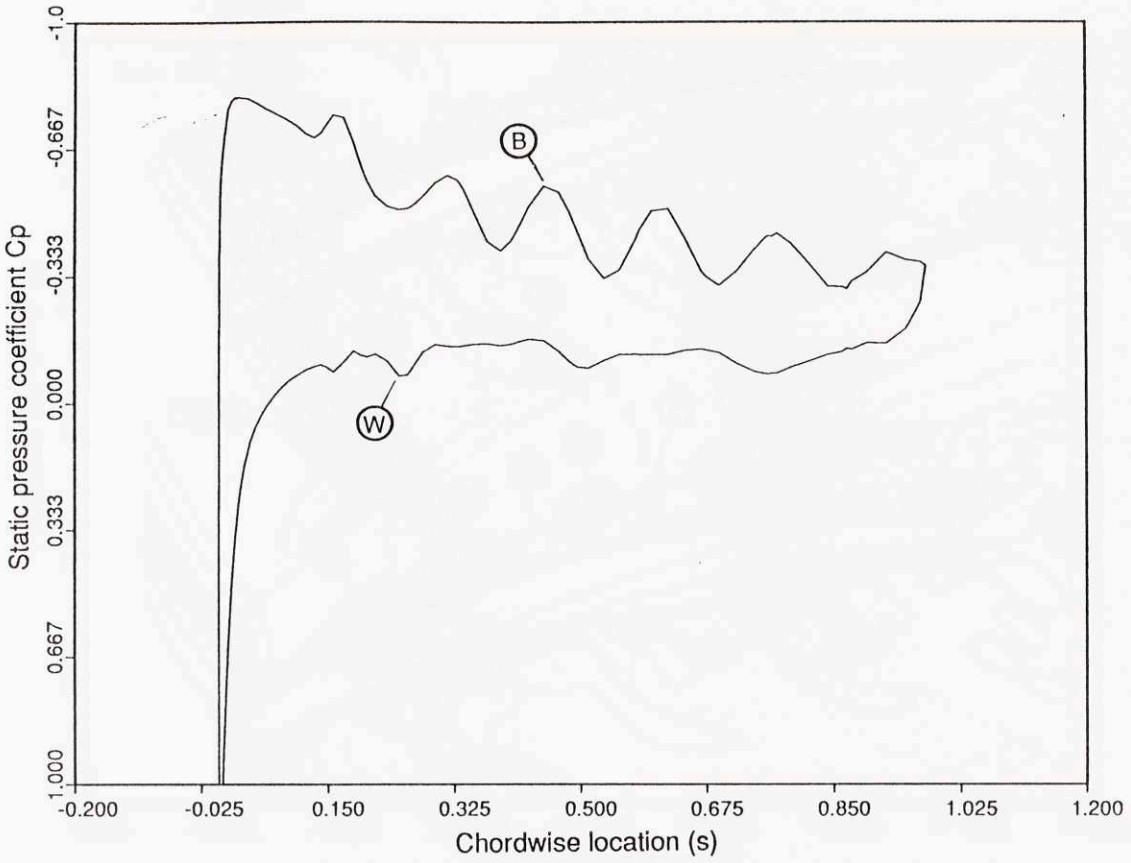

Fig.6.16. Static pressure distribution on the blade surface at time t_0. Laminar calculation with 30% wake velocity defect.

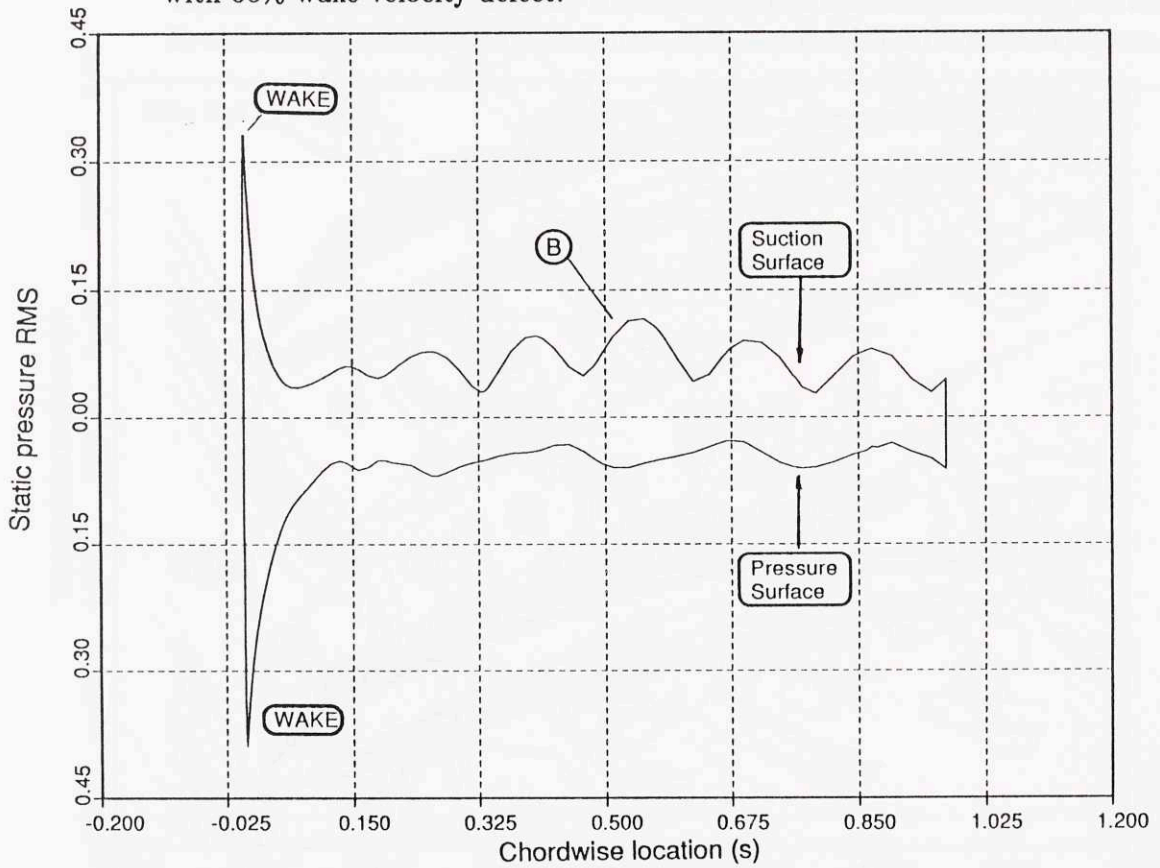

Fig.6.17. Distribution of the static pressure RMS on the blade surface from the calculation with 30% wake velocity defect.

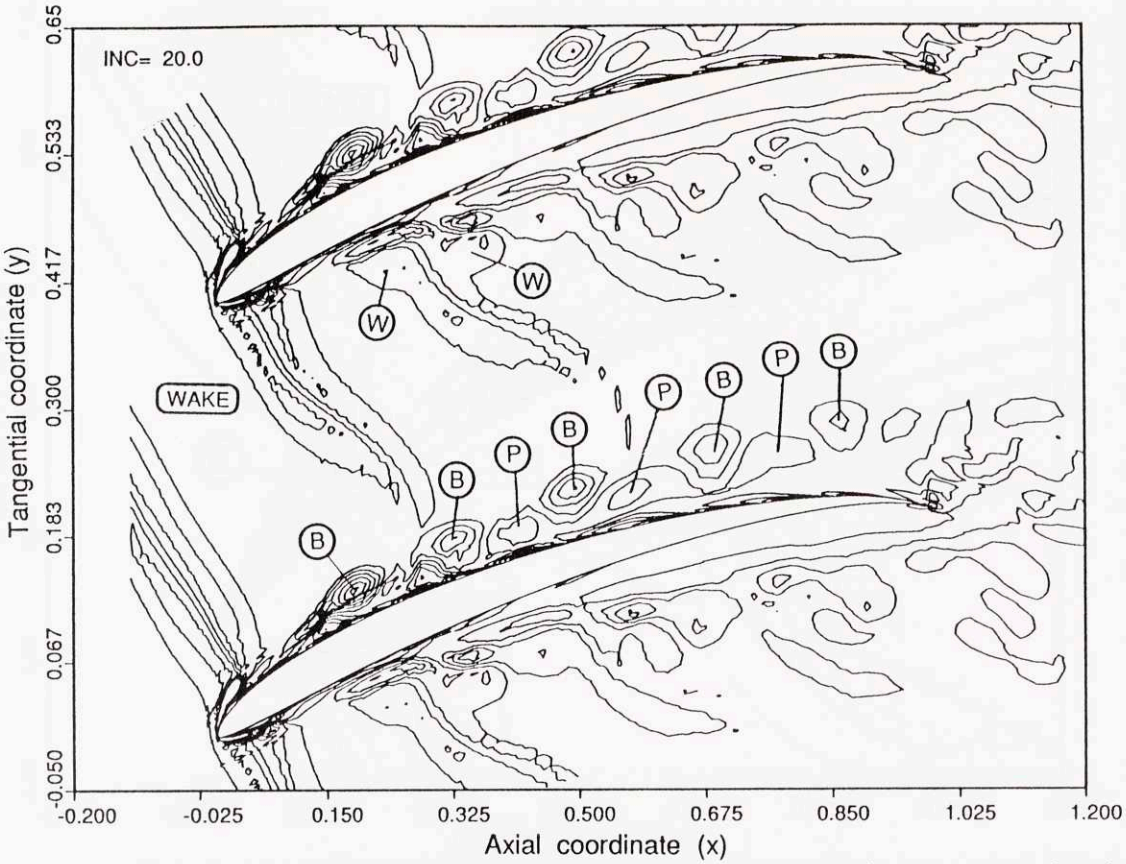

Fig.6.18a. Disturbance vorticity contours in the stator passage at time $t_0 + 0.2$, showing a vortex street of counter-rotating B- and P-vortices and the production of a strong B-vortex at the leading edge. Laminar calculation with 20% wake thickness.

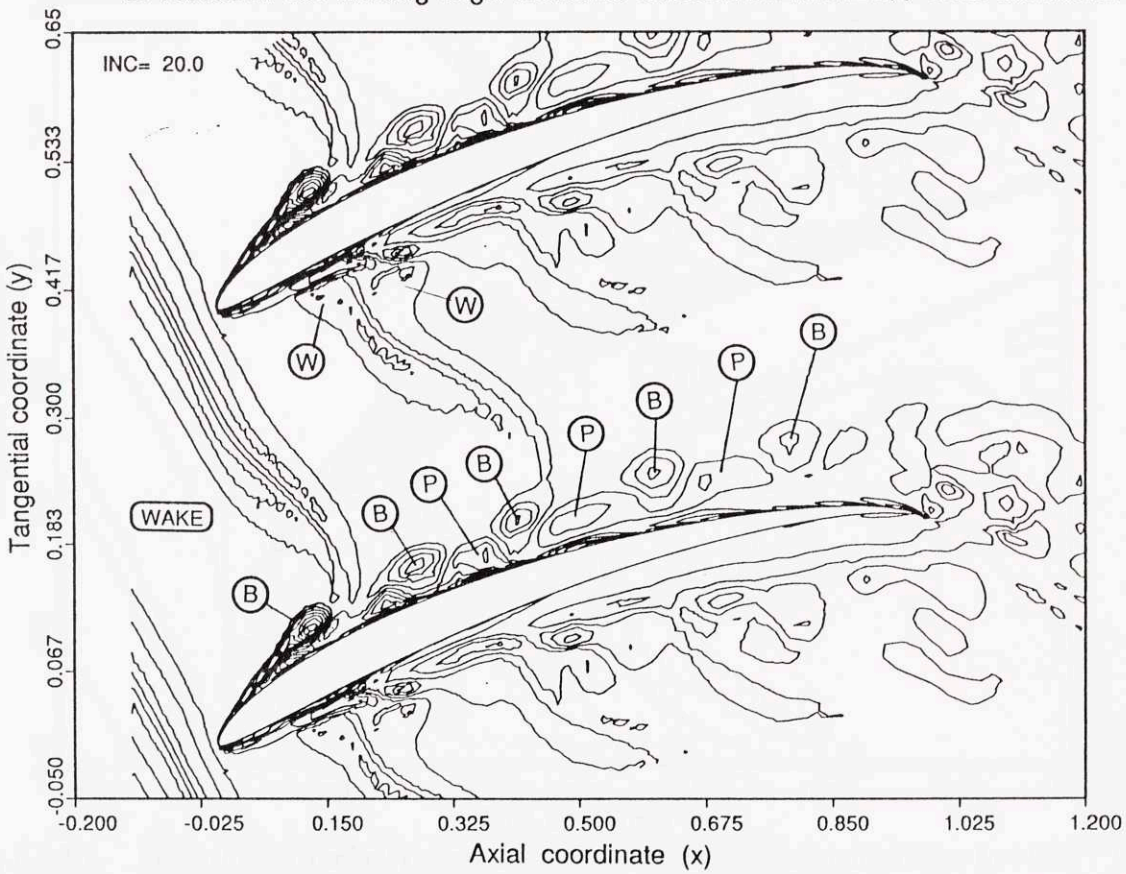

Fig.6.18b. Disturbance vorticity contours in the stator passage at time $t_0 + 0.6T$. Laminar calculation with 20% wake thickness.

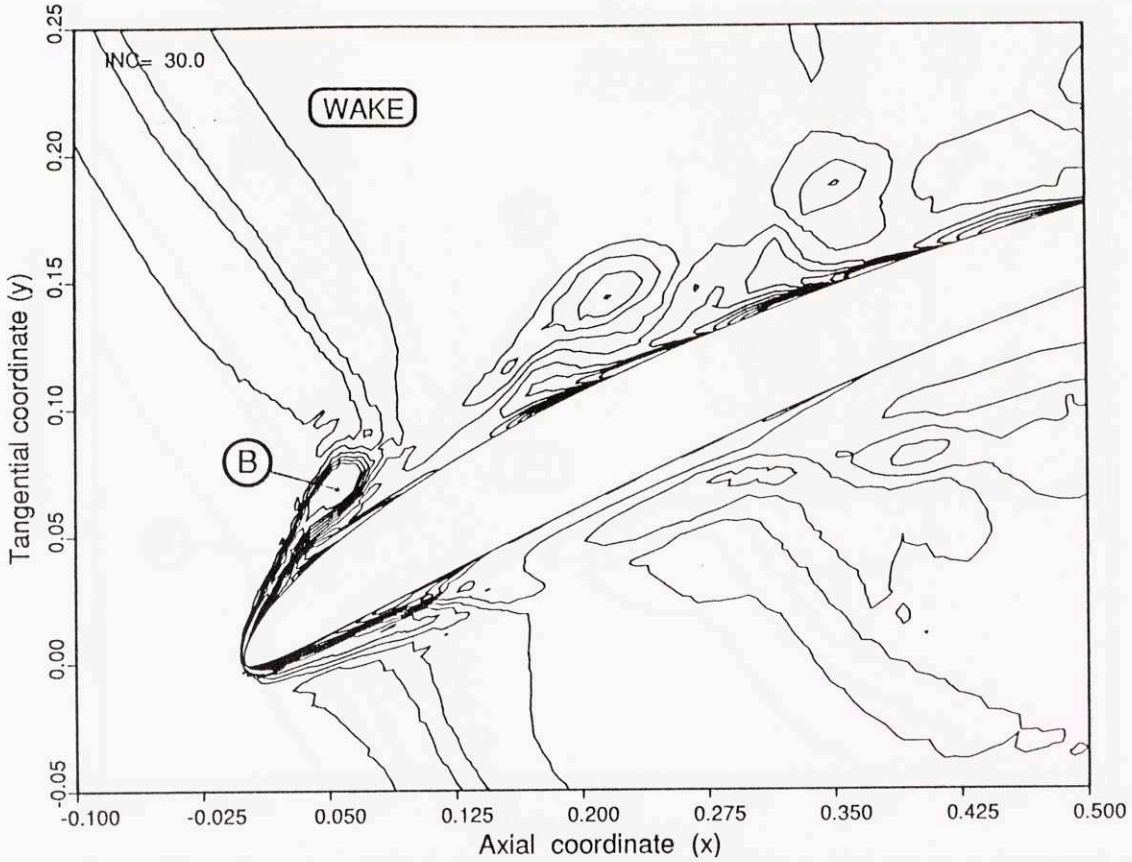

Fig.6.19a. Disturbance vorticity contours in the leading edge region at time $t_0+0.4T$, showing a strong B-vortex. Laminar calculation with 20% wake thickness.

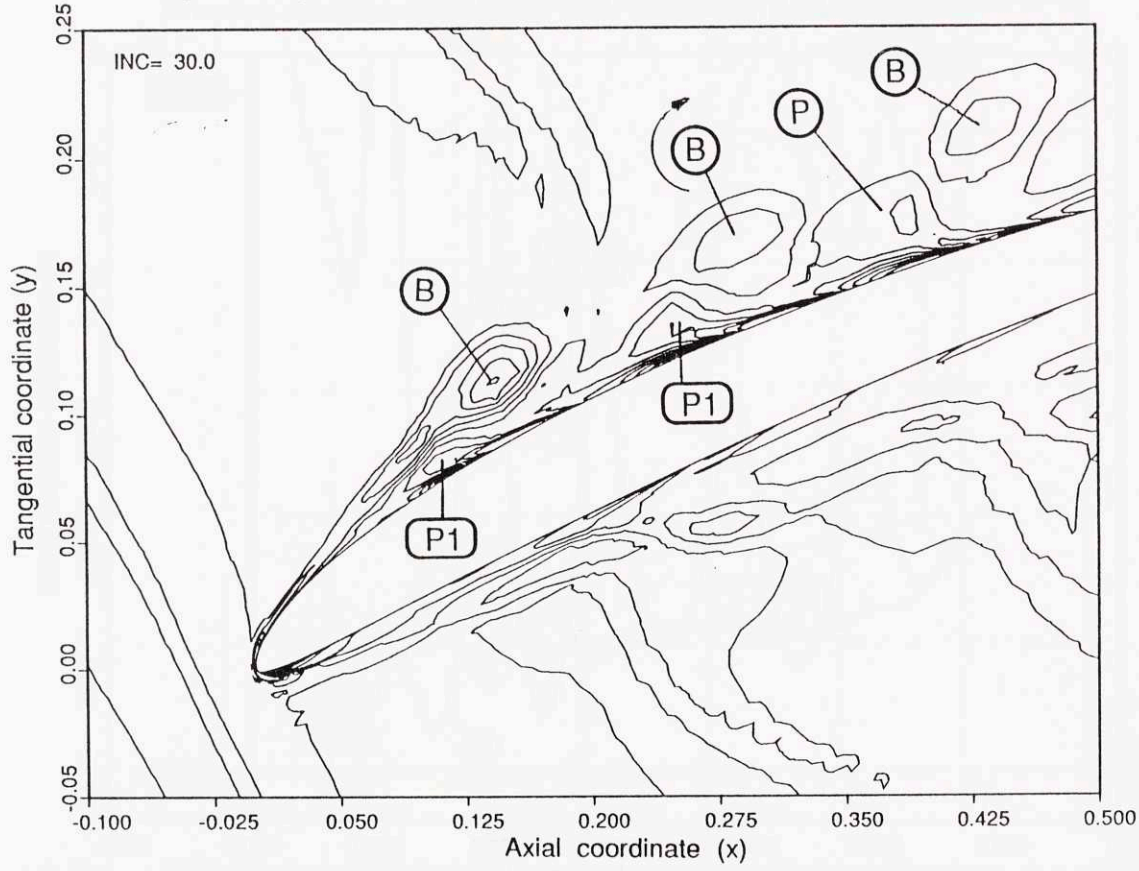

Fig.6.19b. Disturbance vorticity contours in the leading edge region at time $t_0+0.8T$. Laminar calculation with 20% wake thickness.

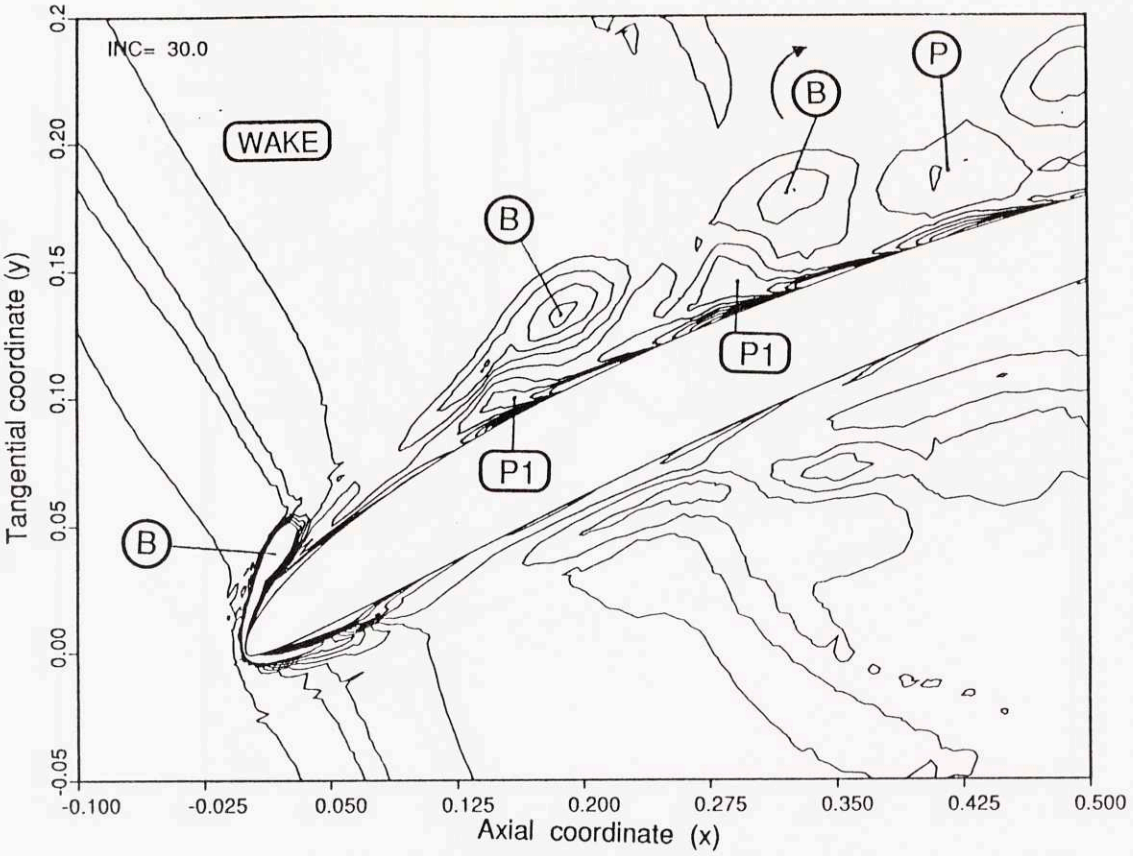

Fig.6.19c. Disturbance vorticity contours in the leading edge region at time $t_0 + 1.2T$; showing distortion and detachment of the P1-region by the B-vortex, leading to a large P-vortex. Laminar calculation with 20% wake thickness.

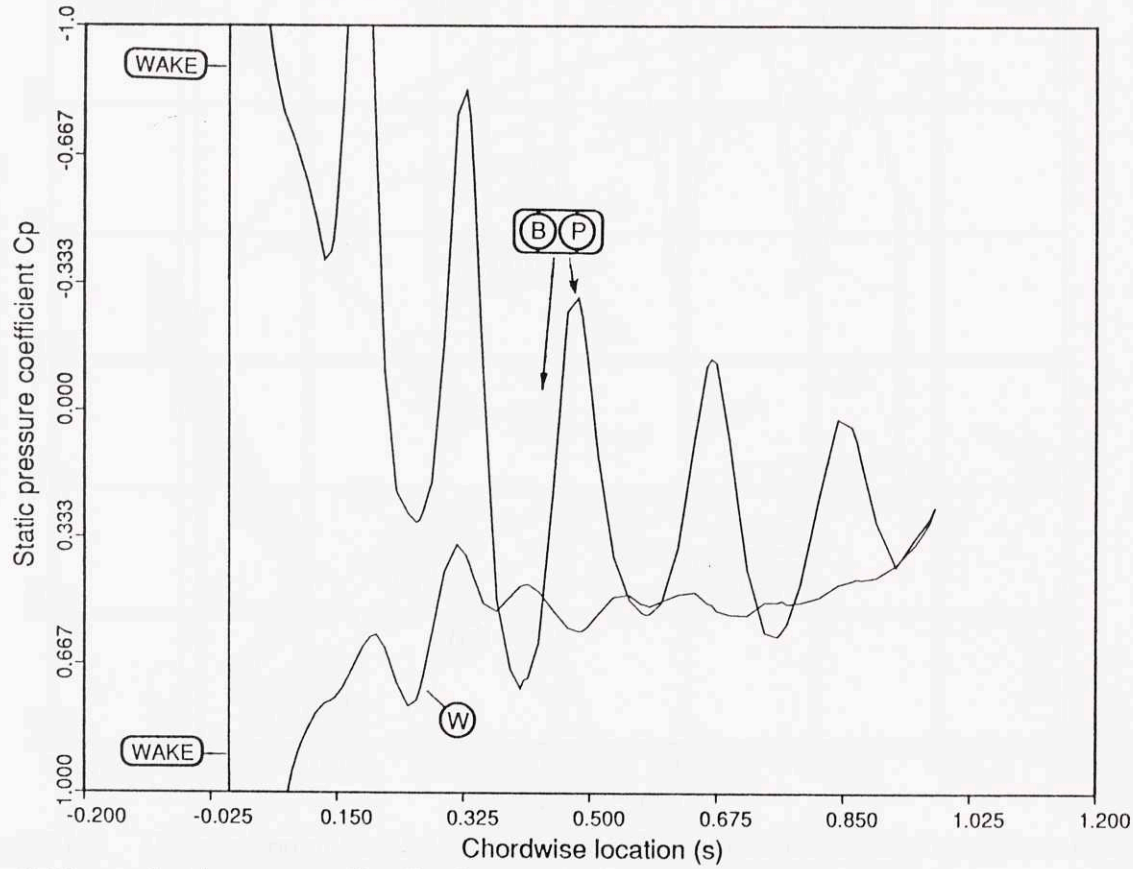

Fig.6.20a. Static pressure distribution on the blade surface at time t_0. Laminar calculation with 20% wake thickness.

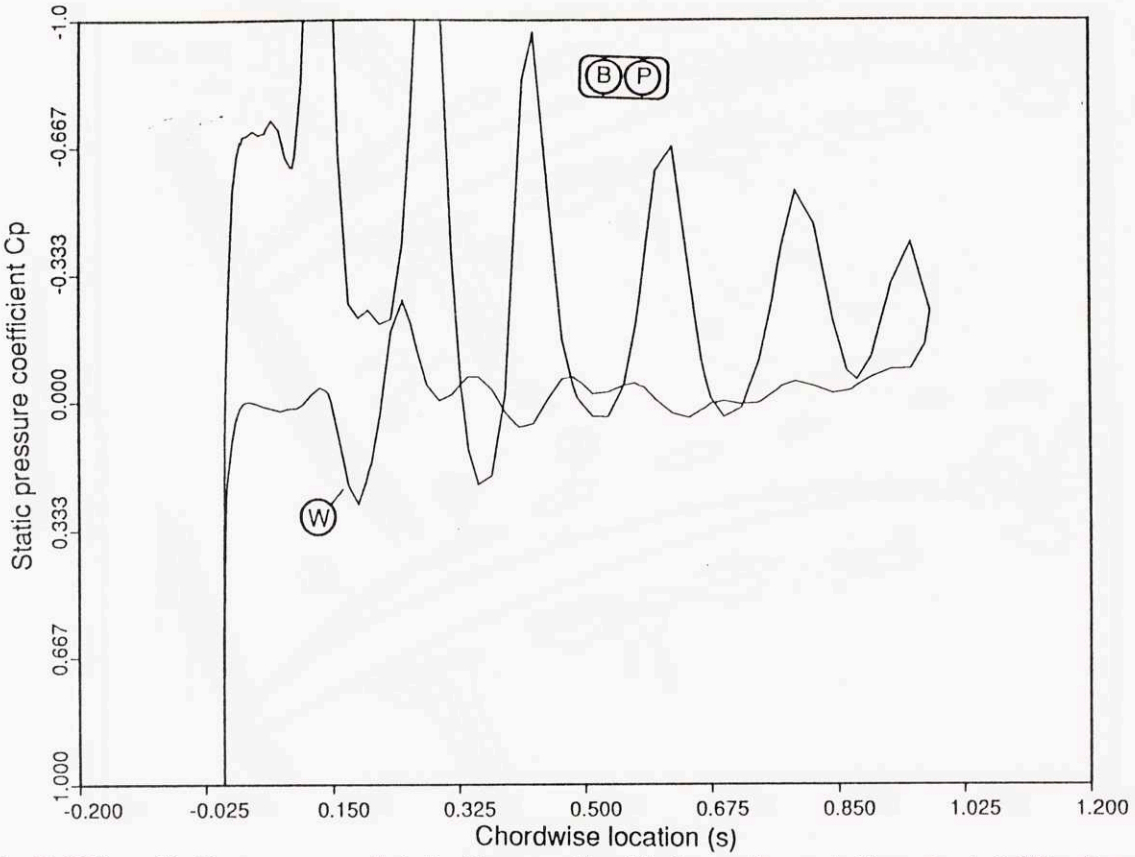

Fig.6.20b. Static pressure distribution on the blade surface at time $t_0 + 0.6T$. Laminar calculation with 20% wake thickness.

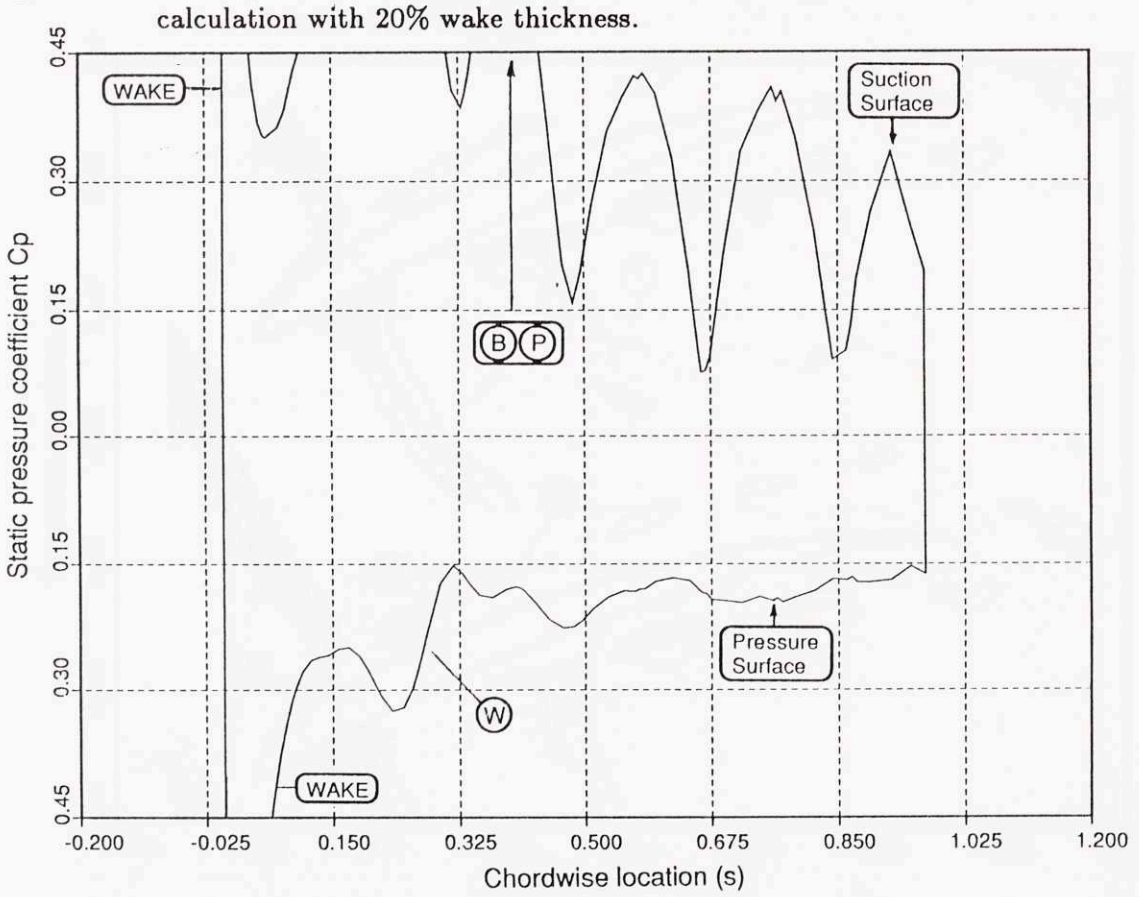

Fig.6.21. Distribution of the static pressure RMS on the blade surface from the calculation with 20% wake thickness.

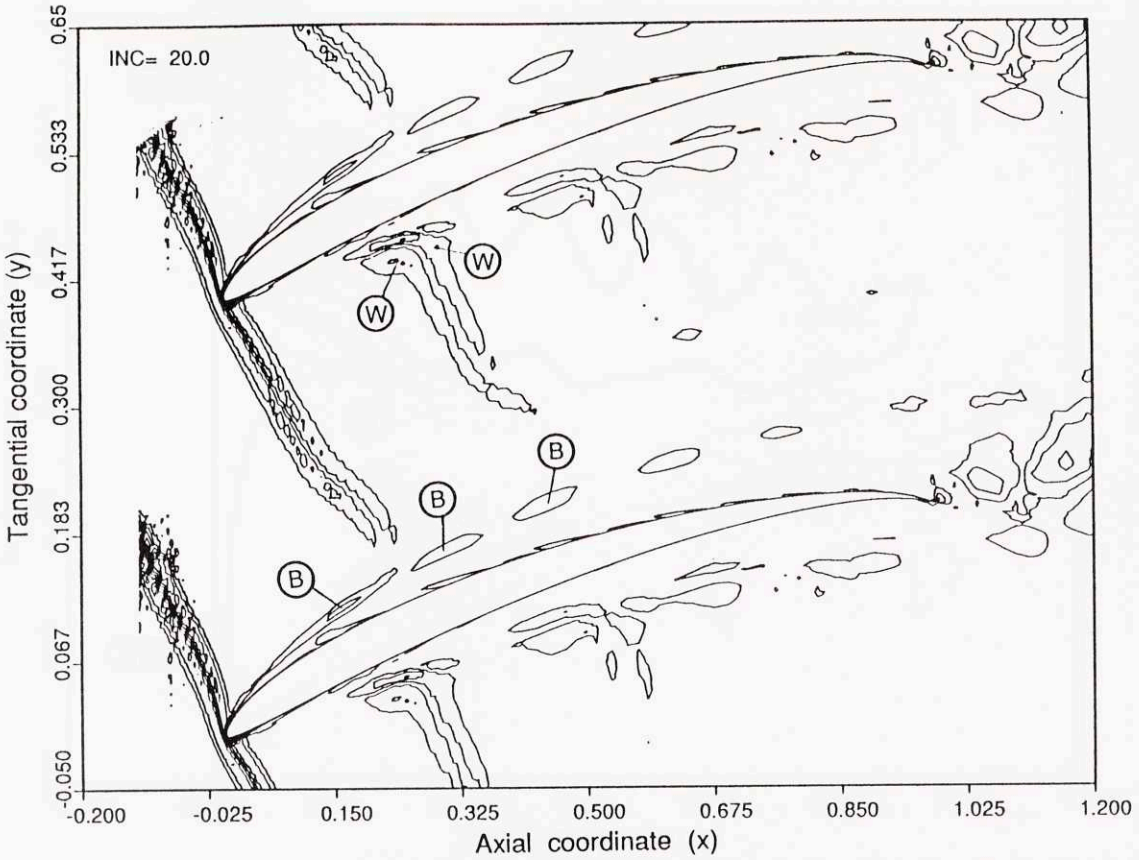

Fig.6.22a. Disturbance vorticity contours in the stator passage at time t_0. Laminar calculation with 5% wake thickness.

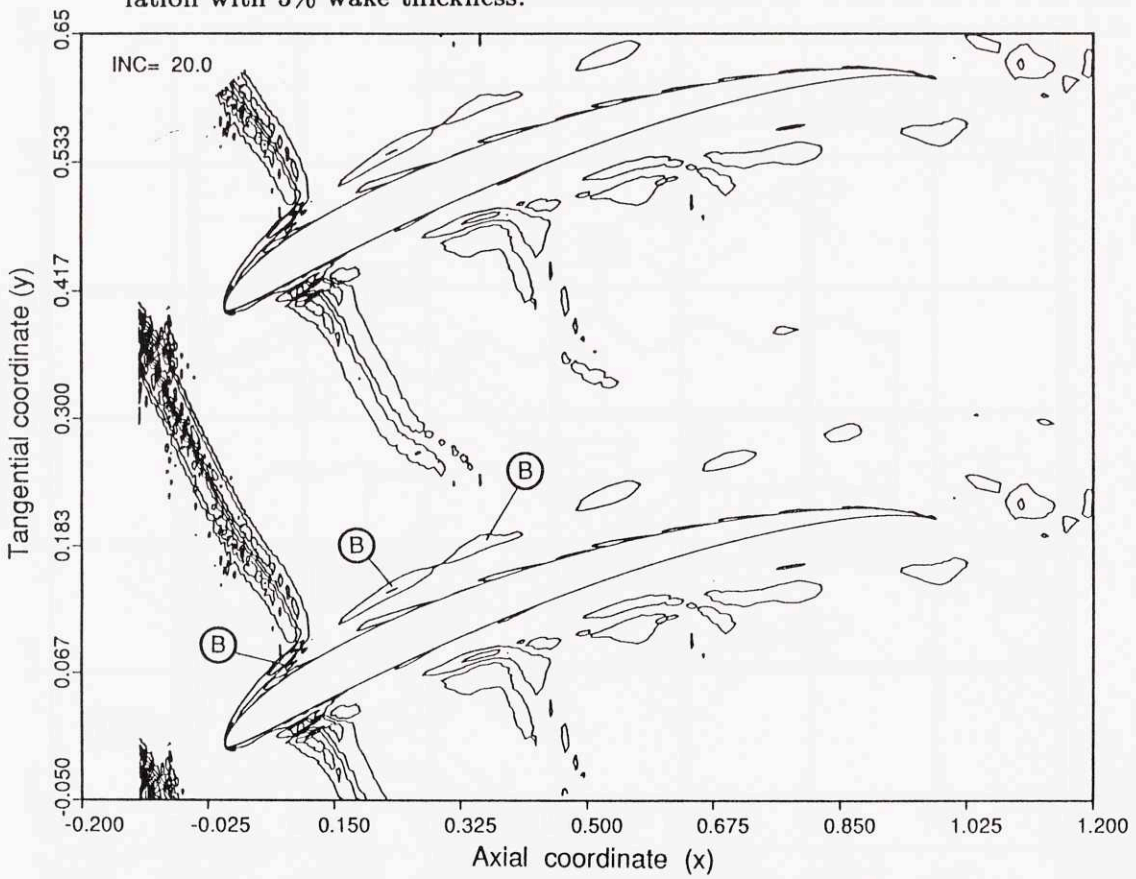

Fig.6.22b. Disturbance vorticity contours in the stator passage at time $t_0 + 0.6T$. Laminar calculation with 5% wake thickness.

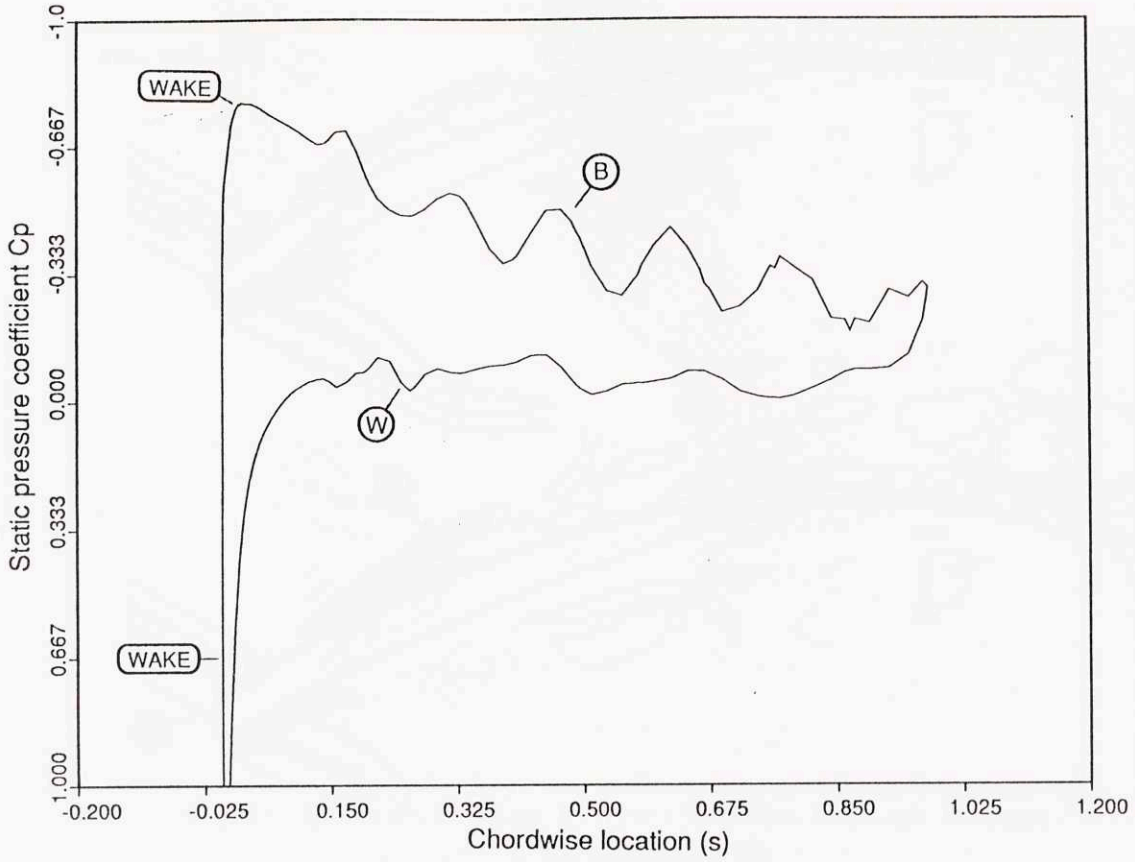

Fig.6.23. Static pressure distribution on the blade surface at time t_0. Laminar calculation with 5% wake thickness.

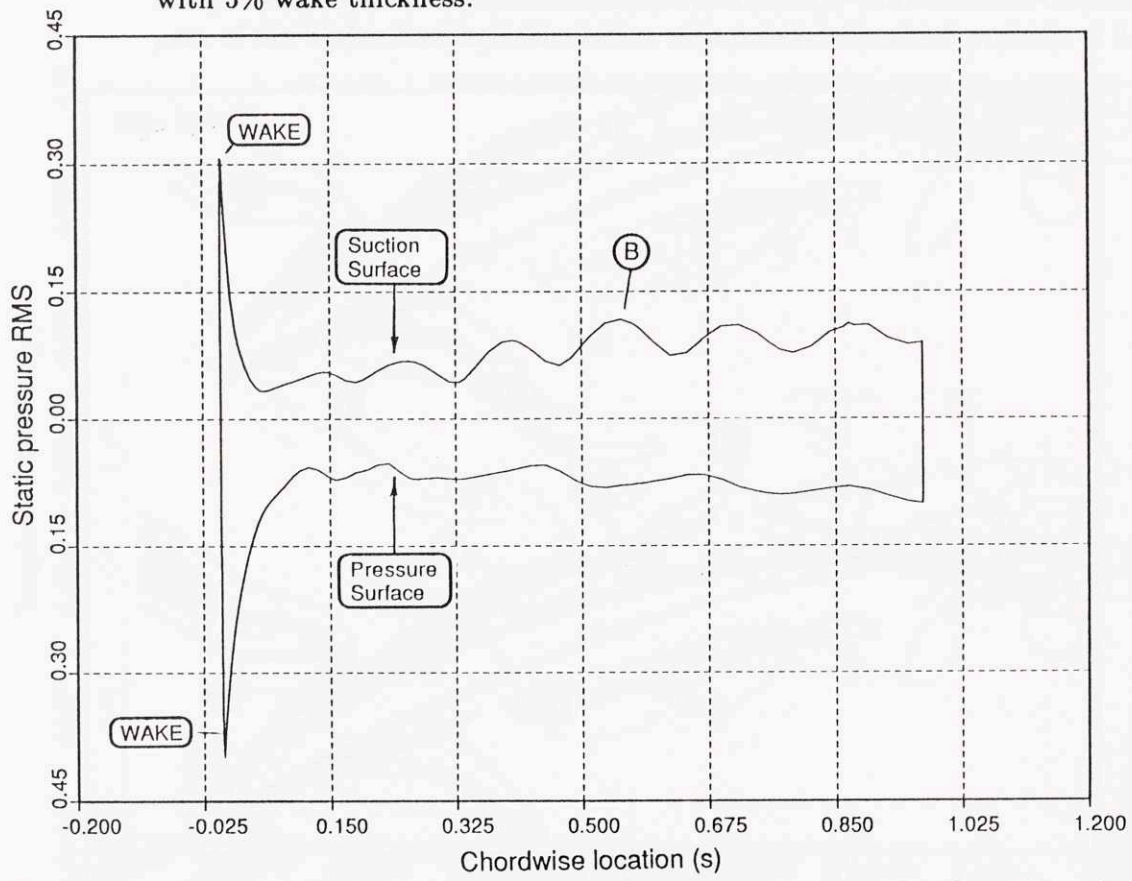

Fig.6.24. Distribution of the static pressure RMS on the blade surface from the calculation with 5% wake thickness.

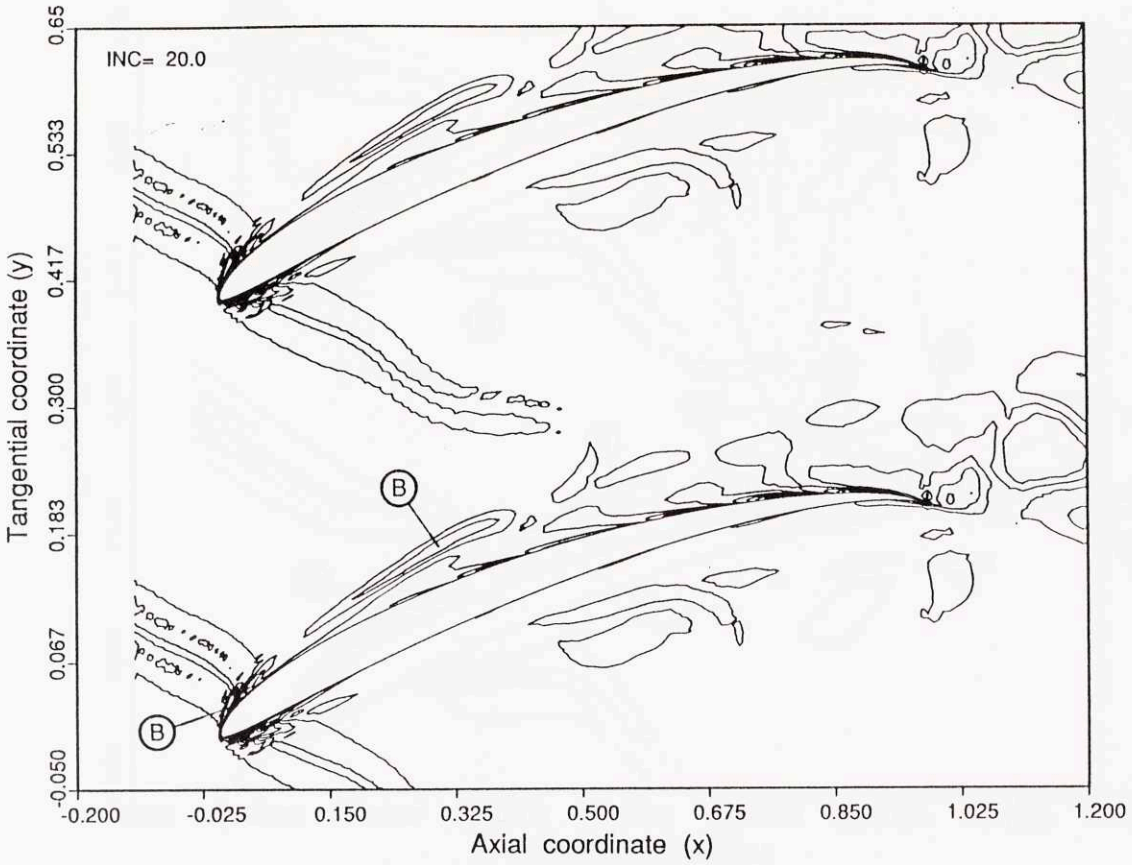

Fig.6.25a. Disturbance vorticity contours in the stator passage at time $t_0 + 0.2T$ showing the production of a B-vortex at the L.E., and a B/P-vortex street over the aft part of the blade. Laminar calculation with a reduced wake frequency of 2.5.

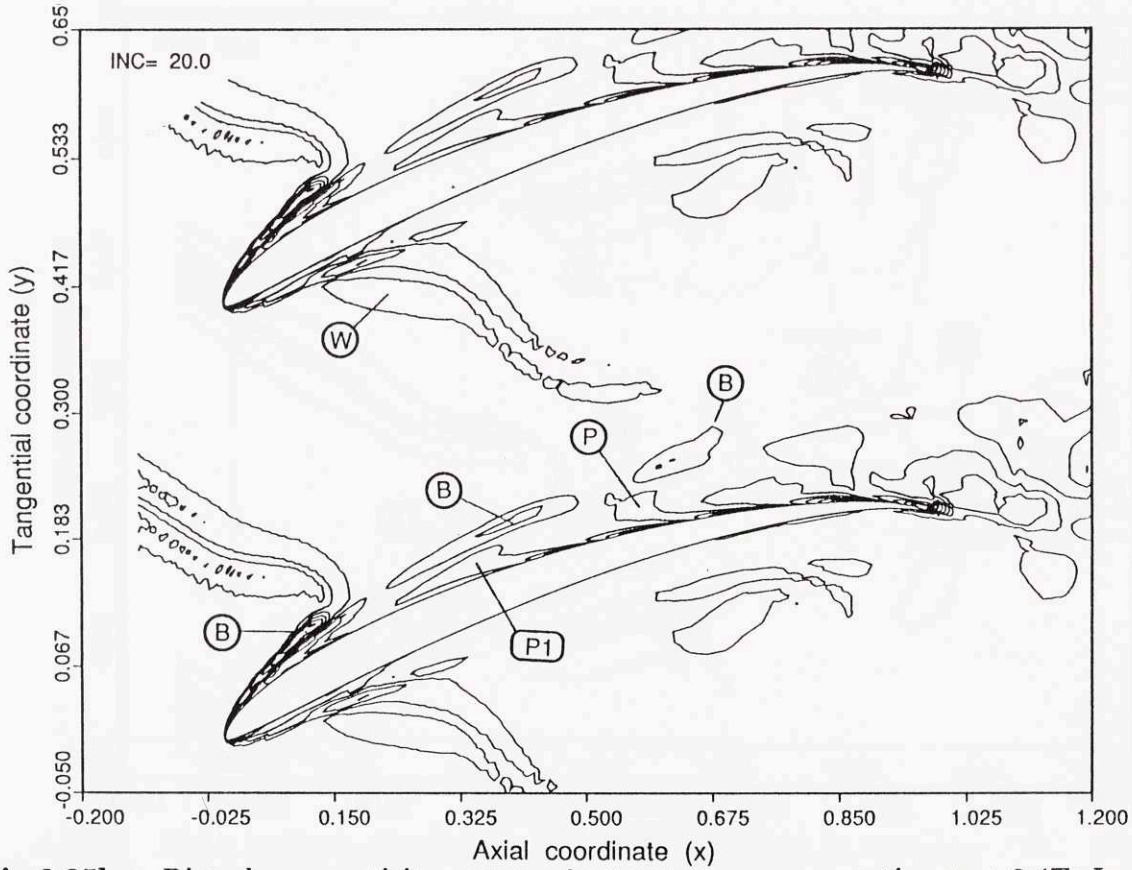

Fig.6.25b. Disturbance vorticity contours in the stator passage at time $t_0 + 0.4T$. Laminar calculation with a reduced wake frequency of 2.5.

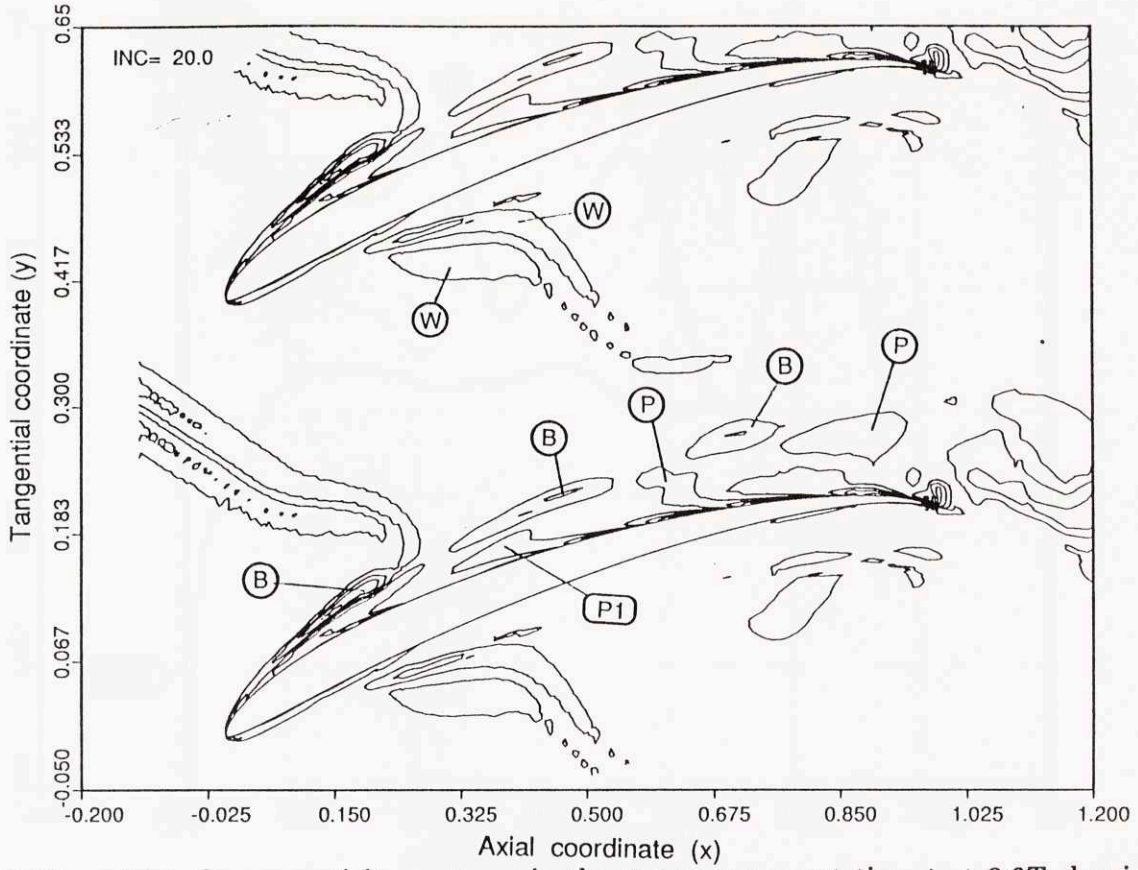

Fig.6.25c. Disturbance vorticity contours in the stator passage at time $t_0 + 0.6T$ showing the detachment of the P1-region by a strong B-vortex, and its evolution into a P-vortex. Laminar calculation with a reduced wake frequency of 2.5.

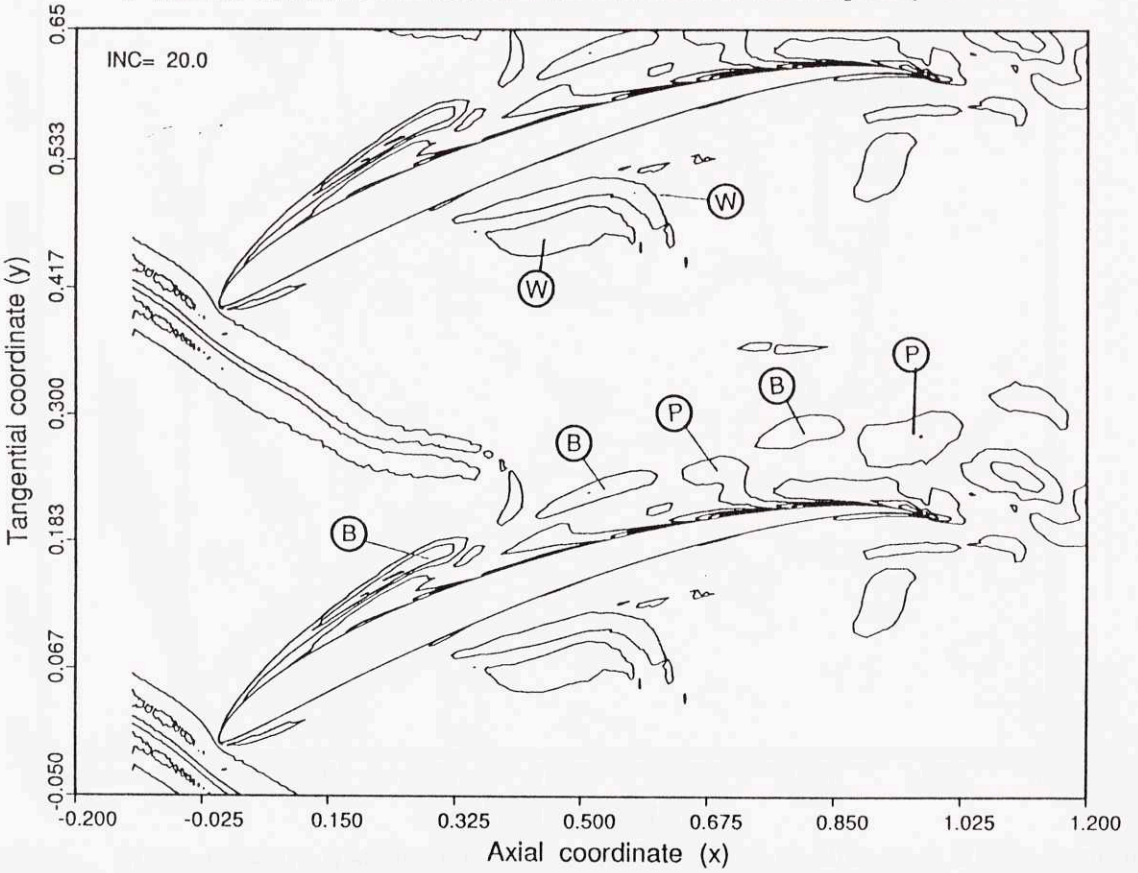

Fig.6.25d. Disturbance vorticity contours in the stator passage at time $t_0 + 0.8T$. Laminar calculation with a reduced wake frequency of 2.5.

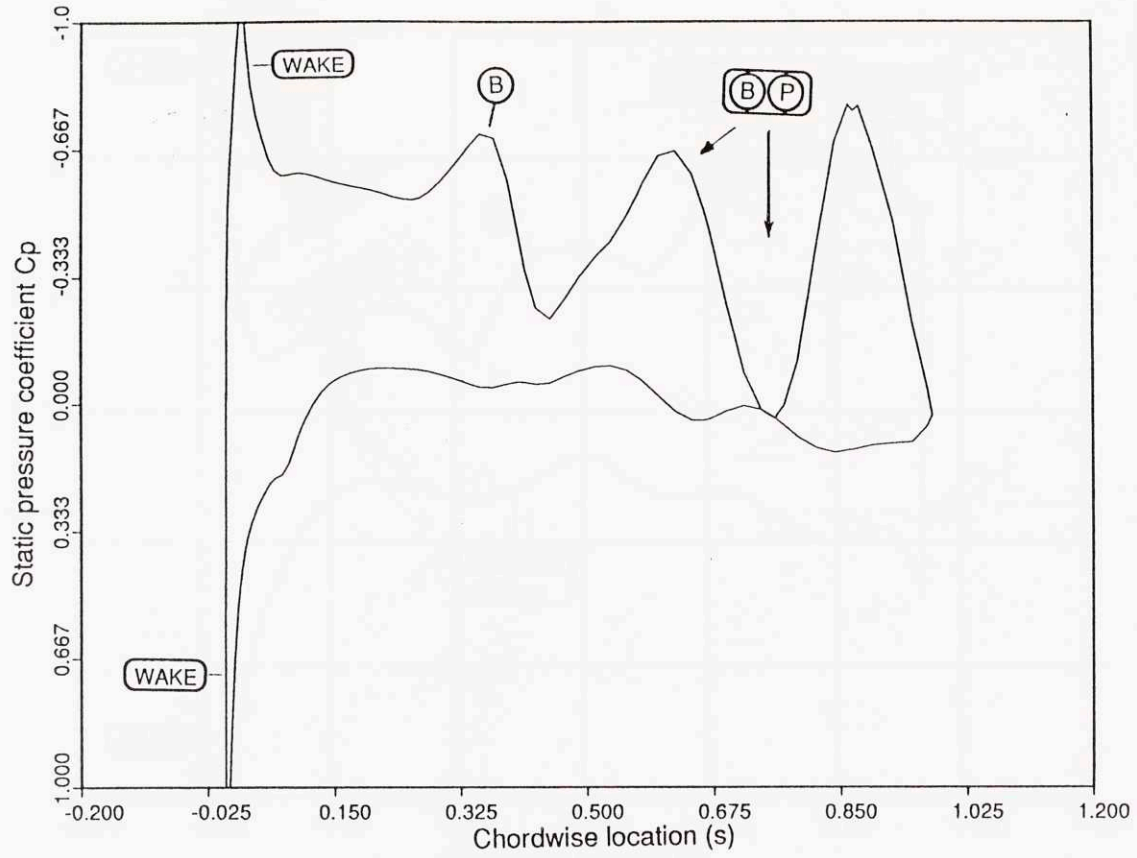

Fig.6.26a. Static pressure distribution on the blade surface at time t_0. Laminar calculation with a reduced wake frequency of 2.5.

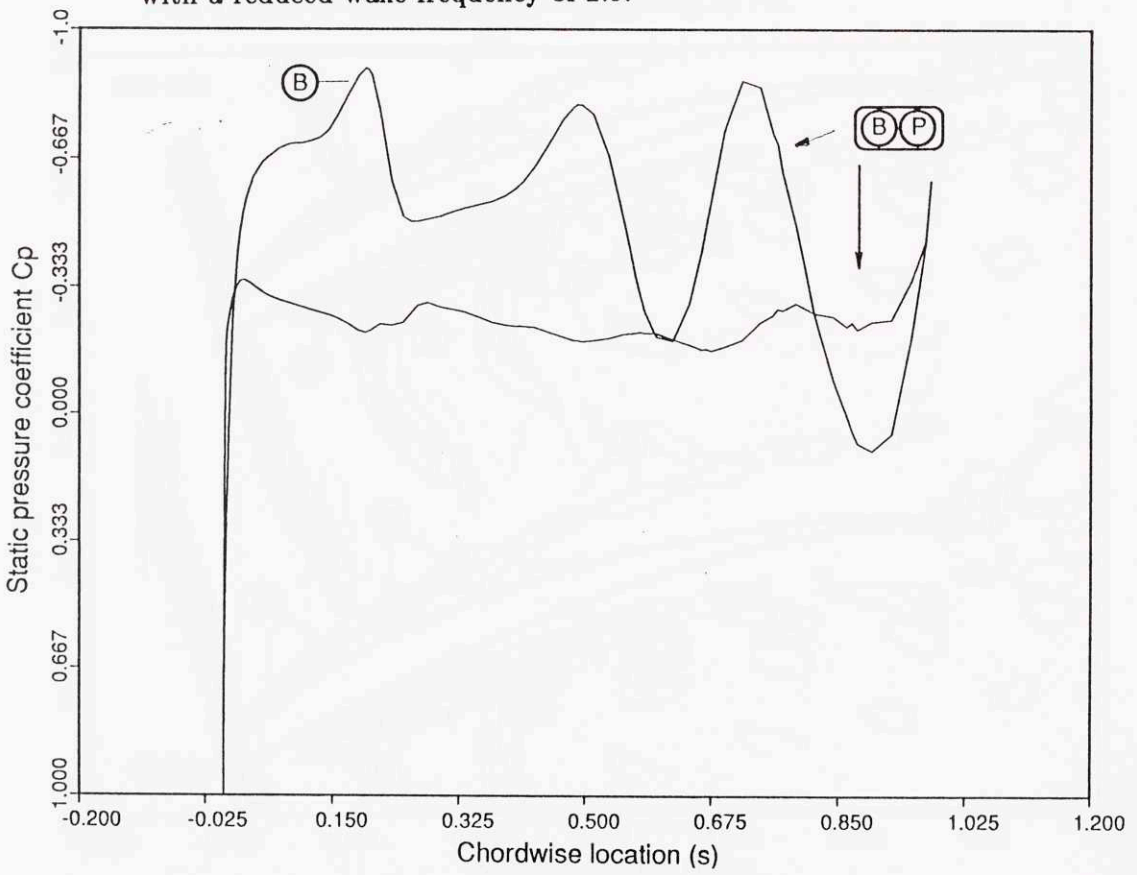

Fig.6.26b. Static pressure distribution on the blade surface at time $t_0 + 0.6T$. Laminar calculation with a reduced wake frequency of 2.5.

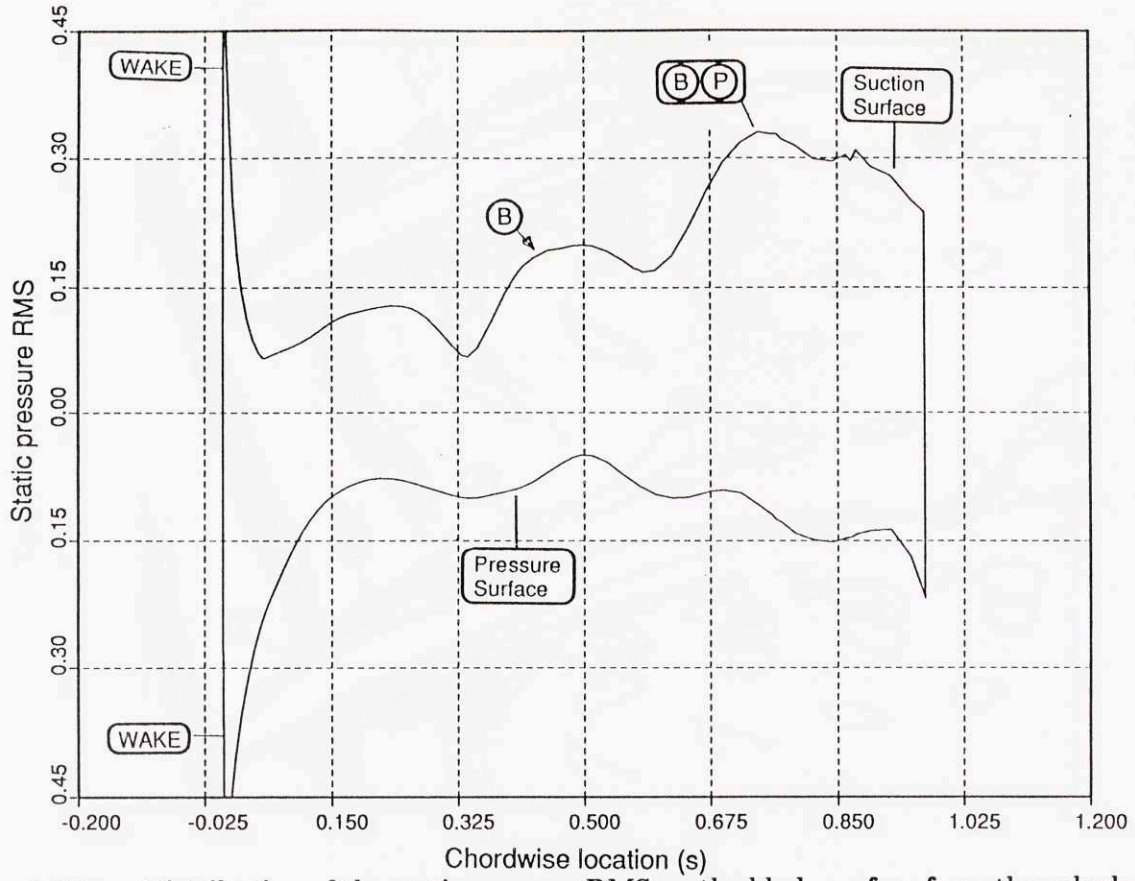

Fig.6.27. Distribution of the static pressure RMS on the blade surface from the calculation with a reduced wake frequency of 2.5.

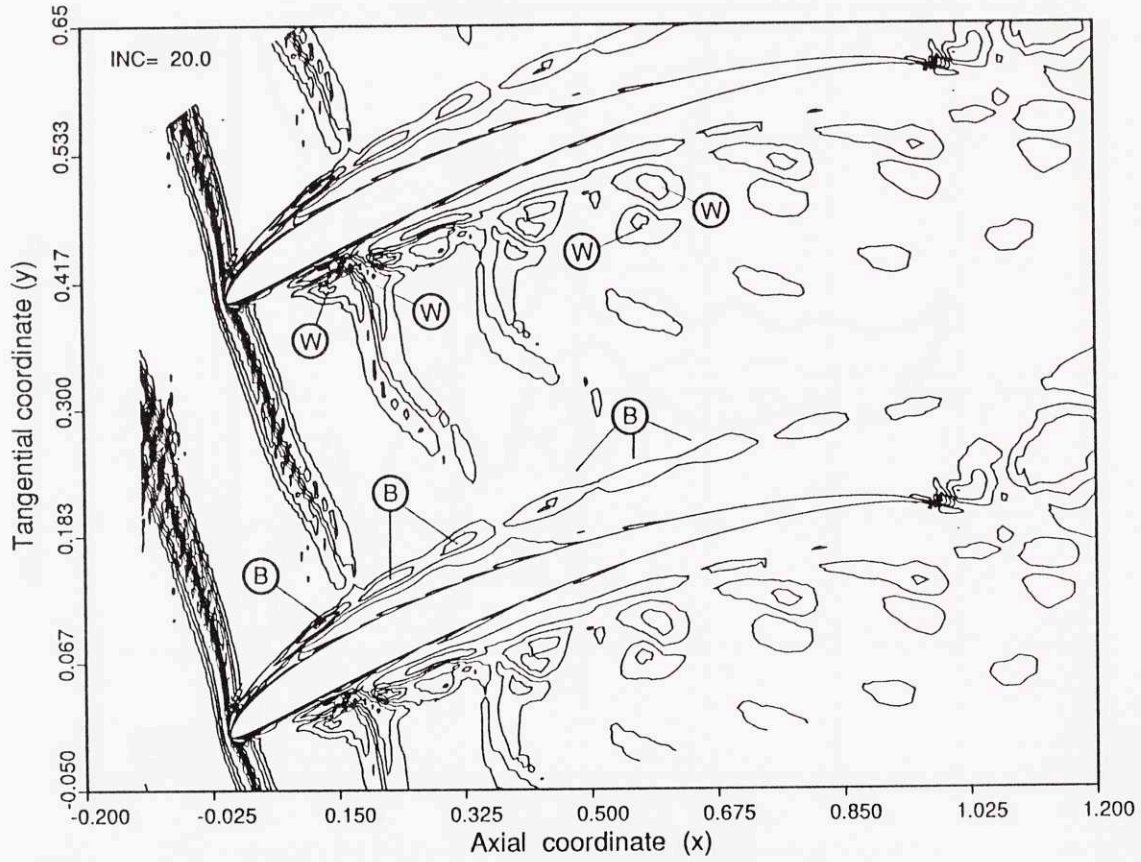

Fig.6.28a. Disturbance vorticity contours in the stator passage at time t_0. Laminar calculation with a reduced wake frequency of 7.5.

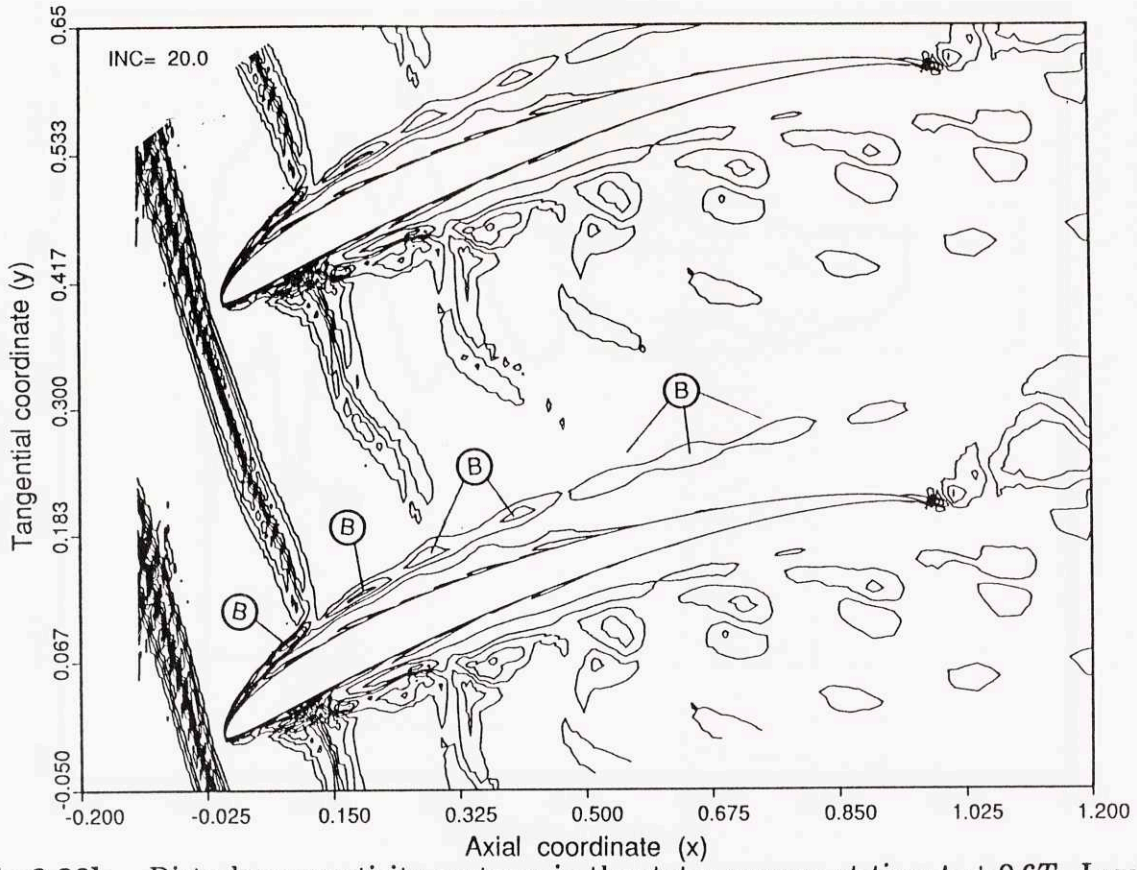

Fig.6.28b. Disturbance vorticity contours in the stator passage at time $t_0 + 0.6T$. Laminar calculation with a reduced wake frequency of 7.5.

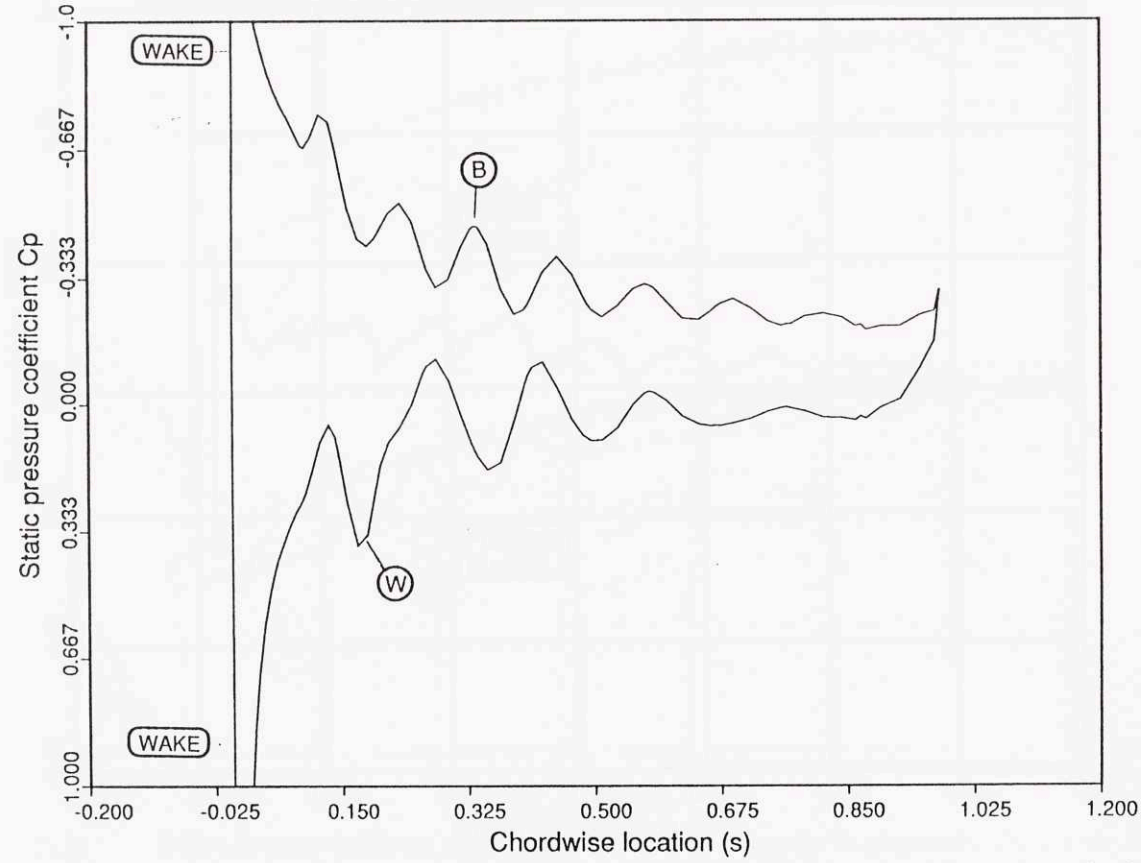

Fig.6.29a. Static pressure distribution on the blade surface at time t_0. Laminar calculation with a reduced wake frequency of 7.5.

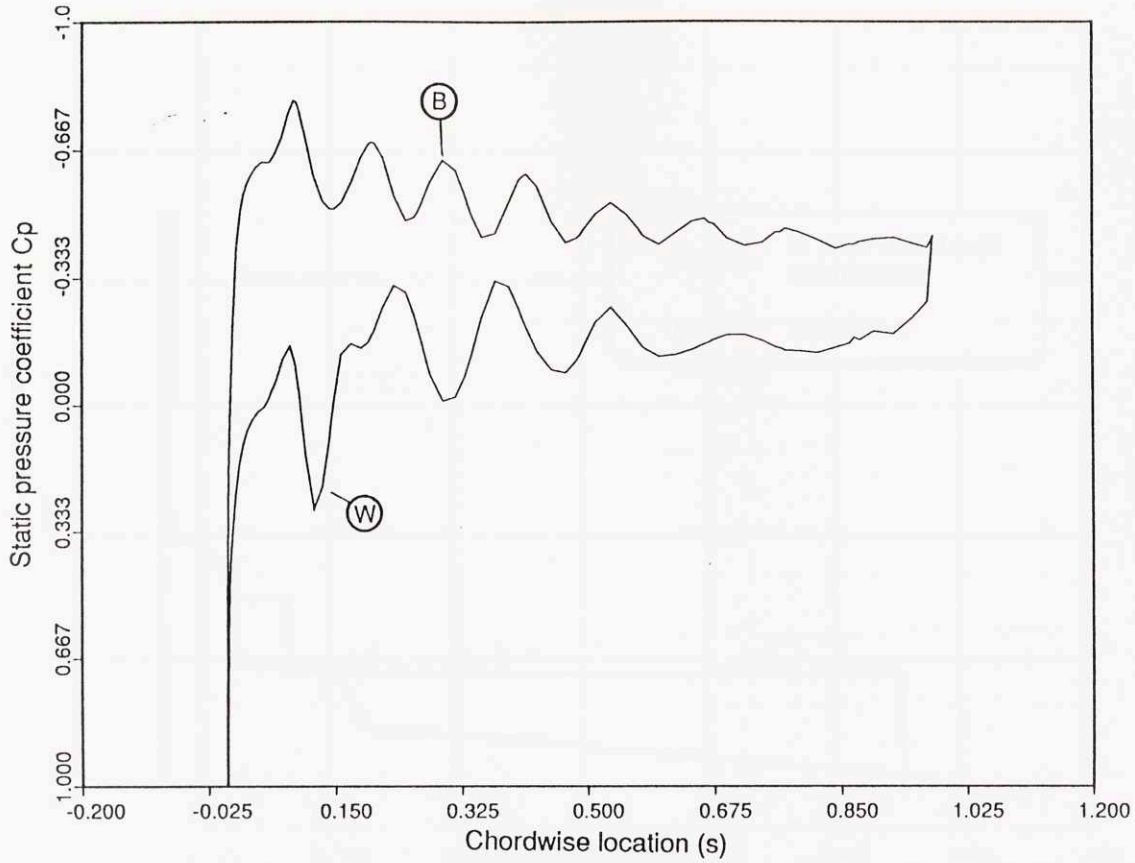

Fig.6.29b. Static pressure distribution on the blade surface at time $t_0 + 0.6T$. Laminar calculation with a reduced wake frequency of 7.5.

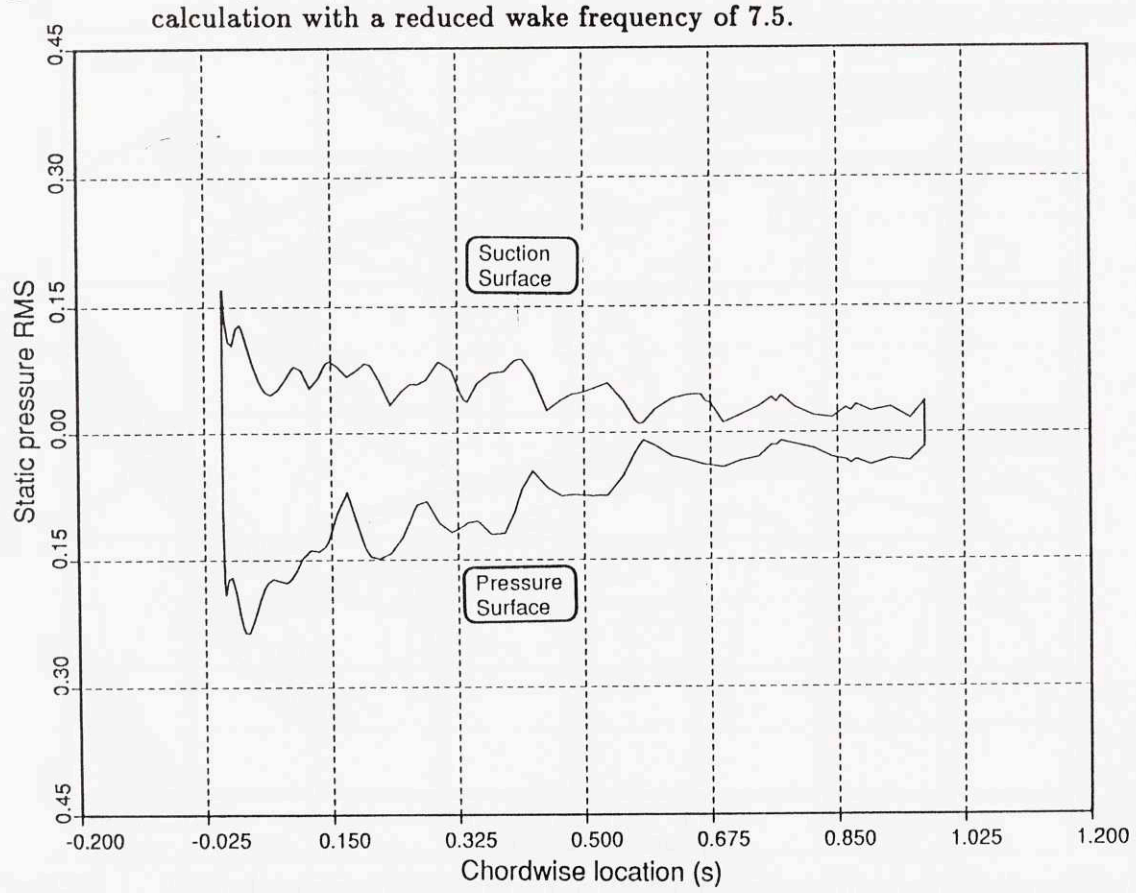

Fig.6.30. Distribution of the static pressure RMS on the blade surface from the calculation with a reduced wake frequency of 7.5.

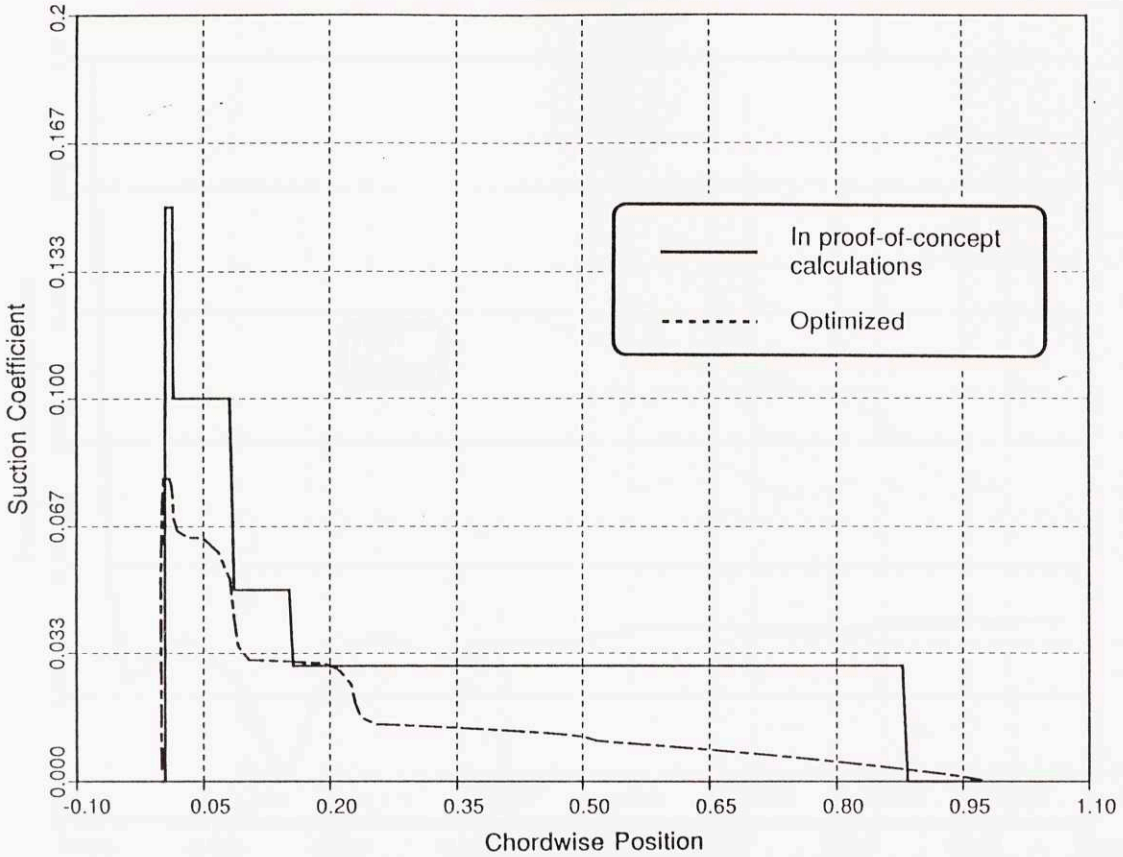

Fig.7.1. Distribution of the suction coefficient over the suction surface of the stator blade.

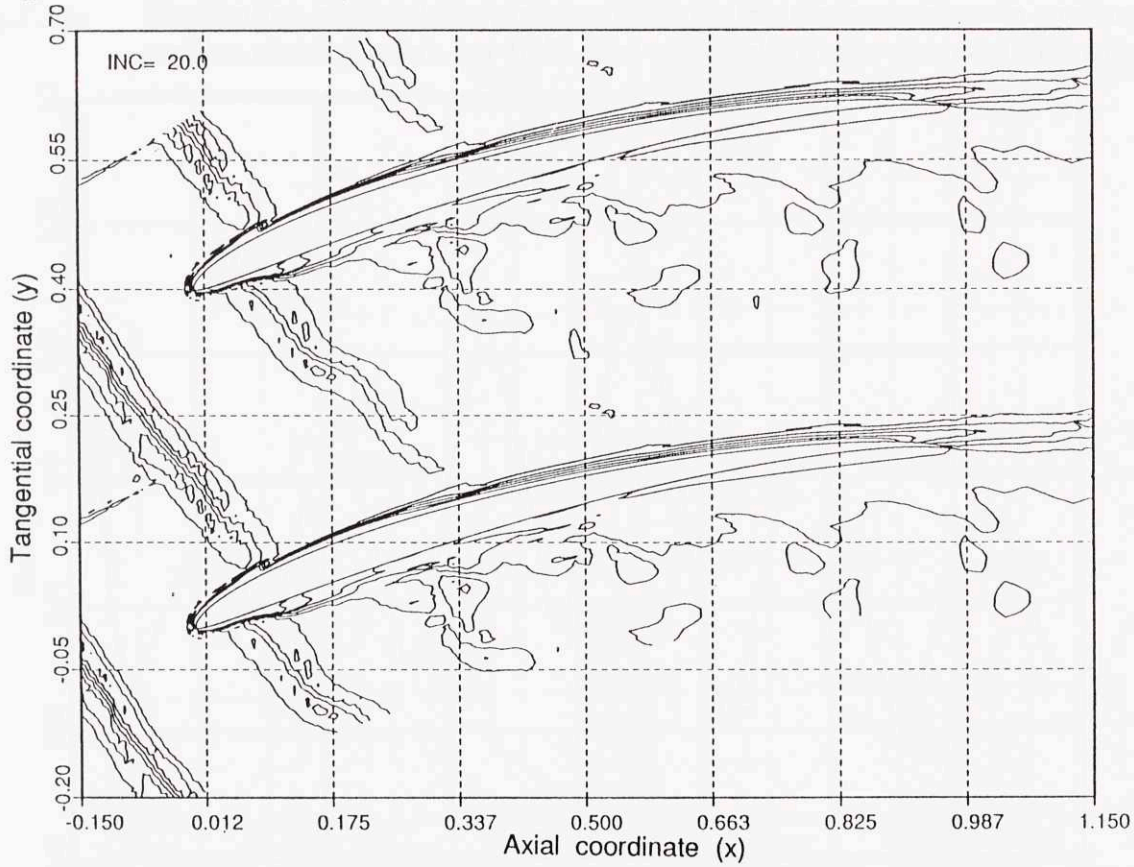

Fig.7.2. Disturbance vorticity contours in the stator passage in presence of suction, showing the absence of B-vortices and boundary layer disturbances.

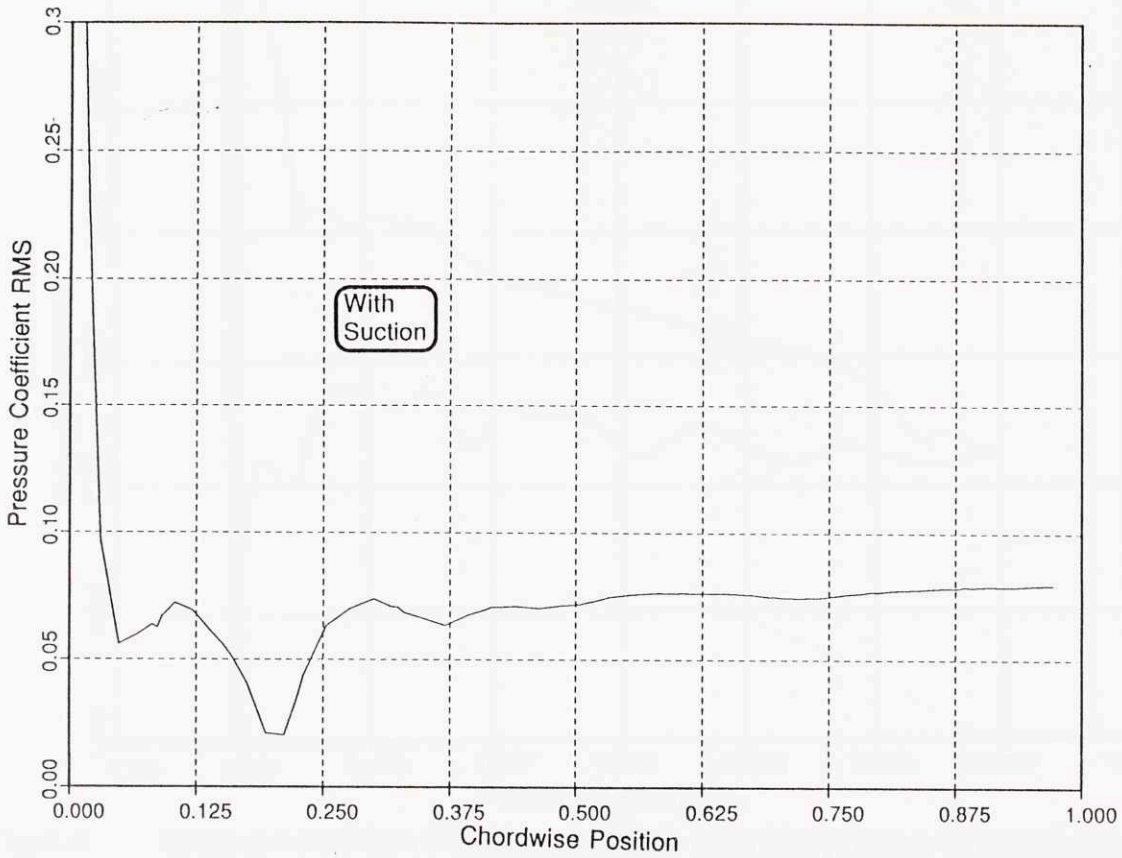

Fig.7.3a. Distribution of the static pressure RMS on the suction surface in presence of suction, showing a flat, low RMS level principally due to potential flow effects.

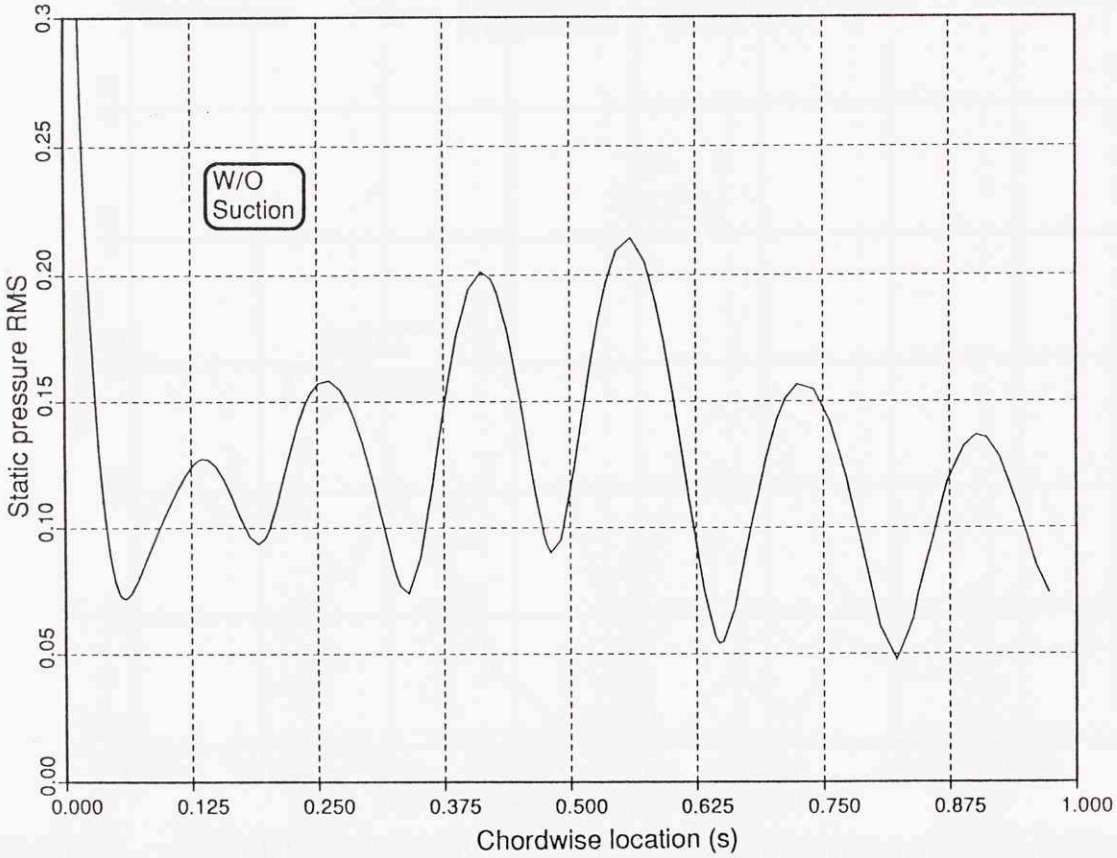

Fig.7.3b Distribution of the static pressure RMS on the suction surface in non-controlled unsteady flow (For comparison to Fig.7.3a).

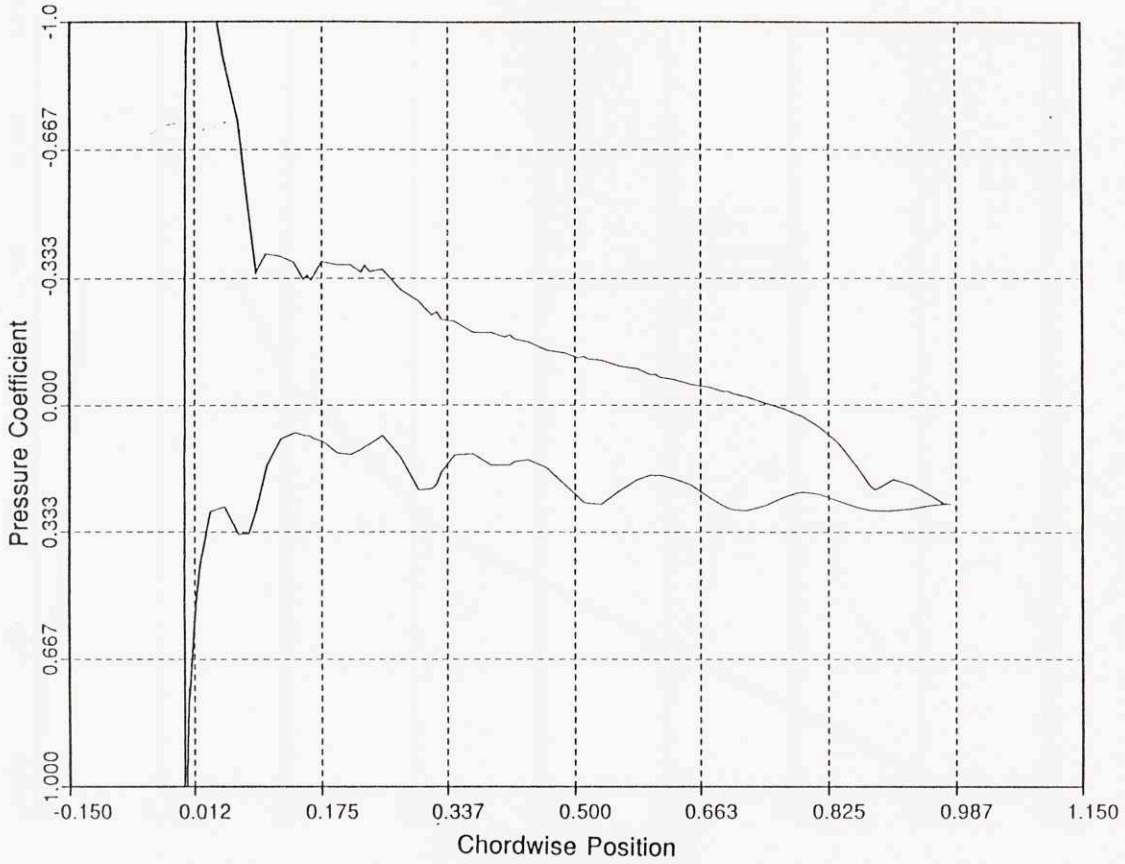

Fig.7.4 Static pressure distribution on the blade surface in presence of suction (The L.E. peak is constant in time and due to the high local suction).

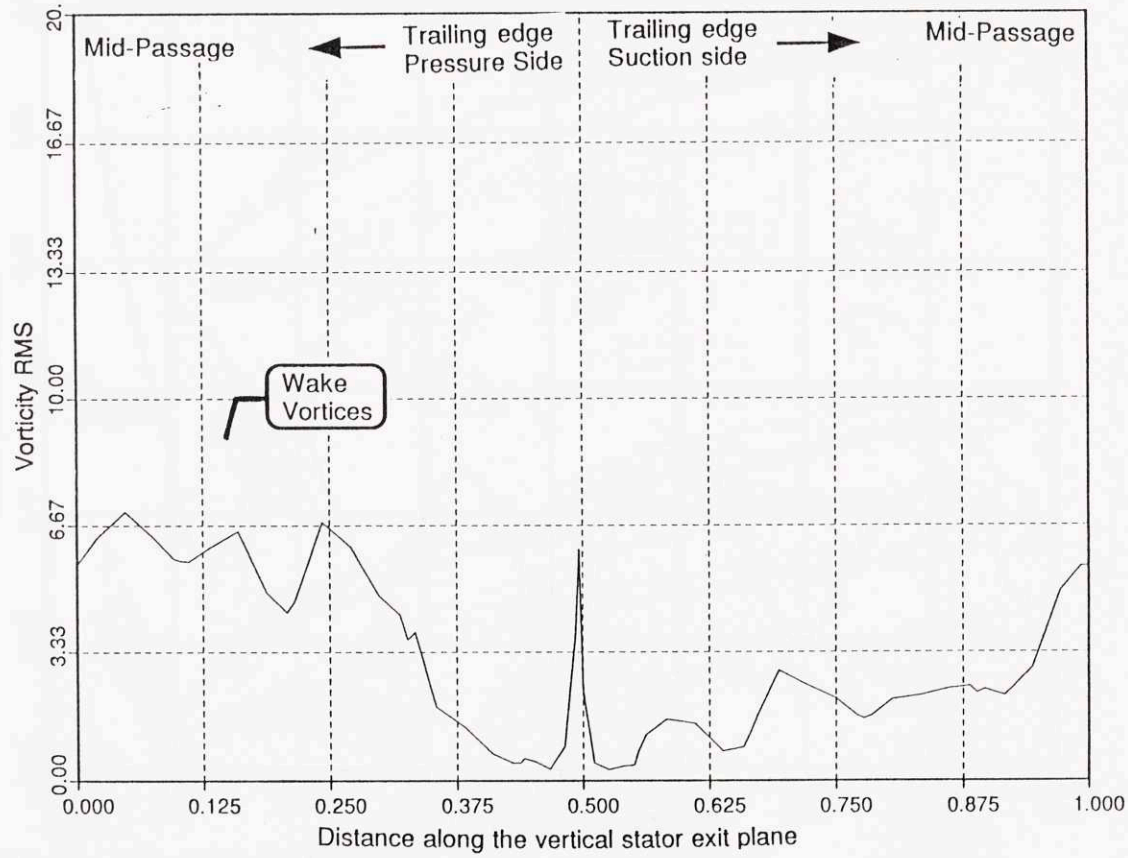

Fig.7.5. Distribution of vorticity RMS along the stator exit plane in presence of suction, showing that the signatures of the A- and B-vortices have been eliminated.

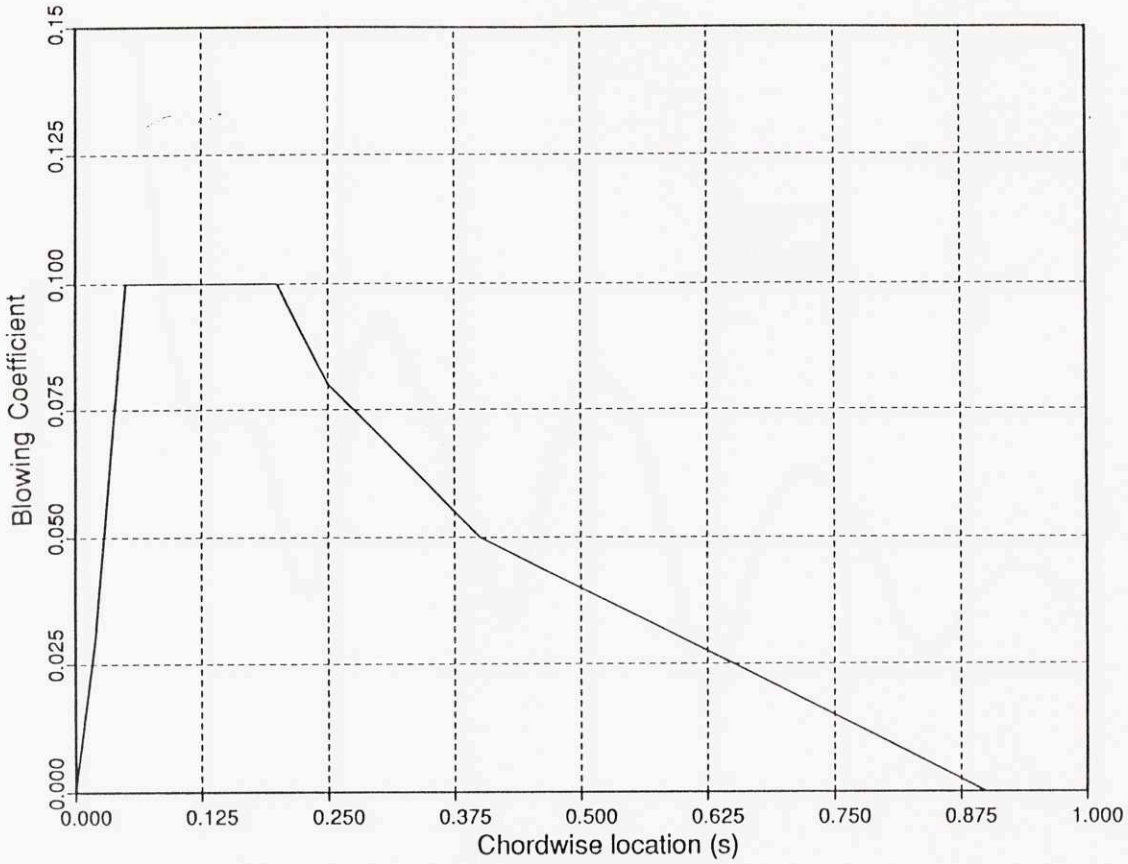

Fig.7.6. Distribution of the blowing coefficient over the pressure surface of the stator blade.

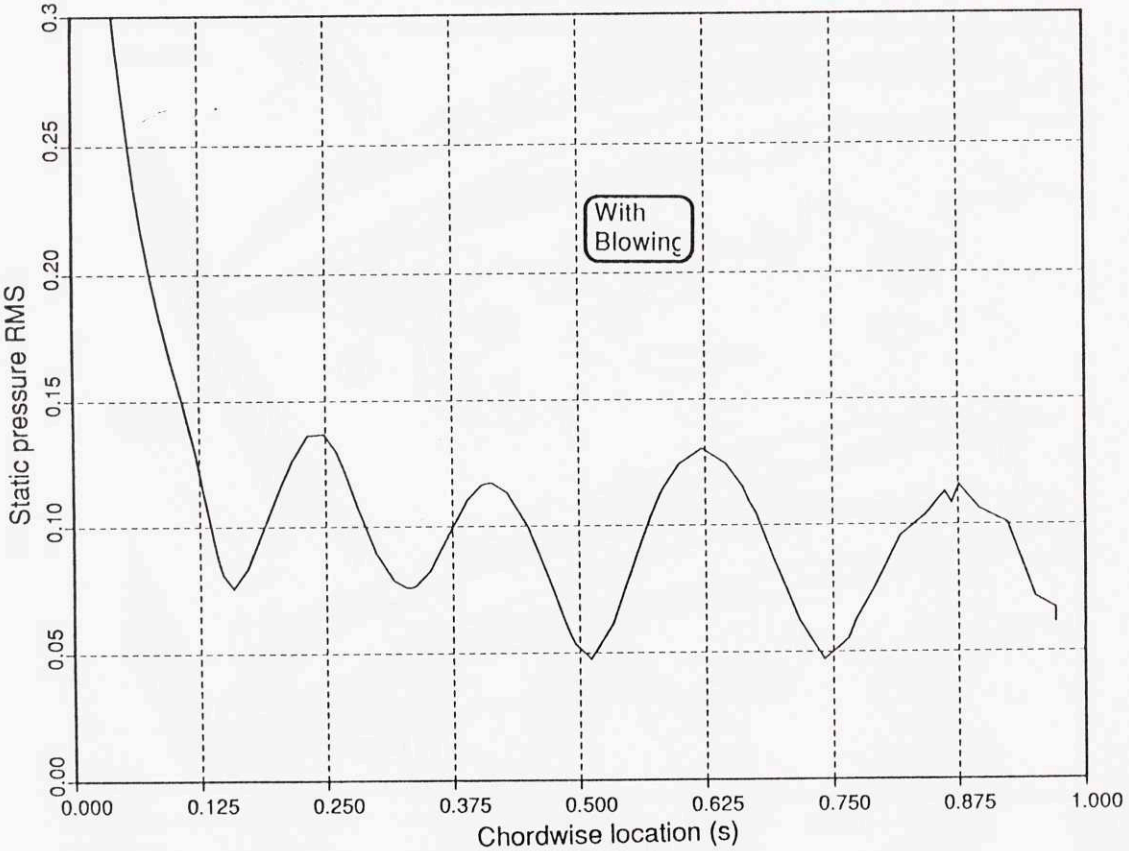

Fig.7.7a Distribution of the static pressure RMS on the pressure surface in presence of the distributed blowing from Fig.7.6.

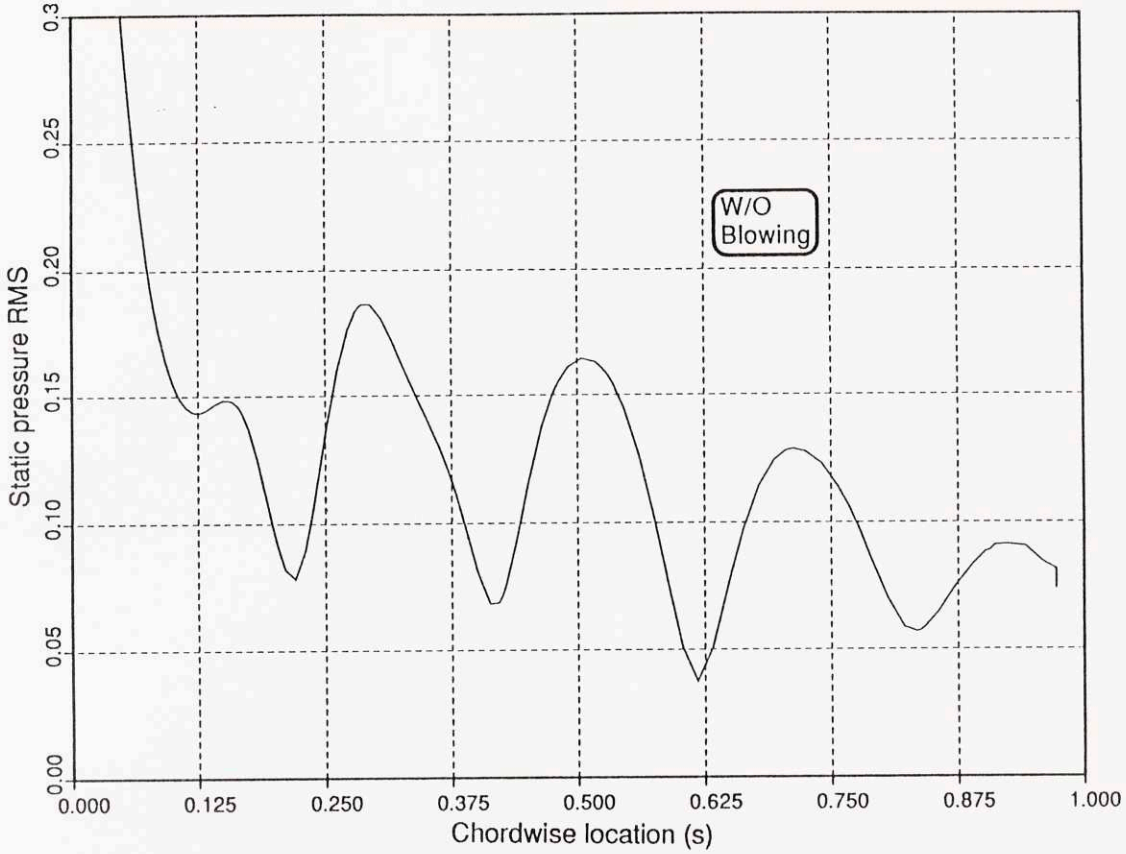

Fig.7.7b Distribution of the static pressure RMS on the pressure surface in non-controlled unsteady flow (For comparison to Fig.7.7a).

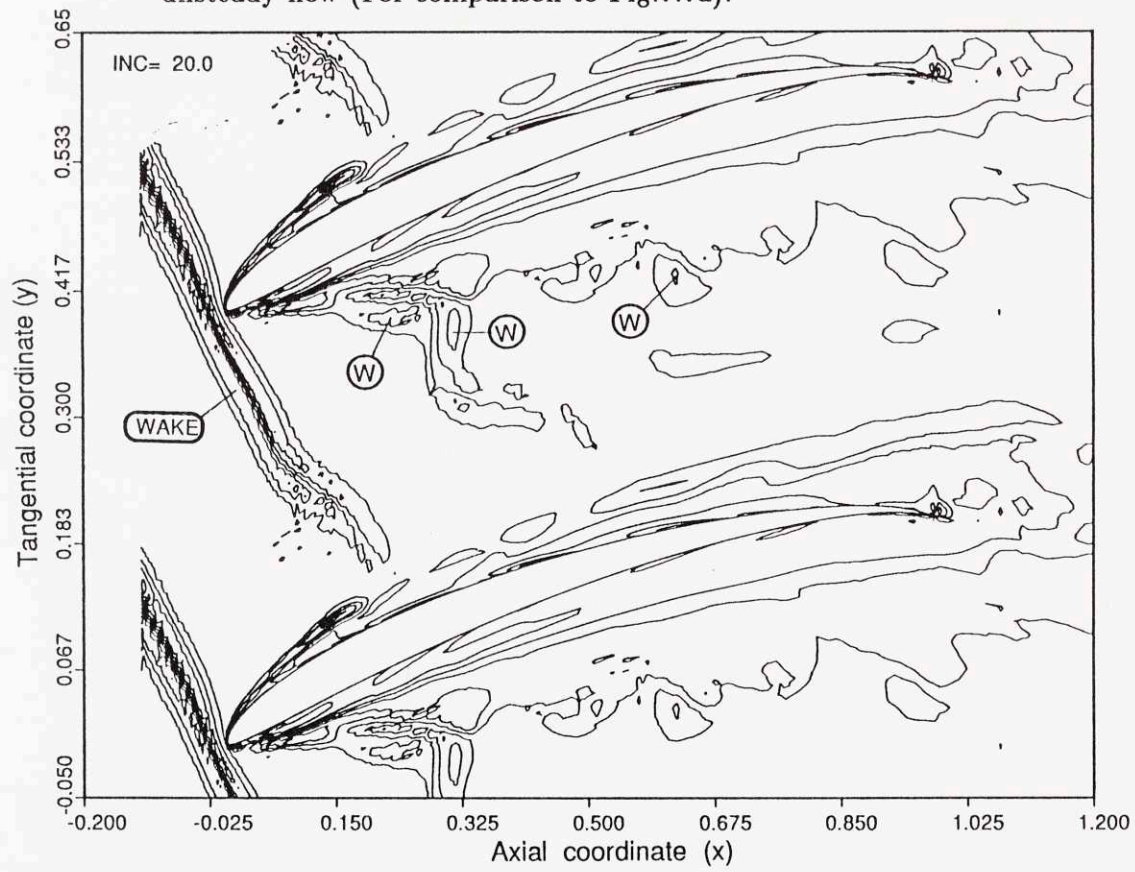

Fig.7.8. Disturbance vorticity contours in the stator passage in presence of the distributed blowing from Fig.7.6.